NORTHWESTERN UNIVERSITY

Thermal Properties of Wood-Derived Silicon Carbide and Copper-Silicon Carbide Composites

A DISSERTATION

SUBMITTED TO THE GRADUATE SCHOOL

IN PARTIAL FULFILLMENT OF THE REQUIREMENTS

for the degree

DOCTOR OF PHILOSOPHY

Field of Materials Science and Engineering

By

Kristen E. Pappacena

EVANSTON, ILLINOIS

December 2008

ABSTRACT

Thermal Properties of Wood-Derived Silicon Carbide and Copper-Silicon Carbide Composites

Kristen E. Pappacena

Wood-derived ceramics and composites have been of interest in recent years due to their unique microstructures, which lead to tailorable properties. The porosity and pore size distribution of each wood type is different, which yields variations in properties in the resultant materials. The thermal properties of silicon carbide ceramics and copper-silicon carbide composites derived from wood were studied as a function of their pore structures.

Wood was pyrolyzed at temperatures ranging from 300-2400°C to yield porous carbon. The progression toward long-range order was studied as a function of pyrolyzation temperature. Biomorphic silicon carbide (bioSiC) is a porous ceramic material resulting from silicon melt infiltration of these porous carbon materials. BioSiC has potential applicability in many high temperature environments, particularly those in which rapid temperature changes occur. To understand the behavior of bioSiC at elevated temperatures, the thermal and thermo-mechanical properties were studied. The thermal conductivity of bioSiC from five precursors was determined using flash diffusivity at temperatures up to 1100°C.

Thermal conductivity results varied with porosity, temperature and orientation, and decreased from 42-13 W/mK for porosities of 43-69%, respectively, at room temperature. The results were compared with to object-oriented finite-element analysis (OOF). OOF was also used to model and understand the heat-flow paths through the complex bioSiC microstructures. The thermal shock resistance of bioSiC was also studied, and no bioSiC sample was found to fail catastrophically after up to five thermal shock cycles from 1400°C to room temperature oil.

Copper-silicon carbide composites have potential uses in thermal management applications due to the high thermal conductivity of each phase. Cu-bioSiC composites were created by electrodeposition of copper into bioSiC pores. The detrimental Cu-SiC reaction was avoided by using this room temperature processing technique. Thermal conductivity values were determined using flash diffusivity at temperatures up to 0-900°C. In the axial orientation, thermal conductivities of up to 207 W/mK at 0°C and 178 W/mK at 900°C were achieved. OOF was also used to model the heat flux distributions and to obtain effective thermal conductivity values for these complex microstructures. The thermal expansion coefficient was determined to be 6.98 x 10^{-6}/°C at room temperature.

Acknowledgements

First and foremost, my advisor, Professor Katherine Faber, has been an inspirational mentor and role model. She has been unstinting in her willingness to discuss research, answer questions, and offer guidance and sound advice. I would also like to thank my committee members, Professors David Dunand, Thomas Mason, David Green, and Scott Barnett for their generous time and guidance throughout this process.

This research would not have been possible without the help of many professional collaborators around the country and around the world: Hsin Wang and Wallace Porter at Oak Ridge National Laboratory for assistance with thermal conductivity measurements; Francisco M. Varela-Feria and Julián Martínez-Fernández in the Department Física de la Materia Condensada, Universidad de Sevilla and Sujing Xie from EPIC, Northwestern University for assistance with TEM and analysis; and Ed Fuller for valuable assistance with OOF.

I would like to thank the past and present members of the Faber research group: Chris Weyant, Vikram Kaul, Tom Wilkes, Bryan Harder, Michelle Seitz, Harold Hsiung, Noah Shanti, Matt Johnson and Zun Chen. I would like to thank them for all of the conversations both science related and otherwise, and for all of the good times over the years including group lunches, movie nights, conferences, pranks, coffee hours, forcing me to be a fearful leader, and allowing me to perfect funfetti cake baking. They have been wonderful colleagues, as well as friends.

Next, I would like to thank all of my friends but particularly those named here: Alice, Katy and Jamie, who have long been my closest friends - I would like to thank them for all of the support, friendship, chats and visits over the years. They have been important parts of each stage of my life thus far, and I know that will continue in the future. Lesley, Megna and Renee - I would like to thank them for smoothie nights, Argo tea dates, pep talks, countless IM conversations, running conversations, spontaneous roommate conversations - I could not have stayed sane without them. Mat - I am so grateful that he has entered my life, for support, sushi, tv, rides home, and of course for all of the thesis formatting help.

Most of all I would like to thank my family, whose influence on me I cannot even begin to express. My grandparents, aunts, uncles, and cousins have all been amazing role models over the years. My cats, Grace and Addison, who have added love and entertainment in my life over the last 1.5 years. My sister, Lauren (Lucy), who has been a great sister and fashion consultant, and an even better friend. Last but not least, my parents have offered me unconditional love and support and so many opportunities throughout my life. They have helped me achieve each of my goals, and I would not be who I am today without their guidance and example.

This research was made possible through a Graduate Research Fellowship and grants DMR 0710630 and DMR0244258 from the National Science Foundation.

Table of Contents

List of Tables

List of Figures

CHAPTER 1

Introduction

1.1. Motivation

Recently, materials scientists have shifted focus onto porous materials as solutions to a variety of engineering problems. The inclusion of porosity into materials lowers their densities, and consequently weights, and in many cases, also affects their properties. For example, thermal conductivity, elastic modulus, and strength, have all been shown to decrease as a result of porosity in materials.[1] Porous ceramic materials, in particular, have many potential uses in high temperature environments due to their high melting points and structural integrity at high temperatures. Pores in ceramics are often viewed as a negative attribute. However, there are many instances including molten metal filters, diesel particulate filters, catalyst supports, thermal insulators, heat exchangers, and aerospace applications, where pores enhance the usefulness of a material, and where a dense material would not suffice.[2] These potential applications make porous ceramic materials an interesting class to study.

There are many processing methods from which porous ceramics can be created. However, ceramics derived from wood take advantage of a naturally occurring porous microstructure, eliminating several of the high energy steps associated with porous ceramic processing. One such ceramic, biomorphic silicon carbide (bioSiC), is silicon carbide derived from wood precursors. It is fabricated by pyrolysis of wood yielding a carbon

scaffold, which is subsequently melt infiltrated with silicon. There are a wide variety of microstructures of wood in existence, and thus a wealth of possible wood-derived bioSiC pore distributions. This plethora of possible microstructures leads to the potential of tailorable resultant properties.

Porous materials also offer a template for further infiltration to produce composite materials. In the case of SiC, which is known for its high thermal conductivity, bioSiC affords the development of composites for thermal management. Thermal management is a challenging problem faced in industry, particularly in areas of microelectronics and optoelectronics.[3] As electronic devices become smaller in size, they generate more heat, and thus more efficient heat sinks and electronic packages are necessary for quick heat removal, to maintain the electronic part integrity. These thermal management materials need to have a combination of high thermal conductivity for efficient heat removal, a thermal expansion coefficient that is close in value to the substrate, to avoid potential thermal stresses at elevated temperatures, low density in order to minimize weight, and low cost. It is also desirable for materials to be processed in the net-shape, due to difficulty in machining materials containing hard ceramic phases. Many materials have one or more of these desired property values. However, the perfect material containing all of these requirements is nonexistent. Composite materials are an ideal solution because they take advantage of the desirable properties of each constituent phase in order to improve the resultant material. A table of properties of traditional and ultra-high thermal conductivity thermal management materials is shown in table 1.1[4].

Silicon carbide-aluminum composites are widely used in electronic packaging applications, including notebook computers, and cellular telephones.[3] However, there is still room

Table 1.1. Properties of Thermal Management Materials[4]

Material	Thermal Conductivity (W/mK)	CTE (ppm/K)	Specific Gravity
Diamond Particles in Copper Matrix	465-600	4.0-7.7	5.0-5.5
Silicon Carbide Particles in Aluminum Matrix	150-255	4.8-16.2	2.7-3.1
Copper/Moly/Copper	125-305	6.2-6.8	9.3-9.8
Diamond Particles in Silicon Carbide Matrix	600-680	1.8	3.3
Carbon Fibers in Carbon Matrix	40-400	-1	1.9-2.0

for improvement, as aluminum only has a thermal conductivity of 218 W/mK at room temperature.[3] Copper has a significantly higher thermal conductivity of ∼400 W/mK.[3] In addition, copper has a lower thermal expansion coefficient than aluminum. The combination of these two properties makes copper a potential substitute for aluminum in a silicon carbide matrix composite, with the prospect of improved thermal properties.

1.2. Objectives

For a material that is designed for potential uses in high temperature applications, it is important to obtain a thorough understanding of its thermal properties. Starting with bioSiC, the first objective is to understand the thermal properties as they relate to the varying microstructures from different wood precursors. While the microstructure and mechanical properties of wood-derived silicon carbide have been well characterized, the thermal conductivity and thermal expansion coefficient have previously only been studied below room temperature, and for materials containing residual silicon.[5,6] The thermal shock resistance had not previously been characterized. In this work, the thermal conductivity, thermal expansion coefficient and thermal shock resistance were studied as a function of wood type, and thus porosity and orientation. To further understand the relationship between the thermal properties and the complex, wood-derived microstructure, finite-element analysis was performed.

Once the thermal properties of porous bioSiC are well-characterized, the next objective is to use bioSiC as a template material for fabrication of high thermal conductivity composites. Previous work has utilized the wood-derived silicon carbide scaffold to create aluminum-silicon carbide composites and copper-silicon carbide composites via melt

infiltration.[7–10] In this work, the objective is to use wood-derived silicon carbide as a matrix for copper-silicon carbide composites, by optimizing and utilizing a low temperature processing technique, in order to create a composite material with enhanced thermal properties.

For the wood-derived metal-silicon carbide composites that have previously been fabricated, the mechanical properties have been studied.[7–10] However, the thermal properties of any of these composites have not yet been investigated. Thus, the third objective is to assess the thermal properties of these newly created composites. This is to be done by measuring the thermal conductivity and thermal expansion coefficient, and subsequently performing finite-element analysis on these materials to further understand the microstructure and thermal property relationship.

This thesis will begin by providing background information on processing techniques for both porous materials and their resulting composites, and the methods of assessing the resulting thermal properties of these materials. Then processing and initial characterization of the carbon scaffold, resulting bioSiC and Cu-bioSiC composites will be discussed in detail. Following this, the thermal properties of bioSiC, and then Cu-bioSiC composites, will be determined. Lastly, a summary will be presented with an assessment of these materials for potential high temperature and thermal management applications.

CHAPTER 2

Background

This chapter describes the necessary background for an understanding of porous ceramics, particularly the processing methods and advantages of use of porous silicon carbide derived from wood. In addition, there is a focus on composite materials processing, utilizing electrodeposition as a way to produce a metal-ceramic composite. The techniques used for thermal property characterization of both porous and composite materials are also discussed.

2.1. Porous Materials

2.1.1. Porous Materials

Porous materials are materials that contain void space as well as a solid phase. There are many familiar examples of porous materials, including foam, sponge, cork, wood, bread, and bone. Porous materials can be classified by their pore architecture as described by Gibson and Ashby.[1] Honeycombs have an anisotropic pore structure, where the pores are arranged in a two-dimensional array, and resemble hollow tubes that are assembled in parallel. The properties along the axis of the tubular pores differ from those in the perpendicular direction. Foams are materials with pores arranged in a three-dimensional array, and tend to have more isotropic properties. Both honeycombs and foams can be classified by the interconnectivity of their pores. Materials with open porosity have an interconnected network of pores that are open to the surface, whereas in materials with

closed porosity, the pores do not connect to each other or the outside surface. There are many potential applications for porous materials including packaging, insulation, light-weight structures, filtration, thermal management, and tissue engineering.

2.1.2. Porous Ceramics

Porous ceramics have many potential high temperature applications, due to the high melting point of ceramics and their structural integrity at high temperatures. Some potential applications include molten metal filters, catalyst supports, diesel particulate filters, heat exchangers and low density insulation for aerospace applications, where the pores serve to filter, host catalytic reactions, and lower the weight of the part.[2] Knowledge of how porous ceramics will behave in high temperature environments, or when exposed to high thermal gradients, is important for use in any of these high temperature applications. Performance is based on several material properties including strength, elastic modulus, Poisson's ratio, thermal conductivity, thermal expansion coefficient, and the complex interaction of these to determine thermal shock resistance. Thus, these properties are essential to study in order to assess the potential use of a material in any of these applications. Thermal properties, including the thermal shock resistance, will be discussed in more detail in section 2.4.

2.1.3. Processing of Porous Materials

There are several methods of producing ceramic materials with controlled porosity as discussed by Studart et al.: sacrificial template, direct foaming, and replication.[11] A schematic diagram of these three methods is shown in figure 2.1.

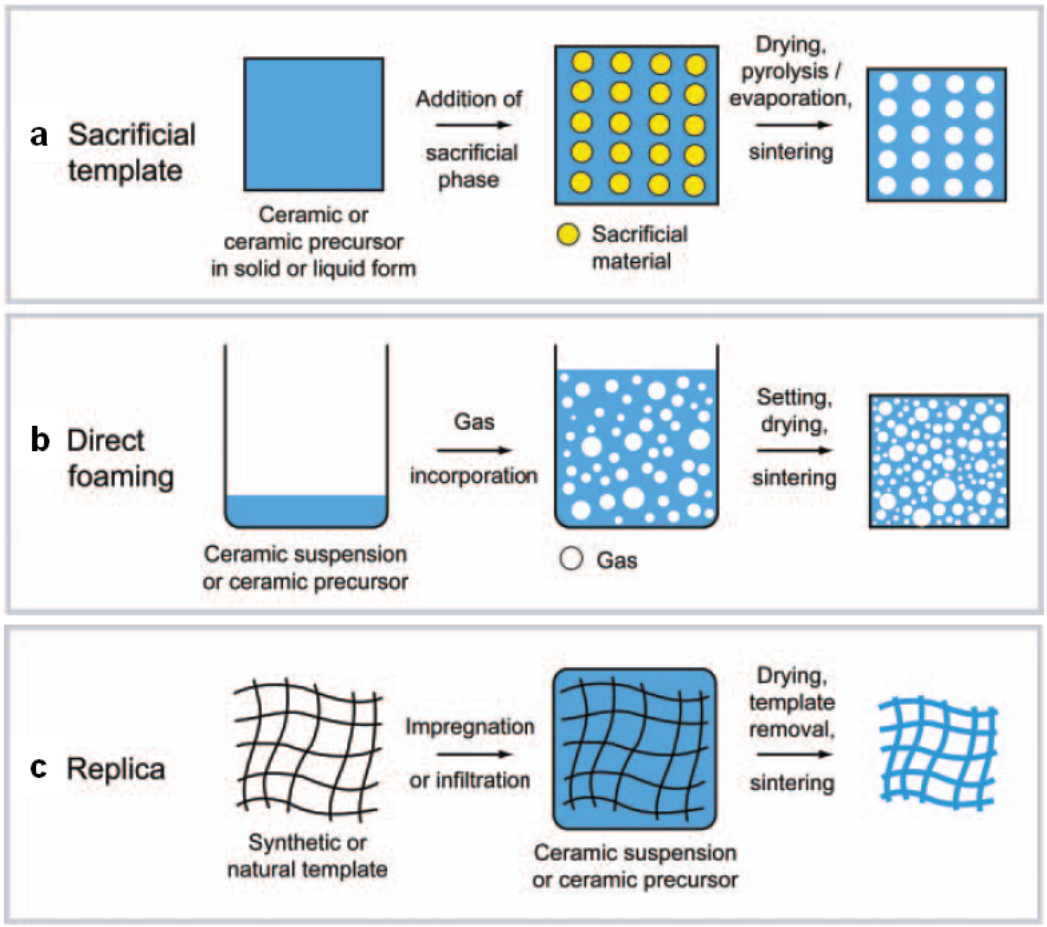

Figure 2.1. Schematic diagram of porous processing methods.[11]

In the sacrificial template method, a fugitive phase is introduced into a ceramic solid or slurry. The sacrificial phase can be metal, ceramic, or polymer, solid or liquid. The template is subsequently extracted from the system by a thermal treatment for a polymer, sublimation for a liquid, or washing or etching for salts or metals. Pores remain in the sample where the sacrificial phase was located, producing a pore structure that is a negative replication of the sacrificial phase. The porous ceramic can then be sintered. A major advantage of this method is that there is a large variety of filler pore sizes readily available, which can lead to tailorable pore structures. The main disadvantages to this method are that the burnout of organic materials can lead to large amounts of gaseous byproducts, and larger samples can necessitate long burnout times.

In the direct foaming method, a gas is forced into the ceramic precursor either by physical blowing or by a chemical reaction. A setting agent is used to avoid coalescence of bubbles. The porosity and the pore size of the resulting ceramic are based on the amount of gas forced into the slurry and the stability of the slurry before it sets, respectively. The resultant porous ceramic is then dried and sintered. The direct foaming method is environmentally friendly, and by using particles as stabilizers to maintain the pore structure prior to sintering, a variety of high porosity materials can be attained. A drawback of this method is the limitation on the shape of porosity.

The replication method takes advantage of an already existing porous structure, such as a polymer sponge, and uses it as a template for the finished ceramic. A ceramic slurry is subsequently incorporated into the template. The template is then burned out, and the resulting ceramic is sintered, maintaining the structure of the original material. Natural templates, such as coral and wood, have been used as an alternative to synthetic sponges,

to take advantage of naturally optimized porous structures. The replication method has the advantage of using an already existing porous structure, and disadvantages include potential cracking and warping of the ceramic as the template is being burned out.

Wood has been used as a template for porous ceramics including silicon carbide, titanium carbide, zirconium carbide, titania, alumina, and chromia.[12–22] To fabricate the oxides, such as alumina, titania, and chromia, a sol-gel reaction is used to create the oxide. The wood template is first infiltrated with the solution and then dried to form the gel. This step is repeated a specified number of times to get a thick and continuous gel coating on the wood, which is then sintered in air to burn out the wood and form the oxide. Figures 2.2(a)-(d) show scanning electron microscope (SEM) images of titania derived from pine and rattan woods.[17] It is clear from these images that the original wood structure is retained, and that the wood based-TiO_2 can have varying microstructures. The pine-based TiO_2 is characterized by a fairly regular array of many small pores, while the rattan-based TiO_2 contains randomly distributed pores of different sizes.

Carbides can also be made using a sol-gel reaction similar to the oxide processing method, replacing the air with argon during the sintering step to retain the carbon from the wood.[12,16,19] In most cases, these carbides tend to retain a significant amount of carbon in their finished state.[12,16,19] Silicon carbide can also be made by melt or vapor infiltration of a carbon preform derived from wood, which is the focus of much of the research on wood-based ceramics, and will be the topic of the remainder of this work.

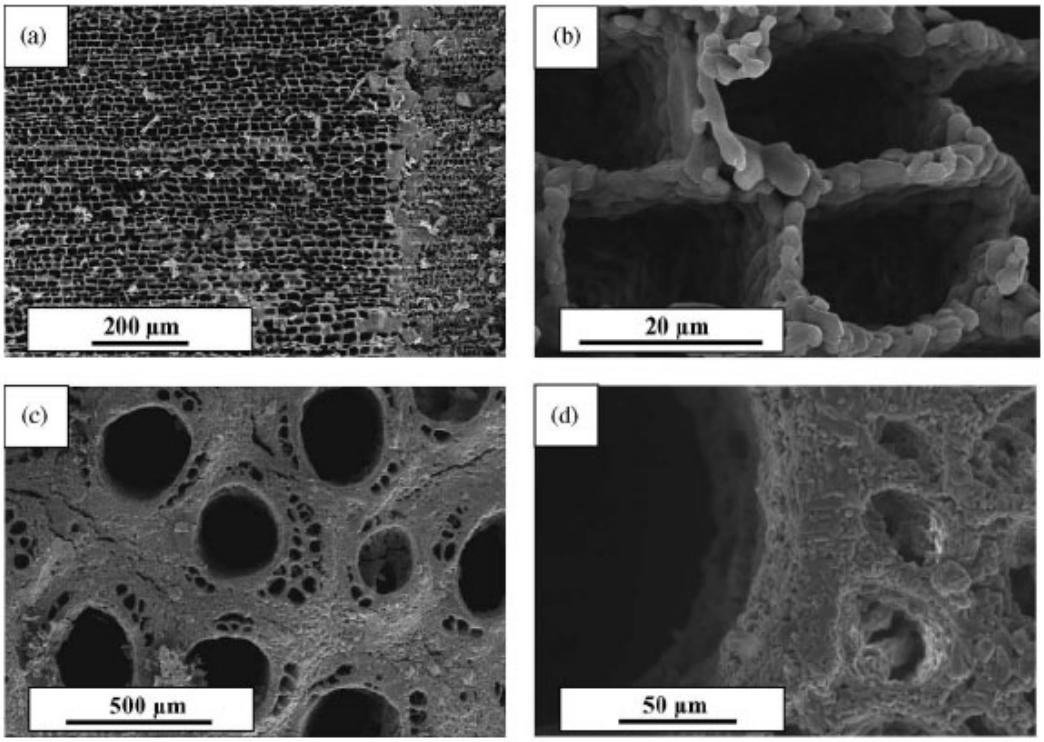

Figure 2.2. Titania derived from pine (a) and (b) and rattan (c) and (d) woods.[17]

2.2. Silicon Carbide Derived from Wood

Silicon carbide derived from wood, or biomorphic silicon carbide (bioSiC), has been a recent area of interest in ceramic research.[12–14] This material was first studied by Ota et al. using the sol-gel method, and was further developed by Greil et al. using melt infiltration.[12–14] The melt infiltration technique for fabricating porous silicon carbide from wood will be the focus of the present work. The first step towards making bioSiC is obtaining the carbon preform. The natural wood is pyrolyzed, which yields a carbon (C) scaffold that retains the initial wood microstructure. SiC results from the subsequent silicon (Si) infiltration of the C scaffold. Excess Si that remains in the pore space after the melt infiltration reaction is removed using a concentrated HF/HNO_3 solution or wicking silicon out of the sample with carbon felt. The distribution of microstructural features in the original wood leads to the unique and varied microstructures of the resultant bioSiC. An example from our work of each stage in the processing is shown in figure 2.3 starting with (a) the initial wood precursor, (b) the pyrolyzed carbon, (c) the bioSiC with residual Si, and (d) the etched porous bioSiC.

2.2.1. Carbon Pyrolysis

To create the carbon preform, the wood is heated slowly at 1°C/minute to 300-1200°C in argon. Pyrolysis of wood and other cellulosic materials have been studied in several capacities. Tang and Bacon investigated in detail the pyrolysis stages of cellulose up to 500°C.[24,25] They found that during the pyrolysis, tars and gases, including CO, CO_2, and hydrocarbons, are removed from the samples as the cellulose decomposes. In addition, about 60% of the volume is lost due to shrinkage.[26] Wood pyrolysis has been studied with

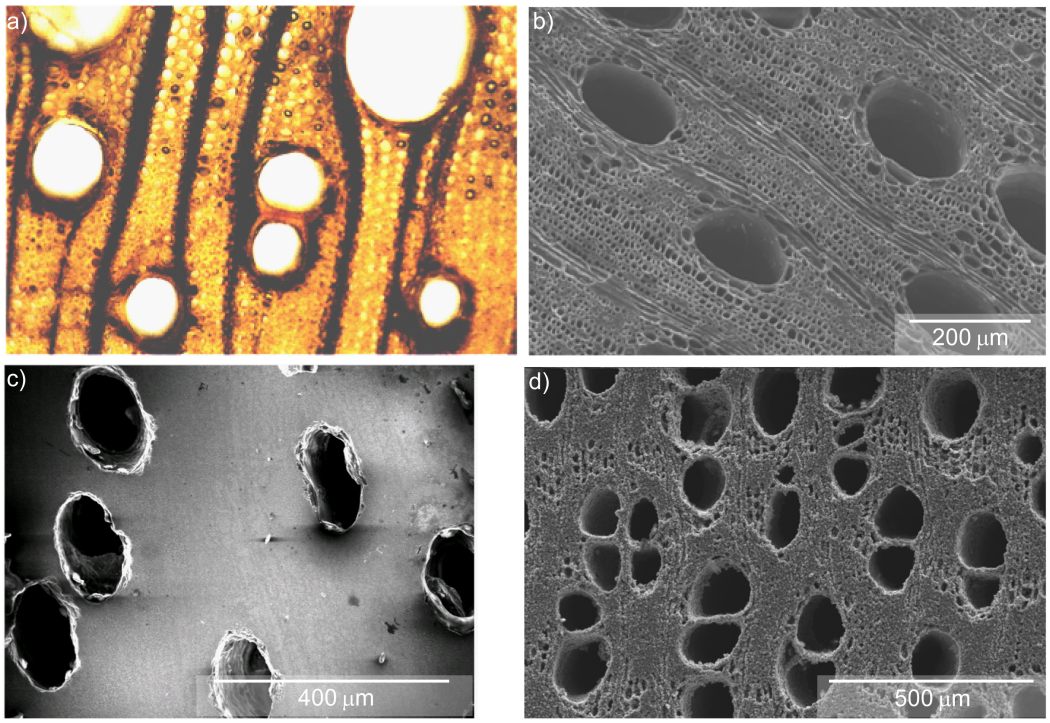

Figure 2.3. Stages in bioSiC processing: (a) wood precursor[23], (b) pyrolyzed carbon, (c) bioSiC and excess silicon, (d) etched porous bioSiC.

thermogravimetric analysis (TGA) by both Singh and Salem as well as by Byrne and Nagle to determine at what temperatures significant amounts of weight loss occur.[27,28] The TGA curves showed similar trends, and Byrne and Nagle's plot is reproduced in figure 2.4. Desorption of water occurs at low temperatures, up to 100°C, which accounts for the first significant weight loss, indicated by region 1 on the plot. As the temperature increases, the organic components, cellulose, hemicellulose and lignin, the three main components of wood, begin to decompose. The hemicellulose breaks down first, between 200-290°C as shown in region 2, followed by cellulose and lignin, which begin to decompose when the hemicellulose is gone, in region 3. The cellulose and lignin continue to decompose in region 4, and the cellulose finishes around 400°C. Above 400°C, the lignin continues to decompose slowly. Byrne and Nagle also showed that the heating rate of pyrolysis affects the resulting sample integrity. Samples heated at 20°C/hour came out warped and cracked, while samples pyrolyzed slowly at 5°C/hour exhibited no cracking.[28] Thus, a slow pyrolysis rate is ideal for processing.

Carbon that is not in the graphitic phase can be considered either graphitizable or non-graphitizable.[29] The graphitizable carbon will arrange into the crystalline graphitic structure upon high temperature heating. Non-graphitizable carbon, however, forms strong cross-linked bonds at low temperatures. While small portions of this type of carbon contain graphite-like layers, these regions are largely disordered overall, and even with high temperature heat treatments, will never become arranged as crystalline graphite.[29] Wood-based carbon can be classified as this non-graphitizable carbon, or hard carbon.[30] Cheng et al. showed that even as the temperatures approach 3273 K (3000°C), graphitization is not fully achieved when wood is the starting material, as demonstrated by analysis of

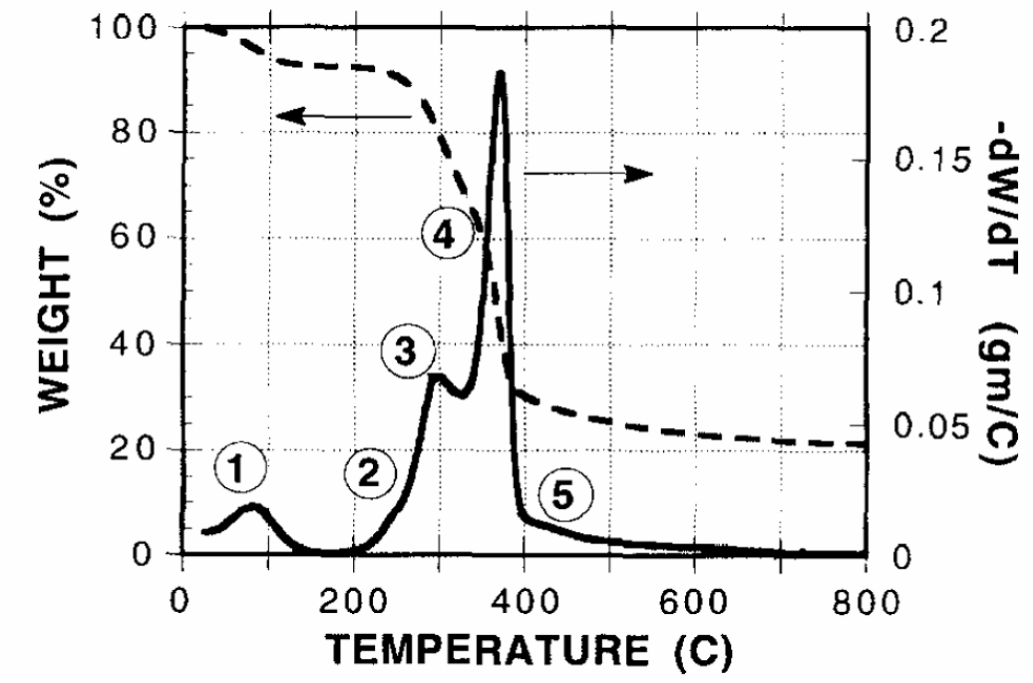

Figure 2.4. Thermogravimetric analysis curve of red oak wood indicating weight loss as a function of temperature.[28]

the (002) d-spacing by X-ray diffraction. Masters and McEnaney studied cellulose-based carbon heat treated up to 1870 K (∼1600°C).[31] Their high resolution micrographs show that there is some increased order as the heat treatment temperature increases, as shown in figure 2.5. At 1170 K (∼900°C), the layered planes are disordered, and occur only in stacks of 2-3, while at 1870 K (∼1600°C), the stack growth increased, though no layer spacing change occurs.[31] This further shows that even at increased temperatures, the graphite phase is not reached when the starting material is cellulosic.

2.2.2. Biomorphic Silicon Carbide Processing

The next step towards producing biomorphic silicon carbide (bioSiC) is silicon infiltration. Silicon infiltration of carbon can be done in two ways: melt infiltration and vapor infiltration.[13,32,33] In the melt infiltration technique, the carbon samples are heated in a vacuum environment with liquid silicon.[13] The silicon is melted and then wicked into the pores by the carbon. The silicon and carbon react to form silicon carbide. Residual silicon present from the reaction is removed by using an acid etch or by wicking with carbon felt, leaving behind a porous SiC ceramic retaining the original wood structure. There is a volume expansion of about 58% associated with the silicon carbide formation reaction.[34]

The silicon carbide melt infiltration reaction mechanism has been studied in great detail by Zollfrank and Sieber.[35] They break the process down into four stages. First, as the silicon and carbon are being heated, the silicon begins to vaporize just before it starts to melt due to the high partial pressure of Si present at that point. The vaporized silicon begins to react with the carbon at the surface. This results in a <100 nm thick coating of nano-grained silicon carbide at the pore surfaces. As the temperature rises above the

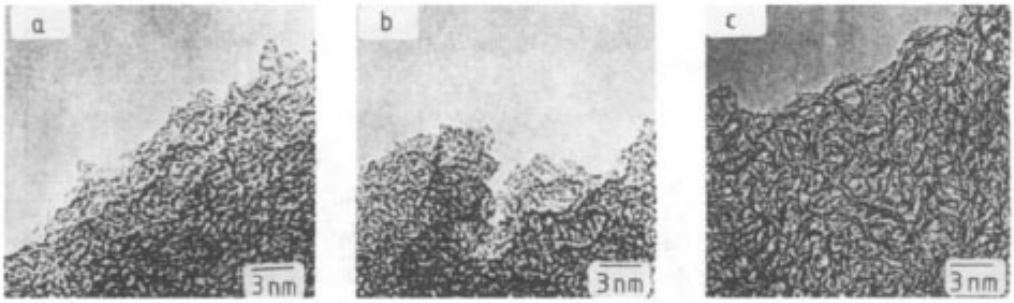

Figure 2.5. High resolution transmission electron microscopy images of cellulose that has been pyrolyzed to (a) 900°C, (b) 1200°C and (c) 1600°C.[31]

silicon melting point, the silicon quickly comes into contact with the carbon and starts reacting to form both nano- and coarse-grained SiC. It is clear from their micrographs that there is always a layer of nano-grained silicon carbide between the unreacted carbon and silicon phases, as shown in figure 2.6. In the third stage, the reaction is limited by silicon diffusion through the already created SiC layer to get to the remaining residual carbon. It is evident that there is much coarse-grained SiC, as well as some residual unreacted carbon, as shown in figure 2.7. Separating these two areas is a layer of nano-sized SiC grains. In the fourth stage, grain coarsening occurs in the larger SiC grains as the nanosized grains and the residual carbon are dissolved into the silicon, and precipitated out on the surface of the coarse grains. After the final stage of processing, the regions of thicker initial struts, or material enclosing the pores, still contain some residual carbon. This is due to both silicon filling the nearby pores and choking them off, not allowing any further silicon to access the remaining carbon and the slow rate of diffusion of the silicon through the already created silicon carbide. Zollfrank and Sieber showed that after 5 hours, struts with thicknesses of greater than 6 μm would contain residual carbon. The carbon in the regions of thinner struts is all converted to silicon carbide at that time.

Vapor infiltration is another possible method for creating bioSiC. It can be accomplished using silicon vapor sources such as Si, SiO, CH_3SiCl_3.[36,37] The carbon samples are heated in the presence of the vapor. The silicon reacts with the carbon to form silicon carbide. Although there is no residual silicon left over from vapor infiltration, in order to avoid residual carbon, the reaction hold time needs to be much longer than 8 hours.[37] This, in combination with the dangerous silicon precursor materials, makes the

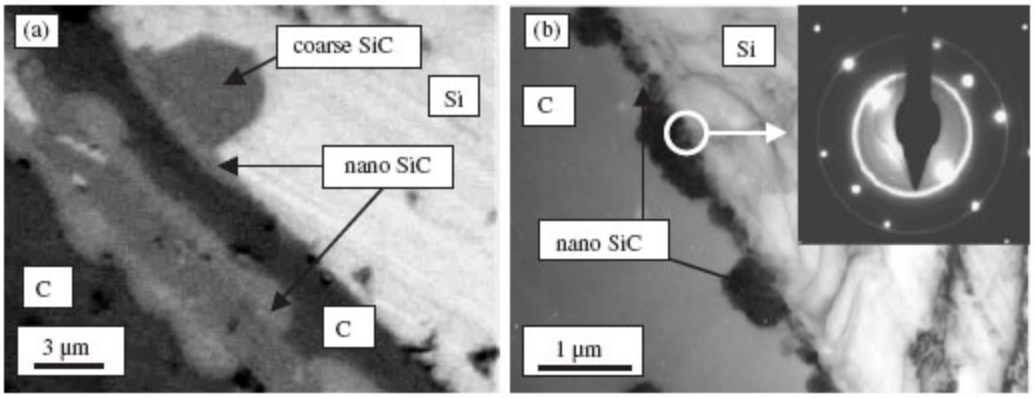

Figure 2.6. (a) Light microscope image and (b) transmission electron microscope image of the phases present after 4 minutes of infiltration at 1550°C.[35]

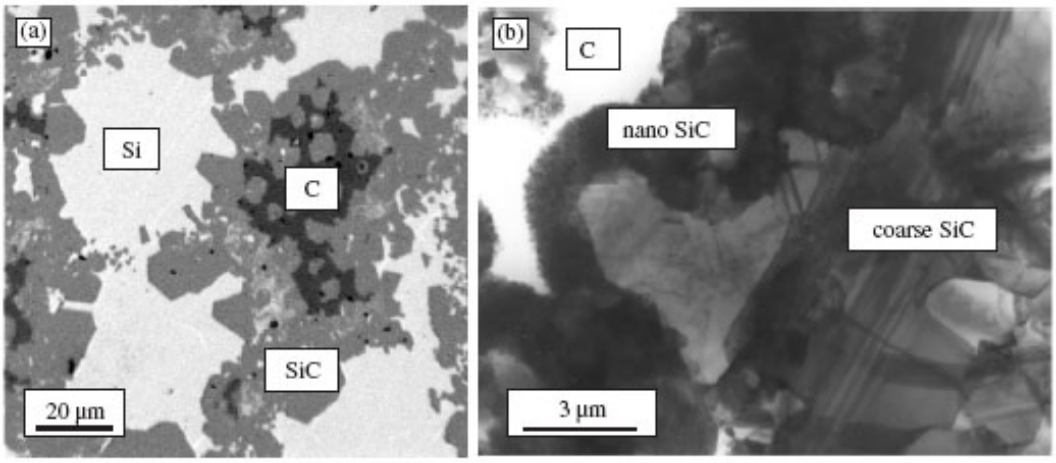

Figure 2.7. (a) Light microscope image and (b) transmission electron microscope image of the SiC forming reaction after 60 minutes at 1550°C.[35]

melt infiltration process more desirable, and thus will be the focus of the remainder of this work.

The residual silicon that remains after the melt infiltration reaction is then removed with an acid etch containing half 49% hydrofluoric acid (HF) and half 69% nitric acid (HNO_3).[38] The reaction is done in two steps, as indicated by the following two reactions:

$$3Si(s) + 4HNO_3(l) \rightarrow 3SiO_2(s) + 4NO(g) + 2H_2O(l) \tag{2.1}$$

$$SiO_2(s) + 6HF(l) \rightarrow H_2SiF_6(l) + 2H_2O(l)$$

First the nitric acid reacts with the excess silicon to form silicon dioxide. Then, the hydrofluoric acid reacts with this newly formed oxide, thus removing the residual silicon from the sample, leaving behind a reactant acid and water. Samples sit in a continuously stirring bath of this acid etch for 1-2 weeks, which results in a porous silicon carbide sample.[39,40]

2.2.3. Wood Microstructure

In order to understand the microstructure and properties relationships between the different types of wood and their resultant bioSiC, it is important to have some background knowledge on the microstructure of the wood itself. As mentioned previously, the wood structure is anisotropic, made up of elongated pores aligned in one direction, which is referred to as the axial direction, in contrast to the transverse directions, radial and tangential. The radial direction extends from the center of the tree out to the external edges. The tangential direction is perpendicular to the previous two, and is tangent the concentric circles around the tree center. These directions are diagrammed in figure 2.8.

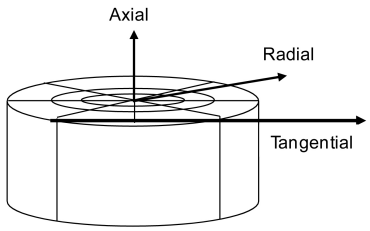

Figure 2.8. Schematic diagram of a tree segment with the perpendicular directions illustrated.

The microstructure of wood, and thus, the resulting bioSiC, look very different in the axial and the transverse directions. An example of the axial and transverse planes of sapele bioSiC are shown in figures 2.9(a) and (b), respectively.

The two main classifications of woods are softwoods and hardwoods, as reviewed by Wheeler.[41] Softwoods mostly contain elongated channels that run in the axial (longitudinal) direction called tracheids, as well as rays, which are aligned perpendicular (transverse) to the tracheids. Hardwoods have large-diameter elongated channels called vessels and smaller channels called fibers, both of which are oriented in the axial direction, as well as rays. Growth rings are bands that signify the early and late wood periods in the growth cycle of a tree. Early wood occurs first in the tree growth season, when the growth rate is fast, and is characterized by larger channels and thinner struts between channels. Late wood sections correspond to slower growth rates, smaller channels, and thicker struts. These different regions produce a density gradient in the microstructure. The severity of the density gradient varies with wood species and climate.

Within hardwoods, there are two classifications based on the ability to distinguish between early and late wood periods. Ring-porous hardwoods have a greater disparity, exhibiting bands with large vessels alternating with bands containing small ones, leading to a bimodal vessel size distribution. Diffuse-porous woods have a smaller variation in vessel size between early wood and late wood, resulting in a more uniform vessel size distribution.[41] The size and spatial distribution of the vessels and fibers dictates the pore distribution in bioSiC, and can greatly influence the resultant properties.

Tracheids, vessels, and fibers run in the axial direction and produce unidirectional pores upon conversion to bioSiC.[41] This gives bioSiC an anisotropic, honeycomb-like

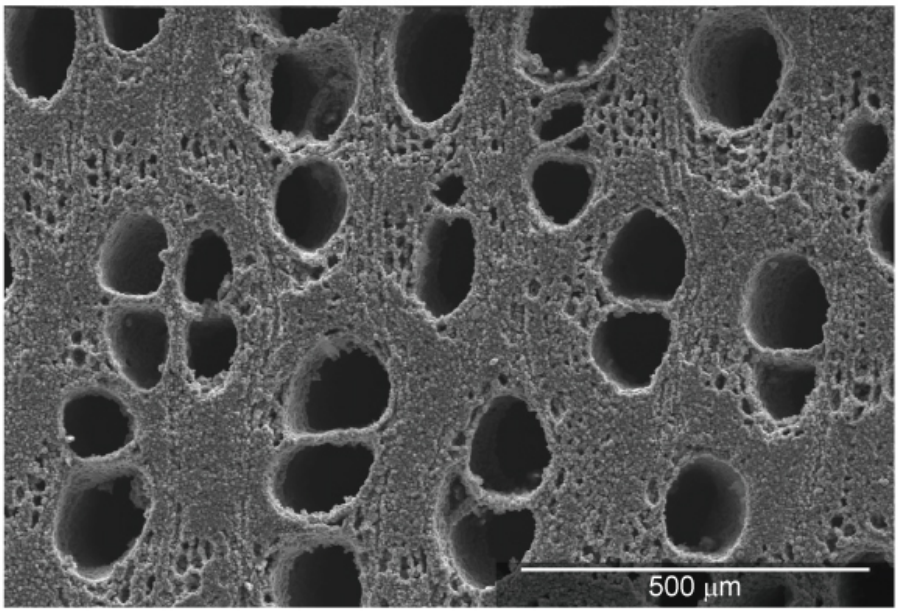

(a)

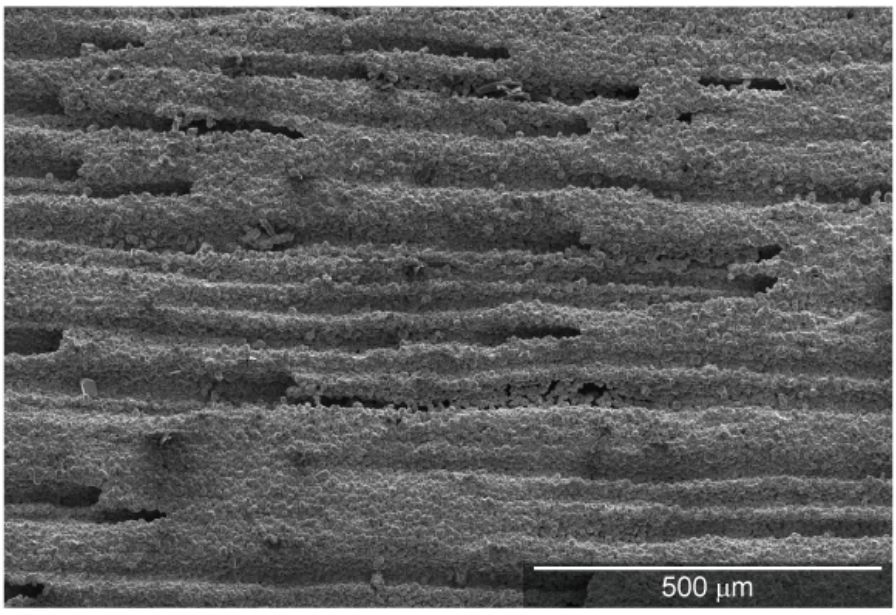

(b)

Figure 2.9. Sapele-based bioSiC in the (a) axial and (b) transverse orientations.

microstructure, and consequently, orientation-dependent properties. The interconnection of the tracheids, vessels, and fibers leads to an open-porous microstructure. The key features of interest are illustrated in figure 2.10. Figure 2.10(a) shows bioSiC from sapele wood, a diffuse-porous wood, while figure 2.10(b) shows bioSiC from red oak wood, a ring-porous wood. The late wood and early wood regions of each wood-based bioSiC are labeled, along with the vessels, fibers and rays. It is clear to see that while there is very little difference in vessel size between early and late wood regions in the sapele-based bioSiC, there is a large difference in the vessel sizes in the red oak-based bioSiC.

2.2.4. BioSiC Motivation

There are several advantages to processing porous silicon carbide from wood, compared to traditional techniques. One is that the maximum temperature that the samples are exposed to during the processing of bioSiC is 1500-1600°C, vs. traditional sintering of SiC, which requires temperatures over 1900°C. BioSiC also takes advantage of the naturally optimized porous structure of wood. There are many different types of wood that exist in nature, with different porosities and pore distributions. The desired properties of the bioSiC can theoretically be attained by choosing an appropriate wood, with a particular porosity and pore distribution.

Much work has been done studying the microstructure and mechanical properties of the bioSiC-Si composite and the porous etched bioSiC.[14,26,39] As expected, mechanical properties, such as compressive strength, elastic modulus, and fracture toughness, have all demonstrated higher values in the axial direction compared to the transverse directions (radial and tangential) for both the etched and unetched bioSiC. For simplification,

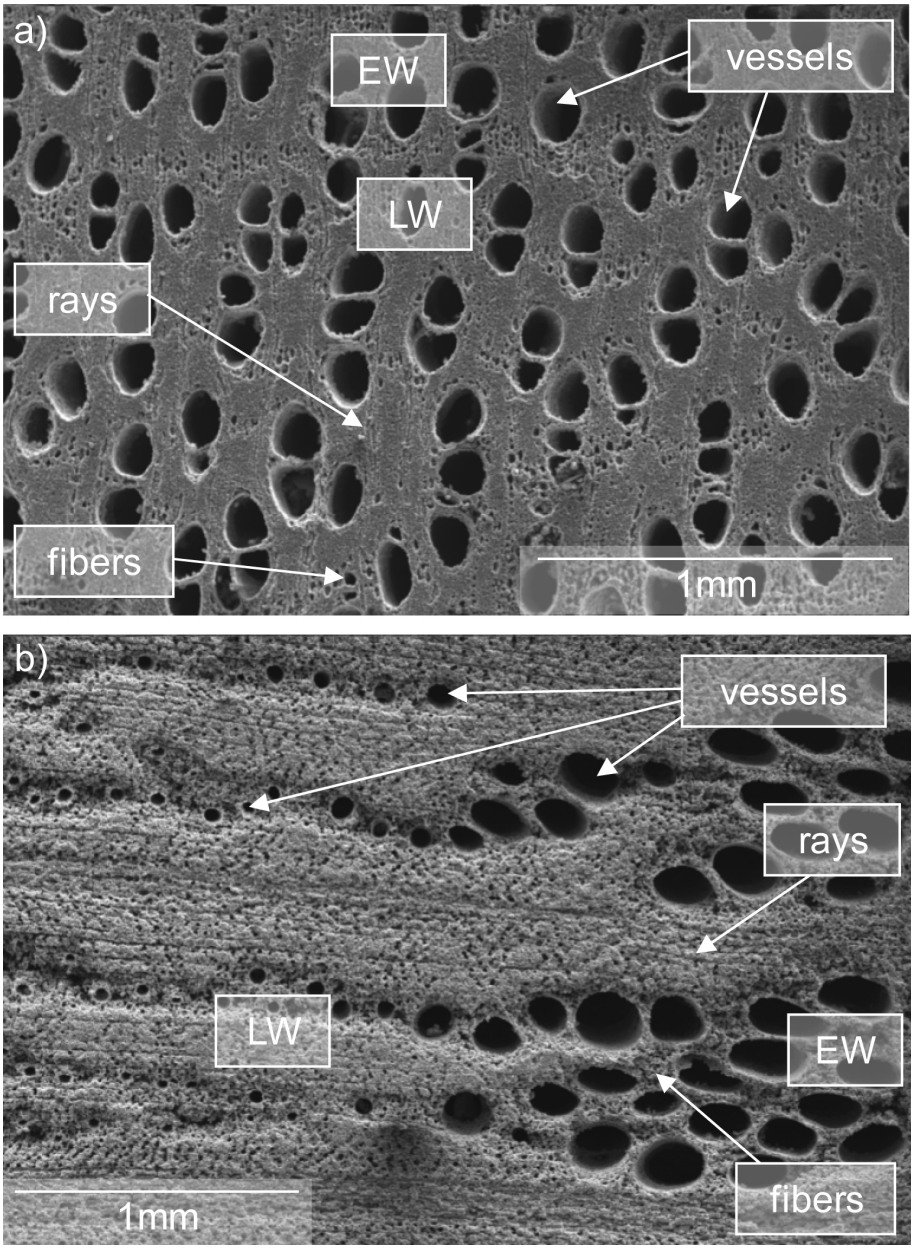

Figure 2.10. Scanning electron microscope images of (a) sapele and (b) red oak - based bioSiC. Features of interest are labeled. EW and LW stand for early wood and late wood, respectively.

since often the radial and tangential directions have similar resulting properties, they are classified together, and will be referred to as transverse. In addition to the orientation dependence, the fracture behavior is dependent on the pore structure, particularly the density gradients associated with the growth ring regions in the material.

While the mechanical properties are very well characterized for both the etched and unetched bioSiC, little work has been done to characterize their thermal properties prior to this work. Although the thermal properties of a bioSiC-Si composite derived from white eucalyptus wood have been determined for the temperature range 5 to 300 K,[5,6] the thermal properties of bioSiC without excess Si had not been studied prior to this work. In addition, the thermal conductivity had not been measured previously at temperatures much greater than room temperature. With the many potential high-temperature applications of bioSiC, it is important to understand the thermal properties at high temperatures in addition to those at room temperature.

2.3. Composite Materials

2.3.1. Composite Materials

Composite materials, by definition, are fabricated by introducing two or more distinct phases, separated by an interface, that together have properties that each component would not have individually.[42] They are created to take advantage of the desirable properties of each phase, to create a new material with enhanced properties. Composites can be anisotropic, for example, with aligned fiber reinforcements, or they can be more isotropic, such as with particle reinforcements. They can have different degrees of interconnectivity between the two phases. The reinforcements can be completely disconnected,

as in particle reinforcements, be individual layers, such as in a sandwich structure, or they can be completely interconnected, as in a melt infiltrated scaffold. These options can be optimized for specific applications.

Ceramics are of considerable interest in composites for many applications in order to take advantage of their wealth of properties, including their high strength and stiffness, low thermal expansion coefficient, and low thermal and electrical conductivities.[42] However, ceramics are extremely brittle, and have a very low fracture toughness. Reinforcing a composite with a more ductile phase, such as metal or polymer, can increase its use in applications in which the material may be susceptible to cracking.

One method of fabricating a ceramic matrix composite is through melt infiltration of a metallic phase into a ceramic preform. In fact, bioSiC is made through a melt infiltration process, which results in residual silicon filling some of the pores. Silicon is very brittle, and is not as desirable a second phase for SiC as other metals may be. BioSiC has also been used as such a ceramic preform to melt infiltrate aluminum alloys, and the mechanical properties have been determined.[7–9] Both copper and an aluminum alloy have been infiltrated into porous bioSiC by Lin et al., and their mechanical properties have also been studied.[10] The thermal properties of these composites, particularly of copper-bioSiC composites, are of interest for potential thermal management applications, but have not yet been tested.

2.3.2. Thermal Management Applications

Electronic packaging, heat sink, and heat spreader materials are, in large part, used to remove heat from integrated circuits, to prevent overheating, and subsequent failure of the

parts.[43] These materials need to have a combination of properties including high thermal conductivity, low thermal expansion coefficient, and low weight. A recent trend has been to use composites for these applications, taking advantage of high thermal conductivities of metals with the lower weights and thermal expansion coefficients of second phases. Anisotropic materials, such as graphite, are also of particular use in heat spreaders, because they have a higher thermal conductivity in one direction, and allow the heat to be dissipated in a particular direction.[44]

An example of an electronic packaging part made of Kovar, a nickel-iron alloy, and of a SiC-Al composite are shown in figures 2.11(a) and (b), respectively. The Kovar is heavier, and has a lower thermal conductivity by 87%, compared to the SiC-Al composite version of this part. Copper is a metal with very high thermal conductivity, making it a desirable candidate for heat dissipation in these thermal management applications. However, copper also has a very high thermal expansion coefficient, which can lead to thermal mismatch, and resulting thermal stresses, between it and silicon-based multichip packaging systems. For this reason, copper would be a desirable candidate for one phase in a composite material. Silicon carbide is an attractive second phase with copper due to its relatively high thermal conductivity for a ceramic and its low thermal expansion coefficient. As mentioned previously, bioSiC has been used as a preform to make metal-bioSiC composites. Thus, a Cu-bioSiC composite has potential uses in these thermal management applications.

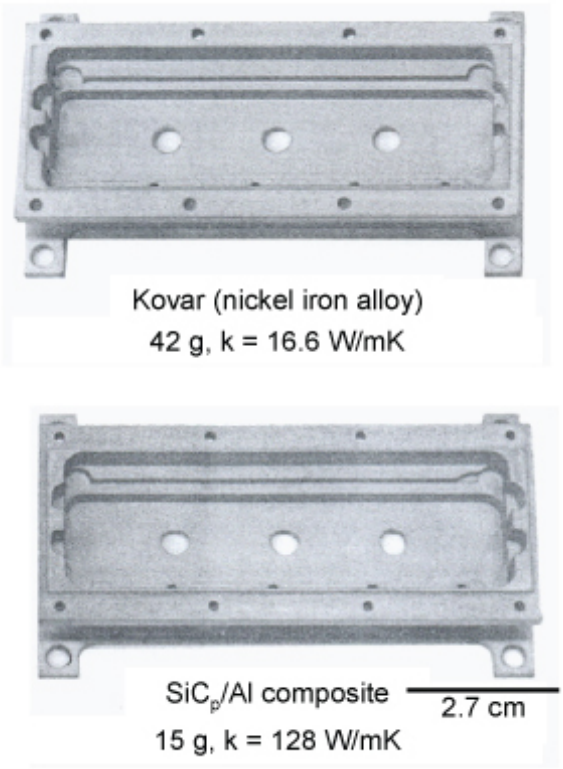

Figure 2.11. Electronic packaging parts made of (a) Kovar and (b) SiC-Al composite.[43]

2.3.3. Copper-Silicon Carbide Reaction

In order to melt infiltrate the bioSiC preform with copper, the wetting behavior of the system needs to be investigated. Gnesin and Naidich, Rado et al., and Nikolopoulos et al., have done extensive studies on the Cu-SiC system, which in all cases, results in reactive wetting.[45–47] When molten copper comes into contact with silicon carbide, the SiC is dissolved into the copper.[46] The copper first attacks the silicon carbide grain boundaries, lowering their mechanical strength.[45] The Cu-Si interactions are very strong, so the silicon dissolves easily.[46] There is low solubility of carbon in copper, and the solution quickly becomes saturated. As more silicon carbide is dissolved into the copper, carbon starts to precipitate out. After the sample is cooled, Cu-Si regions are evident, as well as bands of precipitated carbon, as indicated in figure 2.12.[46]

Squeeze casting copper into a three-dimensional silicon carbide framework at 1150°C showed evidence of the Cu-Si reaction.[48] An et al. studied the interfacial reaction of copper sputter coated onto a silicon carbide substrate.[49] These samples were heat treated up to 950°C and produced evidence of the reaction at temperatures as low as 850°C. Reactivity was also seen by Shimbo et al. in another wetting study where a drop of Cu was deposited on SiC at 1200°C.[50] This reaction can be detrimental to the composite thermal properties, as the addition of as little as 1.5% silicon to copper decreases the copper thermal conductivity by about 85%.[51] Thus the Cu-Si reaction is important to avoid when fabricating copper-silicon carbide composites.

This copper-silicon interaction is also an issue in other areas of electronics research. Copper has been investigated as a heat sink and an interconnect, directly in contact with

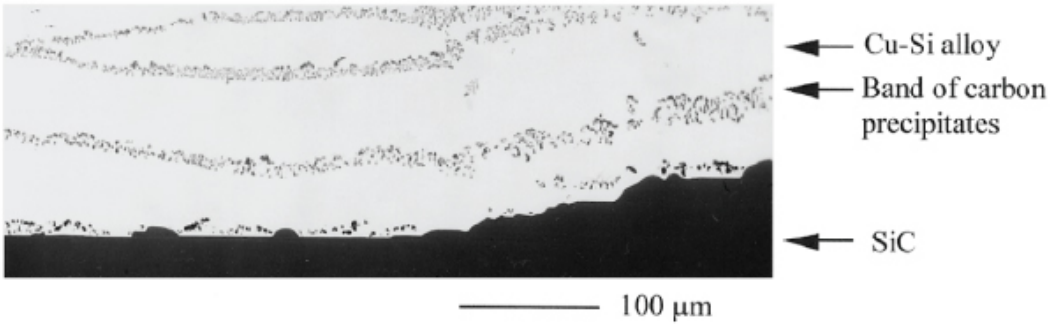

Figure 2.12. Silicon carbide, the copper-silicon alloy, and bands of precipitated carbon after the copper-silicon carbide reaction.[46]

silicon.[52–58] However, the Cu-Si reaction occurs at much lower temperatures than the Cu-SiC reaction, where the Cu needs to be molten in order to dissolve the Si and C. In the case of Cu and Si, it is the diffusion of Cu interstitially into the Si that causes the reaction, and can occur as low as 200°C.[54,59] The Cu breaks down the Si-Si bonds, and reacts with the Si.[54,57] The most common method of trying to combat this reaction is by introducing a diffusion barrier between the Si and Cu sections. Many different diffusion barriers have been attempted. Nitrides are an attractive diffusion barrier option because they have high melting points, high thermal conductivity, and are stable at high temperatures.[54] Titanium nitride (TiN) and tantalum nitride (TaN) systems have been studied at length in the Cu-Si system.[60–66] These barriers ranged in thickness from 25-100 nm, but failed at temperatures from 500-900°C. Failure temperatures are determined by both measuring the sheet resistance of the samples, which increases when the Cu reaches the Si, and by performing X-ray diffraction, which shows evidence of the Cu-Si phase formation, and also of Si reaction with the titanium or tantalum elements of the barrier.[54,57] In addition, other barriers have been explored, including Ta[55], Ta_2O_5 and TiO_2,[58] TiZrN[53,54], TiSiN[56,67], and HfO_2 and Al_2O_3.[52]

The diffusion barrier concept has also been applied to Cu-SiC composite processing.[68] Sundberg et al. coated SiC rods with four different types of diffusion barriers, and submerged them into molten copper for 30-60 minutes. The four coatings they used were TiN, diamond like carbon, and multilayered coatings of TiN/TiC/TiCN/TiN and TiN/TiC/Al_2O_3. The resulting thermal conductivity of the Cu phase after testing was greatly improved for coated SiC as compared to the bare silicon carbide rod. Despite the fact that there was some evidence of Si presence in the Cu region even with the coating,

the thermal conductivites of the Cu region were all near that of the theoretical value of Cu (398 W/mK at room temperature[69]), ranging from 379.25 W/mK - 401.3 W/mK, compared to Cu region where the SiC rod was uncoated, which had a value of 233 W/mK. Thus the barriers were effective at maintaining the thermal properties of the copper for this system.

2.3.4. Electrochemical Depostion

Another method that can been used to fabricate Cu-SiC composites is electrochemical deposition. Electrochemical deposition exists in two formats: electroplating and electroless plating.[70,71] Both methods involve reducing metal ions in an aqueous solution, the electrolyte, so that they deposit onto a substrate. Electroplating requires a current flowing through a circuit, while in electroless plating, no current, or electrodes, are needed.

In electroplating of Cu, specifically, the basic electroplating baths contain a copper salt and an acid, but they can have any number of additives to improve plating efficiency.[67] The copper salt, usually copper sulfate, provides the Cu ions in solution, which will eventually plate on the sample. The acid, sulfuric acid, increases the conductivity of the solution, and leads to a more uniform deposition on the sample surface. Some additives include polymers, such as polyethylene glycol (PEG), which alter the plating kinetics and the deposited film properties.[72]

The sample, which is negatively charged, attracts the positive Cu ions during deposition, and needs to be electrically conductive in order to be successfully used in electroplating. The pure Cu electrode is positively charged, and replenishes the Cu ions in the solution as they are used up coating the sample.

Electroless plating occurs when a metal catalyzes a chemical reduction reaction, leading to plating of that metal onto a sample surface.[71] For the Cu electroless plating system, formaldehyde is the chemical that reduces the metal. Since the formaldehyde is more efficient at high pH, sodium hydroxide is added to the solution. A copper salt is used as the copper metal source, and other additives are used to keep the Cu ions in solution. A major advantage of electroless plating is that a conductive sample is not required. However, the solution contains expensive chemicals and does not last long before it decomposes, and the copper ions form copper oxide, which leads ultimately to the production of copper powder in the solution.

Electroless plating was used by Shu et al. to coat silicon carbide powders with copper prior to mixing and sintering them with copper powder.[73] They made composites of varying silicon carbide volume fractions, and tested the thermal expansion coefficient from 50-550°C. The coated silicon carbide powders produced better composite bonding than the uncoated powders.

Yih et al. studied a SiC whisker/copper composite in which SiC whiskers were electroless and electroplated with copper prior to hot pressing at 950°C.[74] These Cu-coated SiC composites showed less porosity, higher thermal conductivity, and lower thermal expansion coefficient than composites made by mixing SiC whiskers with Cu powder and hot pressing. This improvement in properties is attributed to the better Cu-SiC bonding that occurs with electroplated copper. As the processing temperature of 950°C is below that of the melting point of Cu, the Cu is unable to dissociate the Si-C bonds and react with the Si.

Brendel et al. used electroplating to coat SiC with Cu to make composite materials for fusion reactors.[75] It is desired to achieve a thermal conductivity of 200 W/mK up to 550°C for maximum efficiency. SiC is a good second phase for Cu due to its mechanical stability at higher temperatures where Cu would begin to soften. SiC fibers were electroplated with Cu, and some had an interfacial Ti layer between the SiC and Cu. The samples were hot isostatically pressed to 650°C. Samples with the Ti layer showed improved mechanical properties in a fiber push out test.

Copper electrodeposition has also been performed in pores created in anodized aluminum in order to make copper nanowire devices.[76] Olevsky et al. used sequential electrodeposition to first make a coating of porous alumina, and subsequently impregnate copper into the pores.[77] This resulted in a composite resembling alumina particles in a copper matrix. Olevsky et al. also coated porous silicon carbide with a layer of copper using electrodeposition, that resulted in enhanced thermal properties.

Based on these examples of composite fabrication, electrochemical deposition of copper onto bioSiC seems like a feasible processing method. Silicon carbide has a low resistivity, between 1.0 and 10^9 Ωm, compared to other ceramics, such as alumina, which has a resistivity greater than 10^{13} Ωm. This allows electrodeposition to occur more easily for silicon carbide.[78] For the processing temperatures required in these examples, for the powder heating and sintering steps, the melting point of copper is never reached, and thus the Cu-SiC reaction is prevented. If electrochemical deposition is done and no heat treatment is required, then the system will never go above room temperature, further eliminating the possibility of a detrimental reaction. Thus, Cu electrochemical deposition onto SiC is an attractive potential route to fabricating Cu-SiC composites.

The examples previously discussed involve the electrochemical deposition of Cu onto SiC particles or whiskers, which have easily accessible surface area for coating. For electrochemical deposition to be a viable composite fabrication method for bioSiC samples, the challenge of deposition within the long pores must be overcome. With melt infiltration techniques, the liquid metal can be forced into the pores with applied pressure, but with electroplating, it is necessary to ensure that the electrolyte reaches the depths of the pores so that plating can occur. There is work in the literature discussing methods of electroplating into pores and wells in electronic applications, which should prove to be useful to adapt to the case of a porous ceramic.

Many copper electrodeposition studies have yielded similar results as to what additives improve the electrolyte conditions to optimize the plating in wells with high aspect ratios.[67,79–83] The most common additions are PEG and chloride ions (Cl). The PEG and Cl ions work together to control the copper deposition rate. PEG, in the presence of Cl ions, forms a thin monolayer on the surface of the sample, which inhibits the rate of copper deposition.[81,82,84] These additions suppress the current, which then leads to a more even deposition, and smooths the electroplated surface.[67,83] The addition of PEG also lowers the surface tension of the electrolyte, which increases its ability to reach deeper within the pores.[83] Systems with no additives result in large void formation due to uniform filling from all directions as shown in figure 2.13(a), while additives, in this case from the printed wiring board era, are shown to decrease the void size, as evidenced in figure 2.13(b).[67]

Hasegawa et al. studied the deposition in 200 nm wide and 500 nm deep trenches of a SiO_2/Si substrate, with 200 nm spacing between the trenches, using a base electrolyte solution and several combinations of additives.[85] They also began with a sputter-coated

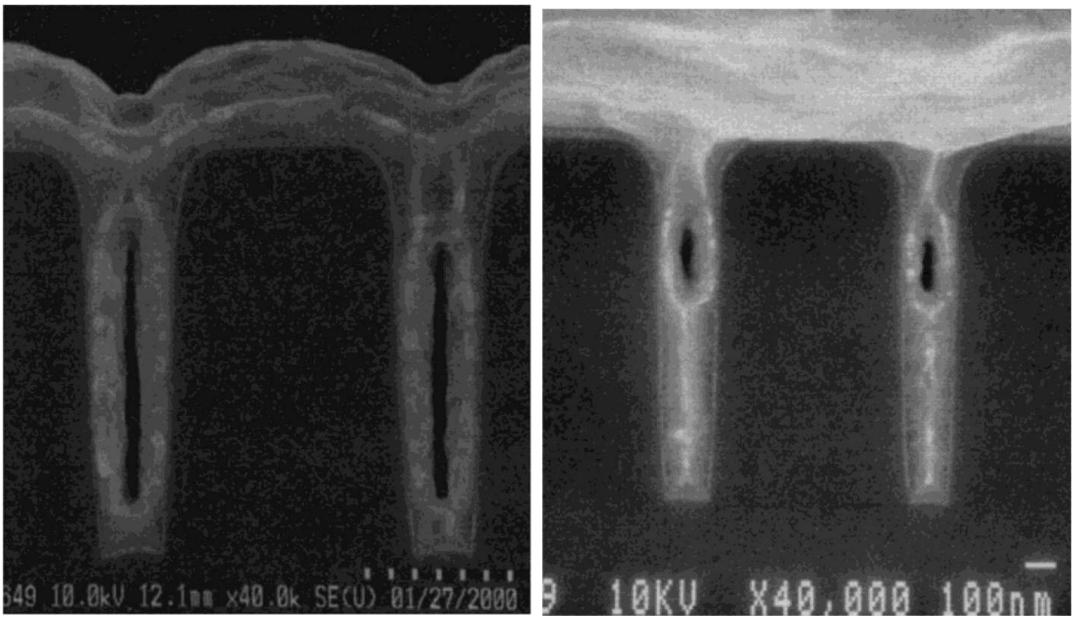

(a) (b)

Figure 2.13. Trenches filled with (a) additive free electrolyte and (b) printed wiring board era based additives.[67]

copper seed layer in the base of their trenches to encourage the deposition to begin at the bottom. Their base solution consisted of copper sulfate, sulfuric acid, PEG and Cl ions. Other additions included varying concentrations of bis(3-sulfopropyl)disulfide (SPS) and Janus green B (JGB). The additive-free solution shows a large amount of overfill, which occurs when large humps of Cu deposit on the surface beside and above the trenches. This is indicated in figures 2.14(a)-(c), which show continuous deposition at 15, 30 and 60 seconds. Overfill can cause the trenches to be choked off prematurely, leading to pores in the final product, as indicated in figures 2.14(a)-(c). The base solution, with additions of PEG and Cl ions, was found to inhibit deposition and fill the trenches better, producing slightly less overfill, as indicated in figures 2.14(d)-(f). Additions of SPS and JGB show less overfill than the solution with no additives but still exhibit choking off of the pores, as shown in figures 2.14(g)-(i). Agitation of the bath also helped to lower the overfilling of the trenches. Since these additives improved the filling of these trenches, it can be projected that additives will be necessary in order to successfully fill the pores in bioSiC samples. Ideally, the overfill will be minimized in order to maximize pore filling before the trenches are choked off.

2.4. Properties of BioSiC and Cu-BioSiC Composites

To learn more about the applicability of bioSiC and Cu-bioSiC composites in their potential high temperature applications, the properties of interest include thermal conductivity, thermal expansion coefficient and thermal shock resistance. In addition, theoretical models and finite-element analysis will be discussed as additional methods of characterizing these properties.

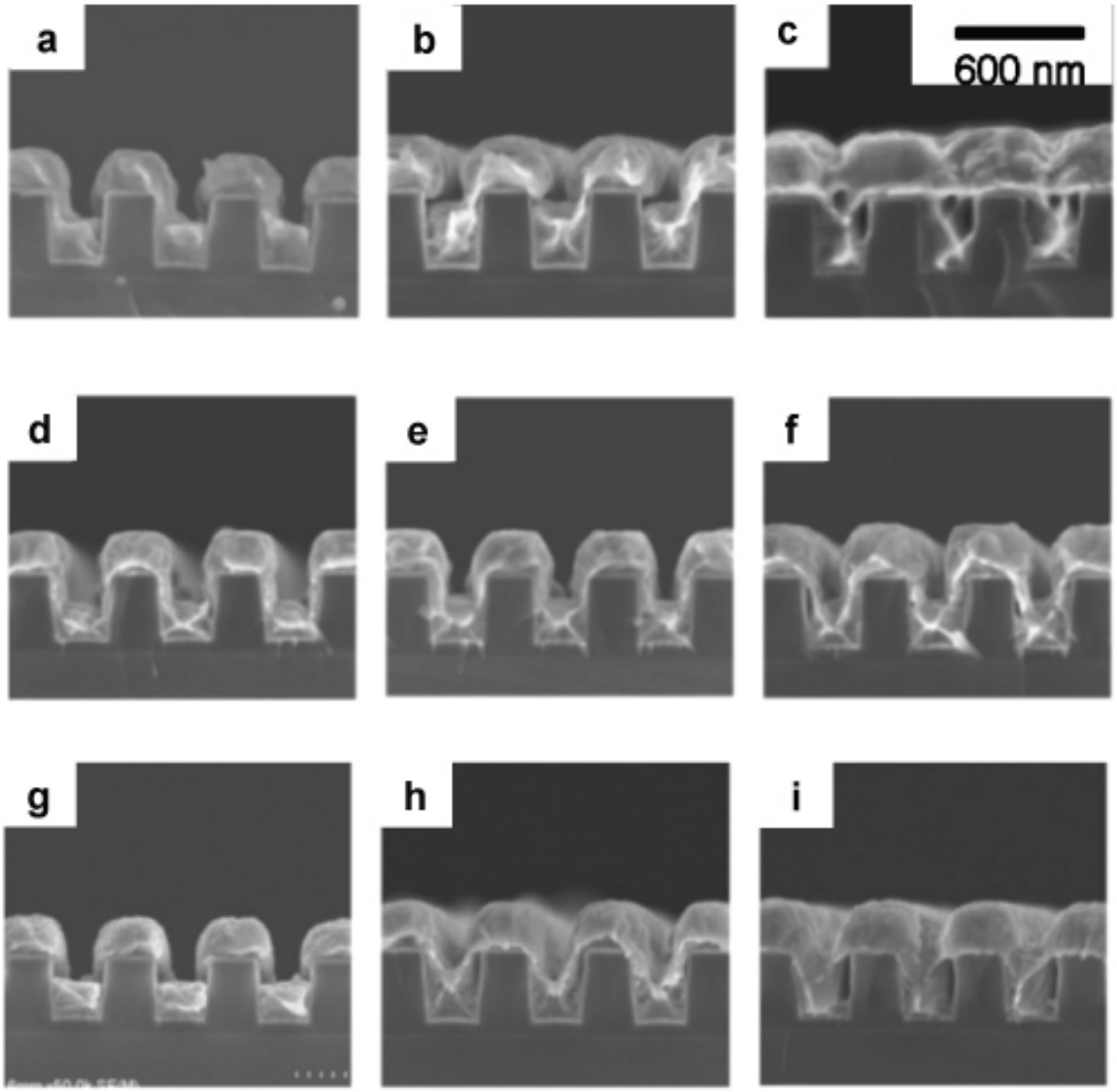

Figure 2.14. Trenches plated with electrolytes with no additives for (a) 15 seconds, (b) 30 seconds and (c) 60 seconds, PEG and Cl additives for (d) 15 seconds, (e) 30 seconds and (f) 60 seconds, and PEG, Cl, SPS and JGB additives for (g) 15 seconds, (h) 30 seconds and (i) 60 seconds.[85]

2.4.1. Thermal Conductivity

Thermal conductivity of porous materials results from several different mechanisms, which include conduction through the porous solid (k^*_{solid}), conduction through the gas contained in the pores (k^*_{gas}), convection (k^*_{conv}), and radiation (k^*_{rad}).[1] The sum of these contributions predicts the thermal conductivity of a porous material, k^*_{eff}, where

$$k^*_{eff} = k^*_{solid} + k^*_{gas} + k^*_{conv} + k^*_{rad} \tag{2.2}$$

There are many models used to determine the effective properties, including the thermal conductivity, of composite materials. Many of these models can be applied to porous materials. However, as they are not designed for porous materials, they are skewed by the low conductivity of air, and greatly underestimate values in the transverse orientation. Rice derived a model to describe the properties specifically of porous materials based on the minimum solid area (MSA) perpendicular to the direction of the applied force.[86] This method can be applied to different material properties, including thermal conductivity, that depend on the percentage of porosity as well as the different pore geometries in both the axial and transverse directions.[86] Elongated pores, such as those present in bioSiC, are expected to result in anisotropic thermal conductivity. Heat can travel on a continuous solid path parallel to the pores, whereas, in the transverse orientation, it must take a more convoluted route through both solid material and voids. This was shown to be true in alumina samples with cylindrical pores, where the conductivity was approximately twice as high in the direction parallel to the pores as opposed to the perpendicular direction.[87] In the axial direction for cylindrical pores, the MSA is equal to the volume fraction of the

solid phase. Thus, the equation to determine the conduction through the solid along the channels is:[86]

$$\mathrm{k}^{*}_{\mathrm{solid,axial}} = (1 - \mathrm{P})\mathrm{k}_{\mathrm{solid}} \tag{2.3}$$

where k_{solid} is the conductivity of the solid with no porosity and P is the porosity of the material. In the transverse direction, where the direction of heat flow is perpendicular to the pores, the MSA is also related to the geometry of the cylindrical pores, and the thermal conductivity is given by:[86]

$$\mathrm{k}^{*}_{\mathrm{solid,transverse}} = \mathrm{k}_{\mathrm{solid}} \left(1 - \left[\left(\frac{4}{\pi}\right)\mathrm{P}\right]^{\frac{1}{2}}\right) \tag{2.4}$$

The solid contribution is normally significantly higher than that of the gas contained in the pores, and thus, the gaseous conduction contribution is considered negligible.[88] The convection contribution is derived from heat transfer within the individual pores. It is largely dependent on the cell size, and when the cells are smaller than approximately 3-4 mm, this factor is also negligible.[89] The radiative contribution, k^{*}_{rad}, is derived from heat radiated throughout the pores, and is highly dependent on porosity, pore size, and temperature. It can be calculated from:[1]

$$\mathrm{k}^{*}_{\mathrm{rad}} = 4\beta\sigma\overline{\mathrm{T}}^{3}\mathrm{t}\exp\left(\frac{-4.1\left(\frac{\rho^{*}}{\rho_{\mathrm{solid}}}\right)^{\frac{3}{2}}\mathrm{t}}{\mathrm{l}}\right) \tag{2.5}$$

where β is an emissivity constant, σ is Stefan's constant ($5.67*10^{-8}$ $\mathrm{W/m^2K^4}$), $\overline{T}$ is the mean temperature, t is the sample thickness, and l is the cell size.[1,88,90] Based on equations 2.3 - 2.5, the thermal conductivity of the materials in the present study is

expected to decrease with increasing porosity, regardless of direction. This has been shown experimentally in alumina, graphite, and partially-stabilized zirconia samples with different degrees of porosity.[87,91,92]

The solid contribution to the thermal conductivity is also expected to decrease with increasing temperature. The mean free path of interacting phonons decreases at high temperatures, causing more phonon-phonon interactions.[93] The radiative contribution should increase with increasing temperature as it is proportional to $\overline{T}^3$. At low temperatures, the solid contribution dominates the total thermal conductivity. At high temperatures, the radiative contribution should surpass the solid thermal conductivity to become the dominant mechanism. Thus, the thermal conductivity is expected to first decrease, and then increase, with temperature.

Thermal conductivity of composites is dependent on the thermal conductivity values of each phase. For fiber-reinforced composites, the thermal conductivity is expected to be anisotropic, as with honeycomb-like porosity. The expressions for thermal conductivity of composites in the longitudinal (k_{cl}) and transverse (k_{ct}) orientations are given in the equations below:

$$k_{cl} = k_f V_f + k_m V_m \tag{2.6}$$

$$k_{ct} = (1 - \sqrt{V_f})k_m + \frac{k_m \sqrt{V_f}}{1 - \sqrt{V_f}(1 - k_m/k_f)} \tag{2.7}$$

where k_f, k_m, V_f, and V_m are the thermal conductivities and volume fractions of the fiber and matrix, respectively.[42,94,95]

Thermal conductivity of fiber-reinforced composites is often higher in the axial direction than the transverse direction, similar to the predictions for thermal conductivity of porous materials. Behzad et al. determined that the thermal conductivity of hemp fiber-reinforced polymer matrix composites was lower in the transverse direction, partly due to the lower thermal conductivity of the fiber phase in the transverse direction.[96] In carbon fiber-epoxy resin composites, the thermal conductivity was also found to be higher in the fiber length direction than in the transverse direction.[97]

There are two main challenges to overcome when attempting to determine the thermal conductivity of a sample experimentally. They are potential loss of heat at the sample surface and thermal contact resistance between the sample and its surroundings.[98] One popular method to avoid these two problems is the flash diffusivity method. Diffusivity is measured by imparting a quick flash of light on the sample so as to not lose much heat to the surrounding environment.[98] The diffusivity, in conjunction with the specific heat capacity, C_p, and the density, ρ, are used to determine the thermal conductivity, k, using

$$k = C_p \alpha \rho \tag{2.8}$$

It is crucial during experimentation to ensure that the conditions are close to the theoretical assumptions by making the flash occur as quickly as possible, making sure the thermocouple or infrared detector is measuring the true back surface temperature, and ensuring that as little heat as possible is lost to the environment.[98] The sample must be thick enough that the half time will be significantly longer than the flash, but thin enough that heat loss is minimized.[98] To test samples at temperatures other than room temperature, the sample can be pre-heated or cooled to the desired test temperature.

The thermal conductivity of porous materials and composites have been modeled using finite-element analysis. Fiedler et al. used both an analytical solution and finite-element analysis to determine the thermal conductivity of a porous material fabricated by a random array of hollow metallic spheres.[99] The finite-element mesh was derived using the average distance between each neighboring sphere, thus discounting the random distribution that existed in the structure, and simplifying the complex numerical solution. Without this simplification, they stated that this calculation would not have been possible. The numerical method values matched well with those of the experimental and analytical methods, despite this simplification.

Farooqi et al. used finite-element analysis on a unit cell of a layered ceramic-matrix composite.[100] The residual porosity found in the samples was represented in the unit cell based on scanning electron microscope images. This analysis is done in three-dimensions, but the actual images are only used to assist in the creation of the unit cell mesh. These modeling values, performed using ABAQUS, also matched well with the experimental data.

Finite-element models based on actual microstructures have been in use in recent studies in order to avoid simplifications of pore distribution. The majority of these are two-dimensional systems, which then encounter the simplification of eliminating possible heat flow in the third dimension. One example of two-dimensional microstructure based finite-element analysis was performed by Grandjean, et al., who created two-dimensional meshes of porous tin oxide ceramics and used ABAQUS finite-element software to determine thermal conductivity.[101] In another example, two-dimensional microstructure based

modeling was performed on porous composite ceramics that were used in ancient metallurgical processes.[102] Scanning electron microscope images were used to create finite-element meshes, and finite-element methods were used to determine the thermal conductivity. Both of these cases produced underestimates of thermal conductivity values due to the isotropic nature of the samples but the limitations of a two-dimensional model.

OOF, a finite-element analysis program developed at the National Institute of Standards and Technology (NIST), uses actual SEM images to model mechanical and thermal properties.[103,104] OOF has been used previously to analyze the thermal properties of thermal barrier coatings.[105] Jadhav et al. created OOF meshes of layered thermal barrier coatings to calculate the effective thermal conductivity based on the solid material and the pores within the coating. They found that the OOF-calculated thermal conductivities matched well with their experimental results, and better than those values attained from the analytical methods. An example of a thermal gradient across their thermal barrier coating is shown in figure 2.15. The cross-hatched regions are pores, the remainder is solid. It is clear that the irregular pores shapes are well meshed by OOF.

Three dimensional modeling of using actual microstructures can also be performed, but this requires a three-dimensional reconstruction of the material using a technique such as X-ray computed tomography. Amsellem et al. used microtomography to produce a three-dimensional representation and a three-dimensional finite-element mesh of plasma-sprayed alumina coatings, and compared these results to a two-dimensional image based finite-element mesh.[106] They calculated the effective Young's modulus and simulated stresses within the microstructures. These three-dimensional results displayed fewer

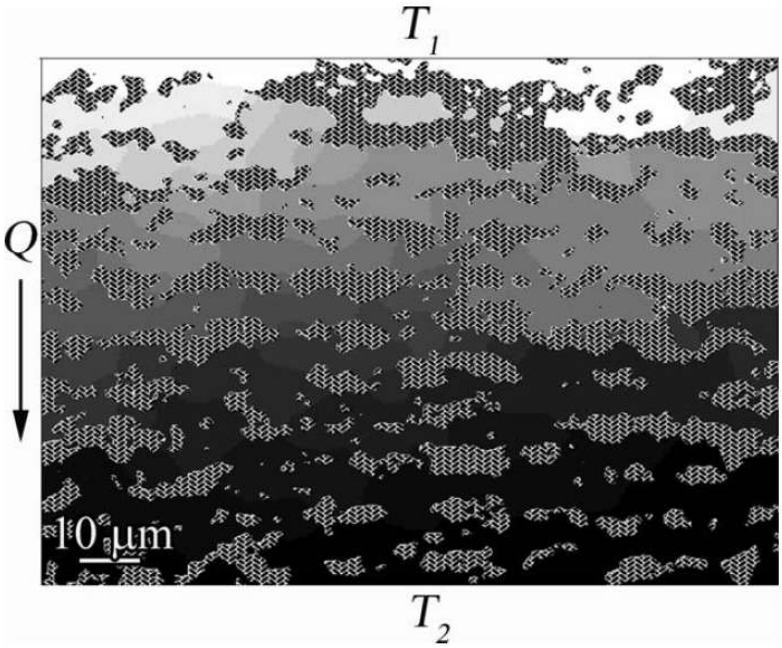

Figure 2.15. Temperature gradient imposed onto an object-oriented finite-element mesh of a thermal barrier coating.[105]

of the microstructural features than the two-dimensional simulations due to lower resolution, and the resulting modulus values matched better with experimental values in the two-dimensional case. This implies that there are advantages and disadvantages to both two-dimensional and three-dimensional finite-element modeling.

The ability of OOF, and the other methods discussed, to create meshes directly from SEM micrographs has an advantage over using more simplified meshes in finite-element analysis software for modeling complex microstructures such as bioSiC. BioSiC has a range of pore sizes, arranged randomly throughout the microstructure. It is difficult to model these structures accurately without taking into account the actual pore distributions in the sample. In addition, the anisotropic nature of bioSiC lessens the limitations of the two-dimensional approximation. Thus OOF is an appropriate method to use to gain more information and study the microstructural effects on the thermal conductivity of wood-based materials.

2.4.2. Thermal Expansion

For the majority of materials, an increase in temperature is accompanied by a volume expansion.[107,108] This is due to the changing amplitude of atomic vibrations with increasing temperature, as indicated by the free energy curve of energy versus distance between atoms. This curve has a deep, asymmetrical trough. Thus as the temperature increases, the average atomic spacings increase due to the asymmetry, leading to thermal expansion. Thermal expansion is not expected to vary with porosity, because the solid portion of the material should expand at the same rate, regardless of the pores.

The thermal expansion of composites is more difficult to model, in that it is dependent on each of the phases present, and unlike in the case of porous materials, mechanical constraint is placed on each phase of a composite, as they expand at different rates.[42] Thermal expansion is also dependent on the geometry, as particles will impose less of a mechanical constraint than fibers in the same matrix.[42] For fiber-reinforced composites, the thermal expansion coefficient is also expected to be anisotropic. With the assumptions of perfect bonding (no chemical reaction) between the fiber and matrix, continuous and perfectly aligned fibers, and invariant property values of each phase with increasing temperature, the following equations for thermal expansion coefficient in the longitudinal (α_{cl}) and transverse (α_{ct}) directions have been derived:

$$\alpha_{\mathrm{cl}} = \frac{\alpha_{\mathrm{m}}\mathrm{E_m}\mathrm{V_m} + \alpha_{\mathrm{f}}\mathrm{E_f}\mathrm{V_f}}{\mathrm{E_m}\mathrm{V_m} + \mathrm{E_f}\mathrm{V_f}} \tag{2.9}$$

$$\alpha_{\mathrm{ct}} = \alpha_{\mathrm{f}}\sqrt{\mathrm{V_f}} + \alpha_{\mathrm{m}}(1 - \sqrt{\mathrm{V_f}})(1 + \frac{\mathrm{V_f}\nu_{\mathrm{m}}\mathrm{E_f}}{\mathrm{E_f}\mathrm{V_f} + \mathrm{E_m}\mathrm{V_m}} \tag{2.10}$$

where α_m, α_f, E_m, E_f, V_m, V_f, and ν_m are the thermal expansion coefficients, modulus, volume fraction, and Poisson's ratio of the matrix and fiber, respectively.[42,95,109] The thermal expansion coefficient of silicon carbide powders that were plated electrolessly with copper and sintered with copper powder to form Cu-SiC composites by Shu et al.[73] was tested. They found that the composite thermal expansion coefficient decreased with increasing volume percent SiC, which correlates with what is predicted by equations 2.9 and 2.10, as the thermal expansion coefficient of SiC is lower than that of Cu. For Cu-bioSiC composites, the Cu can be treated as a fiber reinforcement due to the elongated

channels in porous bioSiC that will be filled with Cu. Thus these predictions can provide estimates for the thermal expansion coefficient of Cu-bioSiC composites.

The thermal expansion coefficient is determined by measuring the change in dimension of a sample with an increase in temperature. This can be done with a dilatometer or thermomechanical analyzer, where a probe is in contact with a sample, and measures the change in length as the sample is heated to a desired temperature. The slope of the curve when the linear change, or strain, is plotted versus the temperature change, yields the thermal expansion coefficient.

2.4.3. Thermal Shock Resistance

The thermal shock resistance is an important property of interest for ceramic materials in high temperature applications. In these situations, often materials are subjected to large temperature gradients, which can cause stresses to build up within the material, and potentially produce crack initiation and growth and even failure. Ceramics tend to have high stiffness and strength, and low thermal expansion and thermal conductivities. These material properties all play a role in determining how the material will behave in these extreme temperature gradient environments.

There are two main theories that have been widely used in predicting how materials will behave in these extreme environments.[110] These are the fracture resistance and the damage resistance approaches. The fracture resistance approach focuses on the initiation of cracks due to built up thermal stresses due to the thermal gradient.[110,111] If a specimen is heated to a high temperature and rapidly quenched, its surface will be in tension and its center will be in compression. If the temperature gradient is high enough, the thermal

stress will reach the strength of the material, causing the initiation of a crack, which can potentially be catastrophic. The magnitude of these thermal stresses are derived from the thermal expansion strain and the modulus of the material, and can be given by:[110]

$$\sigma_{\mathrm{t}} = \frac{\alpha \mathrm{E} \Delta \mathrm{T_c}}{1-\nu} \tag{2.11}$$

where σ_t is the biaxial strength, α is the thermal expansion coefficient, E is the elastic modulus, ΔT_c is the critical temperature difference, and ν is Poisson's ratio. This equation can be rearranged to solve for the critical temperature difference above which catastrophic failure can occur in severe temperature situations, often designated as the R parameter for determining a sample's thermal shock resistance in the situation of infinite heat transfer and a very severe thermal shock:[110]

$$\Delta \mathrm{T_c} = \mathrm{R} = \frac{\sigma_{\mathrm{t}}(1-\nu)}{\alpha \mathrm{E}} \tag{2.12}$$

Not all materials are subjected to infinite heat transfer, depending on the heat transfer properties of the sample and the quenching medium. The Biot modulus, β, describes the severity of the thermal shock, and is a function of the heat transfer (h), thermal conductivity (k) and dimension of the sample through which the heat is being transferred (l). It is given by equation 2.13:[110]

$$\beta = \frac{\mathrm{rh}}{\mathrm{k}} \tag{2.13}$$

Fracture occurs fastest when the Biot modulus is maximized, in situations with large samples, high rate of heat transfer, and low thermal conductivities. This is apparent from

figure 2.16 which demonstrates that as the Biot modulus increases, the time to fracture decreases and the induced stress increases.[108]

In cases of non-infinite heat transfer, the Biot modulus is important, and thus is included in an R parameter for a milder quenching situation:[110]

$$R' = \frac{\sigma_t(1-\nu)k}{\alpha E} \tag{2.14}$$

R' predicts the maximum heat flux that the material can withstand before fracture initiates. Maximizing the R and R' parameters gives a more thermal shock crack initiation resistant material.

The damage resistance approach is concerned with the crack growth and microstructural changes that occur as thermal stresses build up within the sample. It focuses on the elastic energy that is stored from the thermal gradient and builds up in the sample until it is released through crack propagation. There are two R parameters that, when maximized, produce materials with high thermal shock damage resistance. They are:[110]

$$R''' = \frac{E}{\sigma_t^2(1-\nu)} \tag{2.15}$$

$$R'''' = \frac{EG}{\sigma_t^2(1-\nu)} \tag{2.16}$$

Maximizing R''' corresponds to minimizing the stored energy in the system, which minimizes potential crack propagation and maximizing R'''' corresponds to minimizing the distance the cracks will propagate.[88,112]

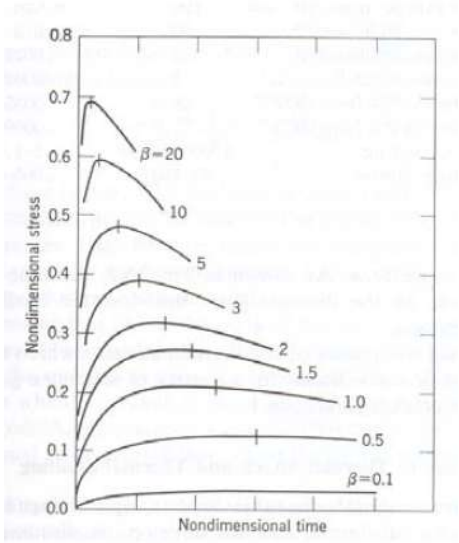

Figure 2.16. Normalized stress vs. normalized time for varying Biot modulus, β.[108]

A unified theory has also been proposed, that predicts, based on the pre-existing cracks, what effect the ΔT_c will have.[113] This theory predicts whether the crack growth will be stable or unstable depending on the initial crack length, crack density (N), and the temperature difference, as illustrated in figure 2.17. Short cracks will grow when the critical temperature is reached until they reach the final length indicated by the graph.[113] The strength is reduced as the crack grows. The crack will not advance further until a higher ΔT_c is reached. If the crack is initially long, the crack will propagate incrementally with increasing ΔT, and the strength will decrease gradually.

There are many experimental methods in practice for testing the thermal shock resistance of ceramic materials.[110] They all involve introducing an extreme temperature gradient, but some occur on rapid heating and some on rapid cooling. Some have very high heat transfer rates, and some are more mild quenches. In rapid cooling experiments, the sample is usually heated to a high temperature using a furnace or infrared lamps and cooling the sample with either a severe quench (high β) or a mild quench (low β). More severe quenches include water,[114–120] oil,[118,120–122] and molten metals.[123] Milder quenches include forced air[124,125] or cool metal contact.[126] In the case of mild quenches, and according to equation 2.16, when the heat transfer coefficient is low, β is also low. Alternatively, in severe quenches, where h is much higher, a higher β results. However, h is also quite variable in the case of liquid quenches. In the case of water, h can change as much as three orders of magnitude between 20-400°C.[127] This is shown in figure 2.18, where the heat transfer coefficient between alumina in water is shown for these temperatures.[127] At low temperatures, the heat transfer rate is high, as the heat is transferred during the nucleate boiling regime, where the bubbles grow and push water to the cooler bulk, allowing colder

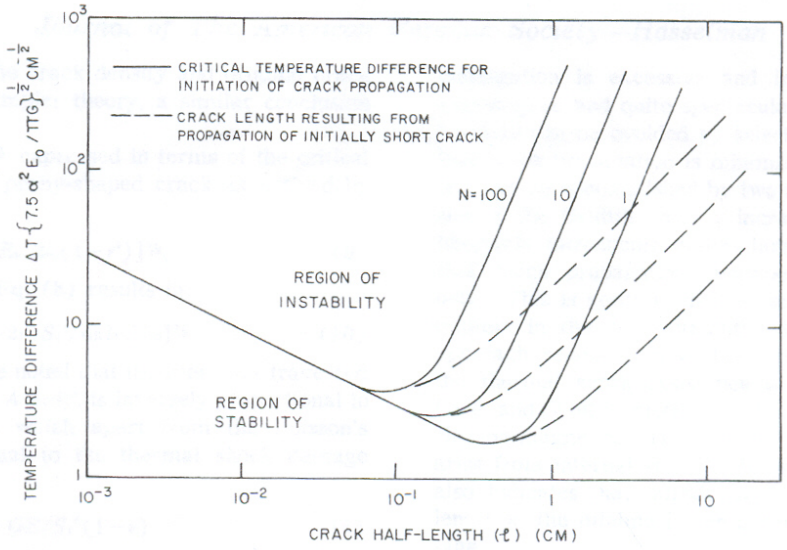

Figure 2.17. Critical temperature differences and lengths of crack growth due to exposure to thermal gradients.[113]

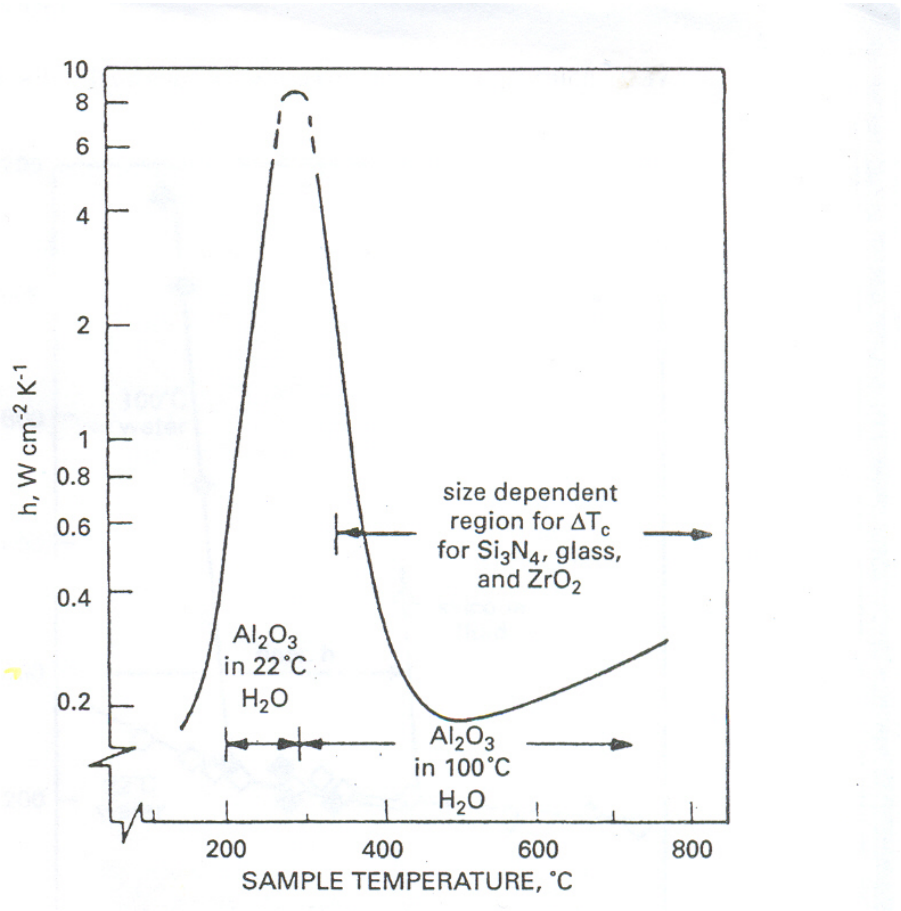

Figure 2.18. Heat transfer coefficient of water to alumina for temperatures up to 400°C.[127]

water to fill in and reach the sample.[110] At higher temperatures, the film boiling regime is reached, and a vapor film is created on the outside of the sample, which insulates the sample, lowering the heat transfer rate.

Boiling water and silicone oil result in lower heat transfer coefficients than room temperature water. The heat transfer coefficient of liquid nitrogen shows less variability with temperature, but is even lower.[110] The thickness of the sample is not critical unless it is so small that the distribution of temperature within the sample is uniform, and the critical temperature difference needed to cause fracture will be extremely high.

After the thermal shock is induced, the extent of damage in the material needs to be characterized.[110] The most common method of damage assessment is the retained strength measurement, typically in bending, as a function of the imposed temperature gradient. The critical temperature difference is determined based on when a significant amount of damage is incurred. An example of a typical strength versus temperature difference curve is shown in figure 2.19.[113] The sample maintains its strength until ΔT_c is reached, where it experiences a sharp drop to its retained strength value. This method is destructive, and thus, requires many samples.

Non-destructive evaluation techniques have also been used to assess sample damage. These methods include monitoring the change in elastic modulus by dynamic resonance,[88] impact-acoustic resonance,[128] and sonic velocity,[117] as well as monitoring crack initiation events using acoustic emission.[117,129] Non-destructive evaluation techniques have the advantage of the ability to test the same sample before and after the thermal shock is induced, ensuring that variation from sample to sample is not a factor. In addition, the

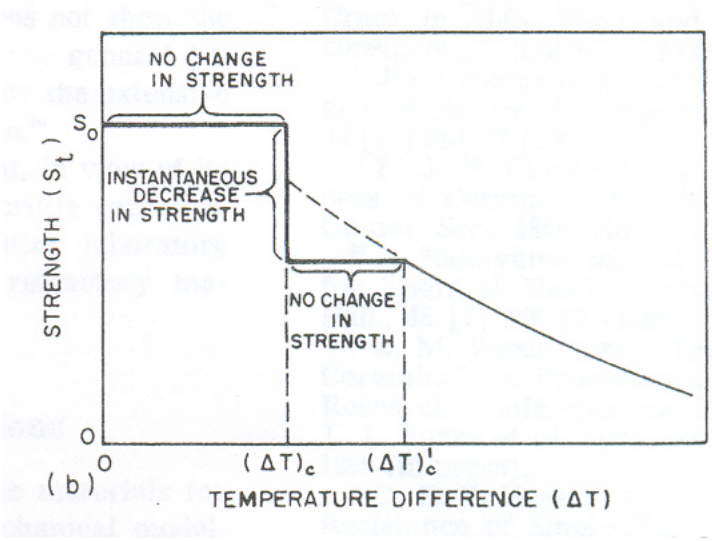

Figure 2.19. Typical strength versus temperature difference curve where the strength drops rapidly when the critical temperature difference is reached.[113]

same sample can be cycled through multiple thermal shock events, allowing the cumulative damage to be assessed.

Thermal shock resistance has been studied for both dense and porous materials. Dense silicon carbide was thermally shocked from temperatures up to 1200°C into an oil bath by Coppola and Bradt.[122] Elastic modulus and fracture strength were used to gauge the thermal shock damage. Modulus decreased with increasing thermal shock temperature. Samples experienced a sharp drop in strength after a thermal shock quench temperature of 300-350°C, after which the strength leveled off between 600-800°C.

Contradictory evidence on the role of porosity on the thermal shock resistance has been provided. Orenstein and Green studied thermal shock of open celled foams of alumina with varying porosities from 78-92%.[118] Thermal shock resistance was determined by quenching the specimens into water or oil baths. Cracks propagated within the struts, and the modulus decreased with increasing initial heating temperature prior to quenching. They found that the thermal shock resistance increased with increasing density and increasing cell sizes. The liquid medium infiltrated the pores, and heated up, causing a decrease in the bulk temperature gradient, lowering the severity of the shock, improving the thermal shock resistance in the larger cells, where permeability of the liquid was easier.

Ding et al. showed that no catastrophic fracture occurred up to 1200°C in their reaction bonded porous silicon carbide ceramics with a porosity of around 50%.[114] They noticed cracks initiated within the struts, which lowered the strength. As the cracks approached pores, they arrested. The strength continuously lowered from 9.8 MPa to 7.9 MPa as the quenching temperature difference increased, but with additional cycles at a given ΔT, the retained strength remained the same. The overall strength loss was

minimal, and the sample did not fail catastrophically, so the sample exhibited a good thermal shock resistance.

She et al. also studied the thermal shock resistance of porous silicon carbide by quenching the samples into a water bath.[119] These samples also showed a slight reduction in bending strength with increasing quenching temperature, due to cracks forming in the strut necks. Cracks arrested upon reaching pores, and thus samples did not fail catastrophically. Further quench cycles did not decrease the retained strength any further, which makes these porous silicon carbide materials good candidates for applications of repeated thermal shocking. Thicker samples showed more thermal shock damage, increasing the value of β, due to larger stresses building up, leading to a more severe shock.

It does not seem from these examples that bioSiC will fail catastrohpically at least up to 1200°C, even after several cycles. Thus porous bioSiC could be a good candidate for applications involving repeated high thermal gradients.

2.5. Summary

BioSiC is a unique ceramic material that utilizes the naturally occurring porous microstructure of wood. This chapter introduced bioSiC as a material useful for high temperature applications, and discussed the processing methods and previous research areas. It also focused on electrodeposition as a means to composite fabrication for thermal management applications. The main thermal properties of interest were discussed and characterization methods were presented. The background information necessary for the remaining chapters of this document was provided.

CHAPTER 3

Processing and Microstructural Characterization of Carbon, BioSiC and Cu-BioSiC Composites

This chapter describes the processing methods used to create carbon and silicon carbide from wood precursors, as well as those developed to produce composites by electrodeposition of these silicon carbide materials. Materials were derived from up to five different wood precursors, resulting in a wide variety of porosity, pore sizes, and pore distributions. A variety of characterization methods were utilized to provide an understanding of the structure and microstructures which developed, including mercury intrusion porosimetry, scanning electron microscopy (SEM), transmission electron microscopy (TEM), X-ray diffraction, Raman spectroscopy, and thermal diffusivity. First the experimental methods for each characterization technique will be detailed. Then the remainder of the chapter will be organized by material (Carbon, BioSiC, and Cu-BioSiC) in order to highlight the evolution of structure and microstructure through complementary techniques as a function of processing parameters, and the unique processing challenges of each material.

3.1. Characterization Methods Employed

3.1.1. Porosimetry

Mercury porosimetry is often used to determine porosity and pore size distributions because mercury does not wet most materials. Thus, pressure is required to force mercury

into the pores, and the magnitude of force required is inversely proportional to the diameter of the pore inlet. An Autopore IV (Micromeritics, Norcross, GA) porosimeter was used in this research and the incremental intrusion of mercury with pressure was recorded. The incremental intrusion was converted into volume percent for a particular pore diameter from:

$$\text{Volume}\% = \frac{\text{I} * \text{P}}{\text{T}} \tag{3.1}$$

where I is the incremental intrusion, P is the porosity and T is the total intrusion. The pore diameters are determined from the Washburn equation, which relates pore diameter (d), pressure (p), wetting angle of Hg (θ), and surface tension between the Hg and the sample (γ_{lv})[130] by:

$$\text{P} = \frac{2\gamma_{\text{lv}}}{\text{d}}\cos\theta \tag{3.2}$$

Equation 3.2 assumes cylindrical pores, and the diameter measured is the smallest opening for a particular pore space.

3.1.2. Scanning Electron Microscopy

Scanning electron microscopy (Hitachi S-3400N-II variable-pressure SEM, Hitachi S-4800-II cFEG SEM) was used to investigate the microstructure of the carbon, biomorphic silicon carbide and copper-biomorphic silicon carbide composites. Energy-dispersive X-ray spectroscopy (EDS) was used to determine the distribution of elements throughout the microstructure. The backscattered electron detector (BSE) was also utilized to readily identify the copper, silicon carbide, and pore phases in composite samples.

3.1.3. Transmission Electron Microscopy

Traditional transmission electron microscopy (TEM) sample preparation was done by thinning discs of 3 mm diameter to a thickness of 100 μm using SiC grit paper on a grinding wheel, with further thinning to a 10 μm with a dimple grinder. The samples were then mounted on molybdenum grids followed by ion milling using a Gatan Precision Ion Polishing System. Several TEMs (JEOL JEM-2100 FasTEM, Hitachi H-800, Philips CM-200) were used to study the nano and microstructure of the material. Multiple TEM machines were used because some of the data collection was done with collaborators at the University of Seville, and the remainder was done at Northwestern University. In addition to micrographs, electron diffraction patterns can also be acquired to identify the material structure, and energy-dispersive X-ray spectroscopy (EDS) was used to determine elemental composition in different regions of the samples.

3.1.4. X-ray Diffraction

X-ray diffraction was performed using a Rigaku ATX-G diffractometer operating at 50 kV and 240 mA, using Cu-Kα radiation (1.54 Å). For the carbon analysis, samples were powdered and 500 mg of carbon was combined with 100 mg of a silicon standard to determine accurate peak locations. A $2\theta/\omega$ scan was performed at a scan rate of 3 degrees per minute with a step size of 0.05°, using 0.5 mm slits. Two known silicon peaks (2θ = 28.4° and 47.3°) were used to establish a linear correction factor for the 2θ axis so that the location of the carbon signal could be compared from sample to sample. The intensity was normalized to the 28.4° silicon peak for each specimen to allow direct comparison of peak intensities from one sample to the next.

For the composite evaluation, bulk samples or cross-sections were used to obtain X-ray patterns. A Soller optic (0.46°) was used to obtain higher surface intensity. A 2θ scan was performed with ω set at 0.6°, at a rate of 4 degrees per minute with a step size of 0.05°.

3.1.5. Raman Spectroscopy

Raman spectroscopy was used to characterize only the carbon materials. In the Raman spectroscopy system (Acton TriVista CRS Confocal Raman System, Princeton Instruments), with an operating current of 40 mA, a laser of wavelength 514.5 nm is incident upon the sample surface, and light is inelastically scattered off of the surface. The resulting spectrum is a function of the bond type and bond length. For carbon in particular, the Raman shifts can provide information about the degree of short-range order and disorder in a particular sample due to the types of bonds present.[131] The G peak, at 1580 cm^{-1}, corresponds to vibrations from the sp^2 bonded carbon, such as graphite. There are three peaks that represent the disorder in the samples. These are called D1, D2 and D3. The D1 peaks represent the sp^2 bonds that are at the edges of graphite sheets. A larger D1 peak indicates more edge disorder, and therefore, that more edges are present. This suggests that there are many smaller units of order, instead of a larger, more homogeneous ordered region. As the full width at half maximum (FWHM) of the peak decreases, the disorder of the system also decreases. This is due to stacking of the polyaromatic rings, breaking up of cross-linked carbon bonds, and volatization of oxygen-based functional groups.[132] The D2 peak, at 1620 cm^{-1}, also represents sp^2 bonds, and these are associated with surfaces. The presence of more surfaces indicates that stacked regions are smaller, and

fewer are aligned into graphite sheets. The D2 peak manifests itself as a shoulder, slightly higher in wavenumber, to the G peak. The D3 peak represents the sp^3 bonding that is present in amorphous carbon. This signal is much weaker than that of sp^2. It is located at a slightly lower wavenumber than the graphite peak, around 1500 cm^{-1}, appearing in the saddle region in between the D1 and G peaks. These 4 peaks are illustrated in figure 3.1.

The relative intensity and width of these peaks indicate how much of the carbon present is ordered or disordered. Large D1 and D2 peaks relative to the G peak indicate that there are many small regions of stacking, but no long-range order. This is indicated by the many free surfaces and edges that are not connected to other groups of carbon. The ratio of the D1 to G peaks indicates the degree of order as well. The larger this ratio is, the more disorder there is in the sample. As the shoulders on either side of the graphite peak begin to disappear and the graphite peak becomes sharper, the order in the sample increases. However, in non-graphitic samples, the D2 shoulder is usually comparable in size to the G peak, making it difficult to distinguish the relative contributions from each of the G and D2 peaks. This makes it impossible to determine the D1/G ratio without deconvoluting the curve.

3.1.6. Thermal Diffusivity

The thermal diffusivity was determined by the flash method.[98] A flash of light or a laser is imparted on one side of the sample surface. The other side has an infrared detector that records the temperature profile as a function of time. An example of a typical temperature

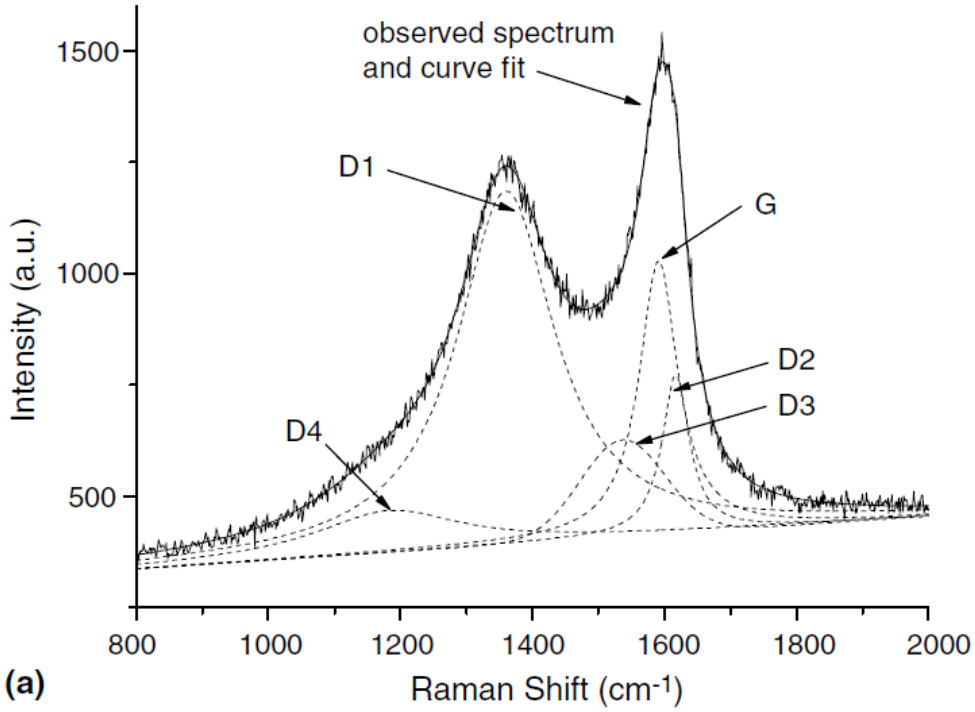

Figure 3.1. Example of Raman spectra for carbon from diesel soot.[131]

versus time curve is shown in figure 3.2, with the half time, $t_{1/2}$, which is the time it takes for the back surface of the sample to reach half of its maximum temperature, indicated.

The thermal diffusivity is determined by relating the half time ($t_{1/2}$) to the sample thickness (L) by

$$\alpha = \frac{\omega L^2}{\pi^2 t_{\frac{1}{2}}} \tag{3.3}$$

Here ω is a constant that equals 1.38 for an ideal curve, when there is no heat loss into the environment during the experiment. A method developed by Clark and Taylor can be used to determine ω for a non-ideal curve.[133] It takes into account the inevitable radiation heat losses by using the shape of the actual experimental curve for each individual sample. There are three Clark and Taylor diffusivities that are assessed during each experimental measurement, called $\alpha_{0.8/0.2}$, $\alpha_{0.8/0.4}$, and $\alpha_{0.7/0.3}$. The fractional subscripts, for example, 0.8/0.2, stand for the ratio between the time that the temperature takes to reach 80% of the maximum divided by that at 20% of the maximum. Ratio correction curves are shown in figure 3.3, and correlate the ratio of the fractional times to the ratio $\alpha t_{1/2}/L^2$, from which α can be calculated. These α values are then averaged to determine the thermal diffusivity of the sample. The thickness of thermal diffusivity samples is dependent on the expected diffusivity, and was 1 mm for carbon samples and 5 mm for bioSiC samples.

3.2. Carbon

3.2.1. Processing

Processing of carbon begins with the selection and pyrolyzation of wood precursors. Five hard wood precursors were chosen for this work: beech (Fagus sylvatica), mahogany

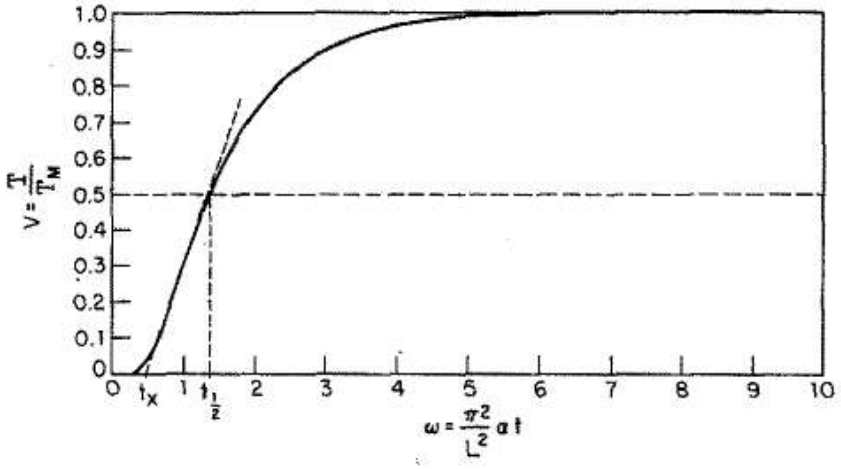

Figure 3.2. Typical temperature versus time curve for calculating thermal diffusivity with the half time indicated.[98]

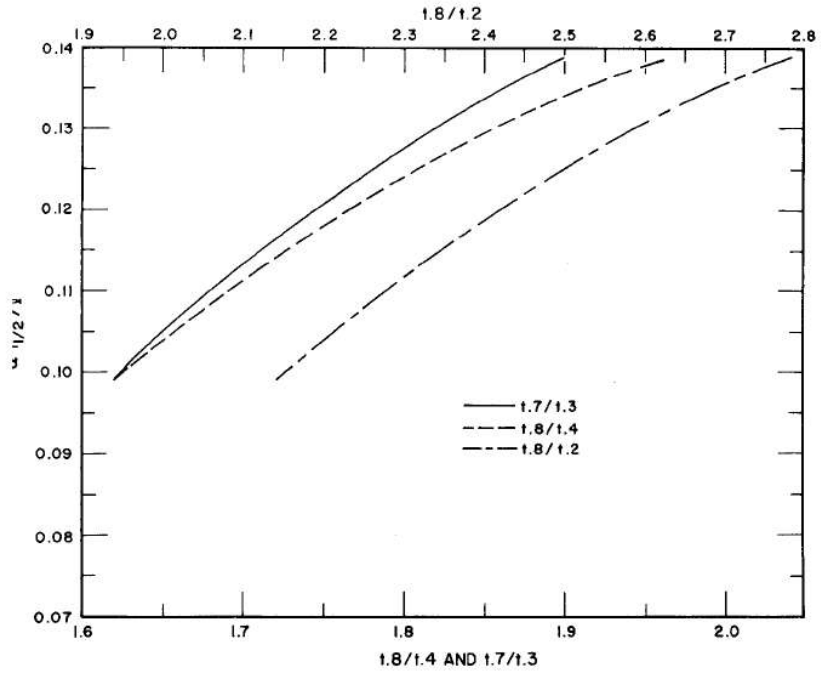

Figure 3.3. Correction curves for calculating diffusivity values using the Clark and Taylor method.[133]

(Swietenia macrophylla), poplar (Liriodendron tulipifera), red oak (Quercus rubra) and sapele (Entandrophragma cylindricum).[134] These woods represent porosities ranging from 52 to 67% and a variety of different microstructures including both ring- and diffuse-porous. Blocks of wood, approximately 5 x 5 x 10 mm, from each precursor were cut and stored in a drying oven at 75°C for at least one night prior to pyrolyzation.

Pyrolyzation is performed by heating the wood precursors to various temperatures between 300 and 1200°C in argon at 1°C per minute. During the heating process, the wood composition decomposes to become a carbon scaffold. The slow heating rate is necessary to minimize warping and cracking of the wood upon heating. The carbon scaffold resulting from this pyrolysis retains the natural wood microstructure. Figure 3.4 shows examples of each wood precursor used in this study, after pyrolyzation to 1000°C. It is obvious from these images that the microstructures vary greatly from wood to wood. Figures 3.4(a)-(d) provide examples of diffuse-porous woods, as the vessel size does not vary significantly from early to late wood. This is in contrast with figure 3.4(e), which shows the ring-porous red oak wood, where the vessel sizes vary greatly between the early and late wood regions.

Additional carbon samples were prepared to characterize using X-ray diffraction, Raman spectroscopy and thermal diffusivity. Some wood was pyrolyzed at 1200°C and then reheated to 1500°C in a vacuum for 60 minutes, and some was commercially pyrolyzed to 2400°C in argon for 30 minutes.

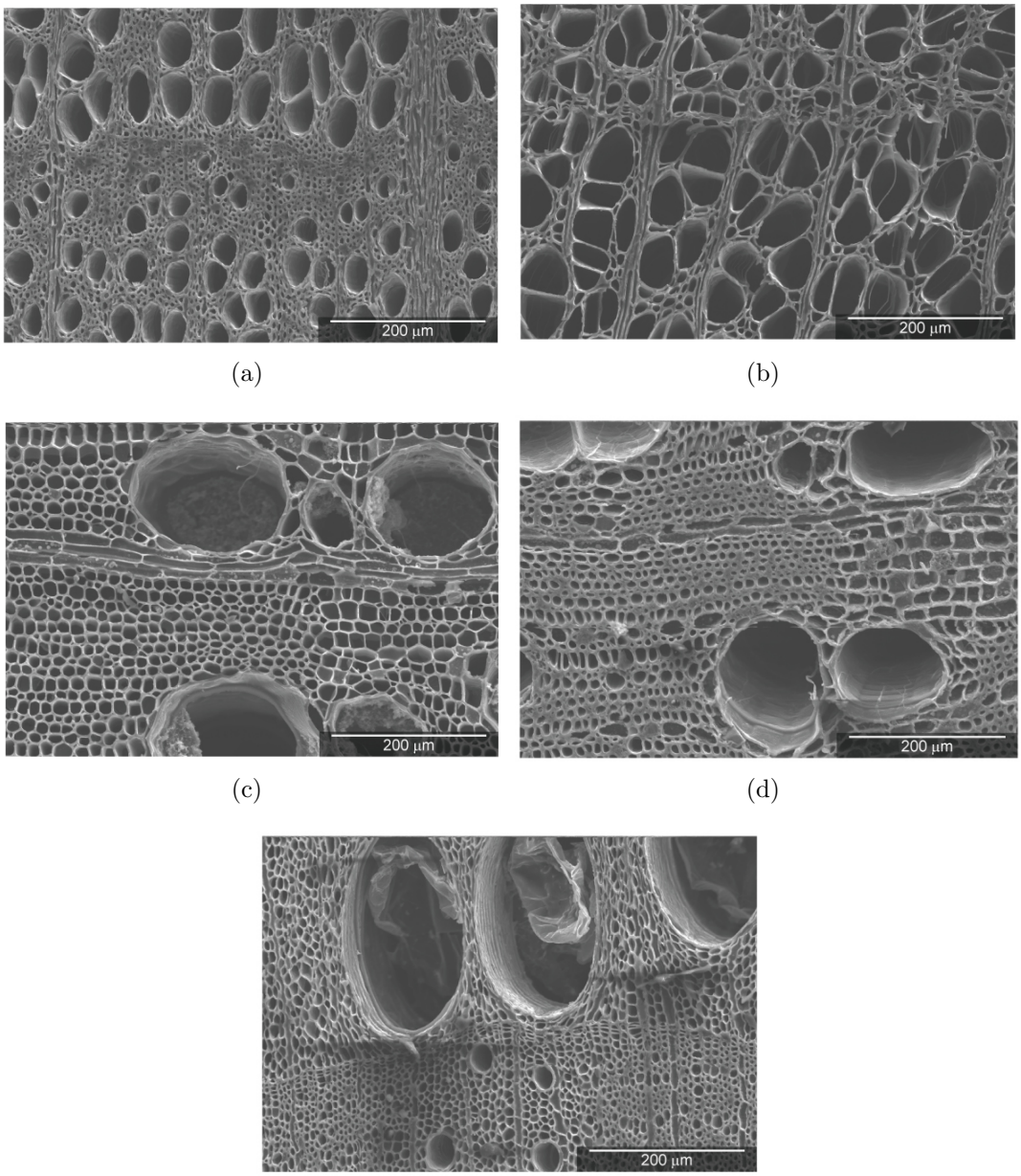

Figure 3.4. Scanning electron micrographs of pyrolyzed wood from five precursors: (a) beech, (b) poplar, (c) mahogany, (d) sapele, and (e) red oak.

3.2.2. Porosimetry

The irregularity of the vessel size distribution is evident in the micrographs in figure 3.4, but becomes more clear when mercury porosimetry is performed. Figure 3.5 shows the pore size distribution of carbon samples pyrolyzed to 1000°C from each of the five woods studied.[135] The pore size distribution varies from wood to wood. Poplar has the most homogeneous distribution, with most of the pore sizes ranging from 0.35-3.2 μm. Red oak exhibits a trimodal distribution of pore sizes with both large and small vessels, as well as smaller fiber cells. Mahogany, which also has a trimodal distribution contains some of the largest vessels seen, but the majority of the porosity comes from pores below 0.7 μm. Beech and sapele exhibit bimodal distributions. The spread between the two peaks is more extreme in sapele than beech. In beech, the entirety of the porosity is contained in between the two peaks of sapele. These pore size distribution differences will lead to significant property differences from wood to wood. Understanding the relationship between these complex and varied microstructures and their resultant properties is a key aspect of working with these wood-derived materials.

The pore size distribution was also determined previously by performing stereology on scanning electron micrographs of the carbon samples.[136] These image analysis results show higher diameters in all cases than the respective porosimetry data. In the SEM images, the cross-sections of the pores, from which the pore diameters were determined, are likely not representative of the smallest openings in the pores, which is what the porosimeter records. Thus, the porosimeter values may be artificially low in some cases. However, the porosimeter is able to resolve much smaller pores than is possible using

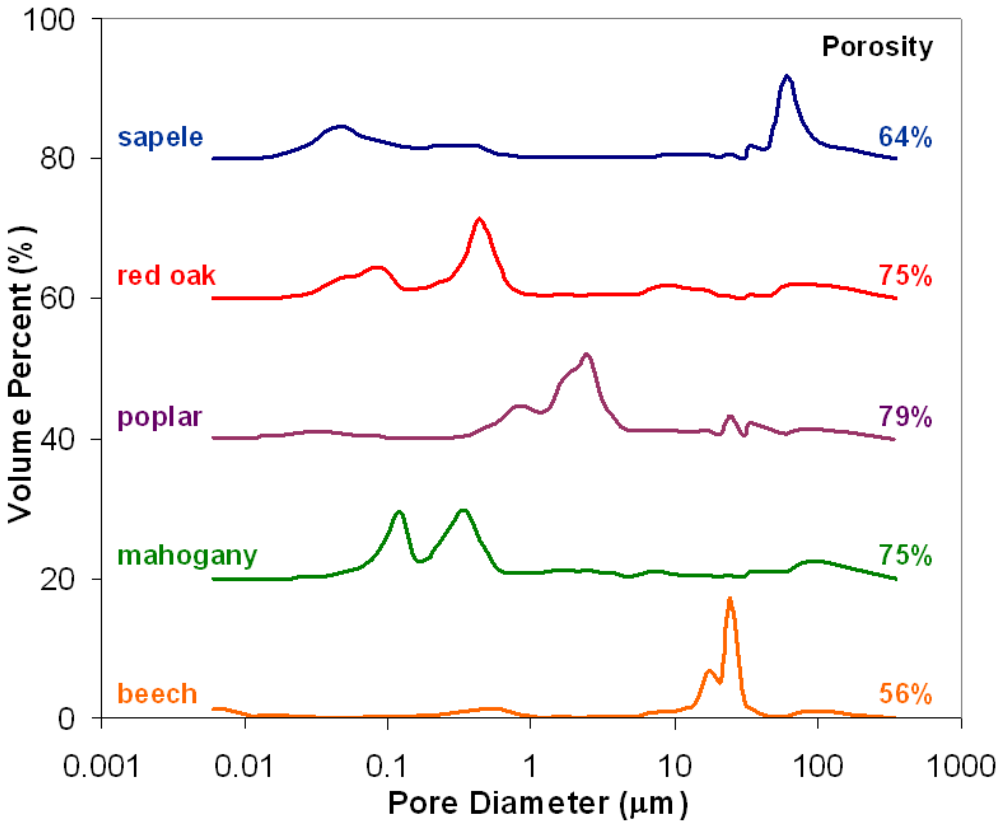

Figure 3.5. Pore size distribution of carbon samples from five wood precursors as determined by mercury porosimetry.[135] Curves are offset by 20 volume% for ease of viewing.

SEM images, which is indicated by the lack of porosity below 1 μm from the stereology approach.

As the carbon is pyrolyzed to higher temperatures, the pore size shifts to slightly smaller values, but the porosity volume fraction remains fairly constant. These relationships are demonstrated in figure 3.6, where mercury porosimetry data from sapele wood pyrolyzed at five different temperatures ranging from 300-1200°C are presented.[135] The peak representing the smaller pores is broadening as pyrolyzation temperature increases, indicating that there is a larger spread of pore sizes encompassed in the region of small pores at higher temperatures. The pore size is also decreasing with increasing pyrolyzation temperature. These changes are in part due to the decomposition of the organic matter and the shrinkage of about 60% that accompanies this decomposition.[26] Another hypothesis is that the carbon is sintering as it is heated to higher temperatures.

3.2.3. Microstructural Evaluation

Materials pyrolyzed at 300 and 1000°C (carbon 300 and carbon 1000, respectively) were selected for further SEM and TEM investigation. These temperatures were chosen because 300°C is below the temperature at which most of the weight loss occurs during the pyrolyzation process,[27] and 1000°C is the processing temperature that has been used in much of the research on bioSiC to date.[8,39,40]

3.2.3.1. Scanning Electron Microscopy. The microstructures of each carbon sample were investigated both on the surface of the sample and the surface of the pores. Low magnification SEM images of each carbon sample are shown in figure 3.7. There does not appear to be any macroscopic microstructural difference between the surfaces of these

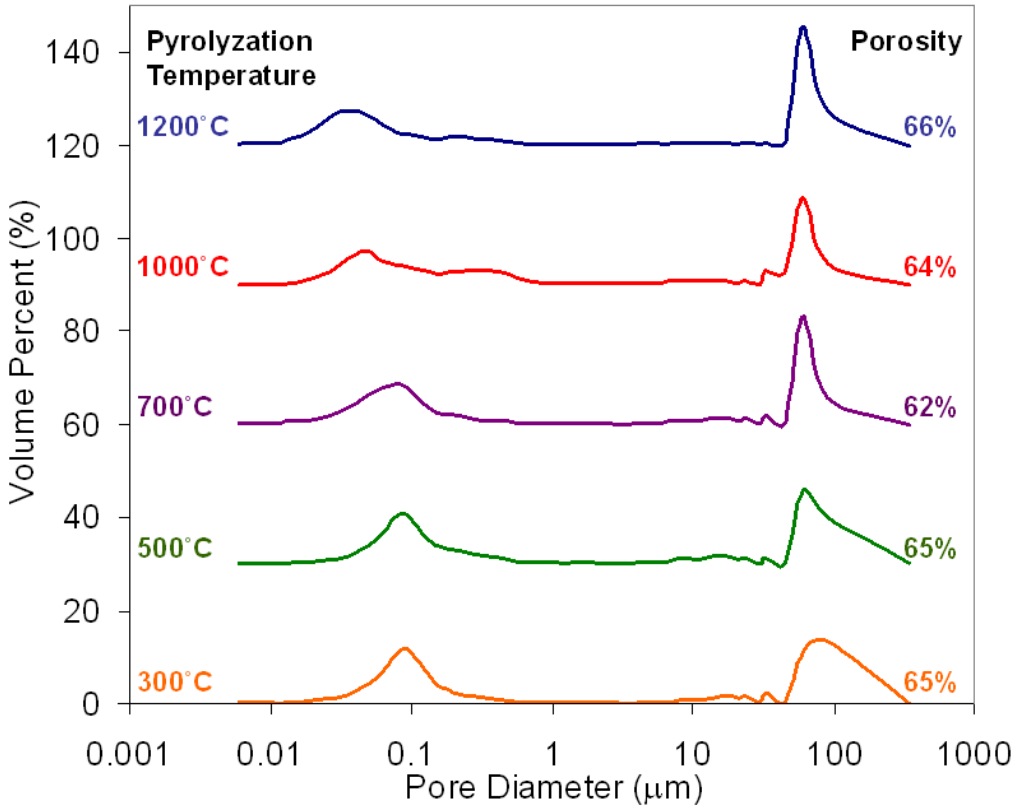

Figure 3.6. Pore size distribution of sapele wood pyrolyzed at different temperatures, as well as their respective porosities, as determined by mercury porosimetry.[135] Curves are offset by 30 volume% for ease of viewing.

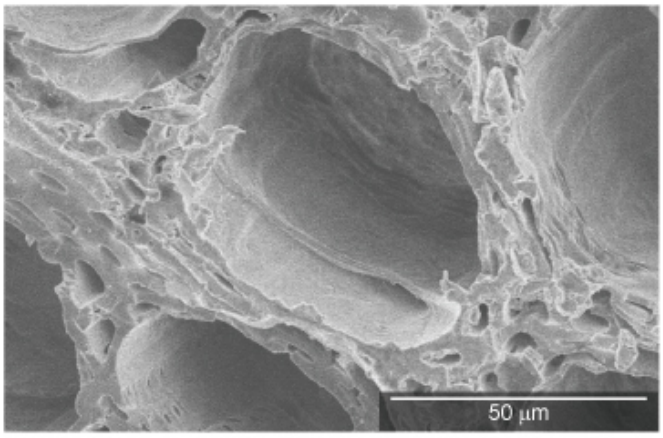

(a)

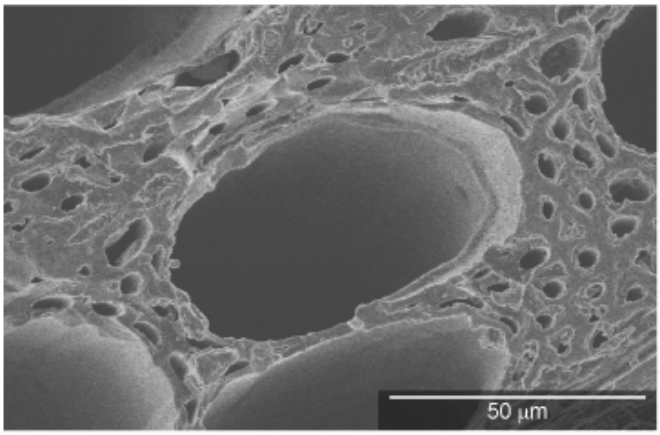

(b)

Figure 3.7. Low magnification scanning electron micrographs of beech-based carbon pyrolyzed at (a) 300°C and (b) 1000°C.

two samples. The samples were also investigated at higher magnifications, focusing on the interior pore wall surfaces. Figure 3.8 shows the different textures that were observed in the different pores of beech-based carbon pyrolyzed at both 300 and 1000°C. Figures 3.8(a) (carbon 300) and (b) (carbon 1000) show a dimpled surface that was seen in many pores of both pyrolysis temperatures. Figures 3.8 (c) (carbon 300) and (d) (carbon 1000) show another texture that is common for the pore interior, in which there appear to be small protrusions from the pore surface. Another common pore interior is shown in figures 3.8(e) (carbon 300) and (f) (carbon 1000). These examples show evidence of the interconnectivity of the individual vessel and fiber cells, as these smaller holes connect the larger pores to one another. It is clear from this set of micrographs that the structure overall and texture of the pore interiors of the carbon pyrolyzed at each temperature are similar. Thus, there are no major microstructural differences between these two materials. These images correlate well with the porosimetry data that show only slight differences in the pore size distribution of samples pyrolyzed at different temperatures.

3.2.3.2. Transmission Electron Microscopy. TEM results of the carbon pyrolyzed at 300°C are shown in figures 3.9(a)-(c). Figures 3.9(a) and (b) show images of the carbon, and figure 3.9(c) is the corresponding electron diffraction pattern. From this diffraction pattern, it is clear that the material is amorphous. This is consistent with Cheng's results that the carbon from cellulosic materials has been shown to be hard, or non-graphitizable, carbon.[30] Figure 3.10 is a high resolution TEM image of the carbon pyrolyzed at 300°C. The carbon shows an amorphous structure, indicated by the lack of long-range order seen at the atomic level in this image. There are small regions of short-range order, but the majority is a disordered structure. This corresponds well to the electron diffraction

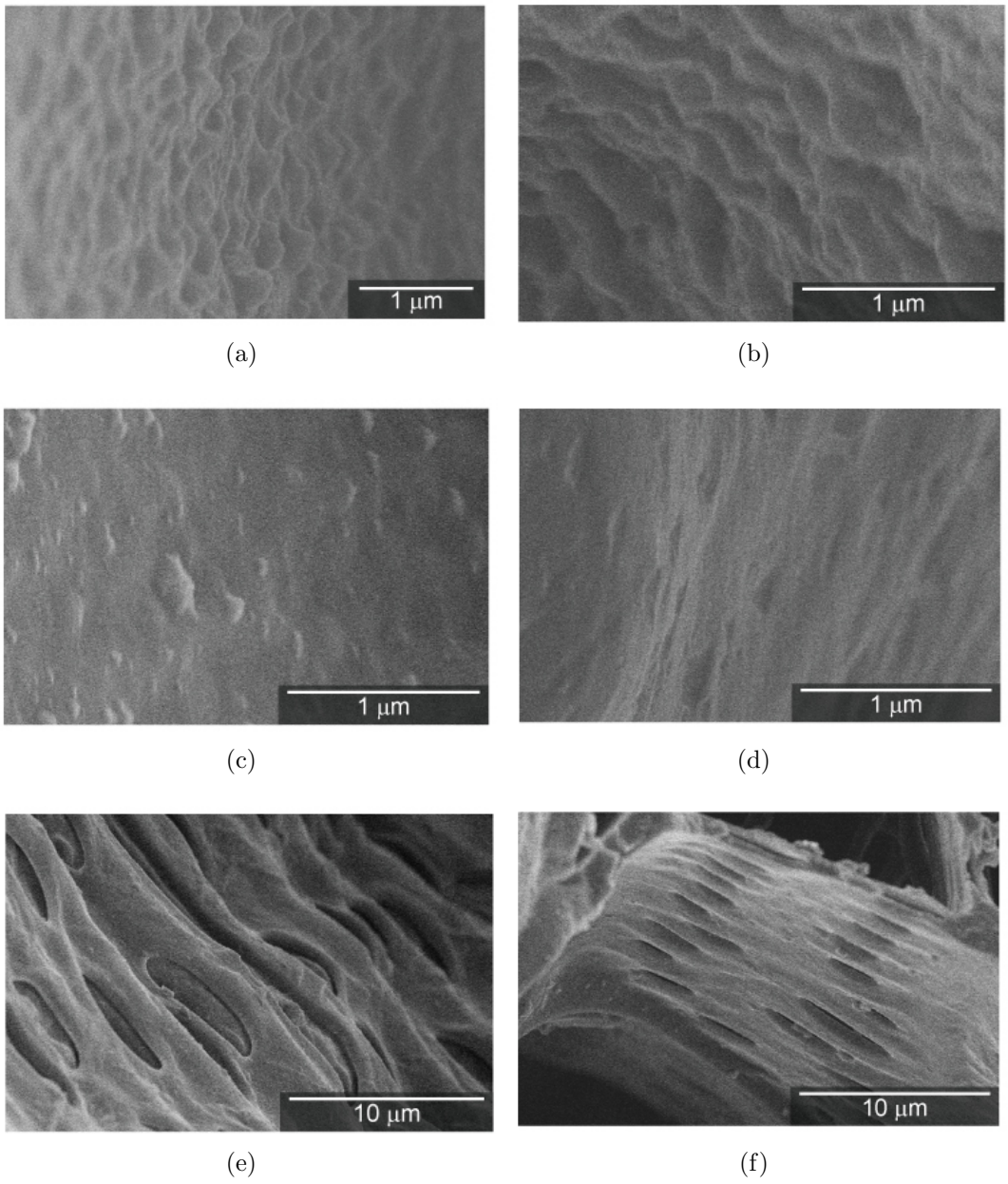

Figure 3.8. Scanning electron micrographs pore interior wall surfaces from beech-based carbon pyrolyzed at (a), (c), and (e) 300°C, and (b), (d), and (f) 1000°C.

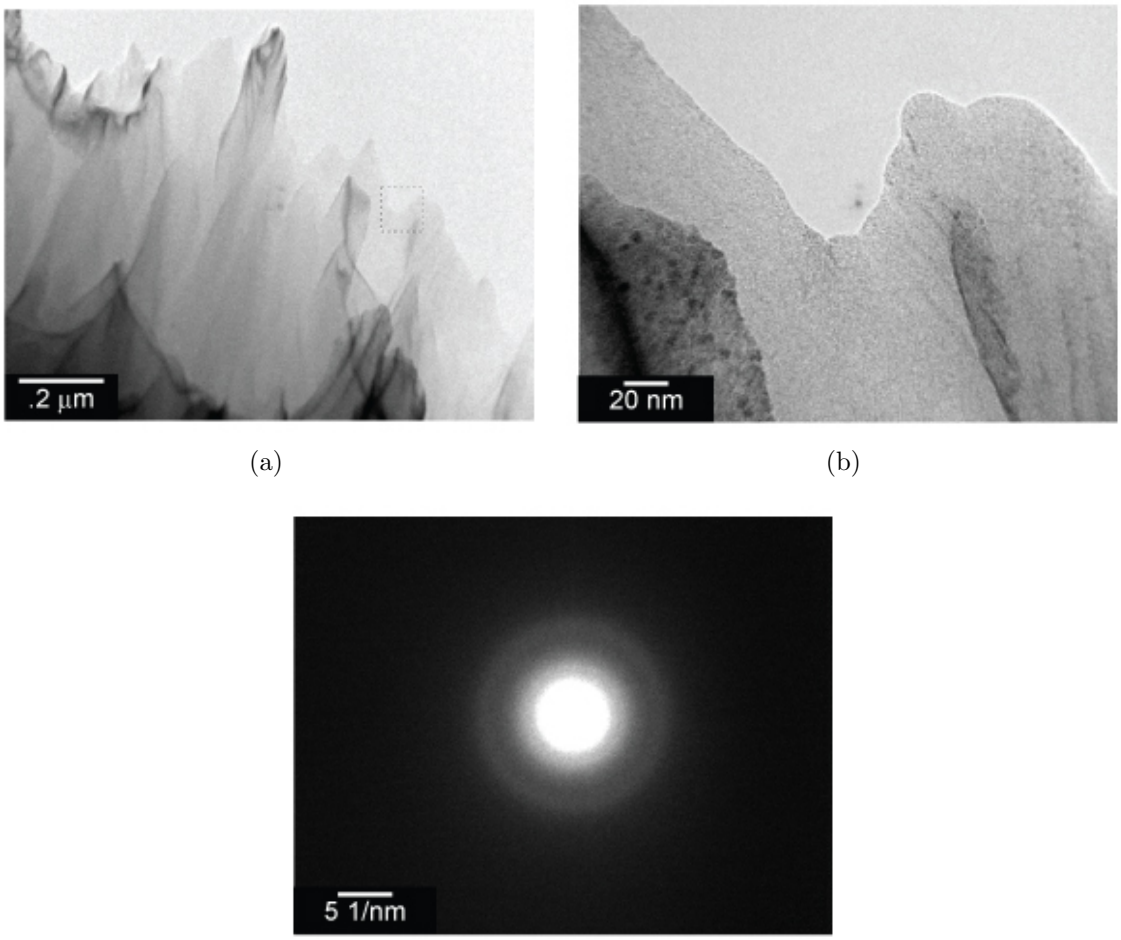

(a) (b)

(c)

Figure 3.9. (a) Transmission electron microscope image of carbon pyrolyzed at 300°C, (b) high magnification image of square in (a), and (c) the corresponding electron diffraction pattern.

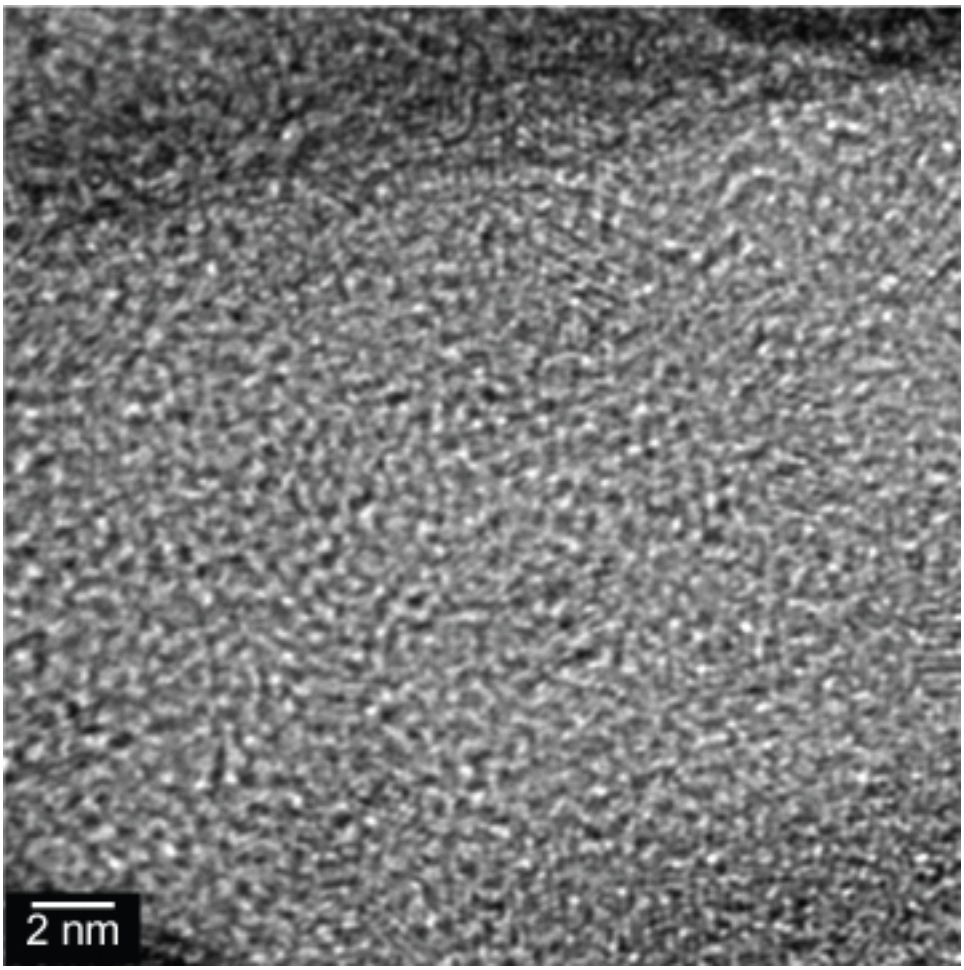

Figure 3.10. High resolution transmission electron microscope image of carbon pyrolyzed at 300°C.

pattern, figure 3.9(c), that also shows an amorphous structure. This also agrees well with the high resolution TEM images from Masters et al. (figure 2.5), that exhibited disordered, amorphous carbon structures.[31]

Figures 3.11(a) and (b) show TEM images of the carbon pyrolyzed at 1000°C and figure 3.11(c) shows the corresponding electron diffraction pattern, which also indicates that the sample is amorphous.

Comparison of these images indicates similarities in the morphology of the carbon materials pyrolyzed at 300 and 1000°C. At high magnifications, the carbon structures appear similar, as the SEM images indicate, and the electron diffraction patterns both exhibit amorphous rings, indicating the absence of long-range order.

3.2.4. X-Ray Diffraction

X-ray diffraction was performed on carbon samples pyrolyzed at temperatures ranging from 300°C to 2400°C to determine if any crystallization of the carbon is occurring with increasing processing temperatures. A plot of the X-ray patterns for carbon of each pyrolyzation temperature is shown in figure 3.12. The two broad peaks that are visible in the patterns are indicative of amorphous carbon, and are present in the general region where the (002) and (101) peaks, corresponding to graphitic or turbostratic carbon, would be. The two sharp peaks in these patterns are due to the silicon standard. The intensity and definition of the broad peaks are enhanced with higher pyrolyzation temperature. This is apparent when focusing on the carbon pyrolyzed at 300 and 500°C, where the two amorphous carbon ridges are nearly flat, as compared to the 1200 and 1500°C samples where they are much more prevalent. In each case, however, the peak of the amorphous

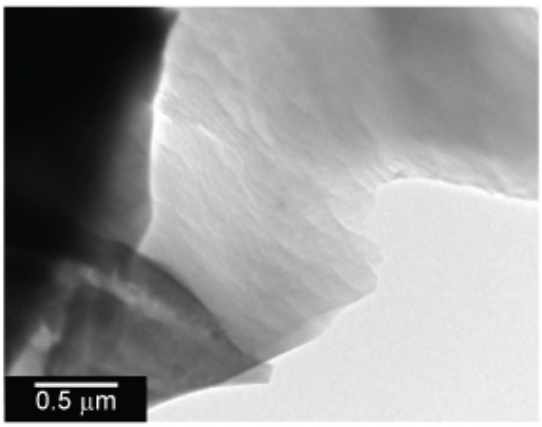

(a)

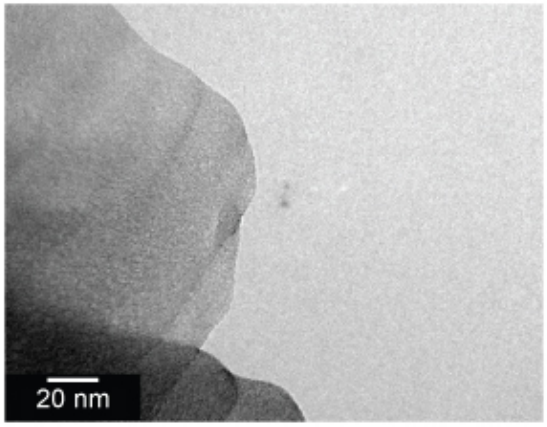

(b)

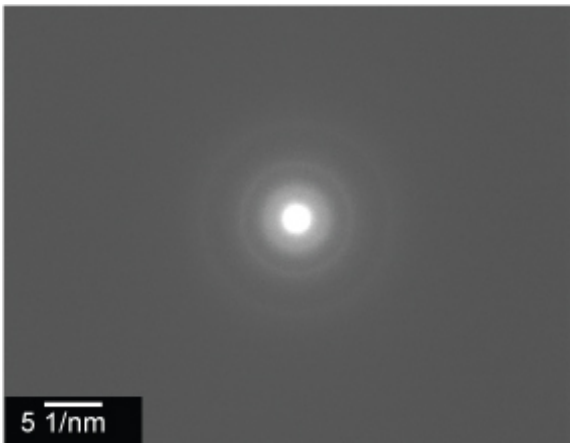

(c)

Figure 3.11. (a) Transmission electron microscope image of sapele-based carbon pyrolyzed at 1000°C, (b) a high magnification image of a region in (a), and (c) the corresponding electron diffraction pattern.

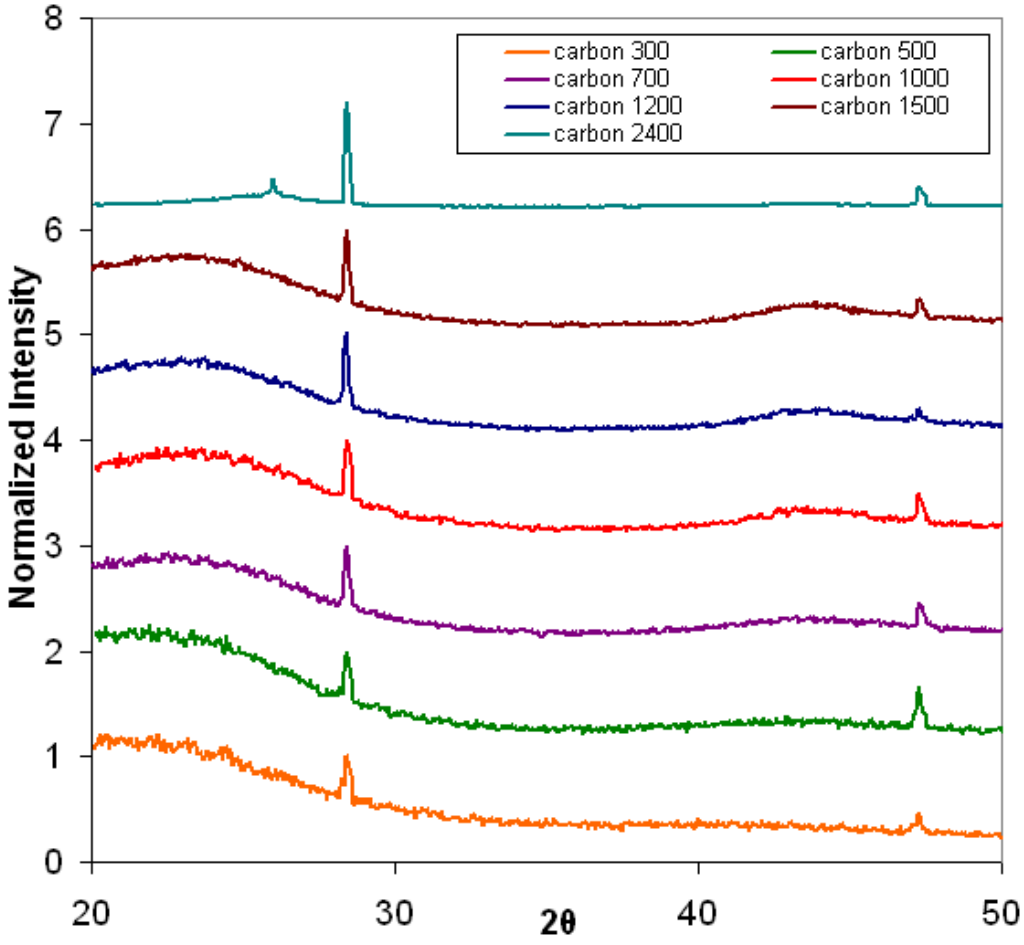

Figure 3.12. X-ray diffraction of carbon pyrolyzed at different temperatures. Curves are offset for ease of viewing.

ridge is shifted to the left several degrees from either the graphitic carbon peak or the turbostratic carbon peak that appear at 26.5° and 26°, respectively.[137] Only with carbon pyrolyzed at 2400°C is there a well-defined peak, and this occurs at 26°, indicating the presence of turbostratic carbon. These results agree well with Byrne and Nagle, who performed X-ray diffraction on powdered poplar-based carbon.[138] They did not see any resemblance to a well-defined peak until the pyrolysis temperature was up to 2500°C.[138]

The minimal increase in definition of the broad carbon peaks with increasing pyrolysis temperature from 300-1500°C and the ultimate formation of a turbostratic carbon peak at 2400°C indicates a slight increase in the degree of ordering among the carbon-carbon bonds and a trend towards a layered structure. More information can be determined by Raman spectroscopy, described in the next section.

3.2.5. Raman Spectroscopy

Raman spectroscopy was performed on beech-based carbon samples pyrolyzed at temperatures between 300 and 2400°C. The Raman spectra are shown in figure 3.13 and the curves are stacked for ease of view. The progression of these curves as the pyrolysis temperature increases reflects the subtle changes in the structure of the carbon that the X-ray diffraction patterns do not indicate. The spectra of samples pyrolyzed at lower temperatures have very broad D1 peaks. There is almost no definition, and it is extremely difficult to determine where each peak begins or ends. As the pyrolysis temperature increases, the D1 peak slowly becomes more defined, and the FWHM decreases, indicating increasing order.

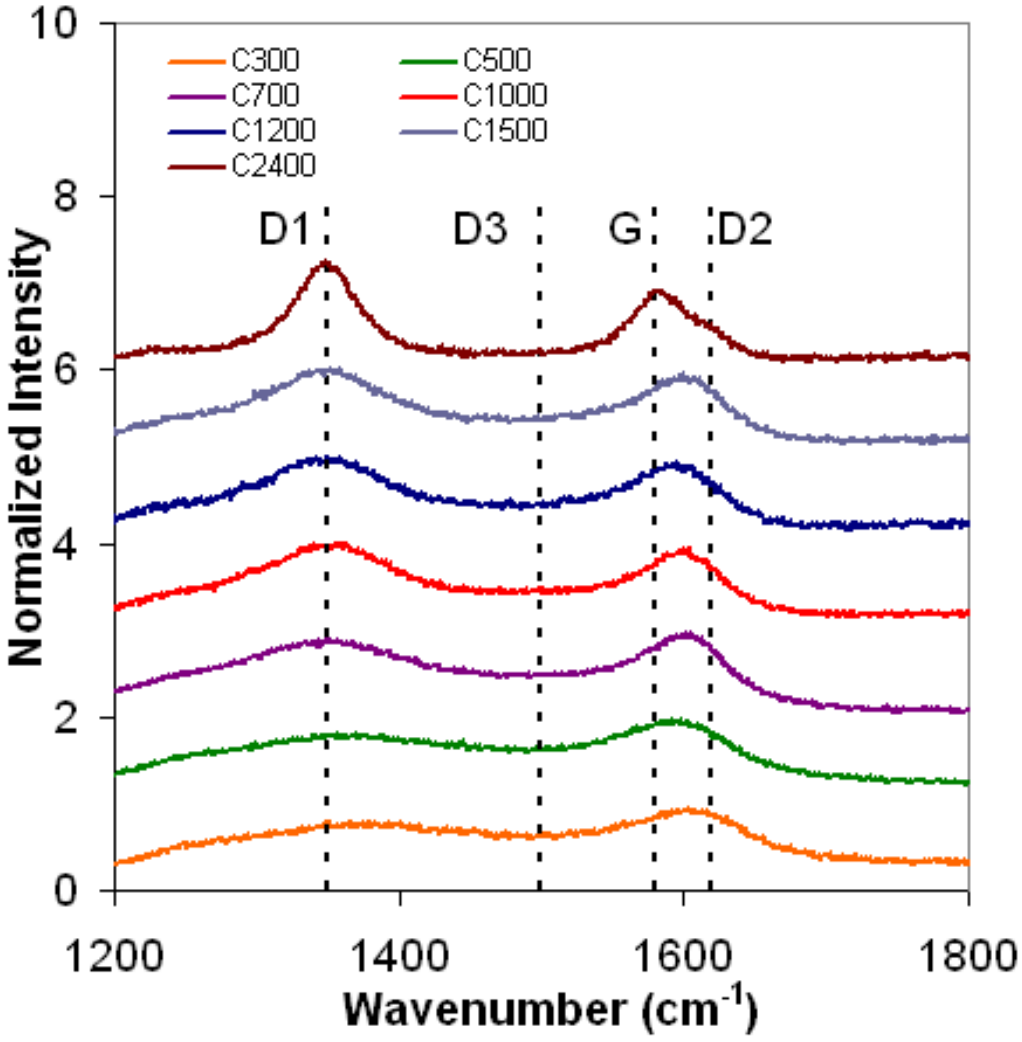

Figure 3.13. Raman spectra of beech-based carbon pyrolyzed at temperatures from 300-2400°C. Curves are offset for ease of viewing.

The region between the D1 and G peaks lacks definition at low pyrolyzation temperatures, which indicates the presence of a large D3 peak. The G peak is also broad, which, along with the peak shift towards a higher wavenumber, indicates that there is a significant contribution from the D2 peak as well. The presence of these well-defined D2 and D3 peaks shows that there is a large degree of disorder among these samples. As the pyrolyzation temperature increases, the combined G and D2 peak begins to shift towards a lower wavenumber, until at 2400°C, it reaches the expected position for the G peak, at 1580 cm^{-1}. This peak shift is mainly a result of the growing G peak accompanied by a decrease in intensity of the D2 peak, indicating improved order resulting from a decreased number of free surfaces. The increased definition at the base of the peak is a result of the decreased intensity of the D3 peak, indicating a decrease in the sp^3 bonds. The sharp change in the combined G and D2 peak that is apparent as the pyrolyzation temperature increases from 1500 to 2400°C indicates the presence of turbostratic carbon. Turbostratic carbon contains crystalline regions, but the sheets are not aligned with each other as in graphite. The D1/G ratio is difficult to determine for most of the samples, as the G and D2 peaks are unable to be distinguished.

It is clear from these Raman spectra that the carbon pyrolyzed at these temperatures are not graphitic, which correlates well with the X-ray diffraction results shown in the previous section. However, it is apparent that there is some progression towards increased order, as exemplified by the improved definition in both the D1 and G peaks and the decreasing intensity of the D2 and D3 peaks. This implies that while the increased pyrolyzation temperature does not produce a graphitic structure, differences exist in the bond characteristics of the samples as a result of altered processing conditions.

3.2.6. Thermal Diffusivity

The thermal diffusivity of beech-based carbon pyrolyzed at 300, 500, 700, 1000, 1200, and 2400°C, as well as mahogany-, poplar-, red oak-, and sapele-based carbon pyrolyzed at 300 and 1000°C was determined using a xenon flash diffusivity system.[139] Three measurements were made on each sample. Software incorporating the Clark and Taylor approximations was used to determine the thermal diffusivity of each sample.[133] In the axial orientation, the samples were too thin and porous and transmitted too much light, giving inaccurate results, so only samples in the transverse orientation were tested.

Figure 3.14 shows the thermal diffusivity of beech-based carbon pyrolyzed at temperatures from 300-1000°C. From this figure, it is clear that the thermal diffusivity increases with increasing pyrolysis temperature, gradually between 300 and 700°C, and then more quickly. While most of the weight loss during pyrolyzation occurs after 400-500°C, as shown in figure 2.4, this indicates that there are other changes that still have not been completed by 700°C.[28]

The increase in thermal diffusivity with increasing pyrolysis temperature can be attributed to the increased order in the system. Thermal energy is transferred via a random process, and diffuses through the lattice by phonons.[93] Thus, the phonon mean free path and velocity are important factors in determining the thermal diffusivity and conductivity. Lattice imperfections limit the mean free path, lowering the diffusivity. Thus, a more ordered lattice will have a higher mean free path, and a more efficient rate of heat transfer throughout the system. As seen in the X-ray diffraction pattern (figure 3.12), as the broad amorphous carbon peak sharpens with increasing pyrolysis temperature, the

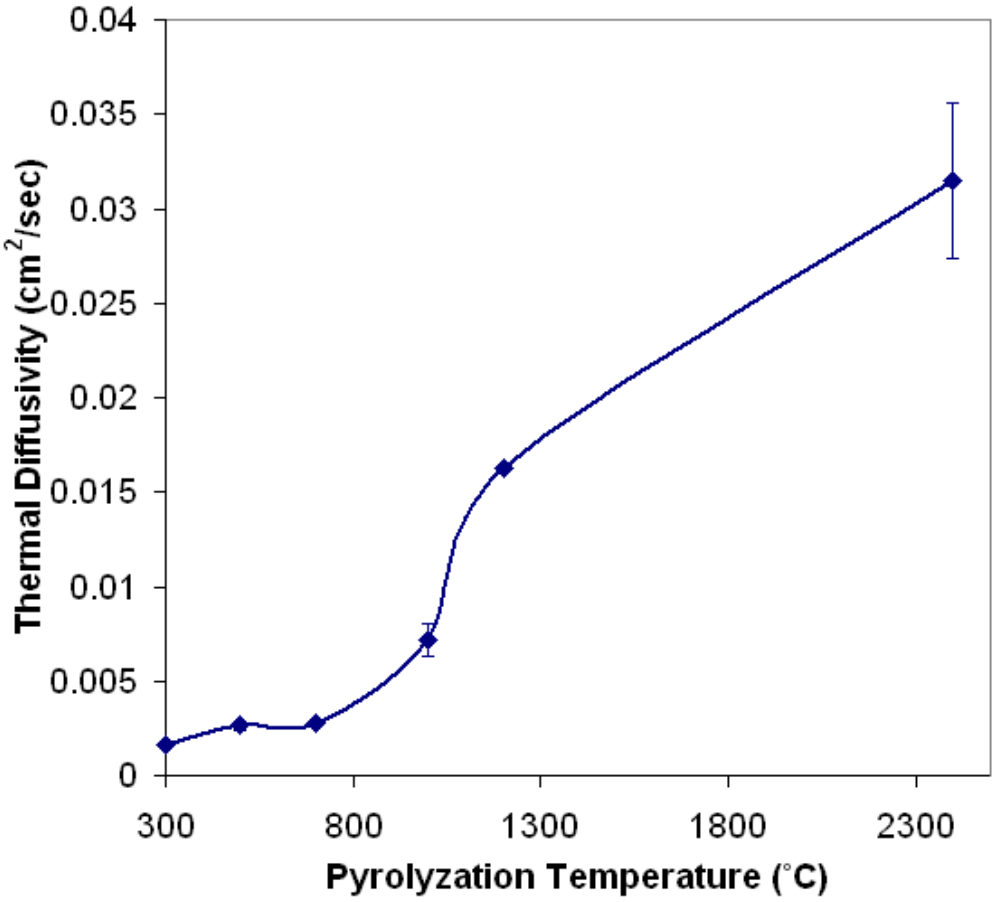

Figure 3.14. Thermal diffusivity of beech based carbon pyrolyzed at different temperatures. Error bars represent one standard deviation.

FWHM increases. This indicates both a decrease in d-spacing, implying smaller interatomic distances, and a decreased variability of interatomic distances. The Raman spectra (figure 3.13) similarly show that the order in the system is increasing with increasing pyrolysis temperature. The decreasing FWHM of the D1 peak and the disappearance of the D3 peak, associated with amorphous sp^3 bonds, also indicate the decrease in distance between nearest neighbor atoms. Thus, at these higher pyrolysis temperatures, where order in the system is increased, so is the thermal diffusivity.

3.2.7. Summary

Porosimetry, SEM and TEM data show many similarities between the structures of the carbon samples pyrolyzed at different temperatures. This indicates that the pyrolysis temperature may not have a significant impact on the microstructural properties of the resultant material. However, other investigation techniques, including X-ray diffraction, Raman spectroscopy, and thermal diffusivity measurements indicate that there are, in fact, more subtle changes occurring in the carbon structure, at the atomic level, and are thus critical for developing an understanding of the atomic structure of carbon. It is clear that the degree of order is increased as the pyrolyzation temperature of carbon increases.

3.3. Biomorphic Silicon Carbide

3.3.1. Processing

As described previously, silicon carbide can be made by melt infiltration of the pyrolyzed carbon. Prior to infiltration, samples of the desired shape can be cut from pyrolyzed

wood. The carbon is easy to machine and the shape is largely retained throughout the remaining processing steps.

The carbon specimens are placed into a boron nitride-coated alumina crucible with silicon powder in excess of the stoichiometric requirement of 1.5 for the Si+C→SiC reaction in order to maximize the conversion of carbon to SiC. The samples are then heated to 1500°C in a vacuum environment and held for one hour to allow the reaction to occur. Samples thicker than 1 cm may need to be held for longer to allow more time for diffusion and more complete conversion. Since the alumina tube used for the reaction can creep and break if it is held at high temperatures for too long, larger samples go through the infiltration step more than once to complete the reaction. The resulting SiC after this step has residual silicon in some of the pores. An example of sapele-based bioSiC with excess Si is shown in figure 3.15. In order to produce a porous ceramic microstructure, the residual Si is removed by continuous stirring in a concentrated hydrofluoric and nitric acid etch for 1-2 weeks. The resulting porous silicon carbide ceramics from five wood precursors are shown in figure 3.16. It is apparent that these microstructures mimic those of their carbon precursors in figure 3.4.

3.3.2. Porosimetry

Porosimetry measurements were also performed on the resultant silicon carbide samples. Figure 3.17 shows the pore size distributions for the five different wood types derived from carbon pyrolyzed at 1000°C.[135] In the beech-based materials, the pore size distribution shifts to slightly larger sizes, due to breaking struts between the pores during the expansion reaction. This causes some of the pores to coalesce. The poplar-based materials exhibit

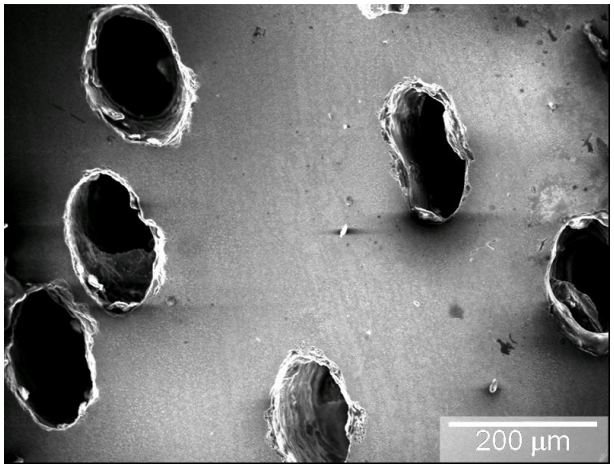

Figure 3.15. Sapele-based bioSiC with residual silicon present.

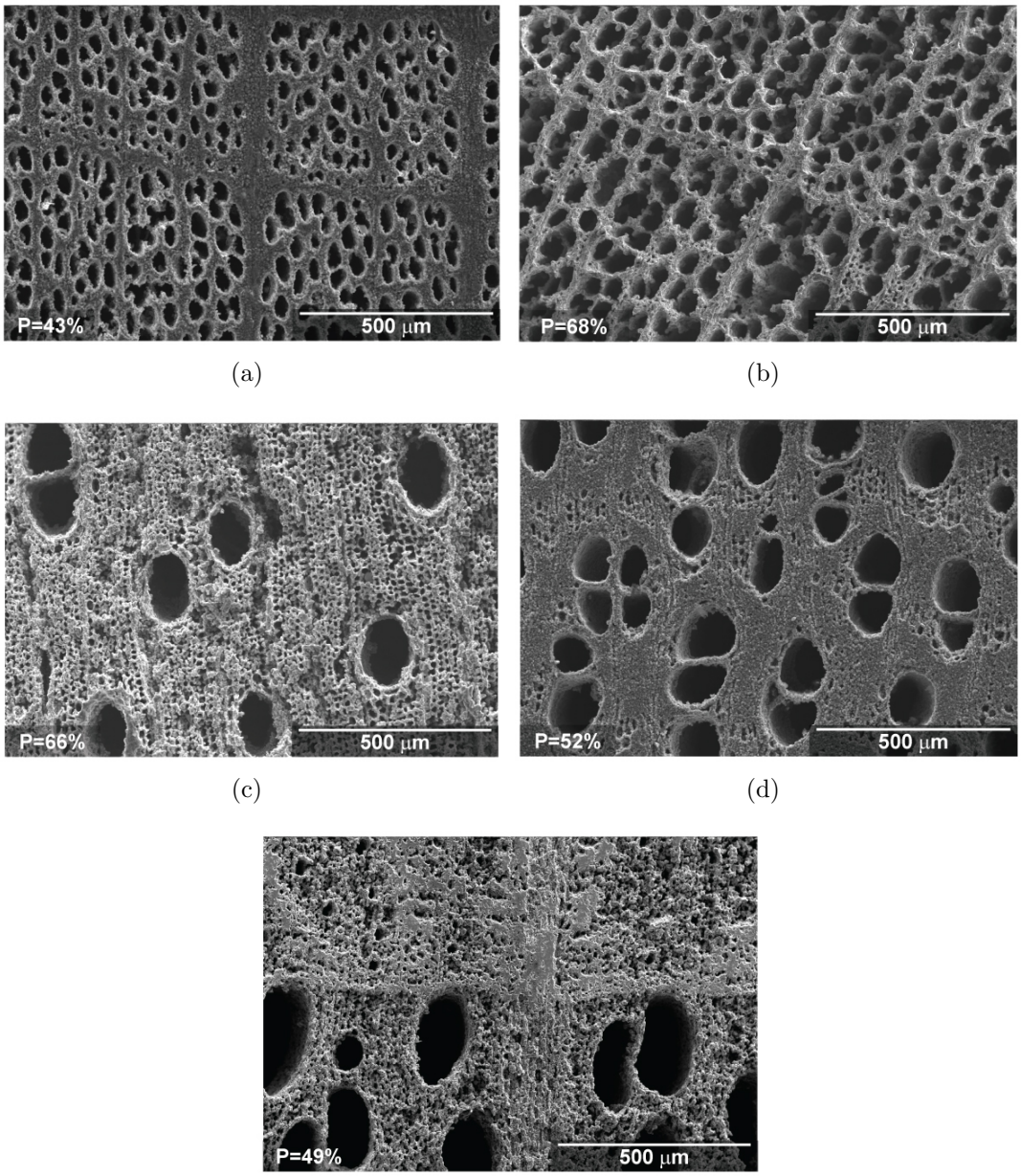

Figure 3.16. Scanning electron microscope images of bioSiC derived from carbon pyrolyzed at 1000°C from (a) beech, (b) poplar, (c) mahogany, (d) sapele and (e) red oak woods.

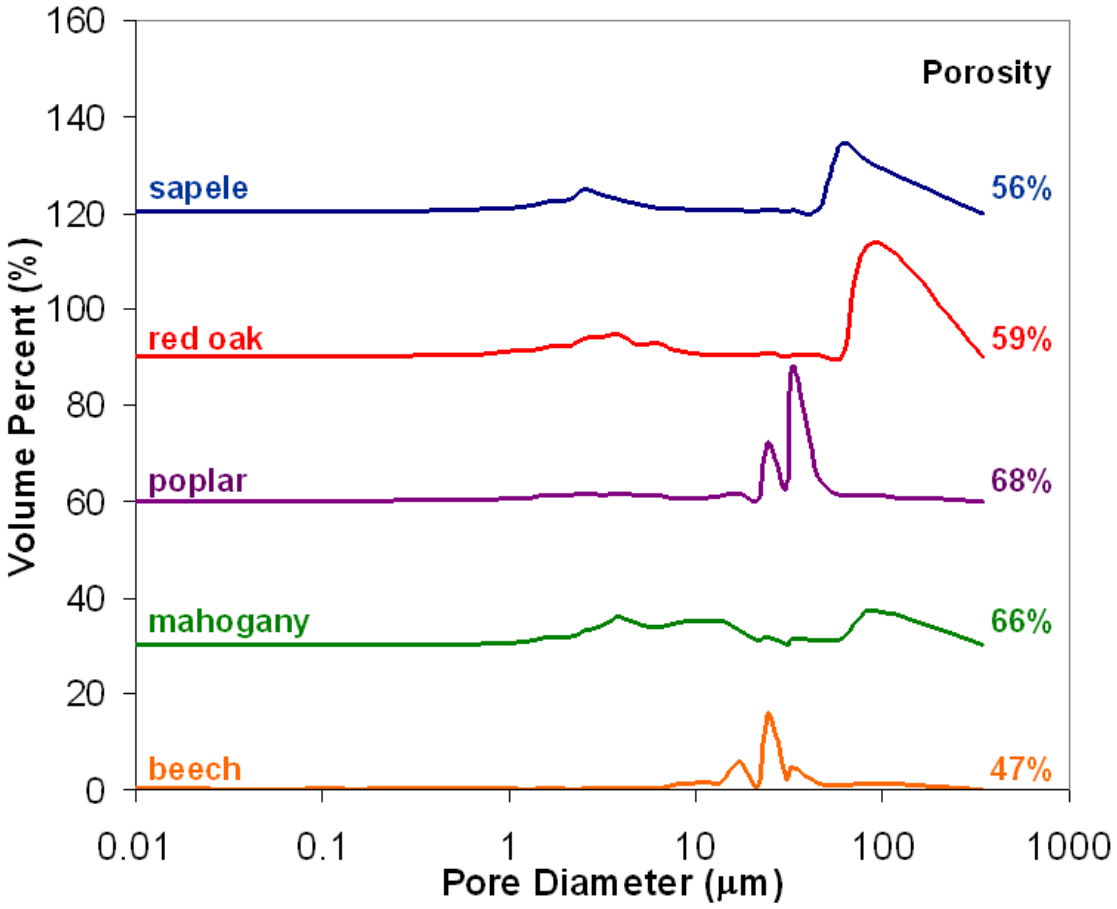

Figure 3.17. Pore size distribution of bioSiC derived from five woods, and their corresponding porosities, as determined by mercury porosimetry.[135] Each curve is offset by 30 volume% for ease of viewing.

a similar trend, but to a much greater degree, as the region of smaller porosities shifts from a range of about 0.5-30 μm to a range of about 20-60 μm due to pore coalescence. In the red oak-based materials, the smallest pores also close up, leaving behind the large pores, which are greater than 60 μm in diameter. The majority of the porosity in red oak-based bioSiC is now made up of large pores, whereas in the carbon, it was made up of small pores. Mahogany varies greatly from wood to wood, and even from position to position within the sample, due to the xylem that blocks the pores. This can be seen clearly in figure 3.4(c). The blockage, which can be either in the center or on the sides of the individual pores, causes the porosimeter to give a reading smaller than the actual pore dimensions, because it is the smallest diameter of a pore that is reported. The smallest pores in sapele also close up, and a new peak appears around 1-6 μm. There is no microstructural evidence for this peak, but it has been seen by other researchers.[135,140]

The porosimetry results for bioSiC were also compared to stereology performed using SEM images.[39,136]. Similar to the carbon comparison, the stereologically determined pore diameters were higher in all cases than those determined from porosimetry. Again, this can be because the porosimeter records the smallest diameter entrance to a pore channel, whereas the values determined from image analysis will be a cross-section of the pore, not necessarily at its smallest point. The results for the bioSiC match slightly better than those for carbon, because the smallest pores (less than 1 μm) close as a result of the SiC formation volume expansion. Thus, while pores of this size were absent from the carbon stereology results due to resolution, they were not present in either case for bioSiC samples.

Figure 3.18 shows the pores size distribution for sapele-based bioSiC derived from carbon pyrolyzed at temperatures ranging from 300-1200°C.[135] The porosity of each sample is listed next to its pore size distribution. The porosities decreased from pyrolyzed wood to silicon carbide, due to the volume expansion of about 58% upon conversion to silicon carbide. The region of small pores, below 1 μm, close due to this volume expansion. The distributions, however, do not vary significantly with pyrolyzation temperature. During the infiltration step, prior to the silcon vaporizing or melting, the carbon is heated to above 1200°C. Thus, pyrolyzation continues in the furnace as the infiltration step is taking place. This leads to the similarities between each of the five curves in figure 3.18. Thus, the pore size distribution and porosity are independent of carbon pyrolyzation temperature for bioSiC materials.

3.3.3. Microstructural Analysis

3.3.3.1. Scanning Electron Microscopy. Scanning electron microscopy was used to study the structure of the bioSiC made from carbon of two different pyrolysis temperatures: 300°C (bioSiC 300) and 1000°C (bioSiC 1000). Figure 3.19(a) and (b) show images of red oak-based bioSiC 300 and bioSiC 1000, respectively. Both of the images show the presence of both nano-and micron-sized grains, indicating a similar morphology for both samples. This provides further evidence that the structure of the bioSiC is independent of initial carbon pyrolysis temperature.

3.3.3.2. Transmission Electron Microscopy. The structures of both bioSiC 300 and bioSiC 1000 were further investigated using TEM. Figure 3.20(a) is a TEM image of a region in bioSiC 300 where nano-sized SiC grains are surrounded by regions of residual

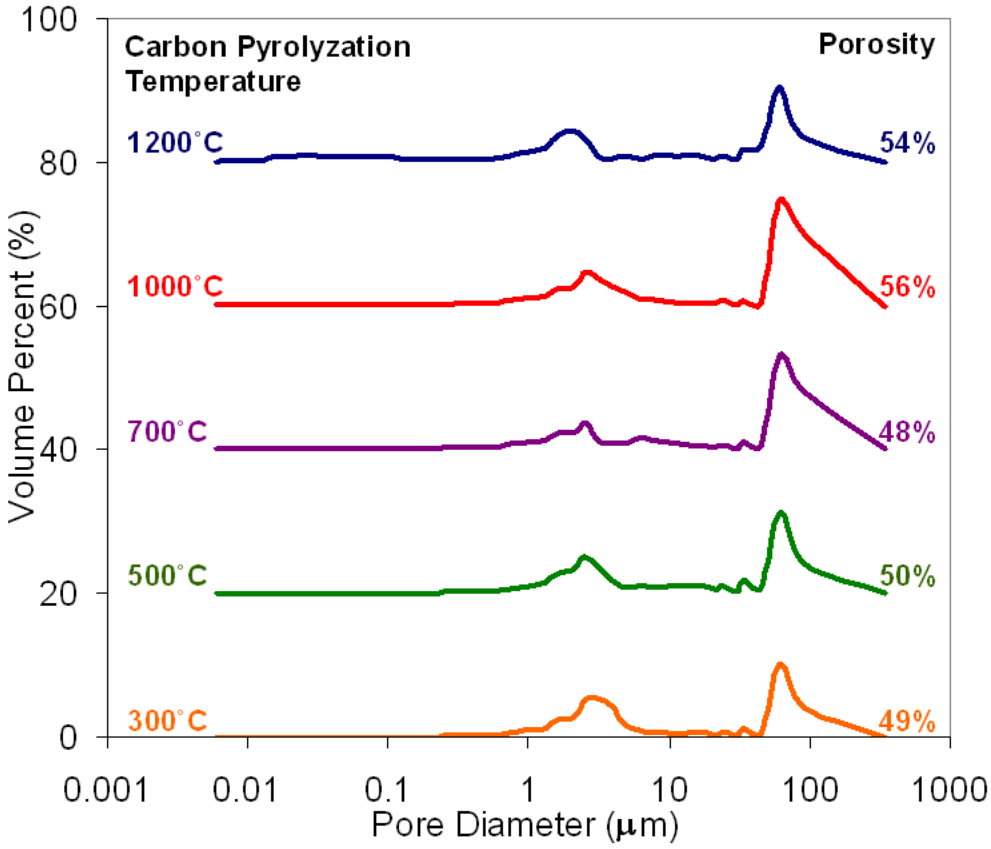

Figure 3.18. Pore size distribution and porosity of sapele-based bioSiC derived from carbon pyrolyzed from 300-1200°C as determined from mercury porosimetry.[135] Curves are offset by 20 volume% for ease of viewing.

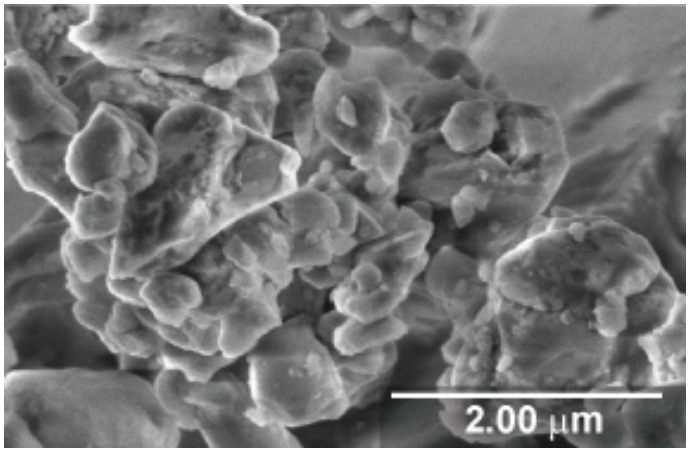

(a)

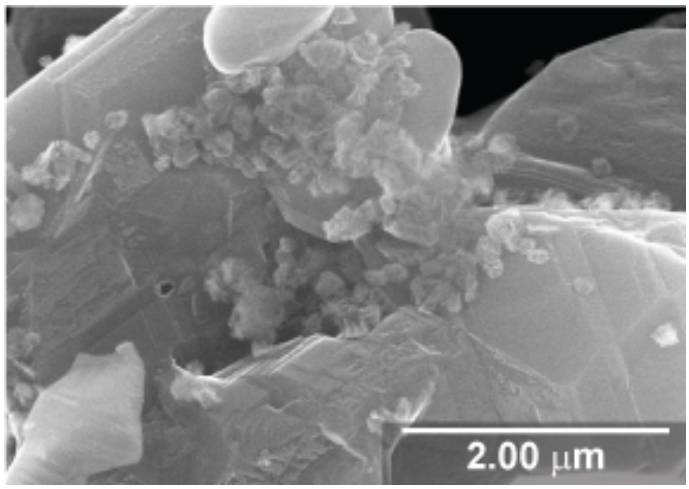

(b)

Figure 3.19. High magnification scanning electron microscope images of nano- and micron-sized grains in (a) bioSiC 300 and (b) bioSiC 1000.

amorphous carbon. Residual carbon has been shown to exist in bioSiC due to the incomplete reaction of silicon and carbon.[35,39] This occurs when pores become choked off due to the SiC formation, and silicon must diffuse through the newly formed SiC. This diffusion is a slow process, so during the 60 minutes of reaction time, not all of the carbon will be exposed to silicon, and thus, some will remain unreacted. Figures 3.20(b) and (c) are the corresponding electron diffraction patterns for the SiC and carbon regions, respectively. Figure 3.20(b) shows distinct rings made up of individual points. This is indicative of a polycrystalline region, where the crystal size is smaller than the point size used to obtain the electron diffraction pattern. Here, a single grain cannot be resolved, and instead, many grains, aligned in many directions, are detected. Analysis of this diffraction pattern clearly indicates that the grains are β-SiC with a lattice parameter of 4.34 Å which is very close to the theoretical lattice parameter of 4.3589 Å.[141] Figure 3.20(c) shows the characteristic rings associated with amorphous carbon. The residual carbon present in this sample is equivalent to carbon that has been pyrolyzed to 1500°C, because it has been heated to the infiltration temperature in the furnace. This diffraction pattern still shows evidence of an amorphous structure, much like the diffraction patterns seen in the 300 and 1000°C pyrolyzed carbon samples.

Figure 3.21(a) shows an example of the coarser, micron-sized SiC grains that are formed in the process of fabricating bioSiC 300. The accompanying electron diffraction pattern, shown in figure 3.21(b), is of a single grain, and indicates that crystalline fcc silicon carbide is present. A lattice parameter of 4.355 $\pm$.02 Å was calculated, using Digital Micrograph software, which is also close to the theoretical lattice parameter of

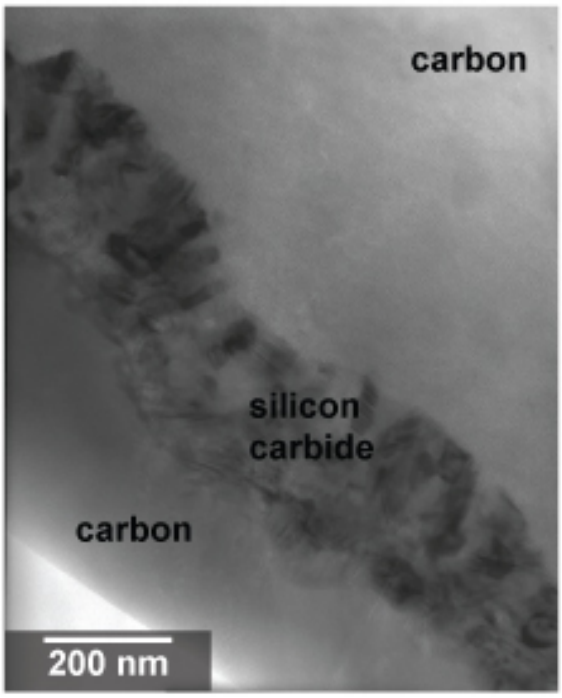

(a)

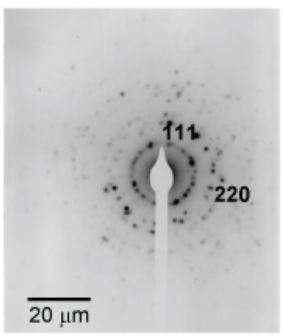

(b)

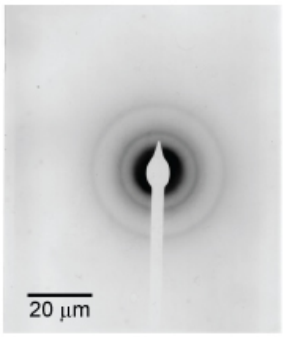

(c)

Figure 3.20. (a) Transmission electron microscope image of nano-sized silicon carbide grains and residual carbon in bioSiC 300 and electron diffraction patterns from (b) the nano-sized SiC region and (c) the residual carbon region.

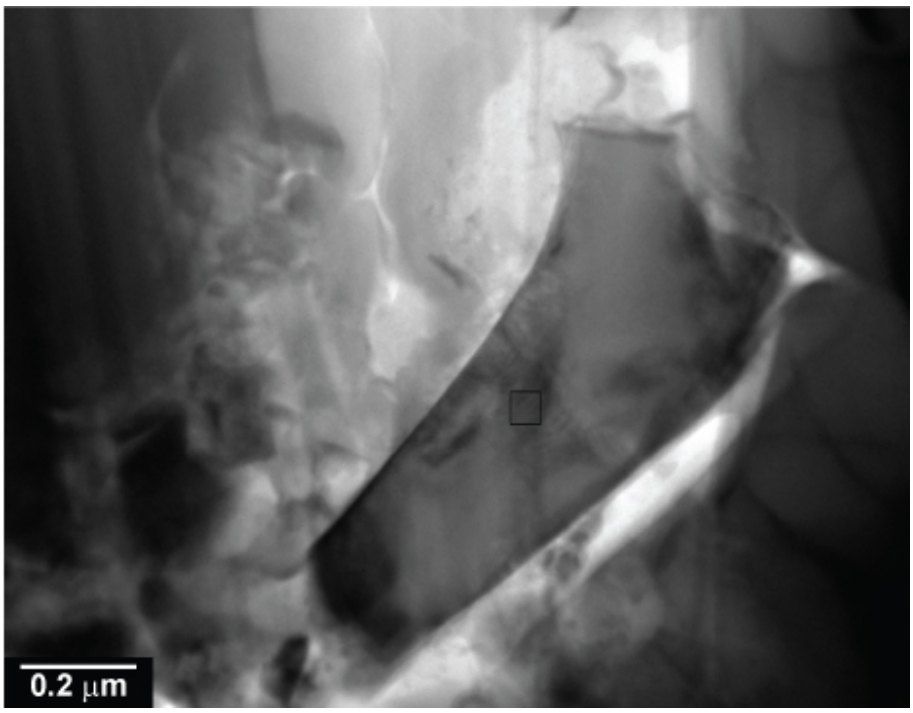

(a)

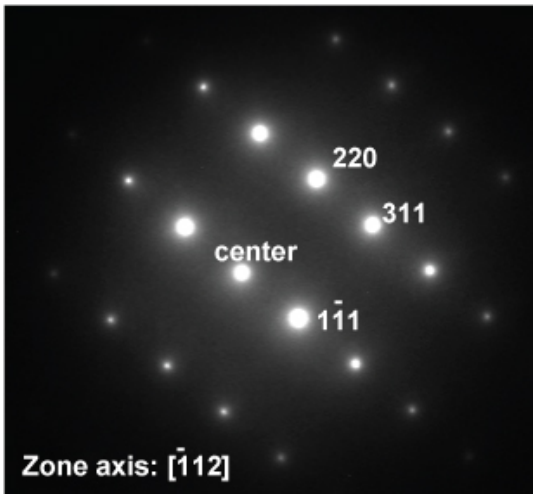

(b)

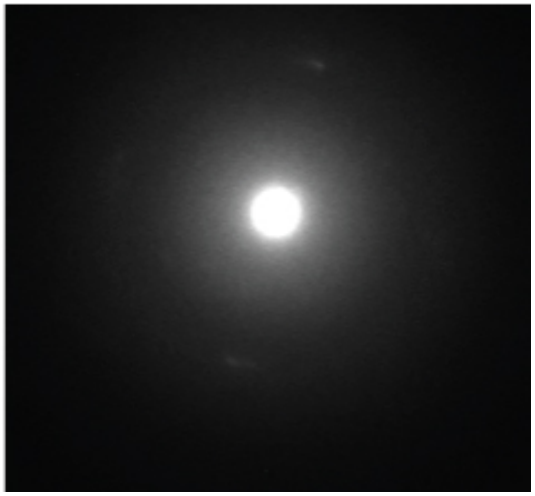

(c)

Figure 3.21. (a) Transmission electron microscope image and corresponding electron diffraction patterns of (b) silicon carbide and (c) carbon from a bioSiC sample made from carbon pyrolyzed at 300°C.

4.3589 Å.[141] Figure 3.21 (c) is from a carbon region of the sample, and indicates the presence of amorphous carbon.

Figure 3.22 is a high resolution electron micrograph of a region in bioSiC 300 that contains both silicon carbide and residual carbon. This image was taken along a zone axis of $[\bar{1}12]$ in the SiC. The left side of the image shows an ordered lattice, indicating the crystalline silicon carbide phase is present. The right side of the image, which is lighter in color, shows an amorphous structure, characterized by the lack of long-range order at the atomic level. This is indicative of the amorphous residual carbon present in the sample. The interface between the carbon and silicon carbide is sharp, indicated by the high color contrast present in the image.

BioSiC 1000 was also studied using the TEM. Figure 3.23(a) shows a TEM image of micron-sized grain SiC with residual carbon. The corresponding electron diffraction patterns for SiC and carbon are shown in figures 3.23(b) and (c) respectively. The SiC pattern was indexed using Digital Micrograph software, and a lattice parameter of 4.39 $\pm$ .06 Å was calculated. Figure 3.23(c) is the electron diffraction pattern from the carbon region, and it indicates that this section is indeed amorphous. This carbon, similar to that in the bioSiC 300, has also been pyrolyzed to 1500°C as a consequence of the infiltration reaction. The structures seen in carbons pyrolyzed at 300 and 1000°C, as well as the residual carbon in the bioSiC materials indicate that these four carbon materials are similar in their amorphous nature.

Figures 3.24 (a) and (b) are high resolution TEM images of regions in the bioSiC 1000 sample. The lack of a repeated ordered structure in figure 3.24 (a) indicates the amorphous character of the carbon region. In contrast, the bioSiC section, taken along the [011] zone

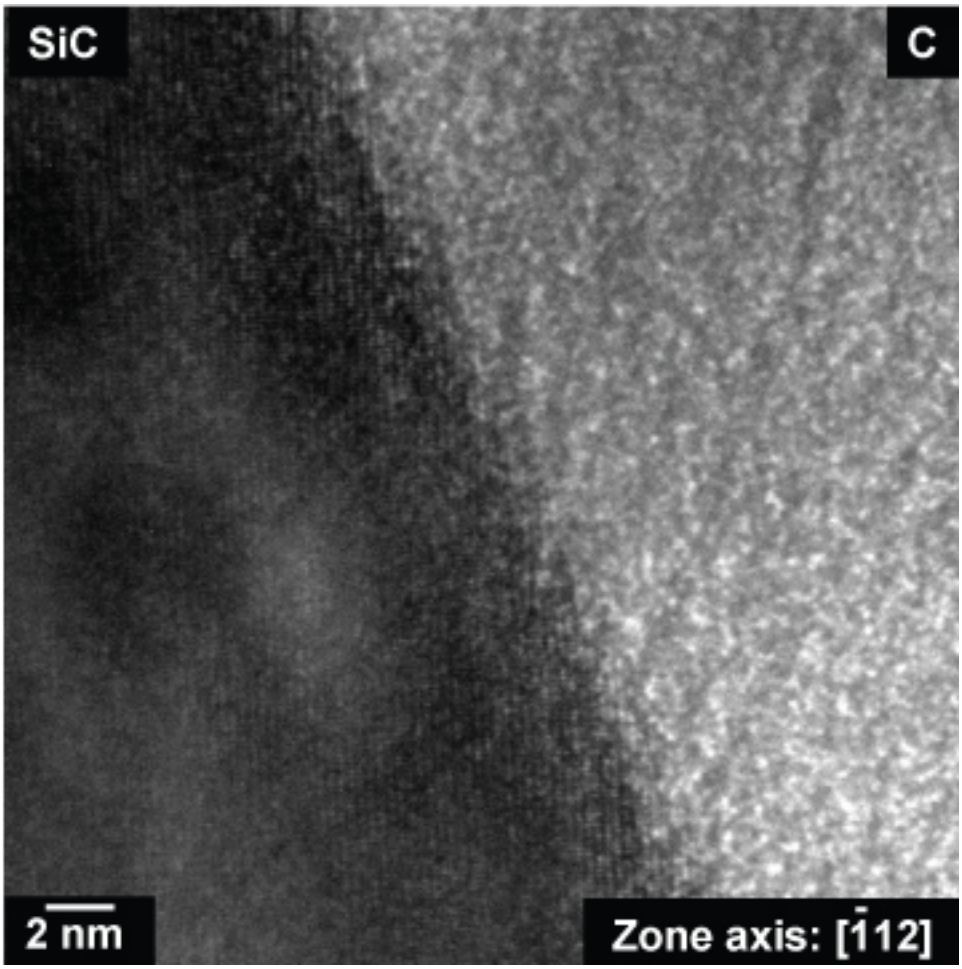

Figure 3.22. High resolution transmission electron micrograph of the interface between carbon and silicon carbide.

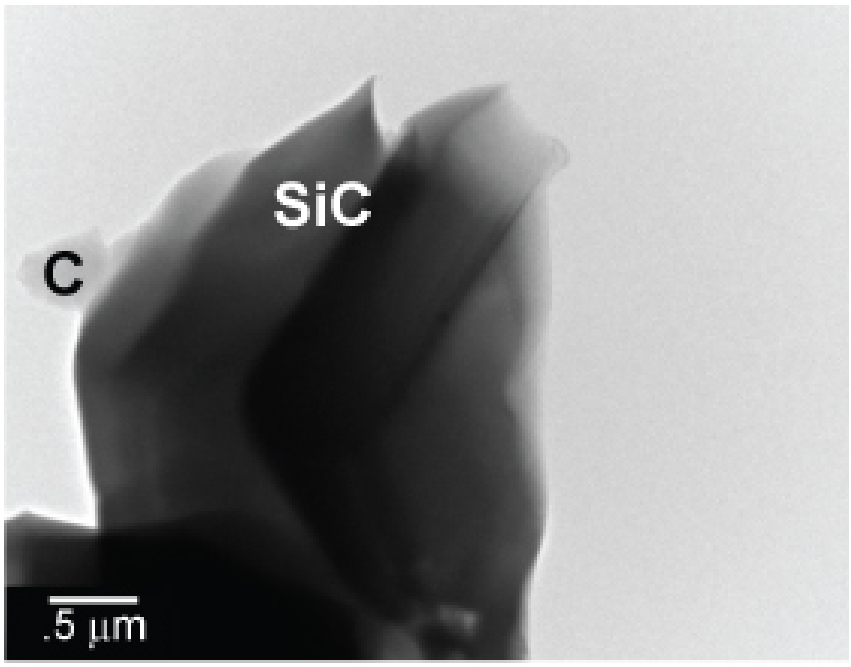

(a)

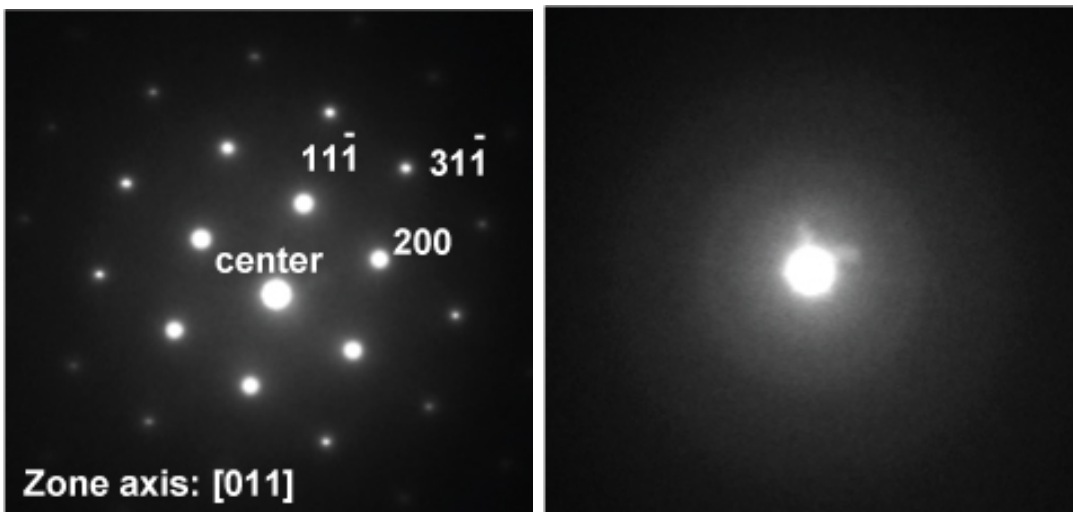

(b) (c)

Figure 3.23. (a) Transmission electron micrograph of bioSiC 1000 and corresponding electron diffraction patterns of (b) silicon carbide and (c) carbon.

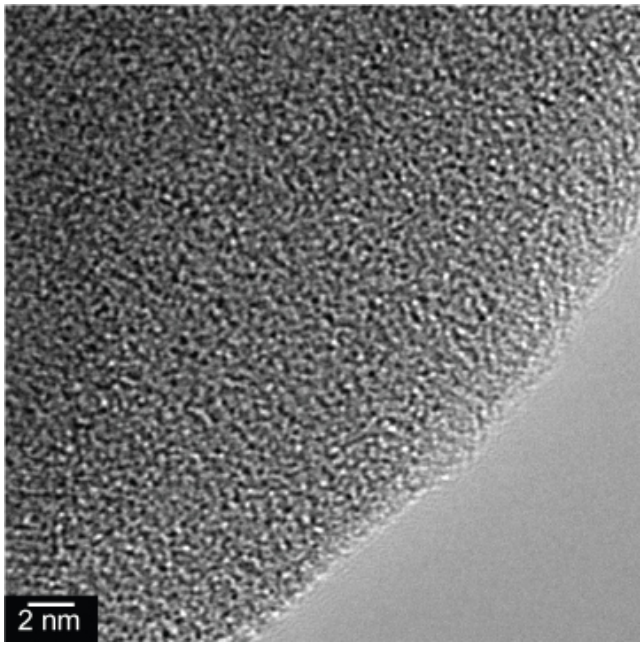

(a)

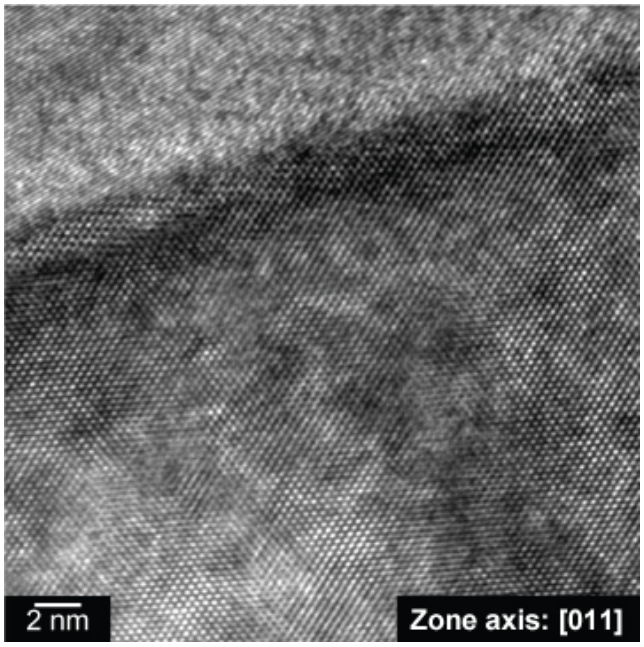

(b)

Figure 3.24. High resolution transmission electron micrographs of (a) carbon and (b) silicon carbide regions in bioSiC 1000 sample.

axis, in figure 3.24 (b), shows a repeating crystalline structure. In this image, there is a grain boundary, evidenced by the change in the orientation of the ordered pattern. An electron diffraction pattern was also taken from this image, yielding a lattice parameter of 4.352 ± .02 Å.

The amorphous, unordered structure that appears in the HRTEM image of residual carbon region of the bioSiC 1000 (figure 3.24(a)) is similar to that image of the carbon pyrolyzed at 300°C (figure 3.10). This indicates that the structure does not lose its amorphous character as it is pyrolyzed at higher temperatures up to 1500°C. The high resolution images of both the bioSiC made from carbons pyrolyzed at both 300 and 1000°C are very similar, indicating the presence of amorphous carbon and crystalline silicon carbide regions. There does not appear to be any significant difference at the atomic level for these two materials.

In both bioSiC 300 and bioSiC 1000, the lattice parameters calculated from the diffraction patterns gave values that were close to that of the theoretical lattice parameter value of 4.359 Å. This indicates that there is no lattice parameter change as a result of the carbon precursor pyrolysis temperature. The residual carbon left in the bioSiC samples are effectively carbon pyrolyzed at 1500°C, which exhibited amorphous ring patterns similar to the carbon pyrolyzed at 300 and 1000°C. These results all indicate that the TEM, SEM and porosimetry data give evidence that bioSiC is morphologically independent of initial carbon pyrolysis temperature.

3.3.4. Thermal Diffusivity

Thermal diffusivity was measured using the Xenon flash diffusivity system for bioSiC samples processed from carbon pyrolyzed at different temperatures.[139] BioSiC samples tested were beech-based, and were fabricated from carbon pyrolyzed at 300, 500, 700, 1000, and 1200°C. Two samples, each approximately 5 mm thick, were tested in the axial and transverse directions (with the exception of the axial sample pyrolyzed at 300°C). Figure 3.25 shows the resulting plot for the thermal diffusivity versus pyrolysis temperature for the beech-based bioSiC. The values of the thermal diffusivity for the resulting bioSiC were higher in the axial than the transverse direction, as expected from theoretical predictions. There is no effect of pyrolysis temperature on these diffusivity values, which is a sharp contrast to what was seen for the thermal diffusivity of the carbon samples that were pyrolyzed at different temperatures, which showed a rapid increase with increasing temperature after 700°C. This indicates that while there are changes occurring in the carbon samples with increasing carbon pyrolysis temperature, these may not be manifested in the resulting silicon carbide.

There is a large amount of error in the diffusivity measurements for the bioSiC samples, particularly in the transverse direction. Repeated measurements of the same sample in the Xenon flash diffusivity system yield values within 10%.[142] The large variation between samples processed with the same conditions can also be due to the inhomogeneity associated with naturally occurring materials. Although these samples should be representative of the microstructure as a whole, variation in the structure is still evident.

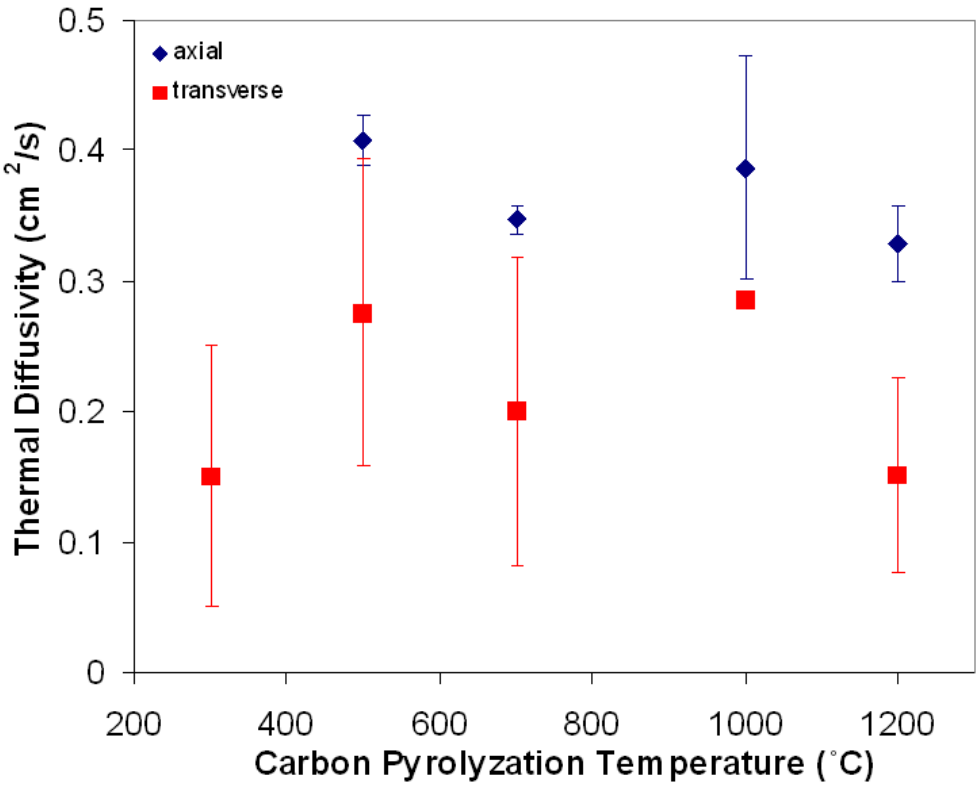

Figure 3.25. Thermal diffusivity of beech-based bioSiC based on carbon pyrolyzed at different temperatures.

3.4. Cu-BioSiC Composites

Composites with high thermal conductivity and low thermal expansion coefficients are desired for use in electronics packaging and heat sinks.[43] Copper-biomorphic silicon carbide (Cu-bioSiC) composites have potential uses in these thermal management applications, due to their predicted high thermal conductivity and low thermal expansion coefficient. The thermal conductivity of copper and silicon carbide are 398 W/mK and 88 W/mK, respectively, and their thermal expansion coefficients are 16.5 x 10^{-6}/°C and 3.3 x 10^{-6}/°C, respectively, at room temperature .[69,124,143,144] These composites can be produced by filling the pores in the bioSiC with copper. However, traditional processing methods, such as melt infiltration of the copper into the bioSiC preform, can be a major drawback to their use. When copper melts and comes into contact with silicon carbide, the copper dissociates the silicon carbide, reacts with the silicon to form a copper silicide, and leaves behind excess carbon.[46] The copper silicide phase is extremely detrimental to the thermal conductivity of copper, as an addition of only 1.5% silicon into copper can lower its thermal conductivity by 85%.[51] Since copper is of interest as an interconnect attached to a silicon wafer in the electronics industry, many different barrier coatings have been employed to prevent this reaction from occurring, aiming for the thinnest and most effective barrier possible. In this work, several methods were attempted to introduce a coating onto porous bioSiC to prepare it for melt infiltration of copper to fabricate these composites.

3.4.1. Melt Infiltration

Prior to investigating barrier coatings, preliminary experiments were done to study the wetting and reaction behavior of copper and bioSiC. Copper was melted onto bioSiC samples at 1200°C for 30 minutes in argon. The resulting composite was investigated using SEM and X-ray diffraction. Figure 3.26(a) is an SEM image accompanied by energy-dispersive X-ray spectroscopy (EDS) elemental mappings showing the regions where copper (figure 3.26(b)) and silicon (figure 3.26(c)) are each present. It is evident that the copper beads up on the surface of the bioSiC, but does not fill the pores. Thus heating the copper above its melting point is not sufficient to make the desired composite samples. An addition of high pressure is required to force the copper into the interior pore surfaces.

Figure 3.27 is an X-ray diffraction pattern of the surface of the beech-based bioSiC-Cu sample shown in figure 3.26. It is clear that while SiC and Cu are prevalent, as expected, there are also peaks present that correspond to the copper silicide phase, $Cu_{6.69}Si$, including one at $2\theta = 46°$.[145] Thus, X-ray diffraction results confirmed that the Cu-Si reaction will occur when copper is melt infiltrated onto bioSiC samples. In order to fabricate a high thermal conductivity composite, it is essential to avoid the direct contact of molten copper with the bioSiC.

3.4.2. Silicide Prevention

Many copper diffusion barrier coatings in the literature are applied to silicon wafers by sputter coating or chemical vapor deposition. These two techniques are successful at depositing thin layers onto a material's surface. However, the porous nature of bioSiC necessitates that the coating also be deposited throughout all of the internal surfaces

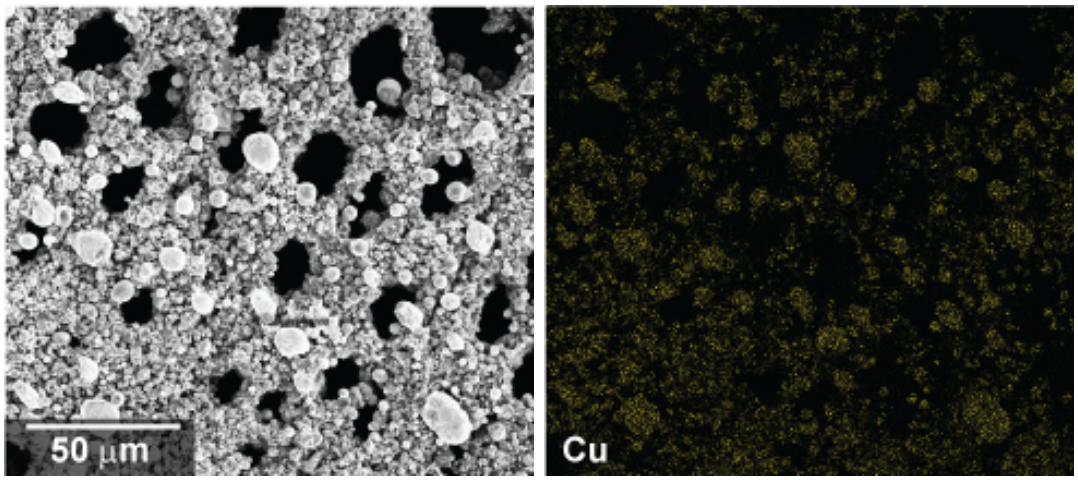

(a) (b)

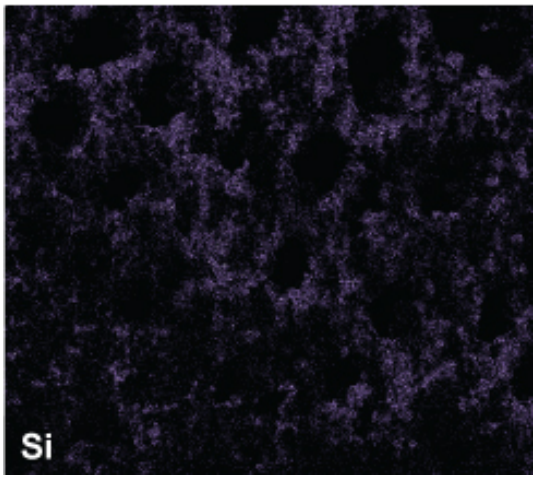

(c)

Figure 3.26. (a) Scanning electron microscope image of copper melted onto beech-based bioSiC, and energy-dispersive X-ray spectroscopy elemental mappings of (b) copper, and (c) silicon.

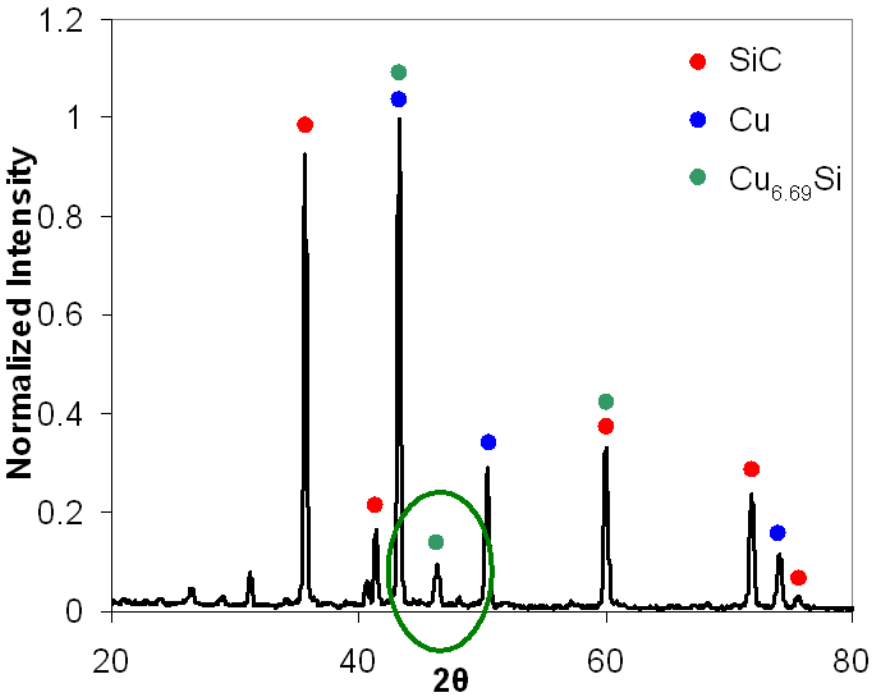

Figure 3.27. X-ray diffraction pattern of copper melted onto beech-based bioSiC.

of the pores. For this reason, sputter coating and chemical vapor deposition are not effective methods for coating the porous material. Two techniques for depositing coatings on internal surfaces of pores are infiltration of a sol-gel solution and chemical vapor infiltration. Chemical vapor infiltration (CVI) is similar to chemical vapor deposition where one or more gaseous species is flowed at a specified rate through a chamber at a set temperature.[42] The precursors react or decompose and deposit on the surface. In CVI, the processing variables are controlled so that the reaction occurs more slowly, and the diffusing gas species have time to travel further into the pores prior to reaction.

A chemical vapor infiltrated coating was deposited into the pores of bioSiC by Ultramet (Pacoima, CA). The coated samples were cross-sectioned and examined using EDS in the SEM to determine the presence of the coating. Elemental mappings of the bioSiC with the coating are shown overlayed in figure 3.28, where the silicon is represented by purple and the coating by blue. While some of the coating material is present on the walls of the pores, the penetration depth was minimal compared to the length of the sample. In addition, only a small fraction of the pores was successfully coated. These two factors combined indicate that chemical vapor infiltration is not a viable method for creating a barrier coating on porous bioSiC.

A sol-gel technique was also employed to make a coating layer between bioSiC and molten copper. Though diffusion barriers reported in the literature are predominantly nitrides, some oxides have been studied. Alen et al. have shown that a 3 nm thick coating of titania has prevented copper diffusion up to 650°C.[58] In addition, titania has been successfully created from wood using a sol-gel reaction.[146] A titanium containing precursor, titanium tetraisopropoxide (TTiP) was infiltrated into the pores, hydrolyzed,

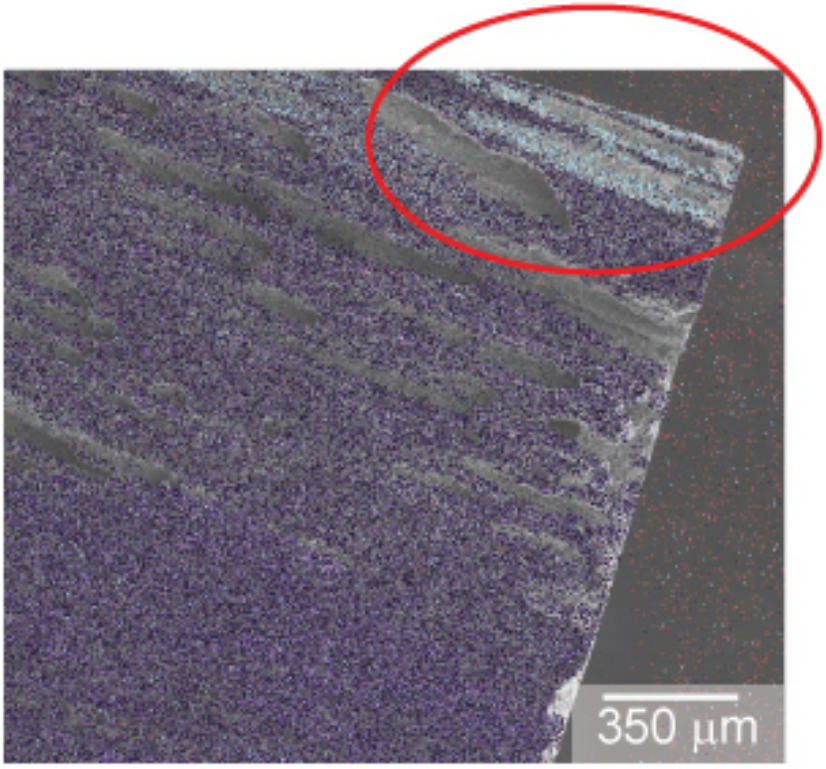

Figure 3.28. Chemical vapor infiltrated coating (circled) in the pores of bioSiC. In this image, purple represents silicon and blue represents the coating. (Coating produced by Ultramet (Pacoima, CA)).

gelled. The sample was heat treated to form the oxide coating and to burn out the wood.[146] This recipe was adapted to deposit titania coatings onto the pore surfaces in bioSiC.

TTiP was vacuum infiltrated into the pores of the bioSiC samples and subsequently sonicated in an isoproponal (2-proponal) solution with 1% DI water for 10 minutes to hydrolyze the TTiP and cause titania gel formation. This specimen was then dried at 110°C for 2 hours. This infiltration, hydrolysis, and gel formation process was repeated up to 5 times, after which the sample was fired to 1200°C for 2 hours in air to form the titanium oxide layer. Samples were cross-sectioned and examined using scanning electron microscopy to confirm that TiO_2 was indeed formed and to determine how well the pore surfaces were coated. Figure 3.29, an SEM image using the backscattered electron detector, where the titania is the lighter colored phase, shows that the TiO_2 has deposited throughout the entire length of the pores. However, upon investigation at high magnification, as seen in figure 3.29, it is clear that the coating is not continuous even after five repetitions of the sol-gel reaction. The depth of titania deposition indicates that vacuum infiltration is more successful at reaching further into the pores than chemical vapor infiltration. However, the discontinuous nature of the coating will make it ineffective as a barrier to the copper-silicon reaction. It is possible that with additional repetitions of the sol-gel reaction, a more continuous coating of titania could be formed. However, the addition of material increases the coating thickness, which decreases the potential amount of copper able to be added to the pores. In some cases, too thick of a coating could potentially close some smaller pores off to copper completely. Thus, the sol-gel titania coating is not a viable barrier coating for the bioSiC system.

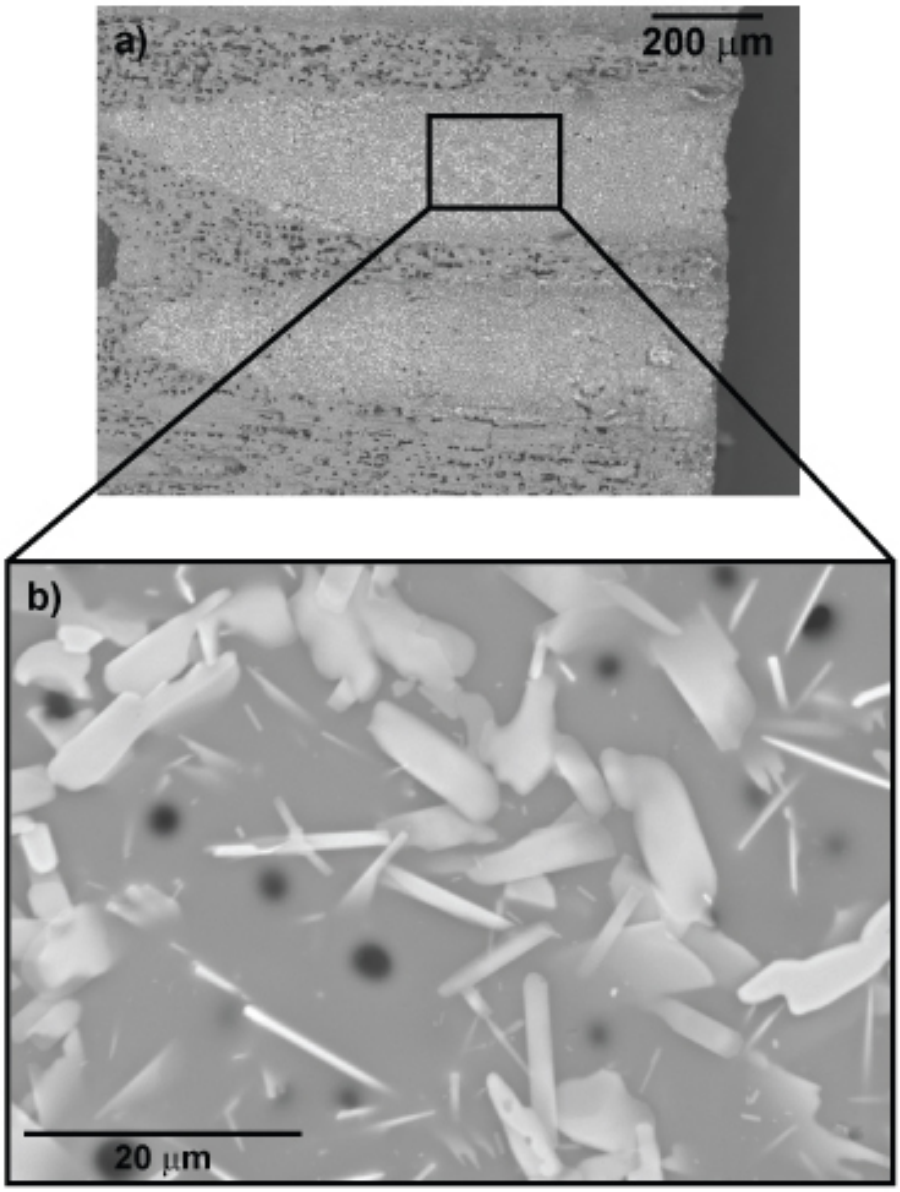

Figure 3.29. (a) Scanning electron micrograph using the backscattered electtron detector showing a TiO_2 coating in bioSiC pores and (b) higher magnification of (a).

3.4.3. Electrodeposition

The SiC dissociation reaction occurs only in the presence of molten Cu, which implies that composite fabrication at room temperature has the potential to avoid silicide formation during processing. Electroless plating and electroplating, both room temperature processes, have been used previously to coat silicon carbide whiskers with copper.[74] These copper coated whiskers were later hot pressed with copper powders to form composites.[74] Electroplating, like the other coating techniques already discussed, is a good method for coating external surfaces of samples, but it is a challenge to electroplate deep within the pores. Standard components of many electroplating solutions are copper sulfate and sulfuric acid. In order to improve the electroplating efficiency, additions such as polyethylene glycol (PEG) and chloride ions (Cl) have been added to the solution to lower its surface tension, allowing the electrolyte to reach deeper into pores and trenches of the sample.[83]

The copper plating electrolyte used in this study follows the standard electrolyte bath described by Kelly and West.[80] The components of this bath are 0.24M $CuSO_4$* $5H_2O$, 1.8M H_2SO_4, 300 mg/mL 3400 MW PEG, 50 mg/L chloride ions in the form of HCl, and the balance DI water. The sample is negatively charged by an external power supply set to a constant current of 25 mA. The positively charged copper ions are in solution from the dissociation of the copper sulfate salt. They are attracted to the negatively charged sample and deposit onto its surface. The copper electrode replenishes the supply of ions in the bath. As mentioned previously, in order to plate deeper into the pores, PEG is added to lower the surface tension of the liquid.[80] In addition, the solution is continuously stirred, which also increases the electrolyte motion into the pores. Prior to adding samples to the solution, they are vacuum infiltrated with the non-acidic portion

of the electrolyte. This forces the solution to initially coat the inner pore surfaces of the material. The low surface tension allows the electrolyte to maintain its presence within the pores for continuous plating. Figure 3.30 is a schematic diagram of the electroplating system, indicating the charges on each component.

Two processing variables were optimized in order to determine the electroplating protocol for the samples: length of time in the plating bath and number of additional vacuum infiltrations throughout the duration of plating. The additional infiltration steps served to introduce more solution into the pores to further encourage deposition deep within the pores. The optimized process consists of plating the samples for five days in a continuously stirring solution, with one additional vacuum infiltration between the second and third day of plating.

Figure 3.31 shows an example of an axially-oriented sample of sapele-based bioSiC that was copper plated. This image was taken using the back scattered electron detector (BSE), and the lightest phase is copper, the darker phase is silicon carbide, and the darkest phases are pores. Here it is evident that the plating reaches through the thickness of the sample, which in this case is 3 mm. Figures 3.32(a) and (b) show images of a cross-section about 1 mm deep into the same sample. Figure 3.32(a) shows that most of the larger vessel pores are well filled with copper, though some still remain unfilled. Figure 3.32(b), at a higher magnification, shows the filled vessels more clearly, but indicates that the smaller fiber cell-based pores are not infiltrated. The diameters of these small vessels are around 2-3 μm, and it is more difficult to get electrodeposition in these pores. This is because as the sample plates, the regions between the pores also plate, and overfilling occurs, prematurely choking off the pores before they are able to be successfully filled.[85]

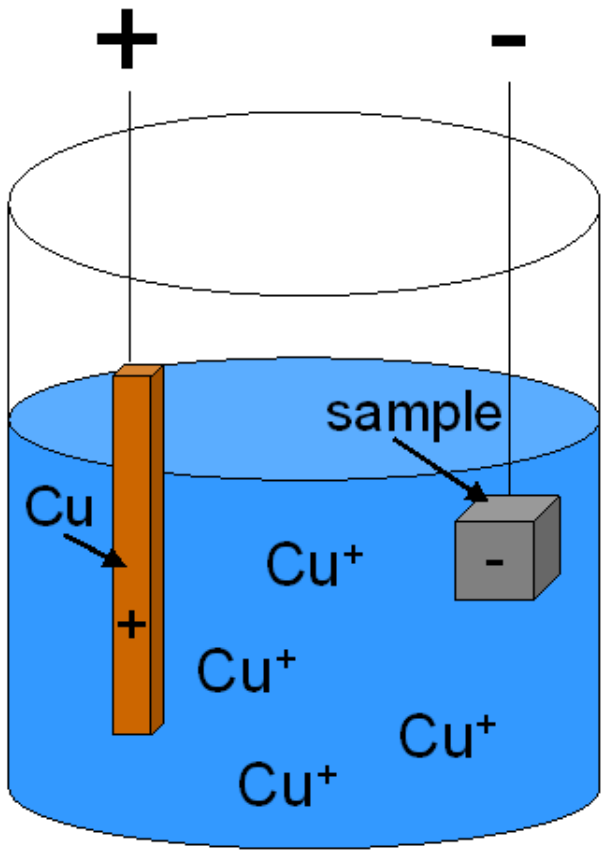

Figure 3.30. Schematic diagram of the electroplating system.

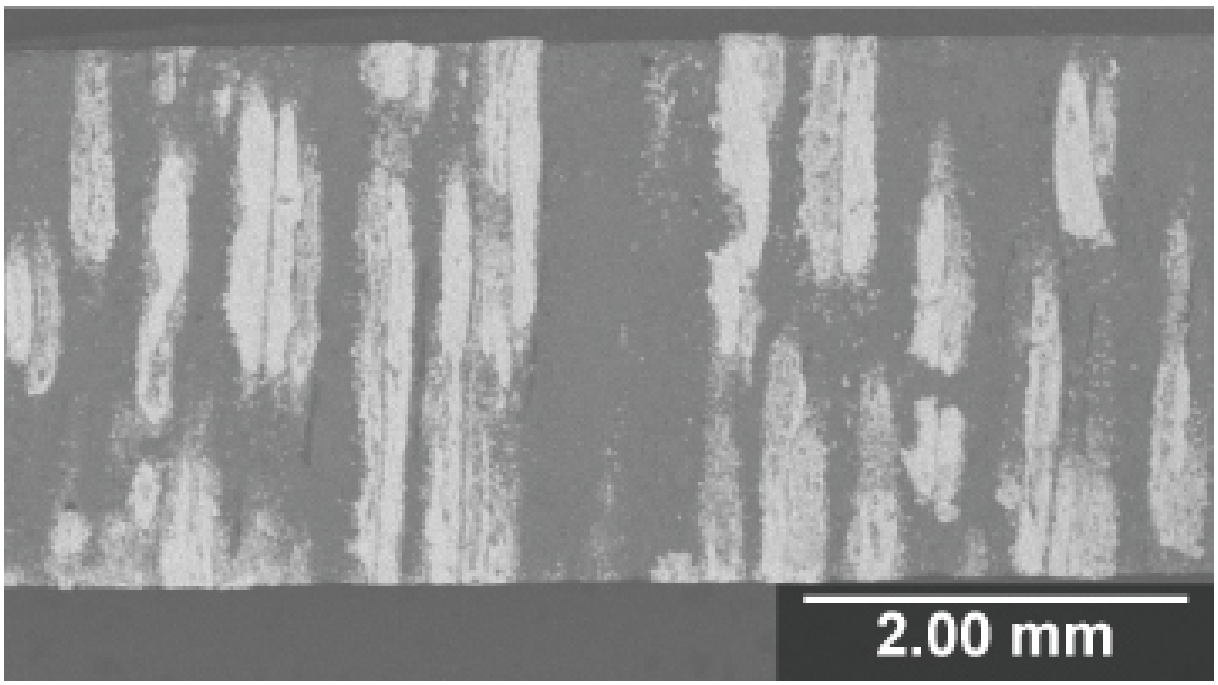

Figure 3.31. Scanning electron micrograph using the backscattered electron detector of a transverse cross-section of sapele-based bioSiC electroplated with copper.

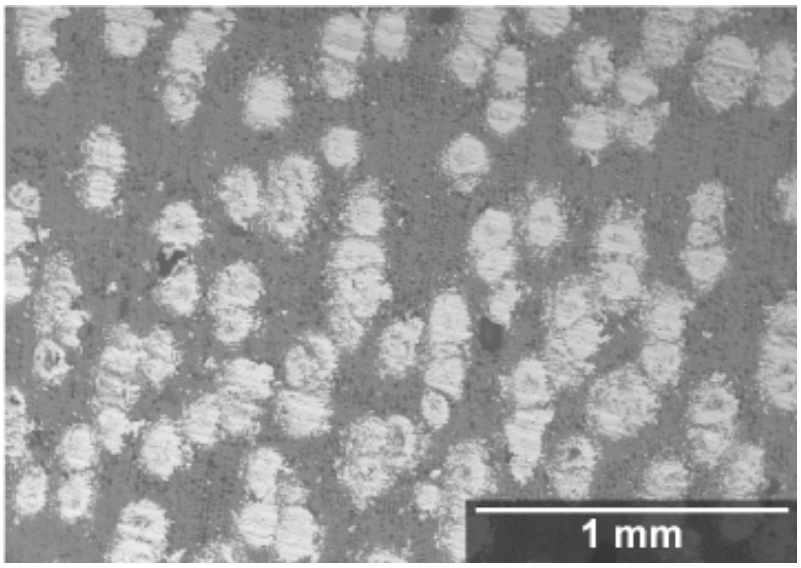

(a)

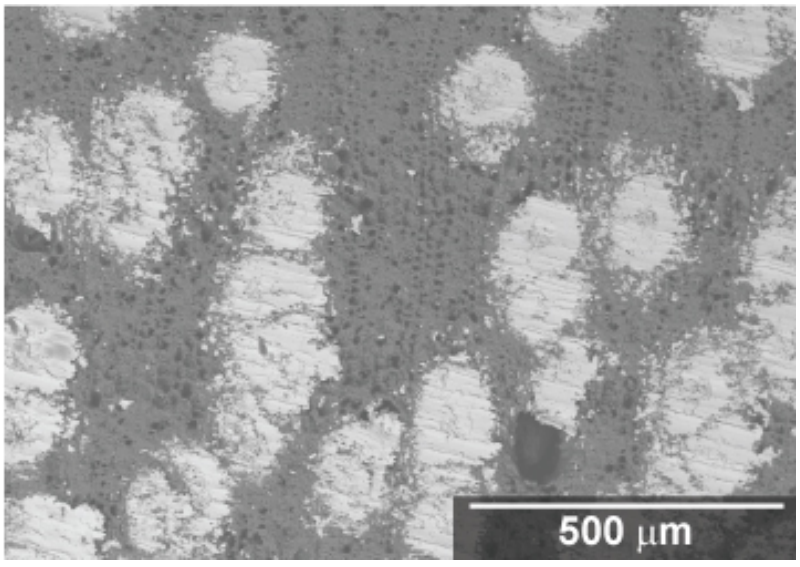

(b)

Figure 3.32. (a) Scanning electron micrograph of sapele-based bioSiC electroplated with copper using the back scattered electron detector and (b) a higher magnification image of (a). The lightest colored phase is copper, the medium gray is silicon carbide, and the dark gray areas are pores.

Figure 3.33 shows examples of the axial direction of the five wood-based bioSiC materials that have been copper plated. These images show that there is variation in how well each type of wood based bioSiC is able to be plated with copper. Beech-(figure 3.33(a)), poplar- (figure 3.33(b)) and sapele-based bioSiC (figure 3.33)d)) plate well, and there are hardly any vessels unfilled with copper. Red oak-based bioSiC (figure 3.33(e)) still maintains some porosity in the bands of smaller vessels, while the majority of each larger vessels is well filled. Mahogany-based bioSiC (figure 3.33(c)), unlike the other wood based composites, is not electroplated well by copper. There are several reasons why some bioSiC materials are plated better than others. One main issue to consider is the pore size distribution of each wood precursor (figure 3.17). Each of the five woods had the majority of their larger pores filled by electrodeposition of copper. According to the pore size measurements, this correlates to pores that are larger than about 10 μm. The smaller fiber cells, in the range of 1-10 μm were not well filled in sapele, red oak, or mahogany. This pore size range is not present in beech or poplar. This implies that there exists a minimum pore size for successful filling by electrodeposition. This observation also explains why the fraction of filled pores in mahogany is so small; because pores smaller than 10 μm make up a large majority of the entire pore volume.

It is clear when the samples are removed from the electroplating bath that there is a continuous coverage of copper across the entire sample surface. This coating needs to be removed by grinding with silicon carbide paper until the surface of the composite is exposed. The continuity of copper on the composite surface implies that the smaller pores are being choked off before they have the chance to be filled. This is because the pore walls and the strut surface between the pores are deposited on simultaneously. On

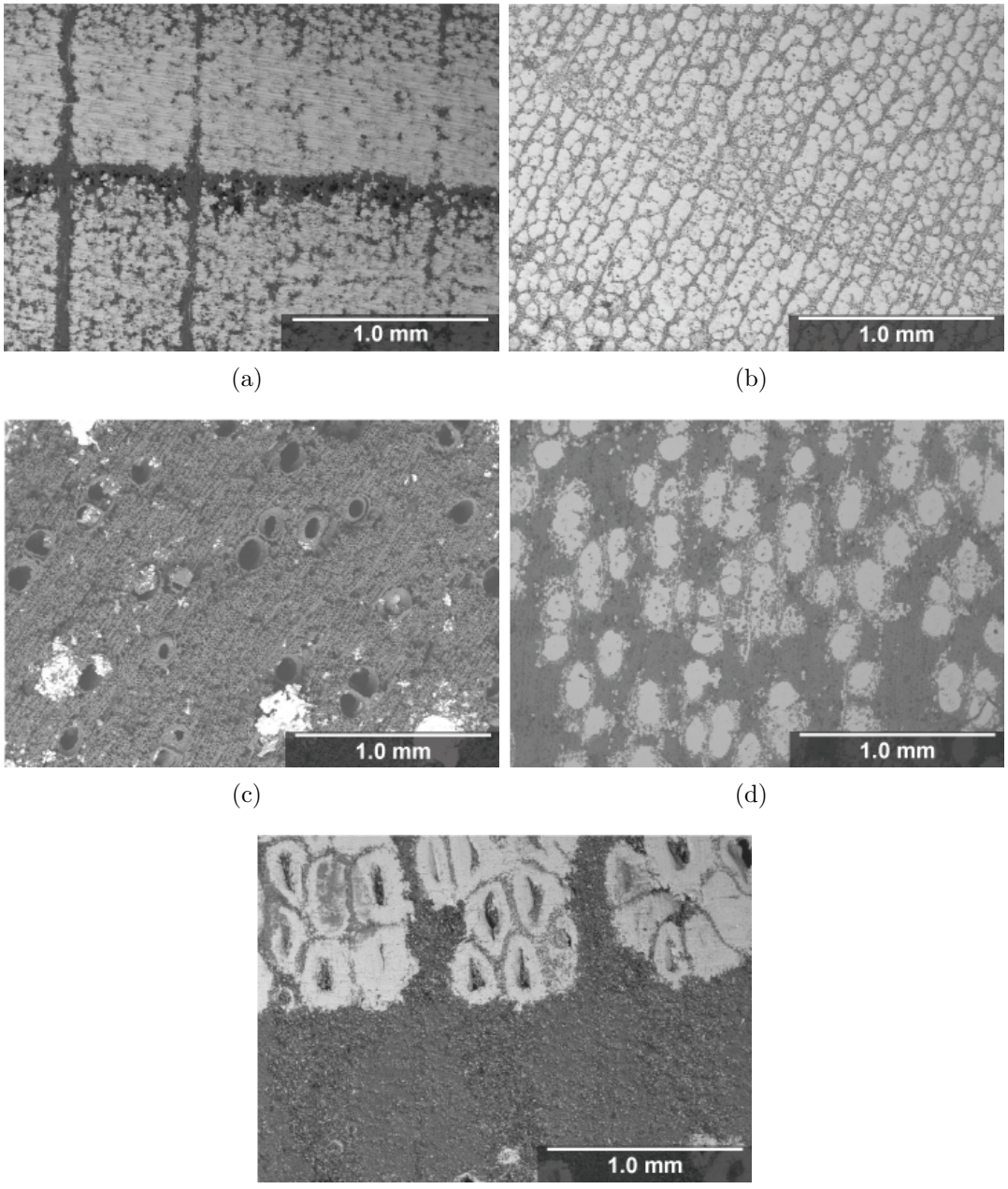

(a) (b)

(c) (d)

(e)

Figure 3.33. Scanning electron micrographs using the backscattered electron detector of copper-bioSiC composites from (a) beech, (b) poplar, (c) mahogany, (d) sapele, and (e) red oak woods.

the strut surfaces, the copper deposition forms a mushroom-like shape. Eventually, these mushrooms meet, causing the pore below their intersection to be choked off from any subsequent copper deposition. This is called overfilling[85], and a schematic diagram of overfilling is shown in figure 3.34. Overfilling is a result of the relationship between the thickness of the strut in between the pores and the pore diameter. If the pore diameter is small, even with a thin strut, it can be choked off before it has plated fully, which occurs in the smaller bioSiC pores. If the pore diameter is large and the strut is thin, the sample can plate fully before becoming choked off. However, some of the largest pores, for example, the large vessels in red oak, do not fill completely even after a longer exposure to the electrolyte and current. This is because they also get choked off prior to complete filling. Thus, the ratio of pore size to adjacent strut size is important in determining the success of copper electrodeposition into the pores of bioSiC materials. Additionally, as evidenced in microscope images in the transverse direction, the pores are not straight, and the diameter varies across the length. This can lead to choking off deeper within the vessels when the more narrow regions become filled.

It has been shown that trenches with small diameters that are 500 nm deep can be successfully filled before overfilling blocks them off.[85] If this is analogous in the Cu-bioSiC composites, it is possible that the smaller pores fill about 500 nm deep before becoming choked off. However, when the outer copper layer is removed by grinding, it is possible that this small coating would be polished away.

After the successful fabrication of Cu-bioSiC composites, it is necessary to investigate the potential reaction of copper with silicon carbide at high temperatures. Cu-bioSiC composites were heated to various temperatures ranging from 600-1000°C in argon and

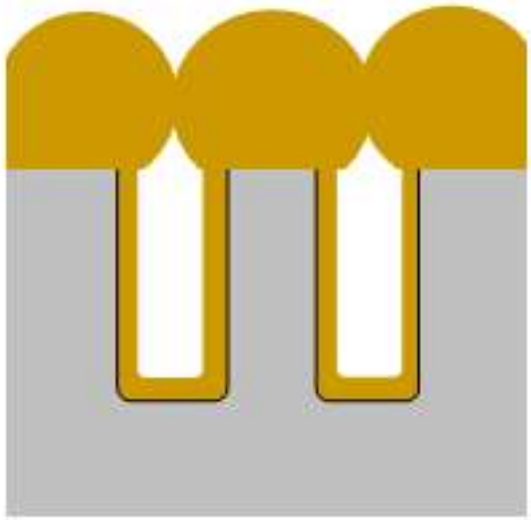

Figure 3.34. Schematic diagram of how the overfilling process chokes off pores before they are able to be filled.

held for a half hour before cooling down to room temperature. X-ray diffraction was performed on cross-sections of these heat-treated samples to investigate the presence of the $Cu_{6.69}Si$ phase, indicative of a reaction. Figure 3.35 shows the X-ray diffraction patterns of samples heated to (a) 600°C and (b) 1000°C. In both cases, there is no evidence of silicide formation up to 1000°C in these composite samples, as indicated by the absence of the $Cu_{6.69}Si$ peak at 2θ=46°.

3.4.4. Transmission Electron Microscopy

A more in-depth study on the interaction between copper and silicon carbide was done using TEM analysis on a poplar-based Cu-bioSiC composite sample heat treated to 1000°C. Figure 3.36 shows a TEM image of the interface between the SiC and Cu phases. The EDS spectra clearly show that the dark side of the micrograph has a high concentration of copper, indicating Cu, while the bright side has a high concentration of Si, indicating SiC. Small traces of Si and Cu can be present in the background of these EDS spectra due to the Si detector and the Cu sample holder. This indicates that no copper and silicon carbide reaction has occurred, confirming the X-ray diffraction results. Electron diffraction patterns were also taken from each side of the interface, and at the interface, and are shown in figure 3.37. The lattice parameters were calculated from these diffraction patterns, and determined to be 3.624 ± .015 Å for copper and 4.359 ± .02 Å for silicon carbide. These values correlate well with the theoretical values of 3.615 Å and 4.3589 Å for copper and silicon carbide, respectively, indicating that there is no lattice strain as a result of composite formation[141,147]. In figure 3.37(c), an electron diffraction pattern at the interface, both the copper and silicon carbide phases are present, as expected.

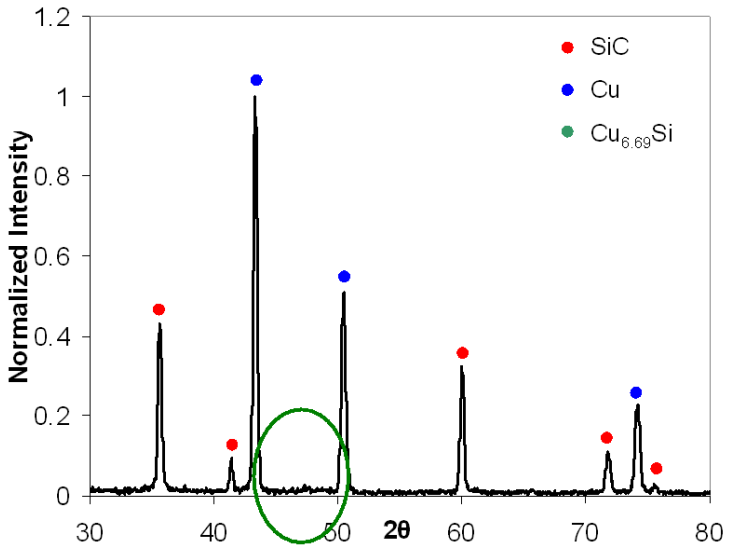

(a)

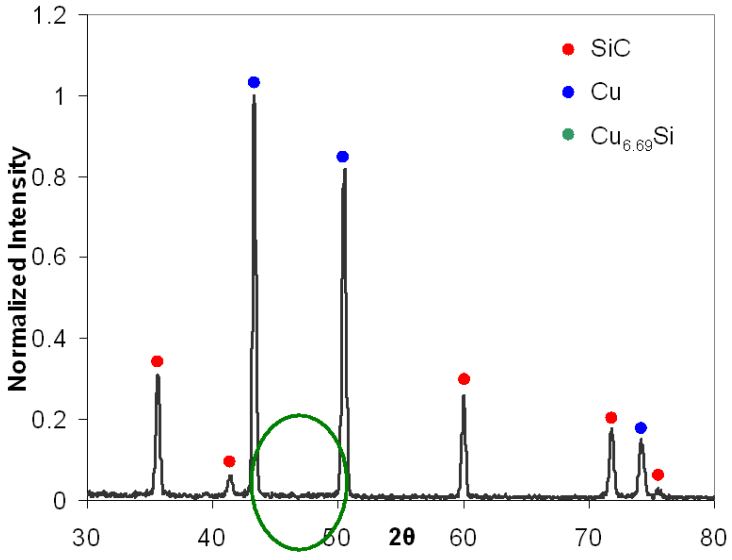

(b)

Figure 3.35. X-ray diffraction patterns of copper-bioSiC composites heat treated to (a) 600°C and (b) 1000°C. The green circle indicates the location of the copper silicide peak.

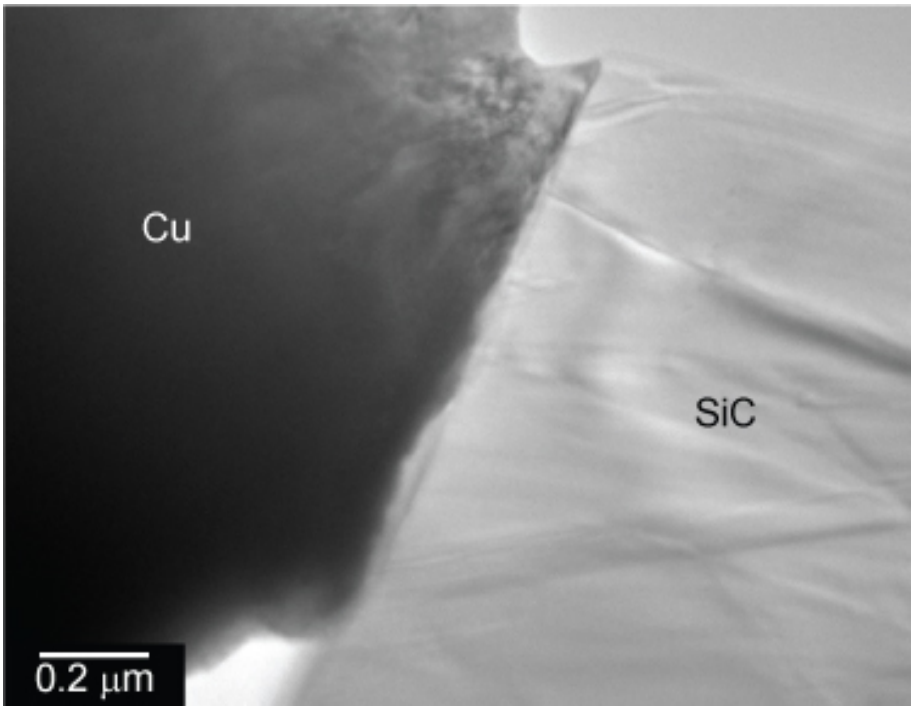

(a)

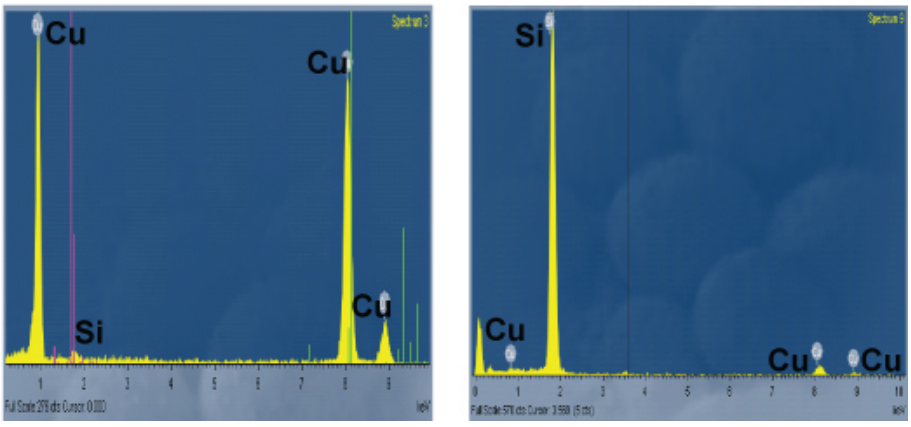

(b)

Figure 3.36. (a) Transmission electron microscope image of the Cu-SiC interface in a composite sample heat-treated to 1000°C and (b) energy-dispersive X-ray spectra of the copper region (left) and the silicon carbide region (right).

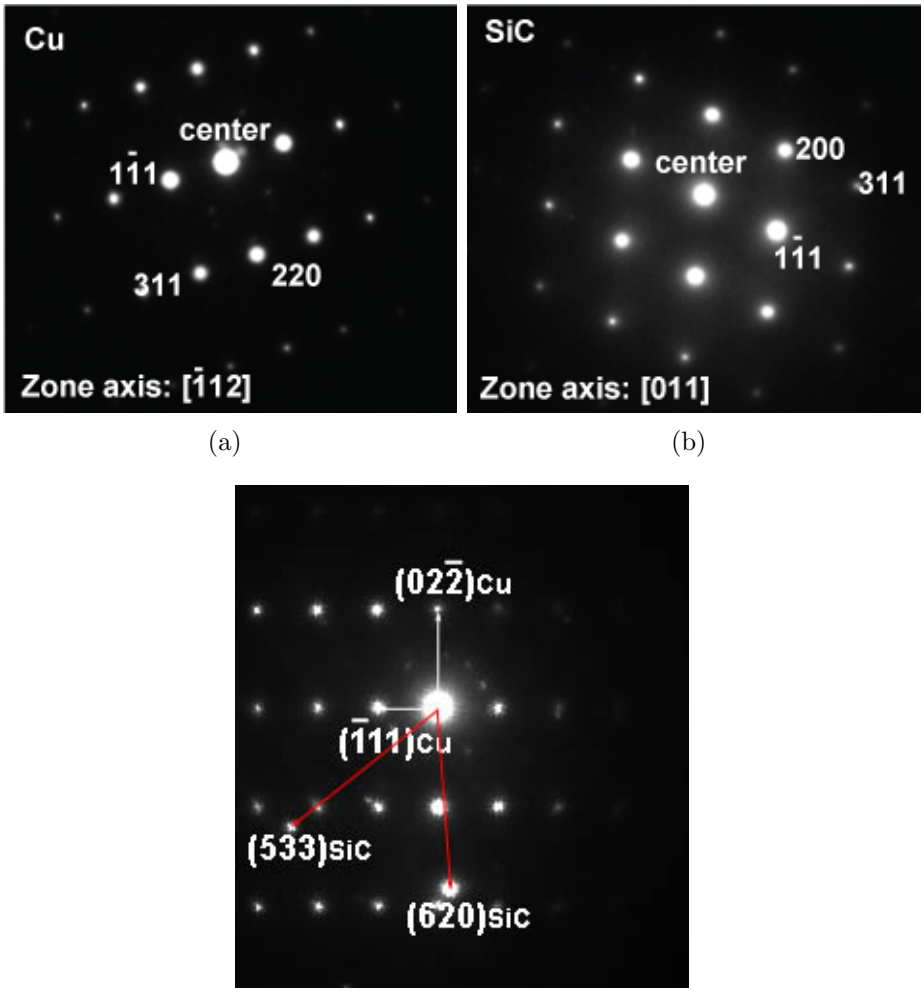

(a) (b)

(c)

Figure 3.37. Electron diffraction patterns from the (a) copper and (b) silicon carbide regions and (c) the interface between copper and silicon carbide in the composite heat treated to 1000°C.

Figure 3.38(a) is a high magnification image of the interface between copper and silicon carbide in this sample. In figure 3.38(a), it is clear that that the interface is very crisp. This indicates that while the sample has been heated to 1000°C, there is still no diffusion across the interface between the two phases. The EDS spectrum at the interface, shown in figure 3.38(d), indicates that both silicon carbide and copper are present, as expected. Figures 3.38(b) and 3.38(c) are EDS spectra of copper and silicon carbide, respectively, taken about 50 nm away from the interface on either side. These two spectra confirm the sole presence of copper on the darker side of the image (figure 3.38(b)) and only silicon carbide on the lighter side (figure 3.38(c)).

Figure 3.39 is a high resolution TEM image of the Cu-bioSiC interface in this same composite material. It is even more apparent from this high resolution image that the boundary between the two phases is clear, indicating no interdiffusion or reaction at the interface. If a reaction had occurred, the contrast between the two phases at the interface would be less apparent.

Figure 3.40 (a) shows a scanning transmission electron microscopy (STEM) high angle annular dark field (HAADF) image of the same interface in this material. In this image, the lighter color represents the heavier element, copper. Figure 3.40 (b) shows an EDS line scan that was taken along the white line in the STEM image. This line scan shows a profile of the elements present immediately at the interface. It is apparent from this interfacial profile that as one follows the line, traversing the interface, the composition begins as a region of solely silicon carbide, then an interfacial region containing both phases, and finally a region where the the copper intensity becomes dominant. This line

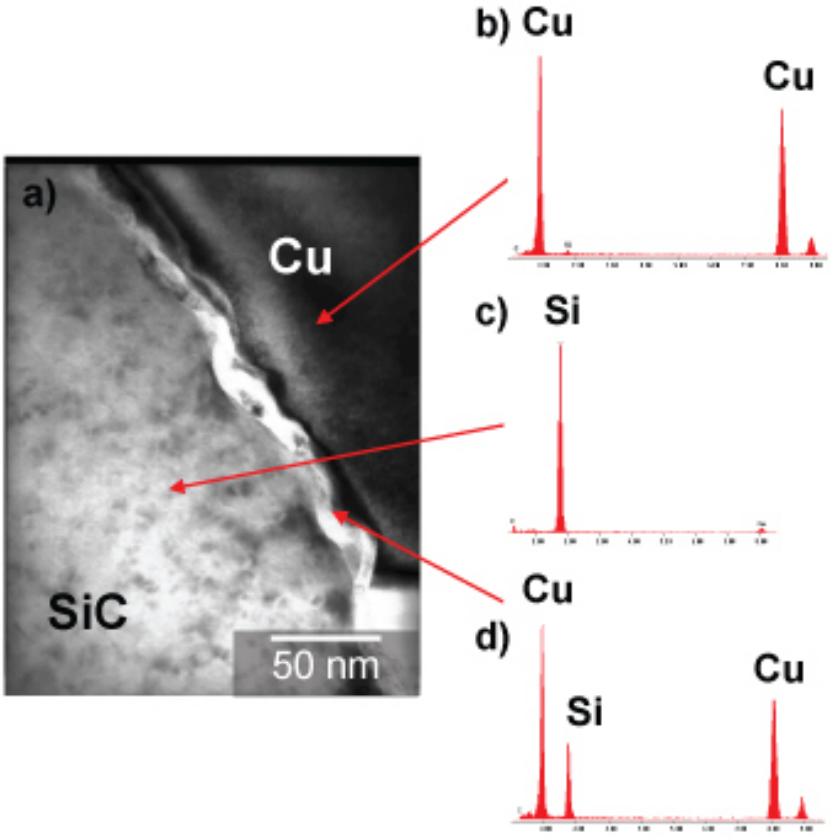

Figure 3.38. (a) Interface of copper and silicon carbide in a Cu-bioSiC composite heated to 1000°C, and energy-dispersive X-ray spectra of (b) the copper region, (c) the silicon carbide region, and (d) the interface.

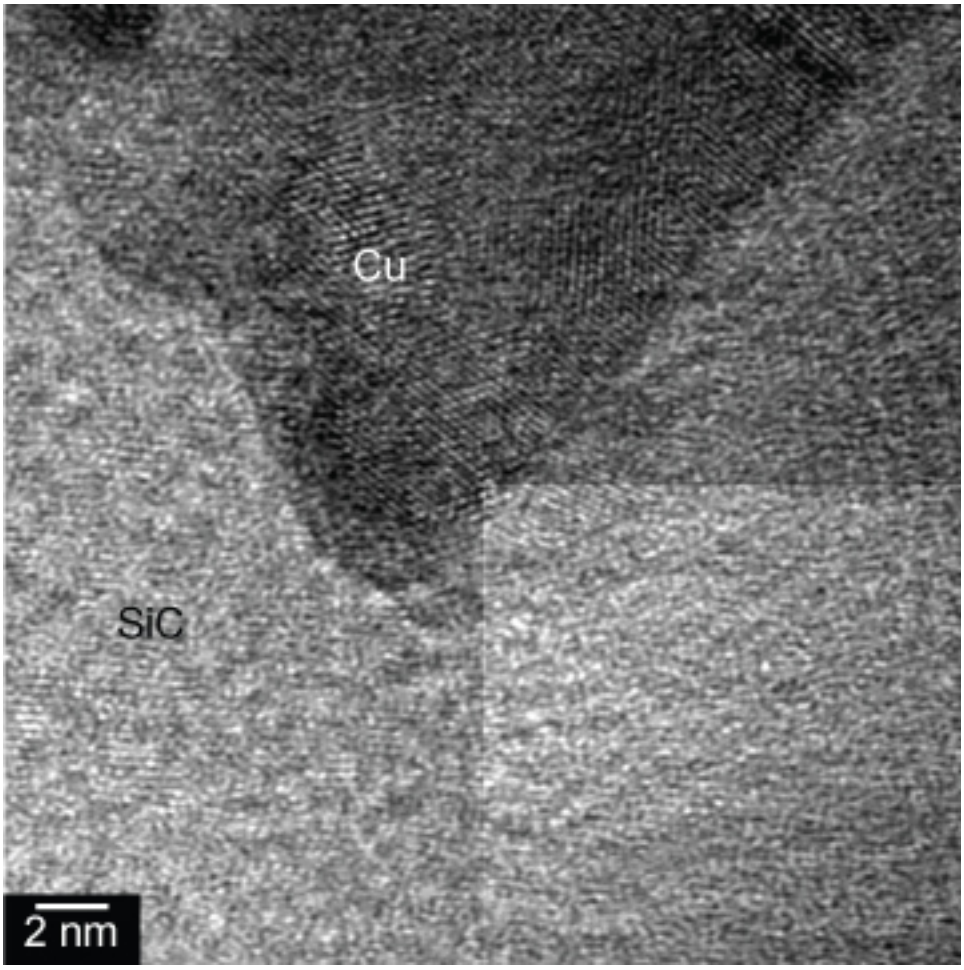

Figure 3.39. High resolution transmission electron microscope image of Cu-bioSiC interface. The box in the lower right corner is an artifact of the camera.

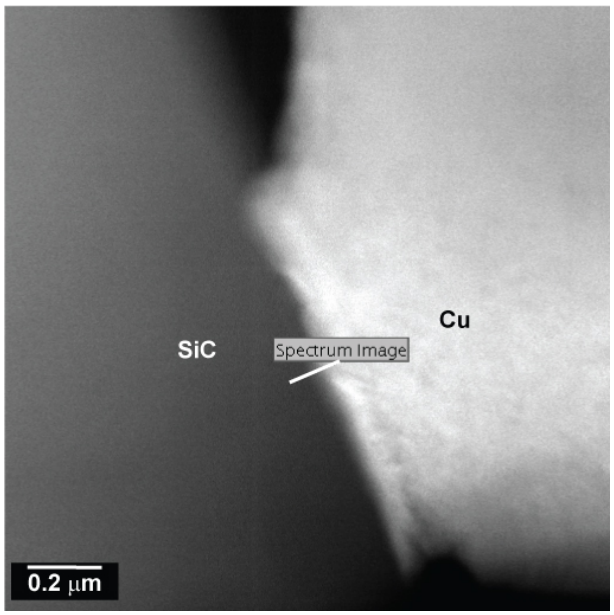

(a)

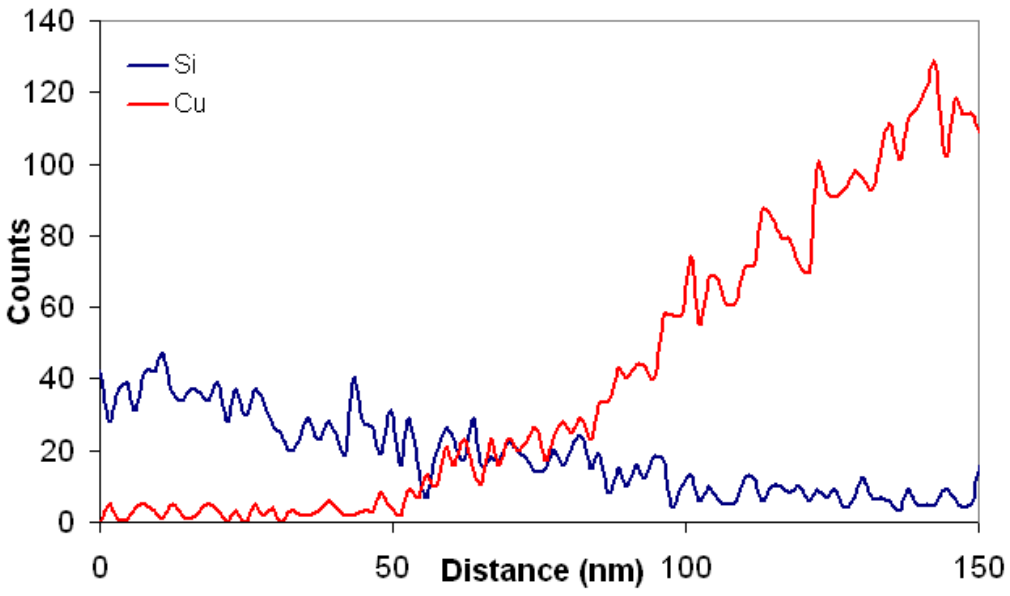

(b)

Figure 3.40. (a) Scanning transmission electron microscope image of the Cu-SiC interface and (b) energy-dispersive X-ray spectroscopy line scan along the white line in (a).

scan provides the ability to estimate the thickness of the interface, which is less than 50 nm.

It is significant to note that the high magnification images, as well as the EDS data at very high magnifications, of the interface region show no signs of diffusion or reaction between the copper and the silicon carbide after a heat treatment to 1000°C. The corresponding electron diffraction patterns also show no evidence of the copper-silicide reaction. In addition, the X-ray diffraction pattern of the Cu-bioSiC sample heat treated to 1000°C also showed no evidence of reaction, as the $Cu_{6.69}Si$ peak was absent. The TEM and X-ray data confirm that at this temperature, where there is no molten Cu present, the Cu is unable to break down the Si and C or react with the Si. Thus, electroplating Cu to fill the pores of bioSiC samples is a successful method for making Cu-bioSiC composites, avoiding the Cu-SiC reaction. The absence of $Cu_{6.69}Si$ should result in an enhanced thermal conductivity over melt infiltrated composites that contain this phase.

3.5. Summary

This chapter discussed in detail the processing of carbon from wood pyrolyzed at temperatures ranging from 300-2400°C, and the silicon carbide structures that resulted from melt infiltration of these carbon scaffolds with silicon. The morphology of these materials was characterized with porosimetry, SEM and TEM. The progression towards a small amount of long-range order that occurred with increased carbon pyrolyzation temperature was illustrated using X-ray diffraction, Raman spectroscopy, and thermal diffusivity. The structure and morphology of the silicon carbide were studied using porosimetry, SEM and TEM, and it was determined that there is no difference in silicon carbide processed

from carbon pyrolyzed at different temperatures. Electrodeposition was shown to be a viable composite fabrication technique, producing composites with as little as 16% residual porosity. It was confirmed using X-ray diffraction and TEM that the detrimental copper-silicon reaction was avoided during the processing of these materials.

CHAPTER 4

Thermal and Thermomechanical Properties of BioSiC

In this chapter, the thermal conductivity and thermal shock resistance of bioSiC materials made from different wood precursors were studied. The thermal conductivity was investigated as a function of porosity, temperature and sample orientation. Object-oriented finite-element analysis was used to model the thermal conductivity and heat flux distributions in these samples. The thermal shock resistance and thermal expansion coefficient were studied as a function of initial wood precursor type and orientation.

4.1. Thermal Conductivity of BioSiC

4.1.1. Experimental Methods

4.1.1.1. Density. Density of the porous bioSiC samples was determined using Archimedes' Method.[148] The specific gravity, bulk density and porosity were calculated for each sample.

4.1.1.2. Specific Heat. The specific heat capacity of bioSiC was determined using a differential scanning calorimeter (Netzsch DSC 404C, Burlington, MA).[149] Only one bioSiC sample, measuring 6 mm in diameter and 1 mm in thickness, was tested because it is assumed that SiC made from different woods would have equivalent heat capacity, due to the microstructural independence of heat capacity and the uniform experimental procedure used to create all bioSiC samples.

4.1.1.3. Diffusivity. The diffusivity of the bioSiC samples was determined at room temperature by a xenon flash system.[139] Disk-shaped samples measuring 12.7 mm in diameter and 3 mm in thickness were used for all diffusivity testing. A xenon flash was shot at each sample three times. Software incorporating the Clark and Taylor approximations was used to determine the thermal diffusivity of each sample.[133] The xenon flash diffusivity was measured both before and after the tests at elevated temperatures to ensure that no changes occurred in the materials during testing. A table of thermal conductivity values measured before and after high-temperature testing is provided in Table 4.1.

The diffusivity of the bioSiC samples at elevated temperatures was determined using a Nd: glass pulse laser (1.06 mm wavelength) flash diffusivity system with FL5000 software (Anter Corporation, Pittsburgh, PA).[150] The 12.7 mm diameter disks were tested in argon in the temperature range of 150 to 1100°C at approximately 100°C intervals. Three measurements were made at each temperature, and the data were analyzed using software that included the Clark and Taylor approximations.[133] At each temperature, three samples from each wood precursor type and orientation were tested. Density was assumed to be constant throughout the high-temperature testing. The axially-oriented samples have some pores that are as long as the sample dimensions, such that light is able to penetrate directly through the 3 mm thickness. Direct contact between the laser signal and the detector can damage the detector, and can also give unreasonable results. For this reason, the axial samples were coated with a thin layer of SiC paste (Aremco, Pyro-Paint 634-SiC, Valley Cottage, NY) to eliminate the possibility of direct contact between the laser and the detector. Samples were tested with the xenon flash diffusivity before and after

Table 4.1. Room Temperature Axial Thermal Conductivity (W/mK) of BioSiC Before and After High Temperature Testing

Wood precursor	Before laser testing	After laser testing
Beech	41.65 ± 4.89	41.44 ± 7.19
Mahogany	15.69 ± 4.32	14.87 ± 3.93
Poplar	18.75 ± 1.17	16.58 ± 1.57
Red oak	27.21 ± 3.97	25.83 ± 4.39
Sapele	28.92 ± 4.67	26.68 ± 5.92

the coating was applied to ensure that the paste did not have an effect on the room-temperature thermal conductivity, as shown in Table 4.2. These data demonstrate that neither the high-temperature treatment nor the paste altered the thermal diffusivity values within the error of the system, which was found to be accurate to within 10%.[142]

After diffusivity measurements were taken, the samples were cross-sectioned and examined in the SEM, which showed that only in a few instances, and only in the largest channels, did any paste seep into the pores. One worst-case example of the paste infiltration into a pore of sapele-based bioSiC is provided in figure 4.1.

The reported diffusivity is an average of three samples, each measured three times. Outliers, which might be caused by the shape of the temperature-time curve, the laser signal strength, the presence of pinholes, or the sample surface roughness, were established based on the past accuracy of the instrument, and were excluded from the dataset. In general, the instrument is found to be accurate to ±10%.[142] Owing to the porous structure of the material and the nonuniformity of the SiC paste coating used to seal the pores, some larger-than-expected scatter was observed in the data, especially at temperatures where the detector is less sensitive. Less scatter was observed in the transverse direction where the pores and paste did not affect the signal.

4.1.2. Results and Discussion

4.1.2.1. Density. The porosity of bioSiC for each wood in each orientation is shown in Table 4.3. It is significant to notice the values of porosity given for each sample type. Referring back to figure 3.16, beech (a) and poplar (b) have similar pore structures, but have very different porosities. The same is true for mahogany (c) and sapele (d). Red

Table 4.2. Room Temperature Transverse Thermal Conductivity (W/mK) of BioSiC Before and After Applying SiC Coating

Wood Precursor	Before coating	After coating
Beech	40.35 ± 1.22	36.43 ± 0.89
Mahogany	9.89 ± 0.09	11.3 ± 0.24
Poplar	17.64 ± 0.34	15.69 ± 0.25

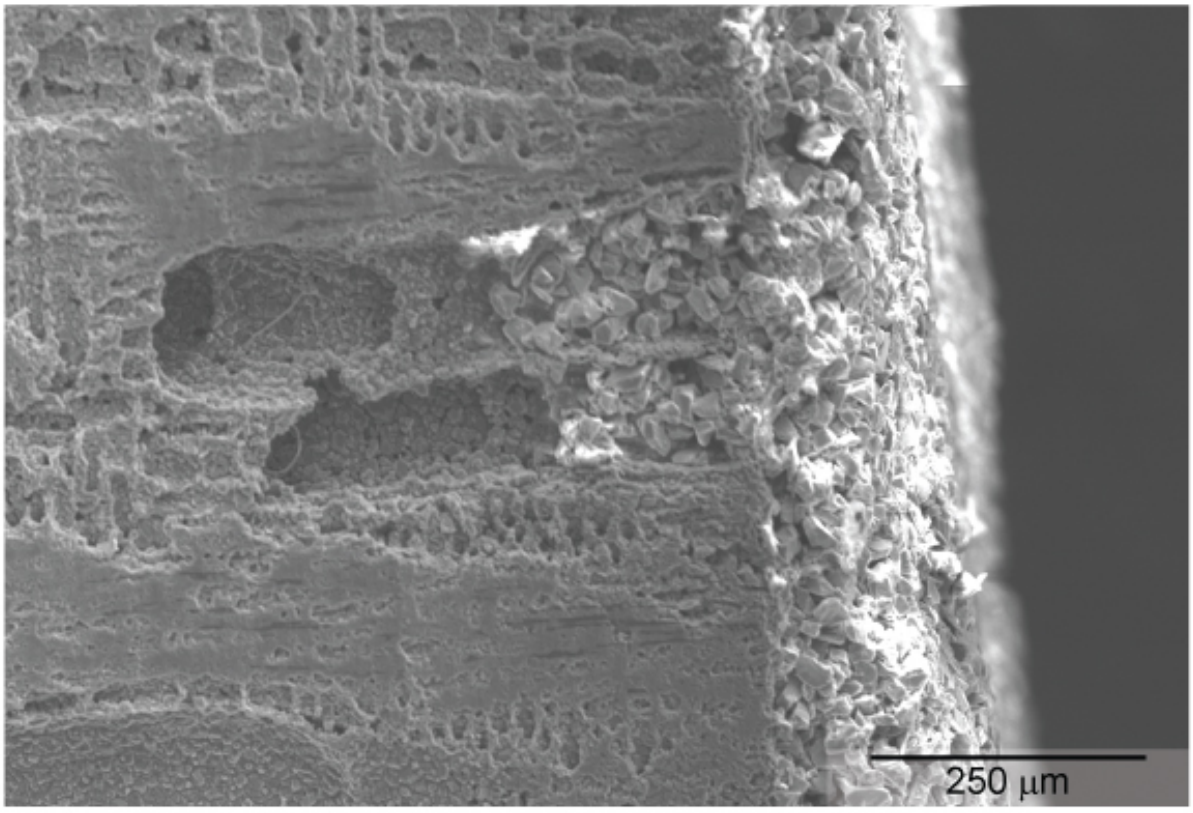

Figure 4.1. Scanning electron micrograph illustrating coating depth in a pore of sapele-based bioSiC.

oak (e) and sapele (d) have similar porosities, but exhibit vastly different pore structures. These porosity and pore structure relationships are important in characterizing the thermal conductivity of these bioSiC materials.

4.1.2.2. Differential Scanning Calorimetry (DSC). The specific heat capacity was measured for one sample of bioSiC (axially-oriented beech) and the results were applied to all other samples. The sample was only measured up to 800°C because any excess Si in, or silicon dioxide on, the sample could react with the platinum components in the DSC system. The heat capacity was extrapolated from 800°C to 1100°C using a fitting function based on the Debye model for C_v and the Nernst-Lindemann relation for C_p-C_v. The heat capacity curve results agree well with the literature values.[151] The results for 25, 400 and 900°C are shown in table 4.4.

4.1.2.3. Thermal Conductivity. Thermal diffusivity and thermal conductivity are plotted in figure 4.2 versus temperature for one representative wood, beech, in the transverse direction. The diffusivity and thermal conductivity both decrease with increasing temperature initially, as predicted by equation 2.2. However, the thermal conductivity of bioSiC never increases as the temperature increases, as suggested by theory. From calculations performed for the porosities, sample sizes, pore sizes, and temperatures tested, using $\beta = 0.87$, the radiative contribution is less than 1% of the total conductivity. Thus, it is clear that the solid contribution to the effective bioSiC thermal conductivity will always be dominant, and the overall thermal conductivity will decrease with increasing temperature.

In figures 4.3(a) and (b), thermal conductivity is plotted versus porosity for three different temperatures in the axial and transverse orientations, respectively, along with

Table 4.3. Porosities of BioSiC Samples in the Axial and Transverse Orientations

Wood Precursor	Axial Orientation Porosity (%)	Transverse Orientation Porosity (%)
Beech	43.37 ±1.84	45.97 ± 1.42
Mahogany	66.49 ± 1.95	59.48 ± 5.49
Poplar	68.52 ± 1.30	68.16 ± 0.72
Red oak	49.15 ± 5.27	55.12 ± 1.52
Sapele	52.01 ± 1.52	51.77 ± 1.38

Table 4.4. Specific Heat Values for Axially-Oriented Beech-Based BioSiC.

Temperature	Specific Heat (J/g°C)
25°C	0.67
400°C	1.09
900°C	1.20

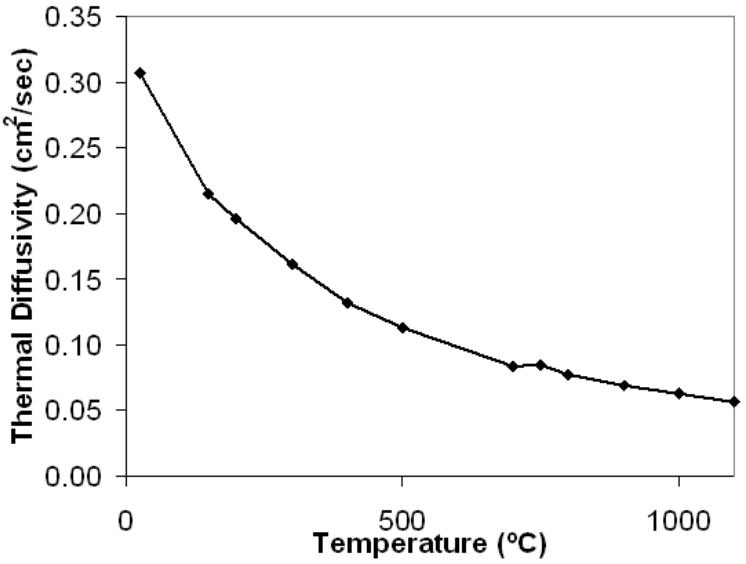

(a)

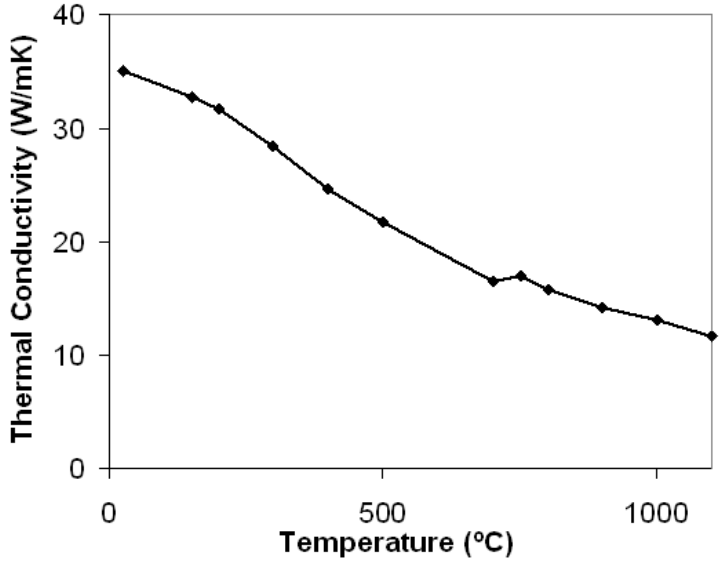

(b)

Figure 4.2. (a) Thermal diffusivity and (b) thermal conductivity versus temperature for an axially oriented beech-based bioSiC sample.

their corresponding theoretical thermal conductivities at room temperature using the MSA model from equations 2.3 and 2.4.

As a general trend, the thermal conductivity decreases with increasing porosity, which is consistent with theory. This trend can be attributed to a decrease in the volume fraction of the solid phase, SiC, which is the dominant contribution to the overall thermal conductivity. The non-monotonic nature of the curves can be largely attributed to the microstructure of the initial woods. The theoretical values decrease linearly with porosity in this region, overestimating the experimental values in the axial direction, while underestimating them in the transverse direction. The experimental values in the transverse direction do not decrease linearly, and thus the MSA model is a particularly poor fit for these data. The MSA model is based on materials with a cubic array of identical cylindrical pores, whereas the bioSiC has a very complex microstructure, with many different pore sizes, distributed unevenly throughout the system, which may give rise to these differences. The object-oriented finite-element analysis, described later, can be used to better understand the role of microstructure in determining thermal conductivity.

Examples of the variation between the thermal conductivity measured in the axial (heat traveling parallel to the elongated pores) and the transverse (heat traveling perpendicular to the elongated pores) directions for ring-porous red oak- and diffuse-porous sapele-based bioSiC are shown in figures 4.4(a) and (b), respectively. As expected, the thermal conductivity is higher in the direction parallel to the pores. Sapele- and red oak-based bioSiC samples have nearly the same porosity, but have very different microstructures and pore size distributions, as seen in figures 3.16(d) and (e). The thermal

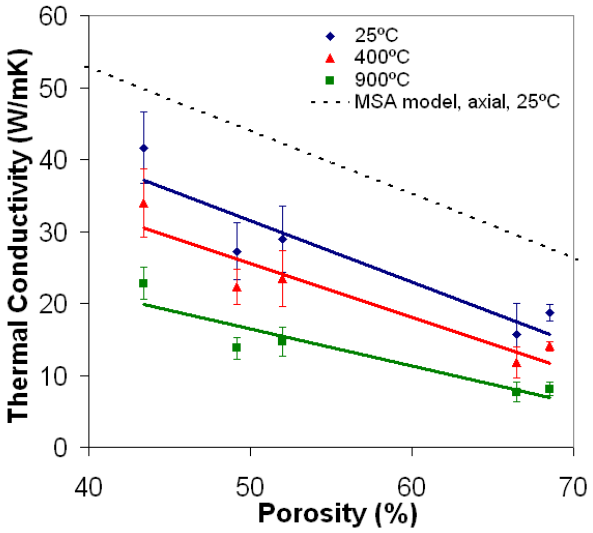

(a)

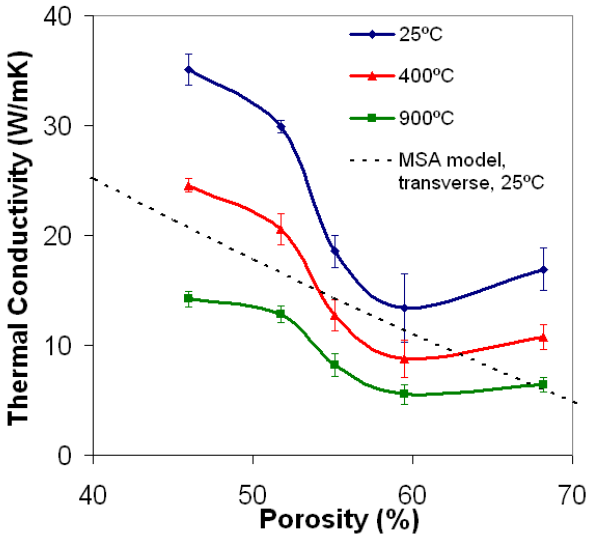

(b)

Figure 4.3. Thermal conductivity versus porosity at 25, 400, and 900°C for (a) axial- and (b) transverse-oriented biomorphic silicon carbide samples, along with a theoretical curve based on equation 2.2, and the minimum solid area model from equations 2.3 and 2.4 at 25°C.[86] (Error bars represent one standard deviation. Solid lines in (a) represent a least-squares fit for the data. Solid lines in (b) connect the data points and are provided as an aid to the reader.)

conductivity of sapele-based bioSiC varies less with orientation than that of red oak-based bioSiC. This indicates that, while important, porosity is not the only factor in determining the thermal conductivity of bioSiC. Pore distribution also plays a significant role. The degree of variation of thermal conductivity with orientation can be sorted into categories based on the characteristics of the structure. The diffuse-porous wood-based bioSiC samples all showed less variation between axial and transverse conductivities than the ring-porous wood-based bioSiC. The ring-porous bioSiC samples have bands of low and high density throughout their structure. In this case, the heat is forced to travel through these regions of extremely low density, which conduct very slowly. There are very few direct paths for the heat to travel through dense material without encountering pores. In contrast, the diffuse-porous bioSiC samples are more homogeneous, and there are more direct pathways through the solid.

4.1.3. Object-Oriented Finite-Element Modeling

To better understand the microstructure-related thermal properties, finite-element modeling was conducted using object-oriented finite-element analysis (OOF). The color threshold was adjusted in an SEM image so that each distinct phase was represented by only one color, and each phase was then assigned the appropriate material properties. Next, a two-dimensional mesh was generated to represent the microstructure of the SEM image. This mesh was altered such that it mimicked the features present in the micrograph. The alterations occurred by subdividing the existing elements and moving nodes so that the energy of the system was minimized. Element edges attempted to align with material interfaces, such that each element was as homogeneous as possible (contained pixels from

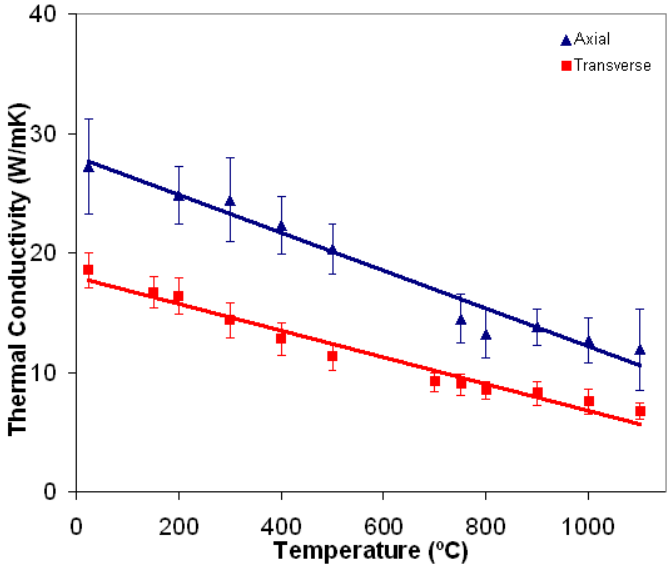

(a)

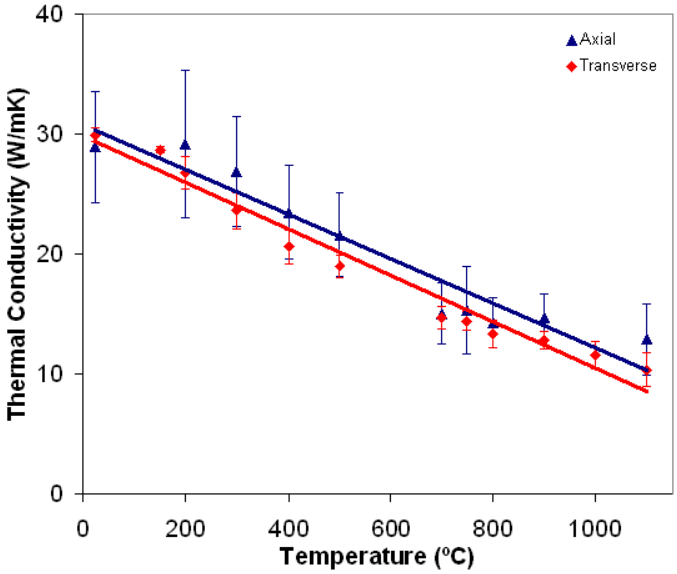

(b)

Figure 4.4. Thermal conductivity as a function of orientation for (a) red oak- and (b) sapele-based biomorphic silicon carbide samples. (Error bars represent one standard deviation.)

ideally only one material). Appropriate solid SiC and gas (air for room-temperature calculations and argon for elevated-temperature calculations) properties were assigned to their respective phases.[124,152] A representative OOF mesh, shown in figure 4.5, was constructed with triangular finite elements representing the solid bioSiC material and the remainder of space representing pores.

After the mesh was created, thermal boundaries were imposed in either the x or y directions in the system, which led to temperature gradients within the sample after the system was equilibrated. OOF can display graphical representations of flux fields throughout the mesh, allowing for further understanding of the microstructural behavior under the imposed thermal gradient. The thermal conductivity can then be calculated based on the heat flux at the boundaries in the direction of the thermal gradient. The resultant effective conductivity in the y direction, $k_{eff,y}$ can be written as:

$$k_{eff,y} = \frac{QL_y}{L_x \Delta T} \tag{4.1}$$

where Q is the heat flux, ΔT is the temperature gradient, and L_x and L_y are the sample dimensions.

For many of the bioSiC samples, there was porosity present on a much finer scale (<20 μm) that was improperly meshed at low magnifications. This led to inaccurately predicted conductivity values for each bioSiC sample, which often over estimated the values due to the inability of the OOF mesh to resolve these small pores. For these materials, an apparent solid conductivity, k_{app}, was determined for each wood type. This was done by first calculating the conductivity of the solid bioSiC material at a higher magnification, using an image that did not contain any vessels. Higher magnification

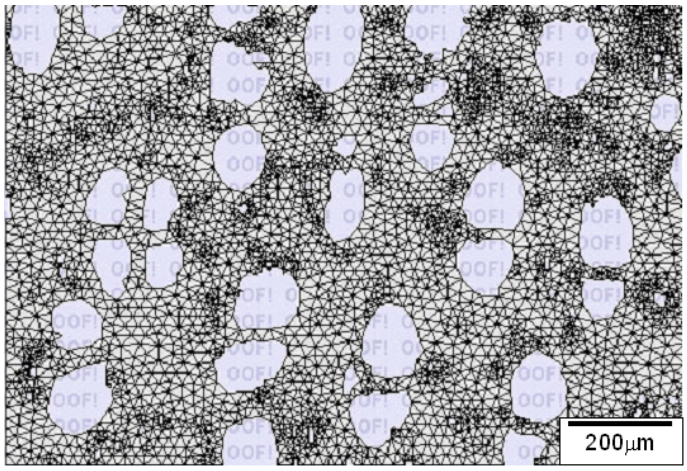

Figure 4.5. Object-oriented finite-element analysis mesh created from a micrograph of sapele-based biomorphic silicon carbide.

images of 400x and 1000x were both used to calculate k_{app}. Figure 4.6 shows a plot containing the experimental values, the MSA model, OOF calculations without k_{app} and OOF calculations with k_{app} values determined using both 400x and 1000x micrographs calculated at room temperature in the transverse orientation. It was determined that the OOF calculations using k_{app} calculated from the 1000x magnification images fit best to the experimental data. Examples of regions used to calculate k_{app} at 1000x magnification are shown in figure 4.7 for (a) sapele and (b) mahogany-based bioSiC.

Red oak, a ring-porous wood, has an even more complex microstructure, due to the large density bands that arise from the great distinction between early and late wood periods. This provides an added challenge when attempting to calculate k_{app} and k_{eff}. Upon inspection at high magnification, it can be seen that the regions in the early and late wood that do not contain vessels have variations in porosity. Thus, both regimes require consideration when calculating the effective conductivity, and high magnification images of each were obtained. Representative images used for k_{app} calculations from early wood and late wood are shown in figures 4.8(a) and (b), respectively. An average value was determined for each of the early wood and late wood regions in the red oak-based bioSiC. These two apparent conductivities were averaged to result in an overall k_{app} for red oak-based bioSiC used to determine k_{eff}.

Table 4.5 shows the k_{app} values for each wood. Between one and five images were used for poplar-, sapele-, mahogany- and red oak-based sample to determine the k_{app} value. No k_{app} value was used for the beech wood as there were no small pores that required additional meshing. These k_{app} values were input as k_{SiC} in OOF calculations of their respective lower magnification microstructures to obtain a more accurate porous k_{eff}. The

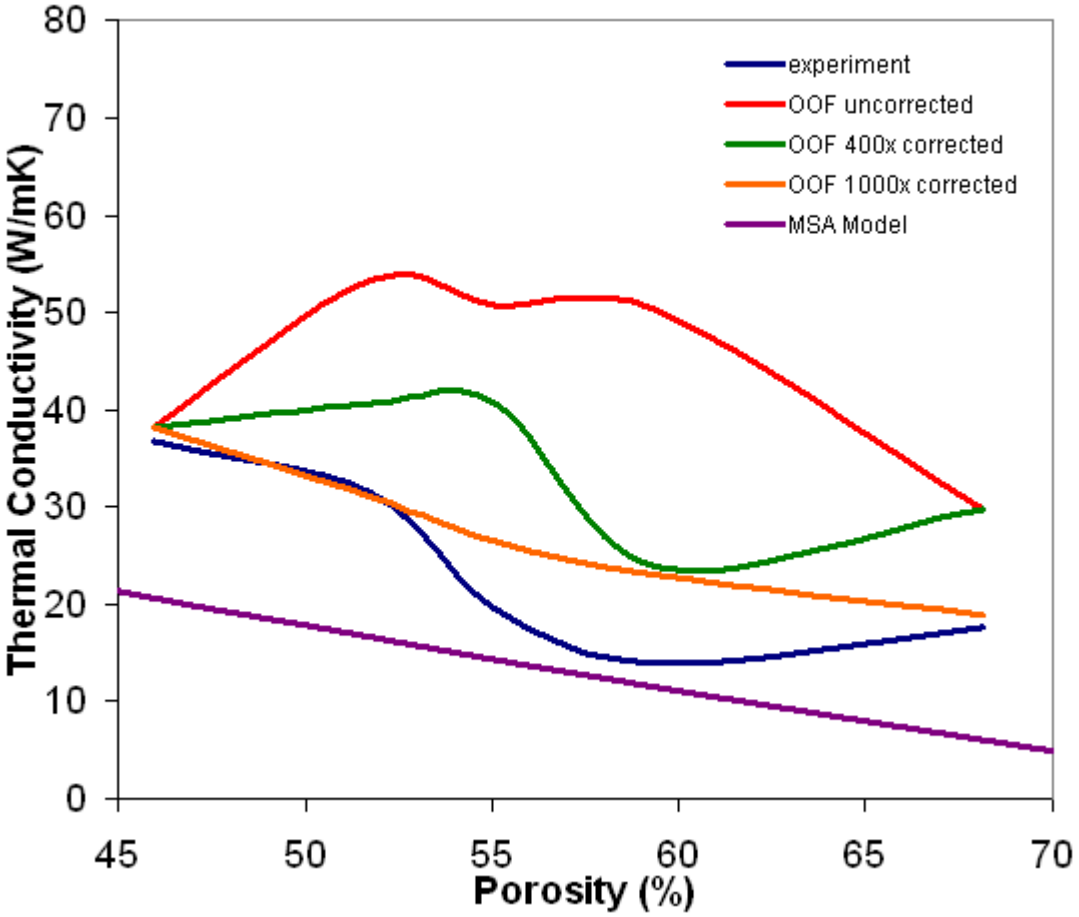

Figure 4.6. Thermal conductivity of bioSiC determined experimentally along with the minimum solid area model and several OOF modeling methods for transversely oriented samples at room temperature.[86]

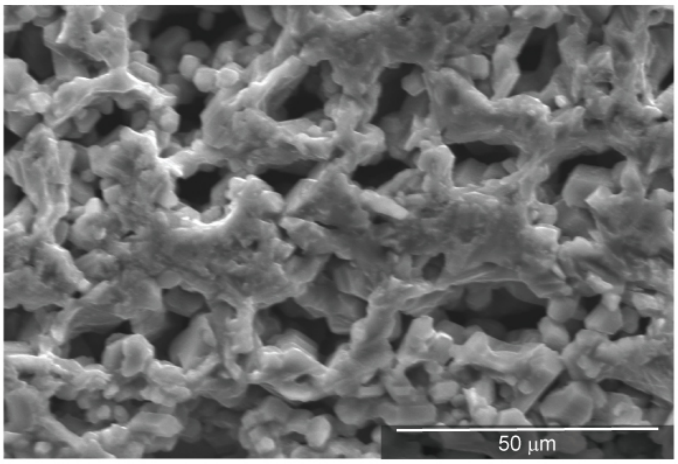

(a)

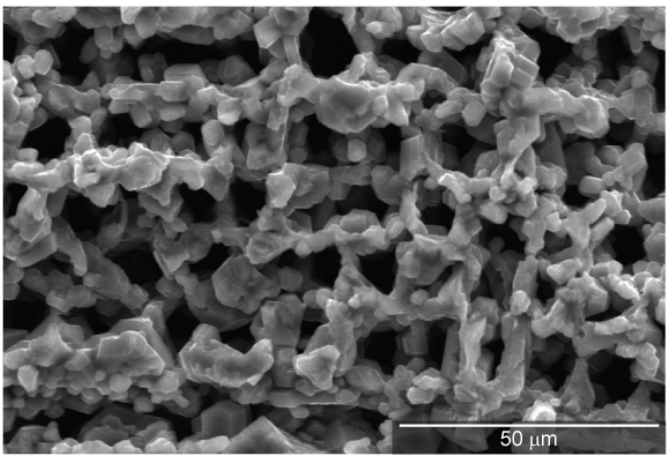

(b)

Figure 4.7. High magnification scanning electron micrographs of (a) sapele- and (b) mahogany-based bioSiC for calculation of k_{app}.

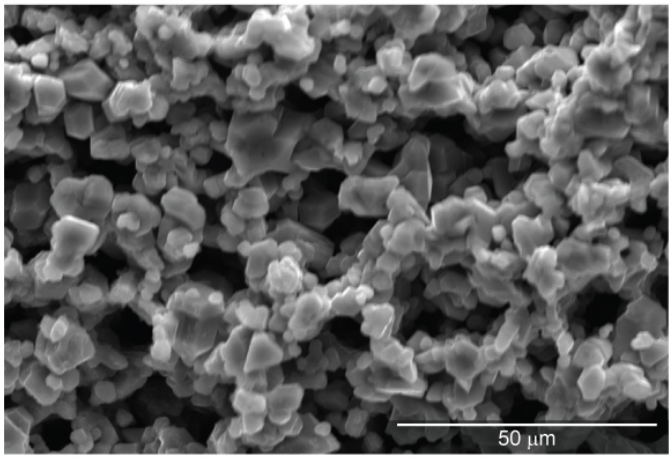

(a)

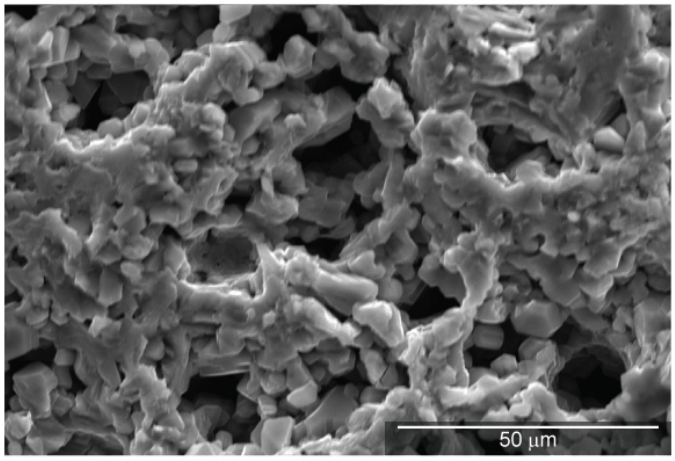

(b)

Figure 4.8. High magnification scanning electron micrographs of red oak based bioSiC used for k_{app} calculations from (a) early wood and (b) late wood regions.

results of the OOF calculated k_{eff} are compared with the experimental values in figures 4.9 - 4.10. In figure 4.9, the thermal conductivity calculated from OOF and determined experimentally are plotted at different porosities for three different temperatures. These OOF results follow a trend similar to that of the experimental data, showing a non-linear decreasing thermal conductivity with both porosity and temperature.

Figures 4.10(a) and (b) show the OOF calculations compared with experimental data for each wood with temperature. Calculations based on three images were used and averaged together for each wood type. The OOF calculations predict the experimental values well for beech-, sapele-, and poplar-based bioSiC. For mahogany-based bioSiC, OOF overestimates the actual values shown experimentally. SEM images, particularly of less dense samples like mahogany-based bioSiC, as shown in figure 4.7(b), show considerable depth of field, allowing the material below the surface to be visible, instead of only a two-dimensional slice. This causes more solid than is actually present in the two-dimensional plane to be retained in the thresholded image, and ultimately in the OOF mesh, leading to a higher k_{app}. A higher k_{eff} results.

Aside from these specific examples, there are additional reasons why OOF calculations, in general, may not exactly match experimental values for bioSiC materials. One is that an OOF mesh is a two-dimensional representation of the microstructure and does not take into account the third dimension or the interconnectivity between the pores. Also, while the SEM images used for the OOF meshes were representative of the actual microstructure, they are not exact due to natural wood variation from sample to sample.

In addition to calculating the effective conductivity of the different bioSiC samples, the heat-flux patterns throughout each material were also illustrated using OOF. Flux

Table 4.5. Apparent Thermal Conductivity (k_{app}) Values for use in OOF Modeling

Wood Type	$k_{app,25°C}$ (W/mK)	$k_{app,400°C}$ (W/mK)	$k_{app,900°C}$ (W/mK)
Mahogany	35	20	14
Poplar	56	30	19
Red oak	40	24	18
Sapele	51	28	19

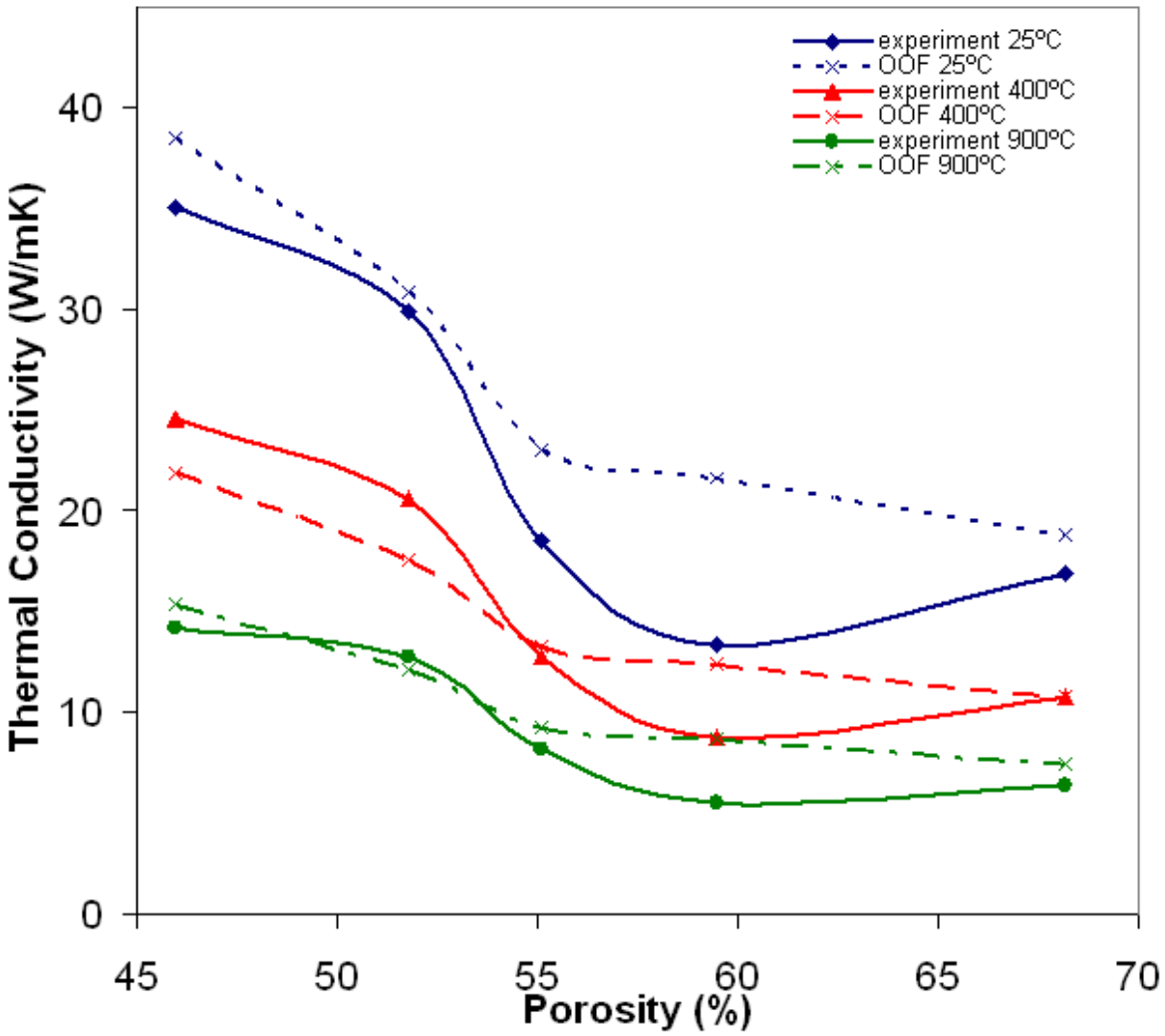

Figure 4.9. Object-oriented finite-element analysis calculations of bioSiC thermal conductivities in the transverse orientation paired with their respective experimental values for three different temperatures.

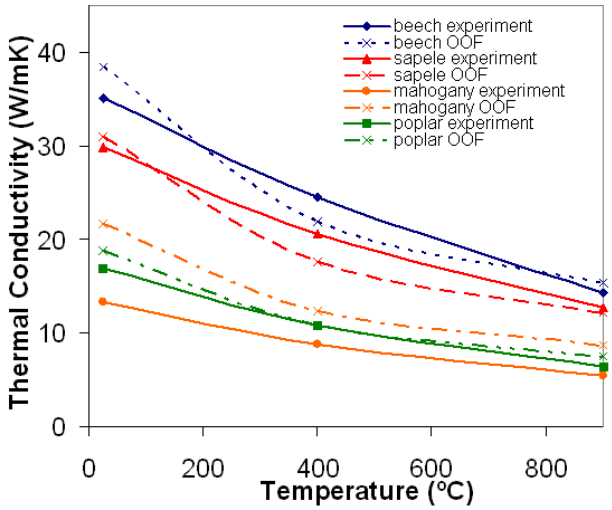

(a)

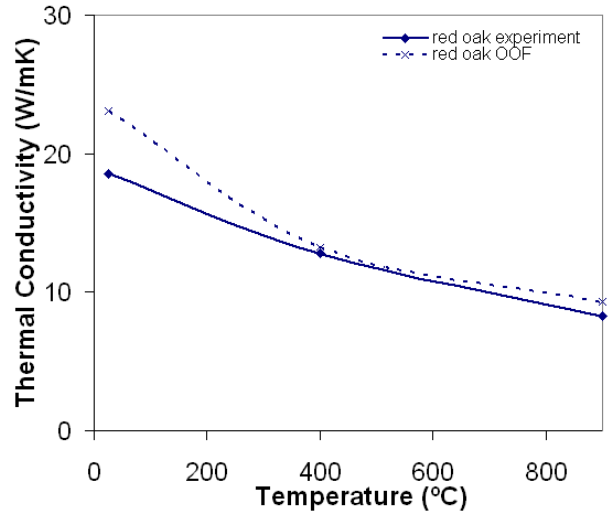

(b)

Figure 4.10. Object-oriented finite-element analysis calculations of transverse bioSiC thermal conductivities paired with their respective experimental values for (a) diffuse-porous and (b) ring-porous wood based bioSiC.

diagrams for representative diffuse-porous and ring-porous wood-based bioSiC are shown in figures 4.11(a) and (b).

In both samples, it is evident that the pores serve as points of deflection for heat flow. In figure 4.11, the yellow areas indicated by arrows represent regions of high heat flux between pairs of pores in the direction of heat flow. When the heat approaches a pore, it is diverted through the adjacent solid material. Because the solid conductivity is significantly higher than that of the gas filling the pore, the solid is the preferred path. The effectiveness of the heat deflection by pores is also illustrated by the narrow struts oriented perpendicular to heat flow, which are circled in figure 4.11. These regions exhibit a low heat flux because they are not located along the most direct solid path. The heat flux is higher in the regions of higher density, which are often in the late wood regions, near the growth ring interfaces, and through the rays.

The thermal conductivity of bioSiC was shown to decrease with porosity, as predicted, and to be highly dependent on the microstructure. The MSA model, which takes into account both the porosity and the pore shape when calculating the thermal conductivity of bioSiC, does indicate a decrease with porosity and orientation. However, this model does not account for the complex pore distributions of the bioSiC microstructure, which play a significant role in predicting the thermal conductivity. BioSiC derived from precursors with different microstructures but having equivalent porosities and pore shapes exhibit vastly different thermal conductivities. For example, ring-porous bioSiC was shown to have a much greater dependence on orientation than diffuse-porous bioSiC with a similar porosity. Utilizing tools such as OOF to model and assess actual microstructures, it is possible to explain thermal properties more effectively. Moreover, heat flux patterns

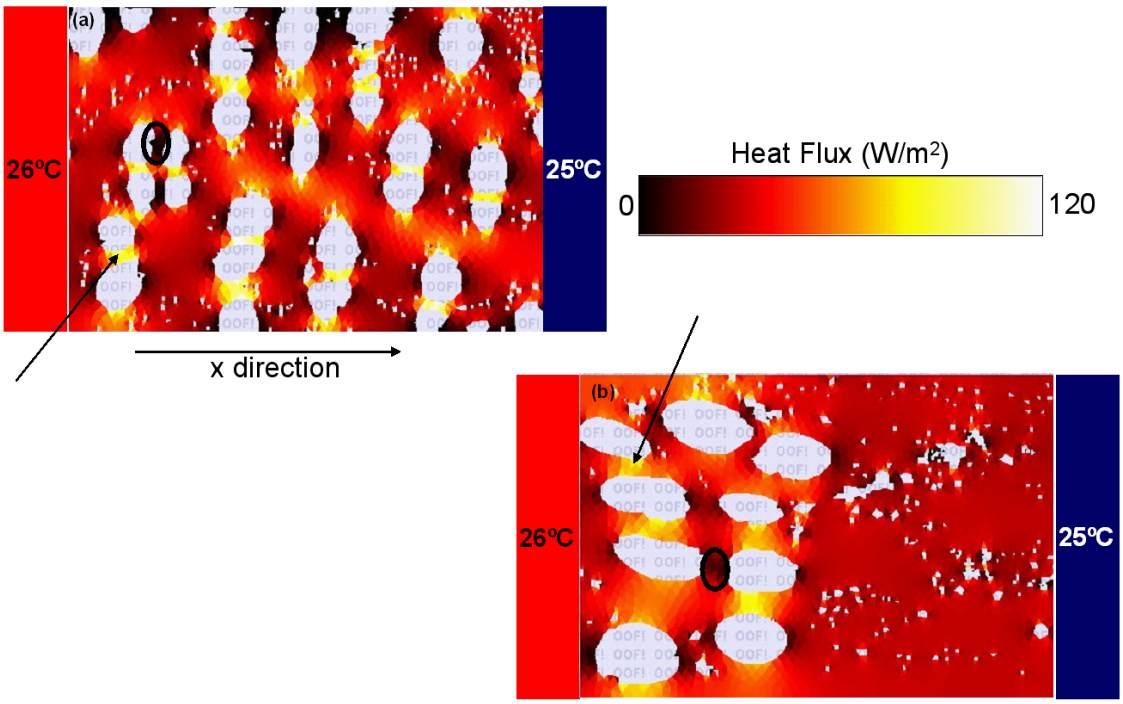

Figure 4.11. Heat flux distribution due to a temperature gradient applied in the x direction in (a) sapele (diffuse-porous)-based bioSiC and (b) red oak (ring-porous)-based bioSiC. Arrows point to regions of high heat flux, and circles indicate regions of low heat flux.

can be analyzed to gain a better understanding of the thermal conductivity of complex microstructures.

4.2. Thermal Expansion Coefficient

The coefficient of thermal expansion (CTE) was determined for bioSiC samples using a thermomechanical analyzer (TA Instruments, TMA Q400). The appropriate applied force of the probe on the sample during testing was calibrated and determined to be 0.5 N. This value ensured that the probe was in constant contact with the sample, yet not compressing it. Samples were heated at 1°C per minute to 1000°C. The linear expansion was recorded as a function of time and temperature. The linear expansion was plotted versus temperature and a best fit line was obtained, the slope of which is the CTE. The CTE was recorded for beech-based bioSiC in the axial and transverse orientations as well as for sapele-based bioSiC in the transverse orientation using this measurement scheme. Each sample was run at least twice to determine repeatability.

The CTE was determined to be 4.8 ± .18, 4.7 ± .05, and 5.4 ± .38 x 10^{-6}/°C for beech transverse, beech axial, and sapele transverse samples, respectively, over the range from room temperature to 1000°C. The CTE is not dependent on the microstructure, but only the bonding between the atoms in the material.[93] Thus, any deviations are due to possible variations in distance between the sample and the thermocouple during the measurement, which could lead to false readings. In fact, from run to run of the same sample, the values obtained varied by up to 10%. However, these values agree well with the literature value for silicon carbide, which is reported as 4.75 x 10^{-6}/°C over the range from room temperature to 927°C.[143]

4.3. Thermal Shock Resistance of BioSiC

4.3.1. Experimental Methods

To begin studying the thermal shock resistance of porous silicon carbide derived from wood, the most appropriate method of testing must be determined. The most commonly used methods to test thermal shock resistance consist of heating a sample and quenching it rapidly either into a liquid medium or with cool forced air. As discussed in section 2.4.3, there are many advantages and disadvantages to each different quenching medium. In this study, silicone oil was chosen as the quenching medium, instead of the more common selection of water. This is because the variation in heat transfer coefficient with temperature is extremely high for water, which makes quantitatively determining the critical temperature difference (ΔT_c) more difficult. The heat transfer coefficient of oil, while also temperature dependent, demonstrates less variability, and thus should give a more accurate value of ΔT_c.

Typically, the thermal shock damage is determined by measuring the retained strength in bending. This method of damage assessment is appropriate for homogeneous materials that have very little variation in strength from one sample to the next. However, with bioSiC, the microstructure is inhomogeneous, and has a high variation in strength and modulus due to the natural variation innate to wood, as shown in figures 4.12(a) and (b).[39]

Due to this high variability in strength, using a destructive testing method, such as bending strength, to monitor thermal shock damage, is undesirable. In order to determine if damage is being imposed upon the sample, the values need to be consistent such that

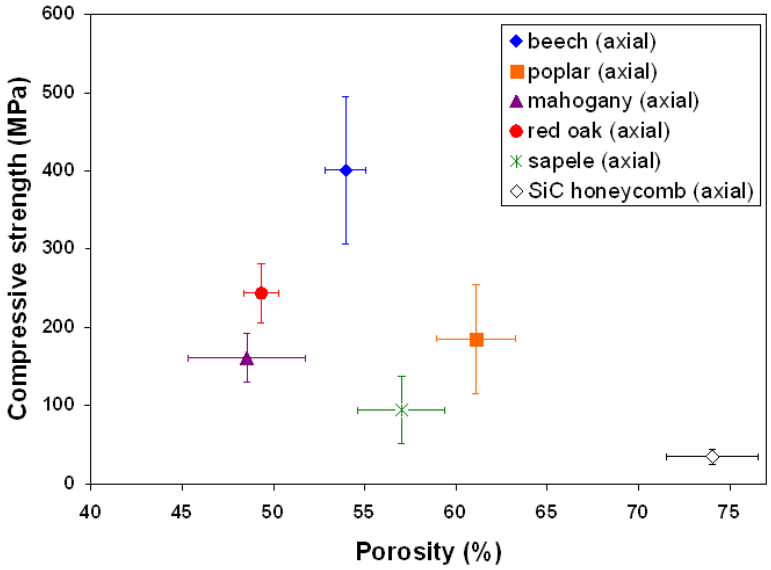

(a)

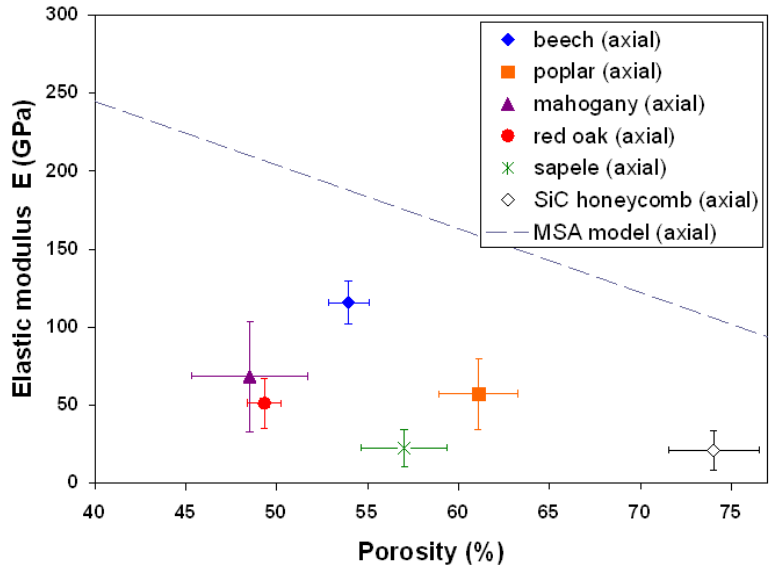

(b)

Figure 4.12. (a) Compressive strength and (b) elastic modulus of bioSiC in the axial orientation as a function of porosity.[39]

even a small change will be noticeable. Thus, a non-destructive method of characterization is necessary for samples such as bioSiC. With a non-destructive test, the same sample can be assessed before and after thermal shock cycles, in order to determine the degree of change within a particular sample. In addition, the sample can be cycled multiple times, while checking the progressive damage that may be occurring. In this work, the non-destructive evaluation technique that was chosen was sonic velocity measurement. The sonic velocity is proportional to the elastic modulus of a material. Both the elastic modulus and the sonic velocity are expected to decrease as cracks initiate and propagate in the sample. Thus, the sonic velocity is expected to decrease as a result of thermal shock damage for bioSiC samples.

As a standard, 5 mm thick samples of dense SiC were tested for comparison to the porous bioSiC samples. BioSiC discs 5 mm thick derived from sapele, beech and red oak woods, as well as 7 mm and 10 mm thick samples derived from sapele wood were tested in the thermal shock apparatus. Samples were each cycled up to five times from temperatures 1400°C to room temperature. Prior to thermal shock testing, the samples were heated to 1400°C and held for two hours in a box furnace to form any stable oxide layer that is known to form during high temperature heating. This ensures that the sample will not gain weight during the thermal shock testing.

A vertical tube furnace was used to heat each sample to 1400°C, where the sample was held for 30 minutes before quenching. The sample sat on an alumina rod that was inserted through a hole in the side of the furnace. The perimeter of the hole was insulated to minimize temperature loss. The temperature was monitored with an external thermocouple, separate from the controller, to ensure that the furnace temperature remained constant.

After the sample was held at temperature for 30 minutes, the alumina rod holding the sample was rotated, allowing the sample to slide off and fall through the vertical tube into a bucket of room temperature oil resting on the ground. After the oil quench, the sample was cleaned by ultrasonicating in acetone to remove the residual oil that remained in the sample pores. This thermal shock cycle was repeated up to five times for each sample to determine the cumulative damage that occurred with each quench cycle. A schematic of the experimental setup is shown in figure 4.13.

The sonic velocity of each sample was tested after each quenching cycle. Sonic velocity was measured in through transmission, which is useful for highly attenuating samples, similar to the porous bioSiC.[153] Two (5 MHz) transducers were placed on either face of the sample, with molasses as a couplant. One transducer emitted a sound wave, either longitudinal or shear, depending on the transducer chosen, and the other received it. The time of flight (TOF), the time the sound wave takes to traverse the sample thickness, is recorded. The measurement is made without and with the sample in place (figure 4.14). The difference between the two spectra yields the TOF through the sample. The measured sample thickness is divided by the TOF value to calculate the sonic velocity, v, of the sample.

In addition to the sonic velocity testing after each thermal shock cycle, scanning electron microscopy (SEM) was used to investigate the sample surface for evidence of crack initiation and propagation. In a thermal shock situation the interior of the sample will be in compression while the exterior will be in tension, and thus, cracks will be initiated on the surface of the sample. Unshocked samples were thoroughly inspected

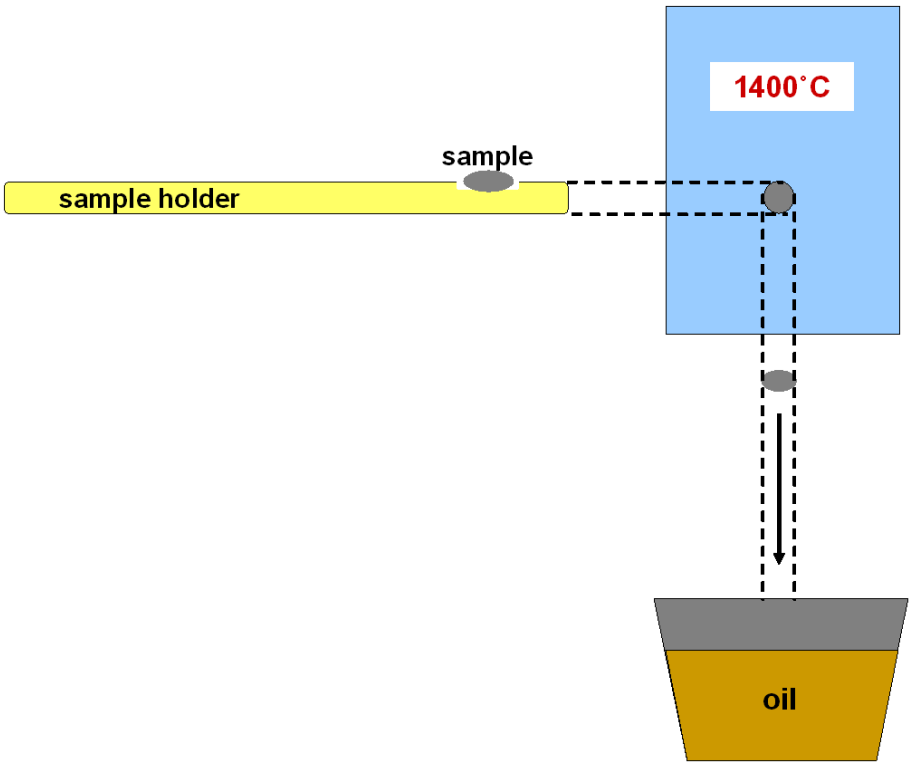

Figure 4.13. Schematic diagram of thermal shock experimental setup.

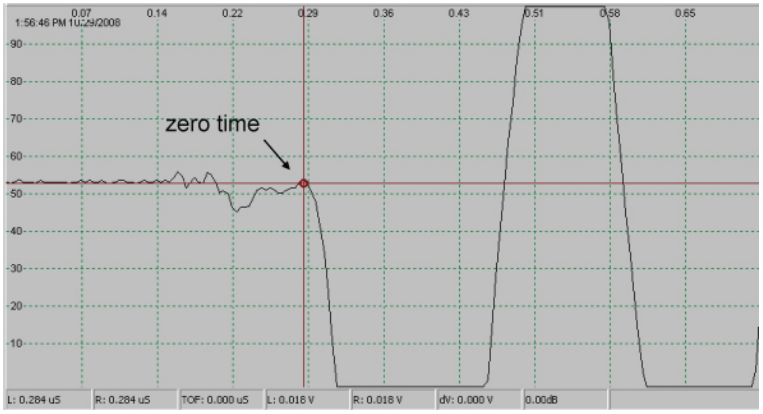

(a)

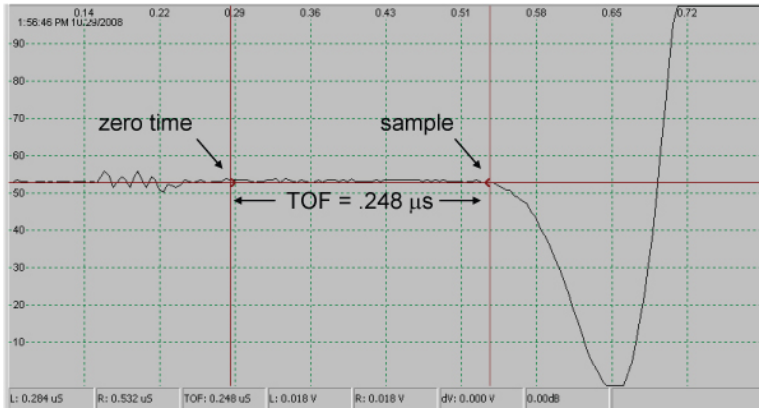

(b)

Figure 4.14. Sonic velocity through ultrasonic transducers (a) without a sample and (b) with a sample.

at high magnifications to ensure that there were no macroscopic cracks prior to thermal shock treatment.

4.3.2. Results

4.3.2.1. Microscopic Analysis. The dense silicon carbide samples that were thermally shocked catastrophically failed during the fourth and fifth cycles. They developed cracks that split the samples in half. A broken dense silicon carbide sample is shown in figure 4.15.

Unlike the dense silicon carbide samples that were tested, none of the bioSiC samples experienced catastrophic failure after five thermal shock cycles. After thermal shock cycles, the samples were investigated, and in each case, initiation of macroscopic cracks was evident. The cracks propagated over considerable lengths of up to 10 mm in some cases. In the transverse samples, the cracks were found to run both parallel and perpendicular to the vessels, as is demonstrated in figures 4.16(a) and (b). In the axial direction, the cracks were seen traveling in the space between vessels as well as through them, as seen in figures 4.17(a) and (b). This indicates some pores did not serve as crack arrestors. The presence of these cracks in thermally shocked samples indicates that some damage is in fact occurring in the samples. However, the initiation and propagation of these cracks is not sufficient to cause catastrophic failure in the bioSiC samples.

4.3.2.2. Sonic Velocity. For the dense silicon carbide samples, although they failed catastrophically, the sonic velocity did not vary with each thermal shock cycle. This is shown in figure 4.18. This implies that no cracks were initiated prior to the cycle in which failure occurred, as the presence of a crack in the sample would have led to decreased

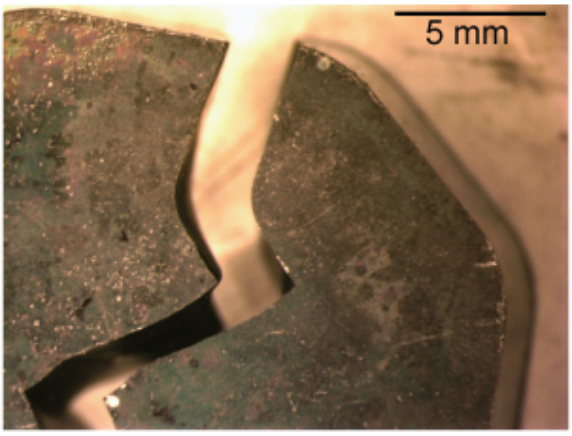

Figure 4.15. Dense silicon carbide after five thermal shock cycles.

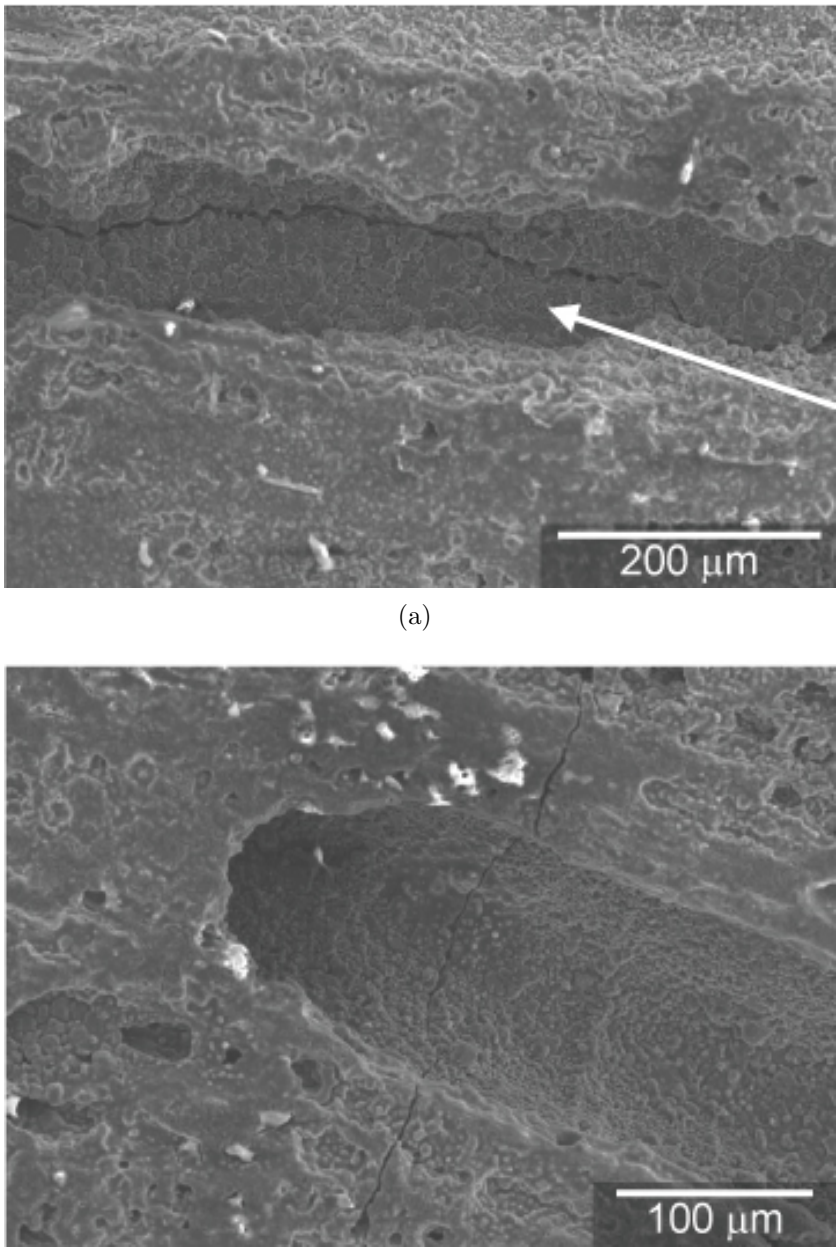

(a)

(b)

Figure 4.16. Scanning electron microscope images indicating cracks due to thermal shock of sapele-based bioSiC samples in the transverse direction (a) running along the vessel and (b) intersecting the vessel.

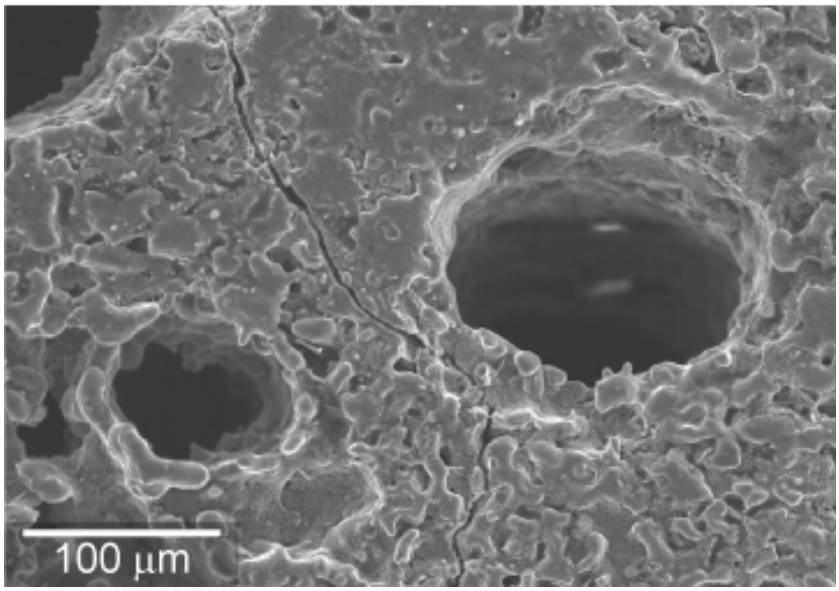

(a)

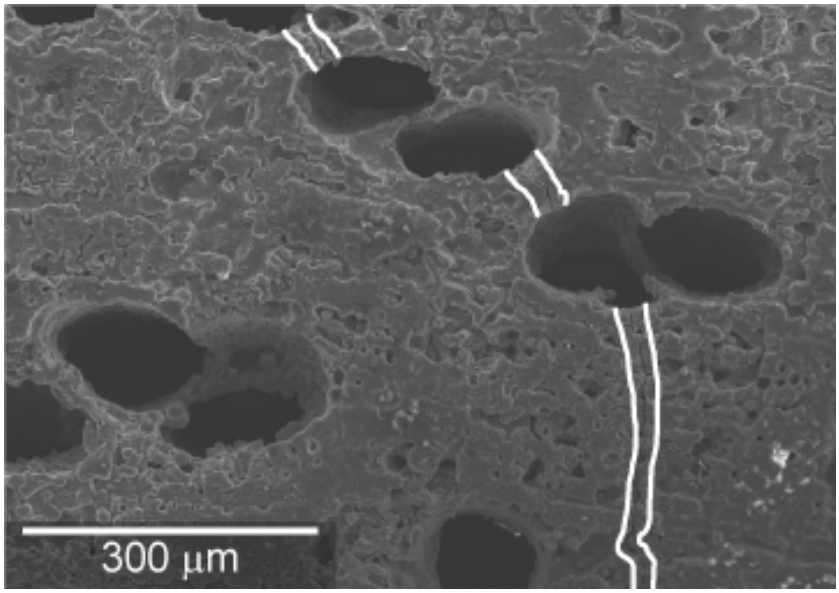

(b)

Figure 4.17. Scanning electron images indicating cracks due to thermal shock of sapele-based bioSiC in the axial direction (a) between vessels and (b) across vessels. The white lines outline the crack for clarification.

sonic velocity. This means that as soon as a crack was initiated, it propagated until catastrophic failure. It took four to five cycles until the energy supplied by the thermal gradient was enough to cause the sample to crack.

The bioSiC samples also did not show any variation in sonic velocity after each thermal shock cycle. This is illustrated in figures 4.19(a)-(b). Figure 4.19(a) shows the sonic velocity as a function of the number of thermal shock cycles for representative samples of red oak-, beech- and sapele-based bioSiC in the transverse orientation. The same is true for samples of different thicknesses and orientations, as seen in figure 4.19(b), where sapele samples in both the axial and transverse directions, as well as at thicknesses of 5 and 7 mm, were tested and showed no variation with number of thermal shock cycles.

It is surprising, in light of the microscopic evidence that damage occurred in each of the samples, that the sonic velocity remained the same, within error, after an increasing number of thermal shock cycles. Additionally, there should be more thermal shock damage with increased sample thickness, as the β value should be higher, resulting in a more severe thermal shock. However, this was not reflected in the sonic velocity measurements. These results show that while there is evidence of some thermal shock damage, the sonic velocity testing is not sensitive enough to register a change. In order to better understand why this is true, finite element modeling was used to model the effective modulus of samples with and without cracks present.

4.3.2.3. Finite-Element Modeling. Object-oriented finite-element analysis (OOF) has the capability of modeling complex microstructures such as bioSiC in order to calculate effective property values. The sonic velocity is related to the elastic modulus of a sample, and thus a change in the modulus should be reflected in a change in the sonic velocity.

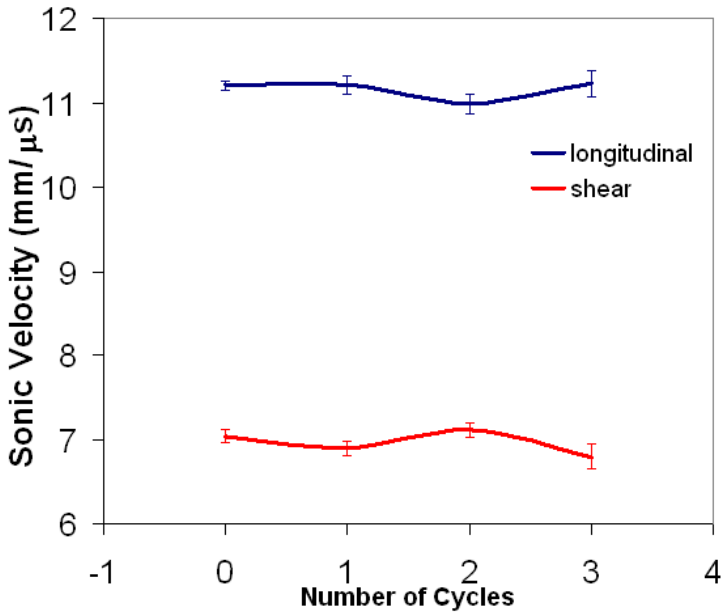

Figure 4.18. Sonic velocity of dense silicon carbide sample that broke after the fourth thermal shock cycle.

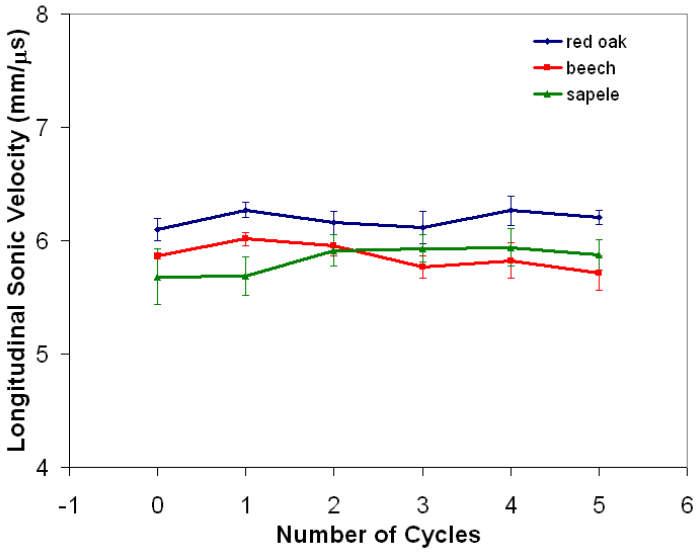

(a)

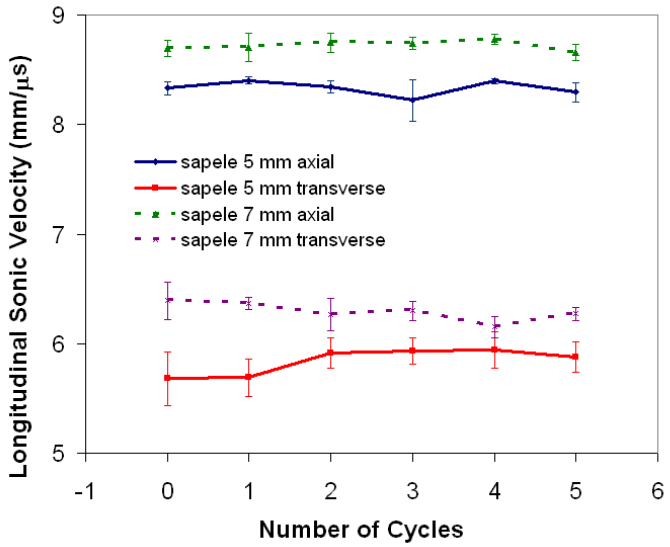

(b)

Figure 4.19. Sonic velocity as a function of the number of thermal shock cycles for (a) red oak, beech, and sapele-based bioSiC and (b) sapele-based bioSiC in both the axial and transverse orientations and at thicknesses of 5 and 7 mm.

OOF was used to determine the effective modulus of sapele-based bioSiC microstructures with and without cracks present, to simulate sonic velocity measurements. The virtual cracks that were introduced in the microstructural images had the same crack width to pore size ratio as seen in figures 4.16 and 4.17. They also had the same length to area ratio, proportional to the actual sample dimensions, in order to compare the model to the actual sample accurately. The cracks were initiated in several directions with respect to the pores in each sample. These virtual cracks would, in three-dimensions, extend infinitely in the z-direction, as the elongated pores do, signifying a worst case scenario in depth for each initiated crack. An average effective modulus was determined from images with these varying crack orientations.

The effective modulus was measured in both the axial and transverse directions. An example of a binary micrograph of sapele-based bioSiC calculated in the axial direction is shown in figure 4.20. In this image, white represents the silicon carbide phase and black, the pore phase. The schematic on the left of figure 4.20 shows that the transducers are afixed to the sample in the axial orientation, with the transducer faces perpendicular to the elongated vessel direction. The arrow underneath the OOF micrograph indicates the direction in which the sonic velocity sound waves would be traveling in the sample. The initiated crack in this example microstructure is circled in red. The modulus value changes from 151 $\pm$ 9 GPa in a sample with no crack to 141 $\pm$ 13 GPa. The modulus calculations are an average of seven different initiated crack orientations, and the error values represent one standard deviation of these values. This indicates an approximately 6% decrease in average values after thermally shocking the sample. According to the t-test at a 95% confidence level, we cannot reject the null hypothesis that $E_{eff,x,nocrack} =$

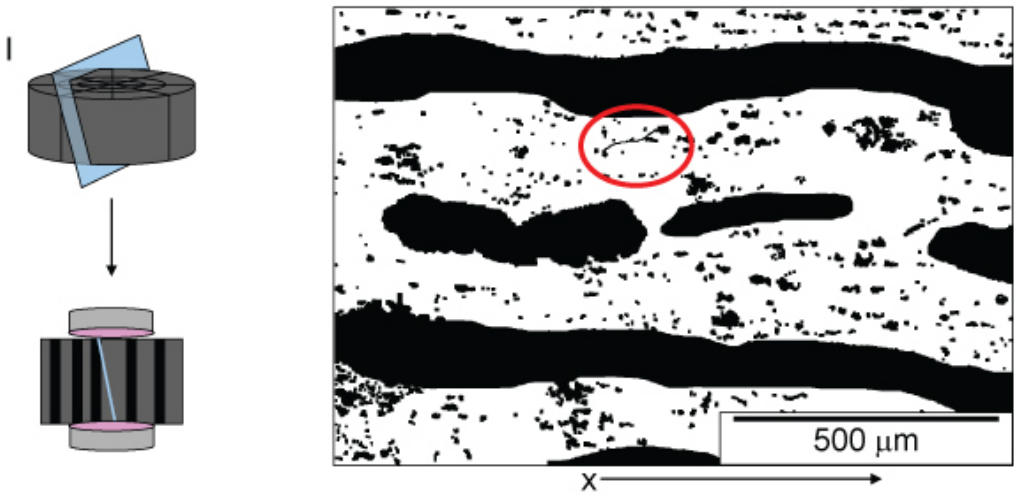

Figure 4.20. Object-oriented finite-element analysis model of sapele-based bioSiC in the axial direction with a representative crack.

$E_{eff,x,crack}$, and thus there is no significant modulus change with thermal shock induced cracks.

Figure 4.21 shows a similar OOF simulation for a sample measured in the transverse direction. Again, the schematic to the left of the image indicates that the sonic velocity was tested in the transverse direction, with the transducer faces parallel to the vessel pores and the sound wave traveling perpendicularly to the pore elongation direction. In the OOF micrograph, the x and y directions both represent the transverse orientation. Both directions were examined to determine the effective modulus change. The initiated crack in this image is circled in red. The modulus here changes from 163 ± 27 GPa to 154 ± 22 GPa in the x direction and from 207 ± 2 GPa to 196 ± 8 GPa in the y direction with addition of a crack. These modulus values are also an average of seven different initiated crack orientations, and the error values also represent one standard deviation of these values. This corresponds to about a 6% change in the x direction and a 5% change in the y direction for a thermally shocked sample. Again, with the t-test performed at a 95% confidence level, the null hypothesis that $E_{eff,nocrack} = E_{eff,crack}$ cannot be rejected, and again, there is no significant change as a result of thermal shock damage.

These OOF modeling results indicate that calculating the effective modulus change is a useful way to determine the presence of damage within a bioSiC sample due to thermal shock. However, they imply that sonic velocity measurements are not sensitive enough to detect the presence of new cracks in the samples. There are several reasons why this is the case. The first is that in a highly porous sample, such as bioSiC, the sonic velocity is already decreased from that of a dense sample by the attenuation due to the presence of many pores. The initiation of a crack that has a small width compared to the pore

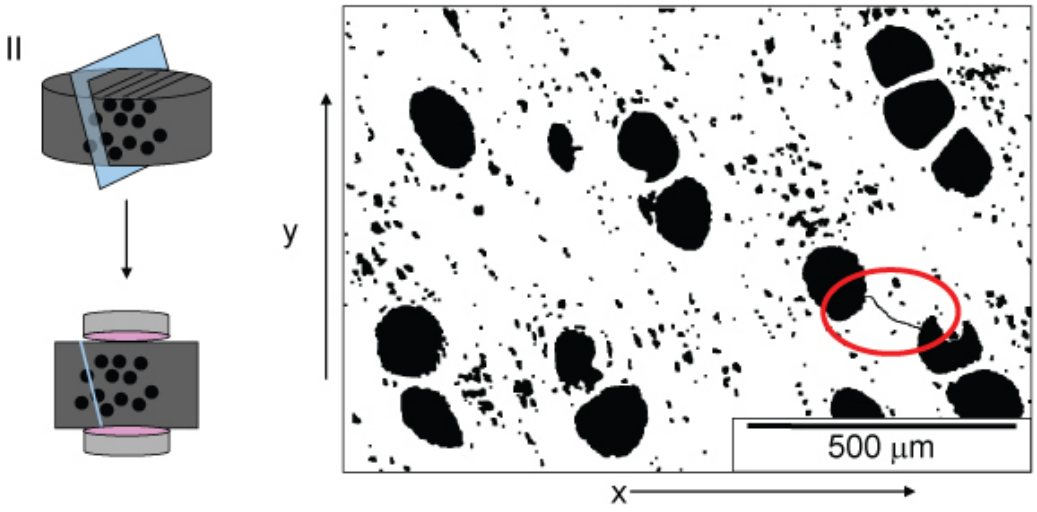

Figure 4.21. Object-oriented finite-element analysis model of sapele-based bioSiC in the transverse direction with a representative crack.

diameters, and a small area compared to the pore areas, is a small addition to the already existing porosity. Thus, the transducers may not be sensitive enough to pick up the small changes associated with these cracks. In addition, in highly attenuating samples, such as bioSiC, the samples need to be thin enough that the sonic velocity signal can be resolved. However, thicker samples should experience more severe thermal shock damage due to the increased value of β. Thus, it is difficult to measure the thermal shock damage of thicker samples that are more likely to exhibit a larger change with each cycle. Due to these constraints, a different thermal shock resistance testing method will need to be created in order to quantitatively determine the damage done as a result of thermal shock, as well as the critical temperature difference that the sample can withstand before catastrophic failure occurs.

She et al. and Ding et al. both tested the thermal shock resistance of porous silicon carbide ceramics by quenching heated samples into water baths.[114,119] Neither case showed evidence of catastrophic failure up to 1200°C, and both showed that the strength remained unchanged with thermal shock cycles after the first quench. Only Ding et al. saw evidence of macroscopic cracking. BioSiC has withstood even higher temperatures than these, of up to 1400°C, without catastrophic failure. In addition, its elastic properties have not diminished at all after up to five thermal shock cycles. This indicates that bioSiC has the capability to withstand these high temperature environments with severe thermal shock situations. BioSiC does indeed have potential for use in high temperature, severe thermal cycling applications.

4.4. Summary

The thermal conductivity, thermal expansion coefficient, and thermal shock resistance of bioSiC were studied. The thermal conductivity was found to decrease with increasing temperature and porosity. Anisotropy in the thermal conductivity was found to be more significant in some wood types than in others, implying that the pore distribution plays a significant role in the thermal properties of bioSiC. This was confirmed using object-oriented finite-element analysis to estimate the effective thermal conductivities of these samples as well as study how heat is transferred through these complex microstructures.

The bioSiC samples were found to have a high thermal shock resistance. No sample failed catastrophically following up to five thermal shock cycles from a 1400°C furnace to a room temperature oil bath. The damage was monitored using scanning electron microscopy and sonic velocity measurements, and while cracks were initiated, there was no elastic property decrease noted.

CHAPTER 5

Thermal Properties of Copper-Biomorphic Silicon Carbide Composites

In this chapter, the thermal properties of copper-biomorphic silicon carbide composites were determined using flash diffusivity. Object-oriented finite-element analysis was used to model the heat flux distributions in the samples and calculate effective thermal conductivity values. The thermal expansion coefficient was also determined for these composite materials.

5.1. Thermal Conductivity of Copper-BioSiC Composites

5.1.1. Experimental Procedures

5.1.1.1. Sample Preparation. Copper-biomorphic silicon carbide samples were prepared by electrodeposition, as described in section 3.4.3. These samples required machining prior to thermal conductivity testing because the electrodeposition resulted in a copper coating of about 1-2 mm thick surrounding the samples, because copper deposition does not discriminate between the pores and the outer surfaces of a sample. This excess copper needs to be removed before testing in order to prevent inflated thermal diffusivity and density values. However, for some applications, a thin outer coating of copper may be useful for bonding to other components in a system, and would not need to be completely removed. The sample surfaces were ground with 60, 180 and 240 grit silicon carbide paper

until the silicon carbide regions on the surface of the sample were visible. The samples were inspected under a stereo microscope to ensure that they were sanded completely.

5.1.1.2. Density. The density of the Cu-bioSiC composites was determined by using Archimedes' Method as described in section 4.1.1.1.[148] Three samples of each orientation, approximately 12.7 mm in diameter and 3 mm in thickness, of beech-, poplar-, red oak- and sapele-based Cu-bioSiC composites were measured. These samples were subsequently used for the thermal diffusivity testing described in section 5.1.1.4.

5.1.1.3. Specific Heat. The specific heat of the Cu-bioSiC composites was determined by using differential scanning calorimetry, as described in section 4.1.1.2. One of each sample of beech-, poplar-, red oak- and sapele-based bioSiC, measuring 6 mm in diameter and 1 mm thick, was measured in both heating and cooling. The specific heat is independent of orientation because it is based on composition, not microstructure. The values attained in the sample orientation tested were used for all thermal conductivity calculations from a particular wood type.

5.1.1.4. Thermal Diffusivity. The thermal diffusivity of the Cu-bioSiC samples were tested from 0-900°C using a Nd: glass pulse laser (1.06 mm wavelength) flash diffusivity system with FL5000 software (Anter Corporation, Pittsburgh, PA).[150] The 12.7 mm diameter disks were tested in air at 0 and 50°C in an argon atmosphere in the temperature range of 100 to 900°C at approximately 100°C intervals. Three laser shots were imparted on each sample at each temperature, and the data were analyzed using software that included the Clark and Taylor approximations.[133] At 0 and 50°C, three samples from each wood precursor type of beech, poplar, red oak, and sapele, in each orientation, were tested. At elevated temperatures, axially-oriented poplar, red oak, and sapele, and

transversely-oriented poplar Cu-bioSiC samples were tested. Due to equipment repair constraints, only these twelve samples were able to be tested at temperatures above 50°C. Density was assumed to be constant throughout the high-temperature testing. The samples that were tested at elevated temperatures were subsequently re-tested at 0 and 50°C to determine if any changes occurred as a result of the high temperature testing.

5.1.2. Results and Discussion

5.1.2.1. Density. The bulk densities and porosities of the Cu-bioSiC samples are shown in table 5.1. Upon investigation of this table, it is clear that different wood types have different quantities of remaining porosity as discussed in section 3.4.3. It is more interesting, however, to note that the samples derived from the same initial wood precursor also have great variation from one sample to the next. Averaging the density and porosity values of the samples derived from the same wood in the same orientation result in large standard deviations. While in most samples the majority of the pores are well filled, some individual samples contain regions with less successful plating. Thus, it is more appropriate to consider each sample individually, and not categorized by wood type, for the discussion of the composite samples.

In general, the amount of remaining porosity is higher in the transverse than the axial direction. This is because in the transverse orientation, the plating was not as successful. Figure 5.1 is a scanning electron microscope image, using the back scattered electron detector, of a cross-section produced by slicing a transverse disc in half. This image shows that a large number of pores have not been filled at all.

Table 5.1. Bulk Density and Porosity of Cu-BioSiC Composites

Sample Type	Bulk Density (g/cm^3)	Porosity (%)
Beech axial 12	1.79	49.80
Beech axial 13	3.61	27.70
Beech axial 15	4.23	21.52
Poplar axial 3t	4.80	18.67
Poplar axial 7tb	5.04	19.68
Poplar axial 9tb	5.10	19.27
Red oak axial 3	1.95	31.65
Red oak axial 1	3.34	33.16
Red oak axial 15tb	4.81	13.55
Sapele axial 12	2.73	39.40
Sapele axial 14tb	3.74	20.65
Sapele axial 1	5.28	16.06
Beech transverse 5	1.97	43.35
Beech transverse 7	2.03	43.95
Beech transverse 3	2.56	29.75
Poplar transverse 3	2.92	29.95
Poplar transverse 10	2.99	43.53
Poplar transverse 11	4.47	26.27
Red oak transverse 4	2.78	39.49
Red oak transverse 9	3.24	30.26
Red oak transverse 13	3.30	17.43
Sapele transverse 14	2.26	42.05
Sapele transverse 3	2.37	36.48
Sapele transverse 6	2.47	34.67

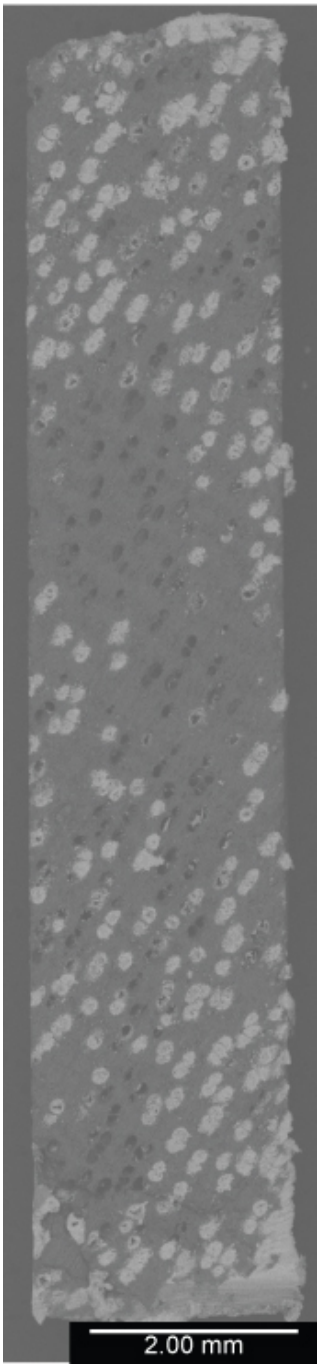

Figure 5.1. Scanning electron micrograph using the backscattered electron detector of a cross-section of a transverse disc of copper plated sapele-based bioSiC.

There are a variety of reasons for the unsuccessful pore filling that is seen in this image. The most obvious is that the filling length of the channels is much greater in the transverse direction than in the axial direction. In the axial direction, the longest dimension that the plating would need to reach is 1.5 mm (half of the 3 mm thickness) whereas in the transverse direction, where the maximum diameter is 12.7 mm, the plating would need to go as deep as 6.4 mm. It is interesting to note that in figure 5.1, the edges have a greater degree of successful plating than the interior of this cross-section. This corroborates well with the idea that longer channels will be more difficult to plate successfully. Channels at the edges have a shorter maximum distance than those in the center of the sample, where the distance approaches the maximum length.

There are many reasons why the longer channel length would lead to less plating efficiency. First, it is possible that some of these pores get choked off at the surface before they are able to fill completely, as discussed in section 3.4.3. In addition, the pores in bioSiC are not straight. Throughout their length they curve in different directions. Figure 5.2(a), a transverse cross-section of sapele-based bioSiC, illustrates several pores that curve and change diameter throughout the length of the sample. As the pores change directions and diameters, there are more opportunities for them to become locally choked off, preventing further exposure to the electrolyte. Figure 5.2(b) shows a red-oak based bioSiC sample that illustrates segmentation that can occur in the long channels. These regions of material between the segments can also lead to premature choking off of the channels. In addition, it is a possibility that some pores that do not traverse the entire length of the sample, are never exposed to the electrolyte, and thus, do not successfully plate.

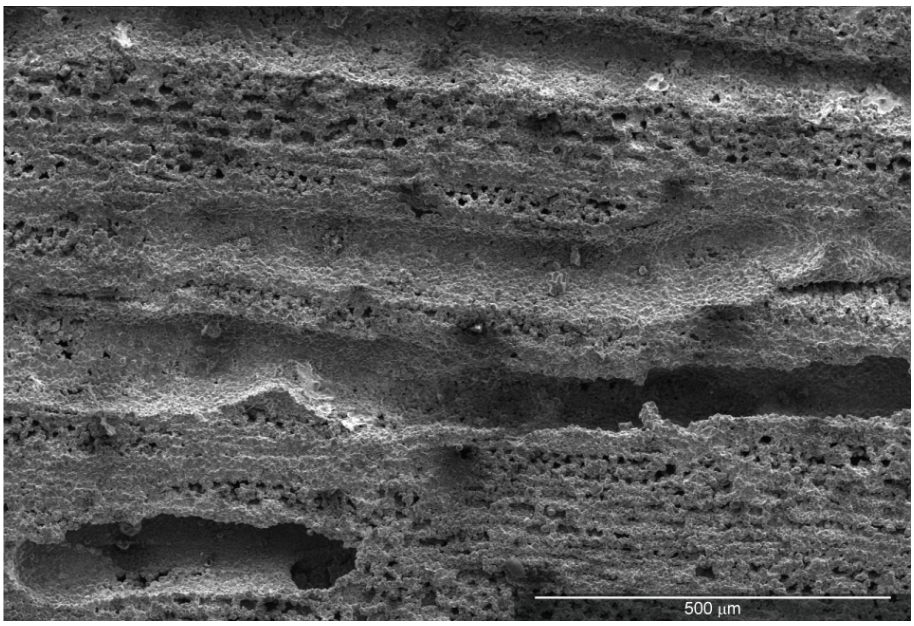

(a)

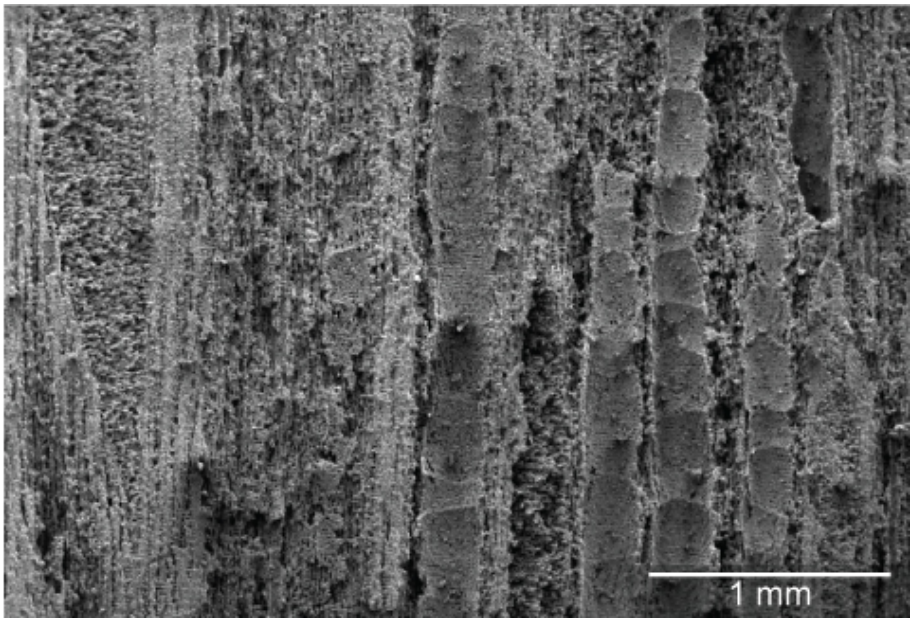

(b)

Figure 5.2. (a) Scanning electron microscope images of sapele and (b) red oak based bioSiC in the transverse orientation illustrating pore channels.

5.1.2.2. Specific Heat. The specific heat was determined for one Cu-bioSiC composite from each of the four wood types using a molybdenum standard. Upon the first measurement in the differential scanning calorimeter (DSC), the samples lost significant weight, indicated by dips in the resulting curve. The largest decrease occurred near 100°C, indicating the loss of water that may have been trapped in the pores. The subsequent, smaller losses, may be due to burning off of remaining polymer and sulfur left from the electrolyte. The first cooling curve, and all other subsequent runs in the DSC did not show any further weight loss, and produced smooth resulting curves. This indicates that the samples would benefit from a heat treatment after electrodeposition and machining, prior to use, to remove any excess electrolyte. The specific heat values are shown in table 5.2 for 0, 400 and 900°C. The range shown encompasses the values for Cu-bioSiC samples from all four wood types.

5.1.2.3. Thermal Conductivity. The thermal diffusivity was determined for three samples of each of four wood types in both the axial and transverse orientation at 0 and 50°C. Figure 5.3(a) shows the thermal conductivity as a function of density for beech-, poplar-, red oak-, and sapele-based bioSiC samples in the axial direction measured at 0°C. Each data point represents one sample. It is clear from this graph that there is a linear relationship between the density and the thermal conductivity in the axial orientation for these Cu-bioSiC composites. Figure 5.3(b) shows the thermal conductivity of these same four wood types in the transverse direction measured at 0°C. These samples all had very similar density and thermal conductivity values, so it is difficult to determine a trend. The values indicate that there is not a large difference from sample to sample in density in the transverse orientation, where the values range from around 2 - 3.5 g/cm^3 compared

Table 5.2. Specific Heat Values for Cu-BioSiC Composites.

Temperature	Specific Heat (J/g°C)
0°C	0.43-0.65
400°C	0.56-0.96
900°C	0.66-1.10

to the axial orientation, where the densities differ from 1.5 - 5.5 g/cm^3. This indicates that, in general, the degree of plating in the transverse direction is equally poor from sample to sample. There is one outlier sample in the transverse orientation that has both a very high density and high thermal conductivity.

The thermal conductivity of poplar-, red oak-, and sapele-based Cu-bioSiC composites in the axial orientation and poplar-based Cu-bioSiC composites in the transverse direction, was measured up to 900°C. The thermal conductivity of poplar-based Cu-bioSiC composites is shown in figure 5.4 as a function of density and orientation. The samples exhibited in this plot had the highest thermal conductivity values in each the axial and transverse orientations of the poplar samples tested. The thermal conductivity of both samples decreases linearly with temperature. The same trend was exhibited in samples derived from red oak and sapele woods. The thermal conductivity is also much greater in the axial than the transverse orientation, which is illustrated in figure 5.4, and can also be seen by comparing the values in figures 5.3(a) and (b).

Figure 5.5 shows the thermal conductivity values at 0°C for sapele, beech and poplar axial and poplar transverse samples before and after high temperature testing. For the majority of samples, there is not a significant change from before and after high temperature testing. Only one sample had changes of greater than 10% at 0°C. Thermal diffusivity measurements were repeated for several of the samples after high temperature testing, and these results also showed a variation of less than 10%. For example, a sapele axial sample had a diffusivity of 0.53 cm^2/sec before high temperature testing. After high temperature testing the diffusivity measured 0.58 cm^2/sec for the first measurement, and 0.53 cm^2/sec for the second measurement. The two post high temperature testing results

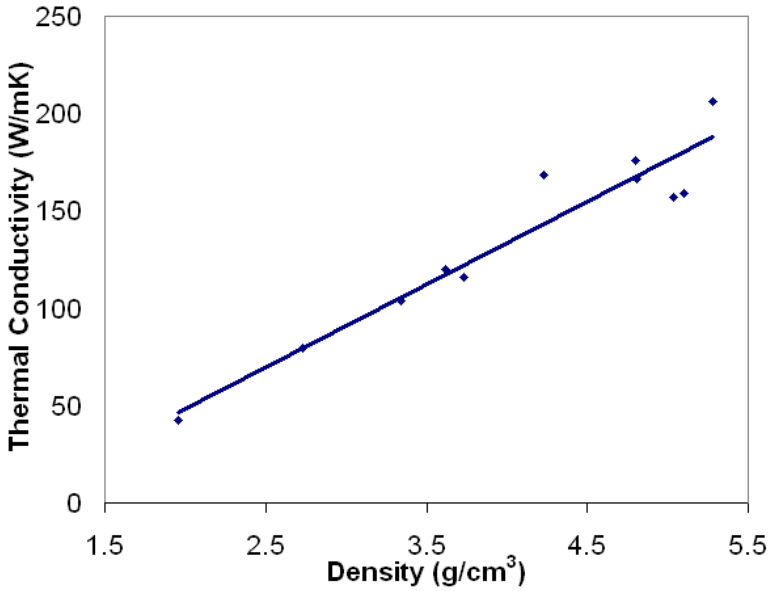

(a)

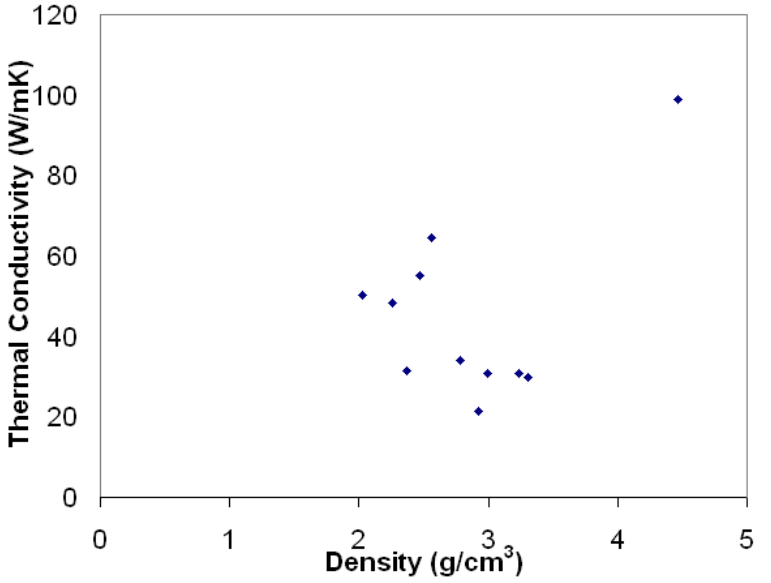

(b)

Figure 5.3. Thermal conductivity of Cu-bioSiC composites derived from beech, poplar, red oak, and sapele woods at 0°C in the (a) axial and (b) transverse orientations.

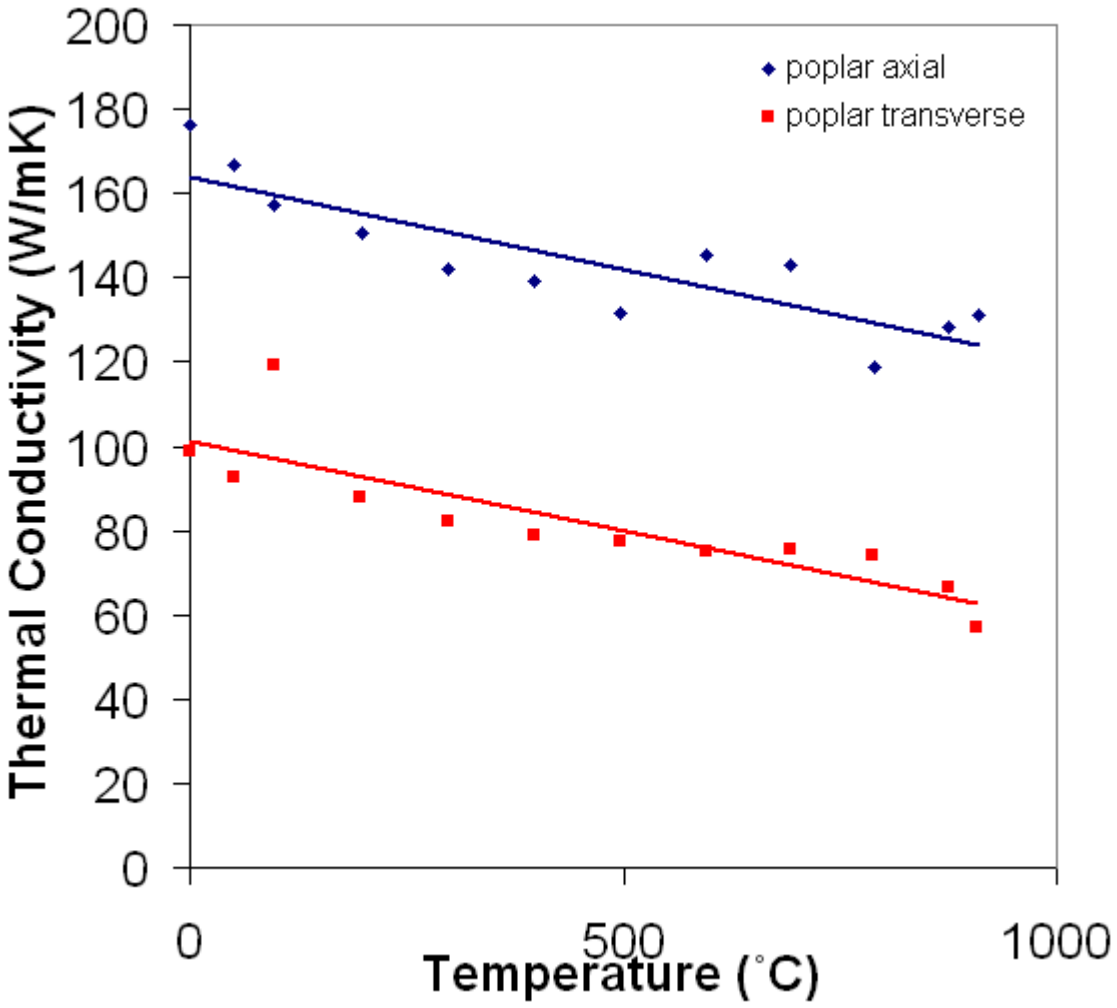

Figure 5.4. Thermal conductivity of poplar-based Cu-bioSiC samples measured from 0-900°C in both the axial and transverse orientations.

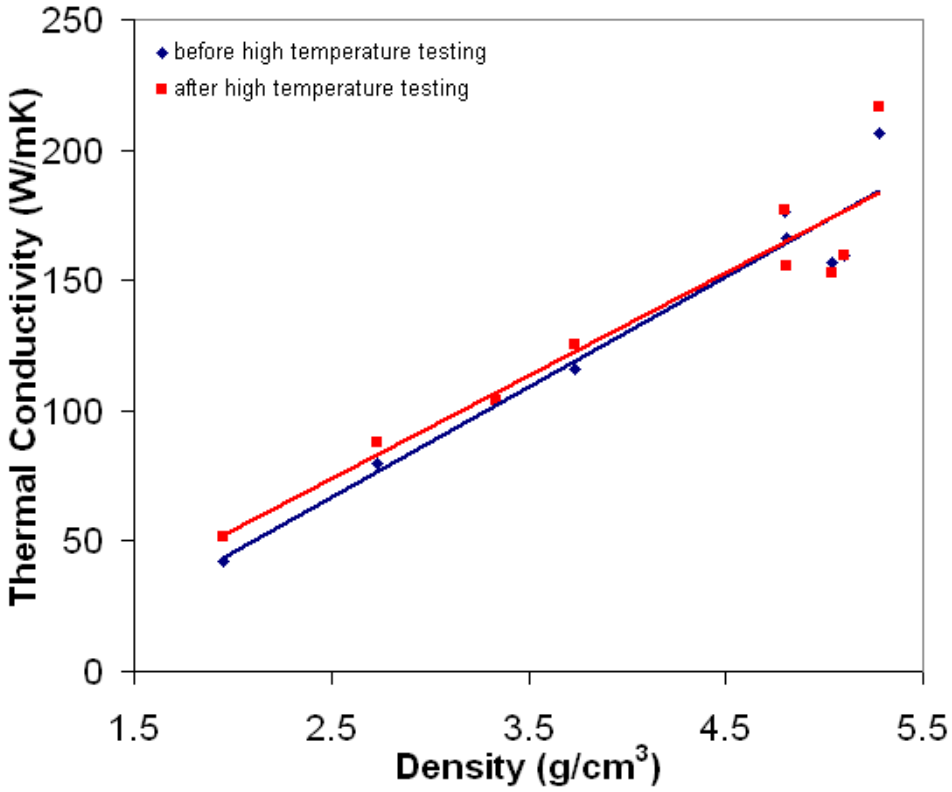

Figure 5.5. Thermal conductivity of samples before and after high temperature testing.

varied by 7.8%, and the values were 10.0% and 1.4% different than the value before high temperature testing, respectively. This indicates that the variations noted between the thermal conductivity values of the samples before and after high temperature testing are within the error of the system. The one sample, red oak axial 3, exhibited changes of 21.2 and 12.5 % at 0 and 50°C, respectively. Given all other results, this indicates that the changes seen are due to experimental variances, such as position in the sample holder, not material changes.

The experimental values at 0°C were compared with theoretical calculations based on models for conductivity of fiber-reinforced composites (equations 2.6 and 2.7) with the appropriate thermal conductivity values for each phase at 0°C. Upper and lower bounds for these models were determined by using the minimum and maximum of all of the measured residual porosity values, respectively. In the axial direction, the porosity was taken into account using a three phase rule of mixtures. In the transverse direction, the Rice model for thermal conductivity of a porous material in the transverse direction, equation 2.4, was used in place of k_m in equation 2.7. These calculated values are plotted along with the experimental values versus the volume fraction of copper in figures 5.6(a) and (b). The volume fraction of copper was estimated by subtracting the volume fraction of porosity for each sample from the volume fraction porosity of the respective bioSiC sample prior to electroplating. In the axial direction, the theoretical values show a similar trend of increasing thermal conductivity with increasing volume fraction of copper. This indicates that this rule of mixtures type equation is a good approximation for the actual thermal conductivity of the sample. In the transverse direction, these theoretical calculations with porosity included provide good upper and lower bounds for the experimental values. The

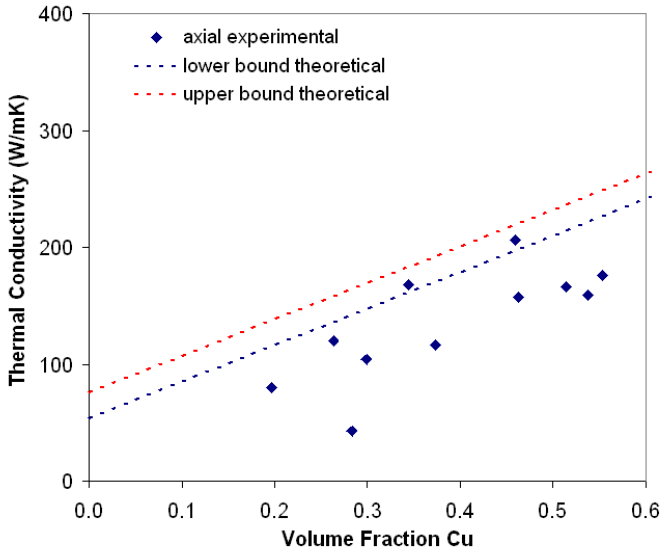

(a)

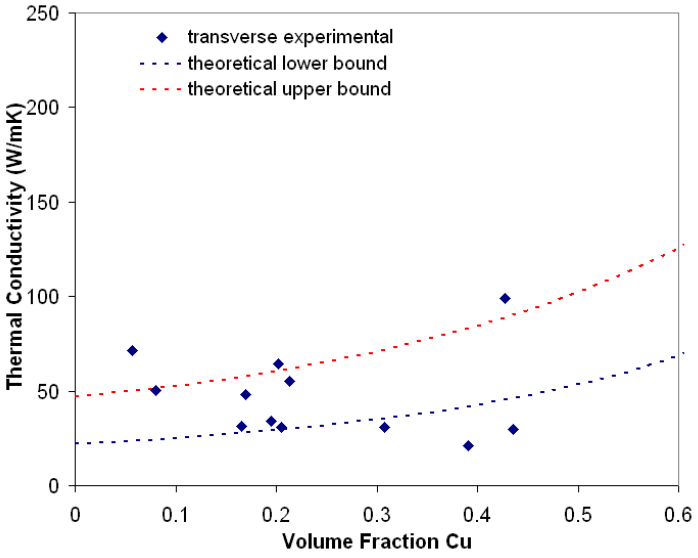

(b)

Figure 5.6. Theoretical thermal conductivity values for composites plotted with experimental values versus volume fraction copper for (a) axial and (b) transverse Cu-SiC composites.[42,86]

inclusion of porosity is important due to the poor plating success in fabrication of these samples. However, it is possible that the theoretical calculations without porosity would predict the thermal conductivity of the well-plated axially-oriented composites if they were to be measured in the transverse direction.

5.1.3. Finite-Element Modeling

Object-oriented finite-element analysis (OOF) was also used to model the heat flux patterns and determine the thermal conductivity of the Cu-bioSiC composites. Meshes similar to those described in section 4.1.3 and in figure 4.5 were created from micrographs of the composite materials. The images were divided into three phases: copper, silicon carbide, and porosity. The appropriate values were assigned to their respective phases. Table 5.3 shows the input values for each phase.

The heat flux distribution throughout the composite samples was studied. Figure 5.7 shows a micrograph of sapele based Cu-bioSiC used for OOF modeling. A one degree temperature gradient was imposed in the axial direction in the sample, and the resulting heat flux distribution is shown in figure 5.8. The dark regions indicate little or no heat flux, which are regions in the image where the conductivity will be low. One of these regions is in between the pores in the direction of heat flow, as circled in blue. This is similar to the heat flux distributions seen in the porous bioSiC samples, and indicates that the heat will travel preferentially through the solid material, and around the pores. This is also true in the composite samples, making it important to fill as many pores as possible with copper to enhance the conductivity. The lightest colored regions, which indicate high heat flux, are where the majority of the heat is present. These areas are found throughout

Table 5.3. Thermal Conductivity Values Used in OOF.[69,124,152]

Phase	k at 0 °C (W/mK)	k at 400°C (W/mK)	k at 900°C (W/mK)
Copper	401	377	342
Silicon Carbide	88	50	35
Pore	0.024	0.033	0.047

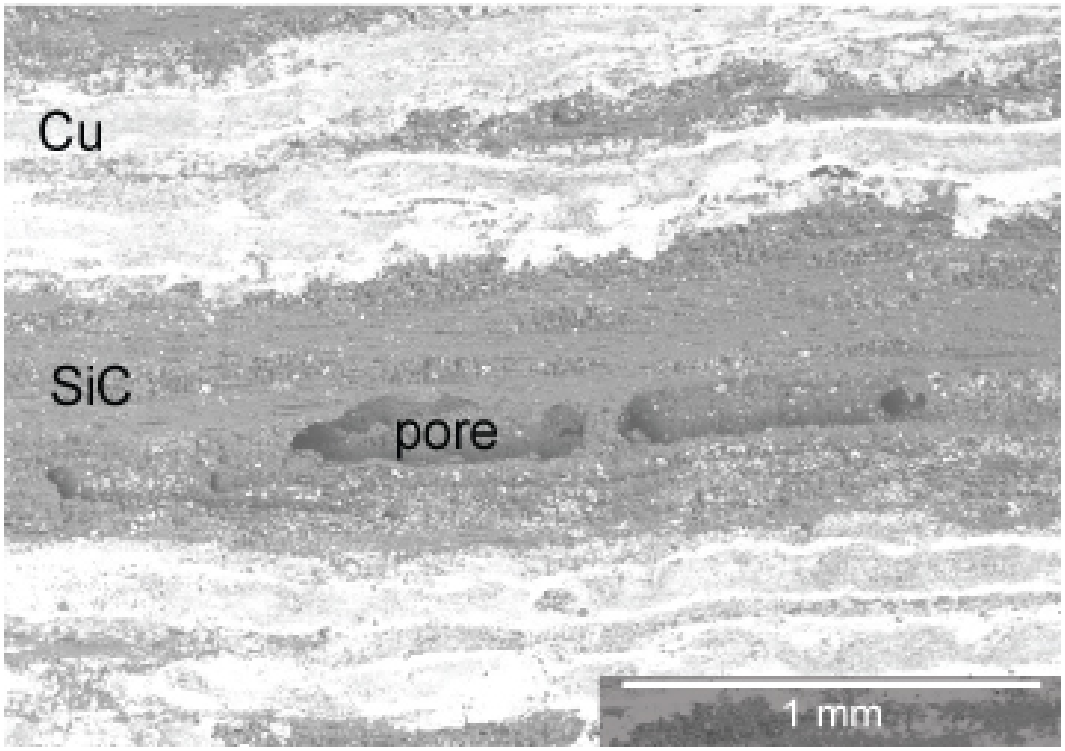

Figure 5.7. Scanning electron micrograph using the backscattered electron detector of sapele-based Cu-bioSiC used for object-oriented finite-element analysis modeling with each phase labeled.

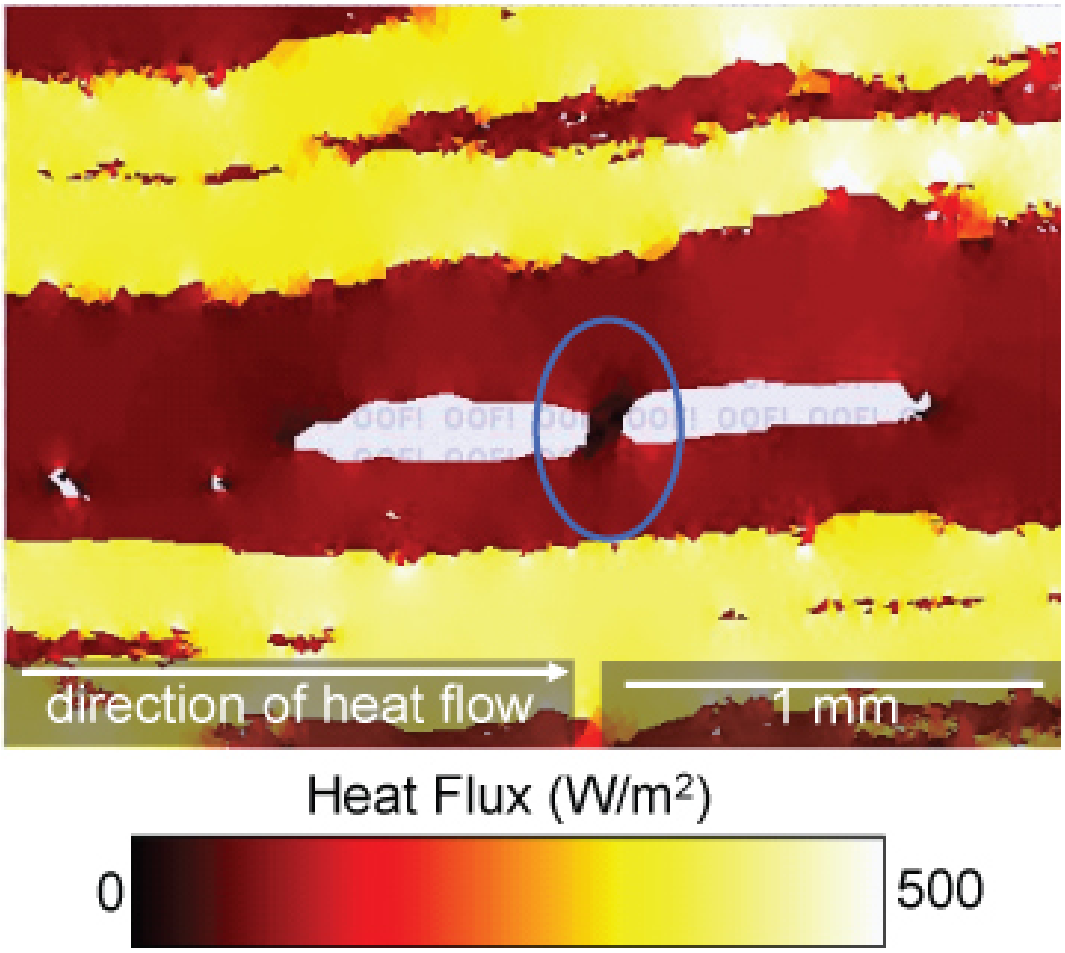

Figure 5.8. Heat flux distribution in sapele-based Cu-bioSiC in the axial direction.

the pores that were successfully filled with copper. This implies that the majority of the heat is transferred through the copper phase, making copper the preferred path through the sample in this direction. Thus, even though the heat will travel locally through the silicon carbide instead of the pore, the majority of heat overall is still transferred by the copper region.

The OOF values for effective thermal conductivity in the axial orientation, much like the experimental values, decrease with increasing temperature, and are significantly higher in the axial than the transverse orientation. In the axial orientation, two meshes of each wood type were used for the thermal conductivity calculations. Image analysis was performed on the images used for meshing, and an area fraction of each phase was calculated. These values were used to estimate the density of each sample from the image. The following equation was used for the density:

$$\rho_{\text{eff}} = (\rho_{\text{Cu}} * \text{V}_{\text{Cu}}) + (\rho_{\text{SiC}} * \text{V}_{\text{SiC}}) \tag{5.1}$$

where ρ_{eff}, ρ_{Cu}, ρ_{SiC}, V_{Cu}, and V_{SiC} are the densities and volume fractions of the composite, copper and silicon carbide phases, respectively. Figure 5.9 shows the effective thermal conductivity predicted from OOF versus density, along with the corresponding experimental results at 0°C. Here it is clear that the OOF results, similar to the theoretical calculations, yield a similar linear trend to the experimentally determined values. With an increase in the sample's overall density, there is a corresponding increase in effective thermal conductivity.

The thermal conductivity and heat flux distribution in the transverse orientation were studied three different ways, depending on the original orientation of the sample, and the

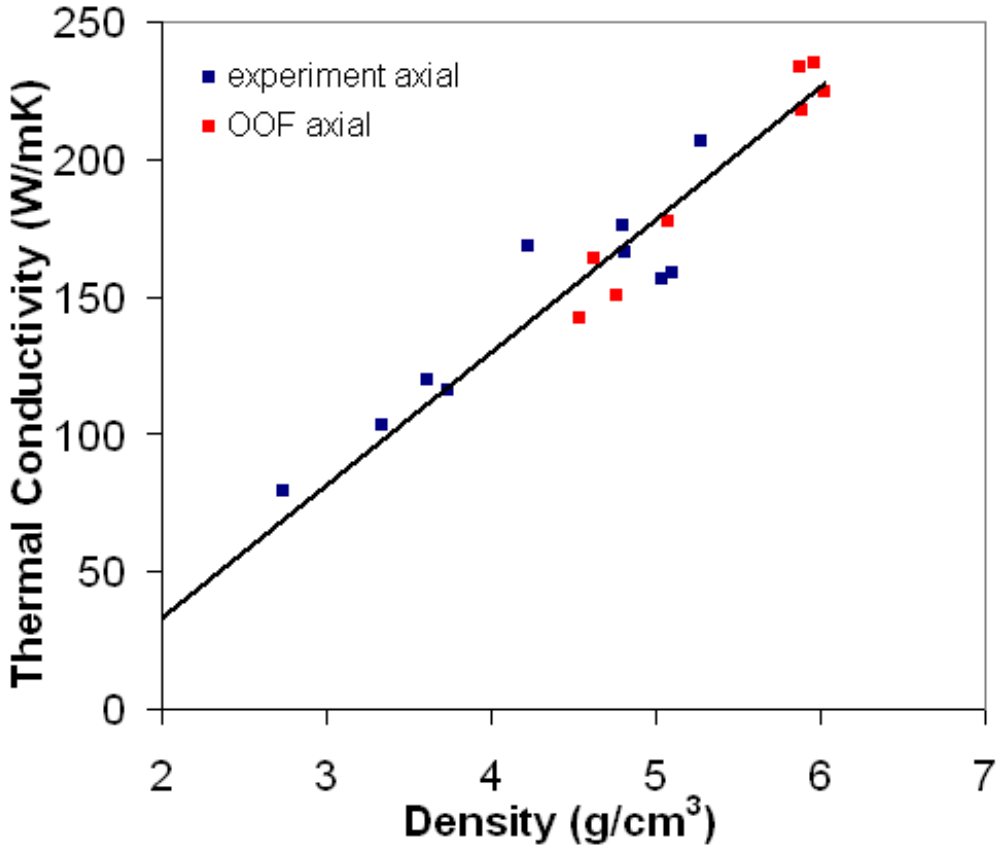

Figure 5.9. Axial experimental and object-oriented finite-element analysis calculated values versus density.

orientation of the cross-sectioned image used for modeling. This was done to compare the three possible scenarios, and to get an understanding of the heat flux in samples that were processed in both the axial direction, and well plated, and the transverse direction, and not well plated. These three configurations are illustrated in figure 5.10. Figure 5.10(I) is the perpendicular direction to the way OOF is modeled in the axial orientation. The image is a transverse cross-section of the sample, and instead of imposing the temperature gradient parallel to the channels, it is done in the perpendicular direction. Figure 5.10(II) shows an axial cross-section of an sample that was oriented in the axial direction during plating. Cross-sections obtained in this way demonstrate the effectiveness of plating of samples in the axial orientation, where the majority of the pores are filled with copper. The third configuration, figure 5.10(III) illustrates an axial cross-section of a sample that was oriented in the transverse direction while plating. This cross-section is characterized by a majority of unfilled pores, indicating the poor plating efficiency in this orientation. For ease of reading, these three configurations will be referred to by I, II, and III for the remainder of this section. The black arrows in the diagram represent the direction of heat flow tested.

A thermal gradient of one degree was imposed in the sapele-based Cu-bioSiC sample used for the axial calculations, but in the transverse direction, using configuration I. The resulting heat flux distribution is seen in figure 5.11. In comparing this with the image of the axial direction in figure 5.8, as the heat approaches a pore, it is similarly diverted through the solid material. This is clearly demonstrated by the large regions of low heat flux, circled in blue, and present on either side of the pore in the direction of heat flow. This is also shown by the regions of extremely high heat flux in between the pores in the

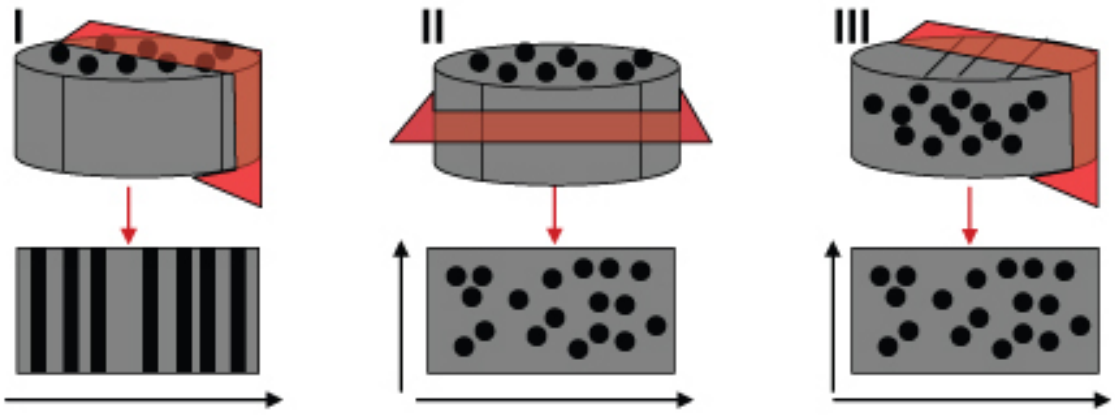

Figure 5.10. Schematic diagrams of the three configurations used to model the transverse thermal conductivity and heat flux distributions in Cu-bioSiC composites.

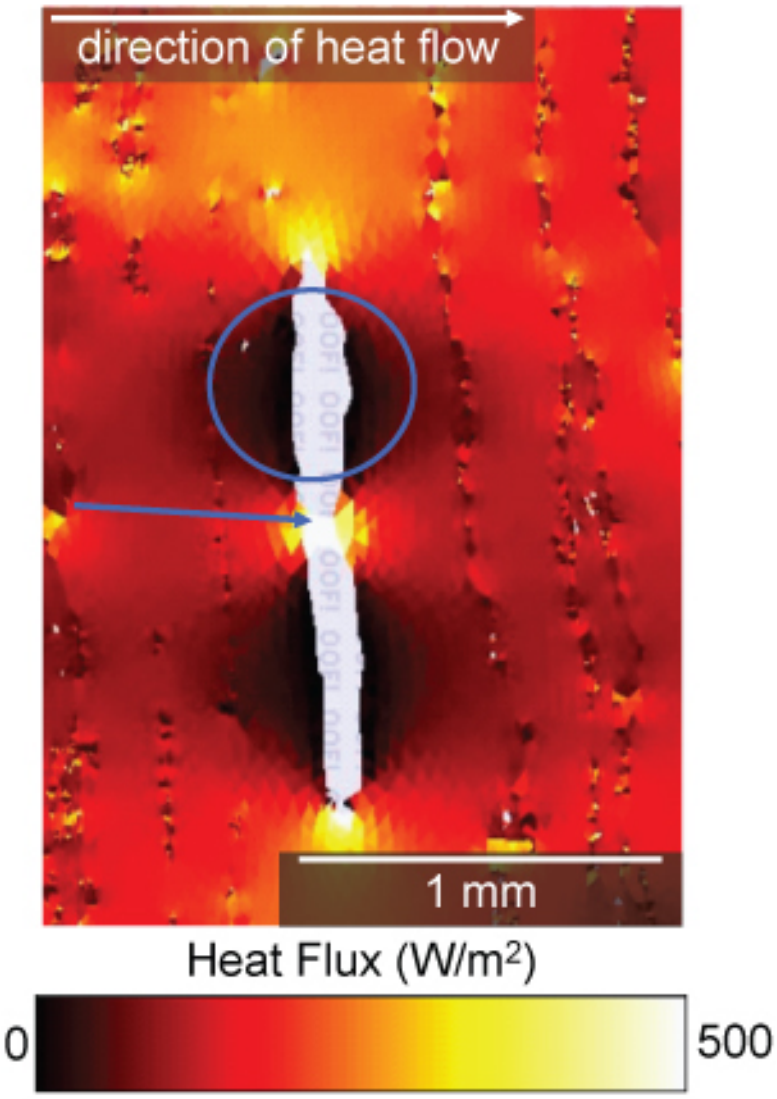

Figure 5.11. Heat flux distribution in sapele-based Cu-bioSiC in the transverse orientation using configuration I.

direction of heat flow, indicated by the blue arrow. These regions indicate that as the heat approaches the region of porosity, it squeezes between the pores, to travel through the higher conductivity solid region. The regions immediately above, below and between the pores are the regions of the highest heat flux in the image overall. Unlike the axial orientation, the Cu phase is not the region of highest heat flux in the transverse direction. In fact, the Cu and SiC phases show similar heat flux distributions in this orientation. This is necessary since heat transfer must occur through bands of both SiC and Cu. This can help to explain why the experimentally determined thermal conductivity values are lower in the transverse direction as compared to the axial direction. The Cu is more successful at enhancing the thermal conductivity in the axial orientation, where there is a direct pathway through the sample in the Cu phase, which does not exist in the transverse orientation of these anisotropic materials.

OOF modeling was also performed on sapele-based Cu-bioSiC images using configuration II. In these samples, similar to the treatment of porous bioSiC samples, the apparent conductivity (k_{app}) was used for the silicon carbide phase conductivity, as seen in table 4.5. Applying a thermal gradient to these meshes gives another estimate of the transverse thermal conductivity and heat flux distribution. Figure 5.12 shows an example of this configuration II axial cross-section used for transverse OOF modeling. An axial disc was sliced to produce this image, and the results will be equivalent to testing this axial disc in the transverse direction. The heat flux distribution after a one degree thermal gradient is imposed on this sample is shown in figure 5.13(a) for the x-direction and figure 5.13(b) for the y-direction. The x and the y directions both represent the transverse orientation. Upon examination of the heat flux patterns in these two images, it is clear that the Cu is

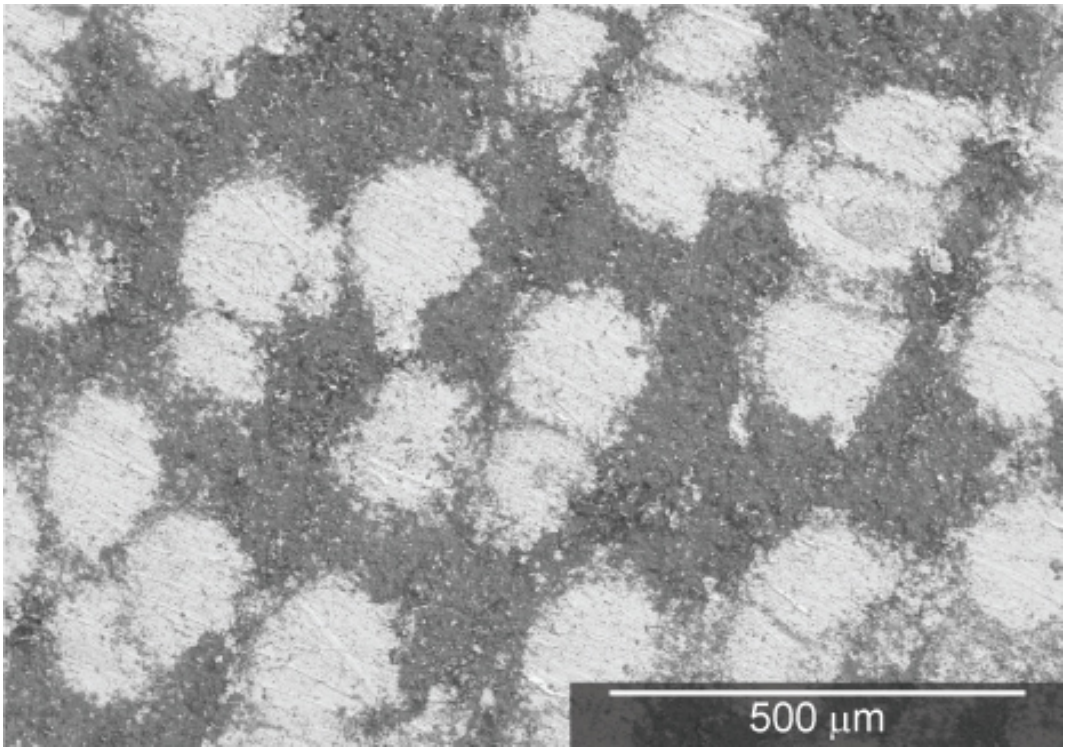

Figure 5.12. Scanning electron micrograph using the backscattered electron detector of a cross-section of an axially-oriented sapele-based CubioSiC used for transverse object-oriented finite-element analysis modeling using configuration II.

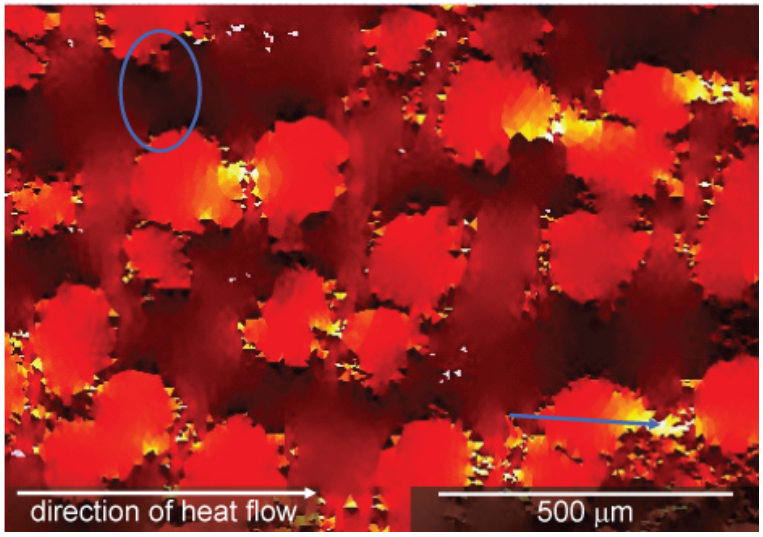

(a)

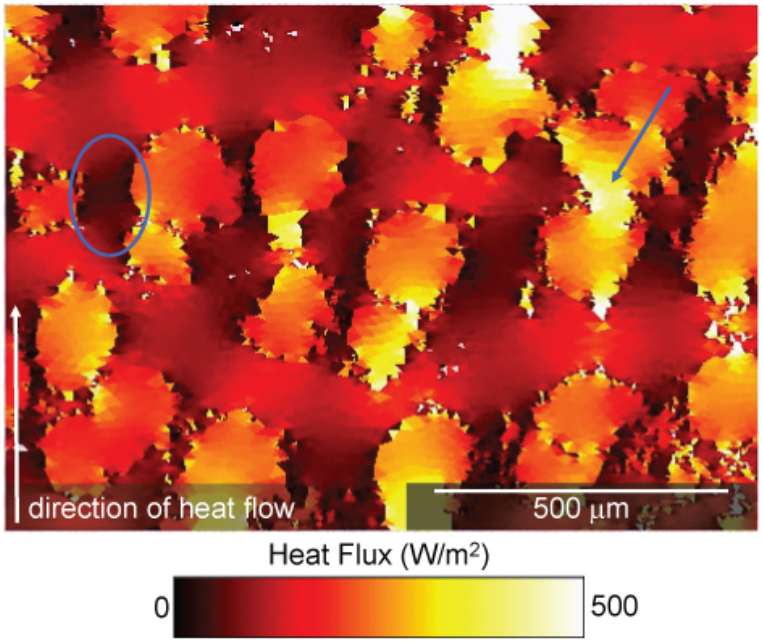

(b)

Figure 5.13. Heat flux distribution of sapele-based Cu-bioSiC in the transverse orientation measured in the (a) x-direction and (b) y-direction using configuration II.

the preferred path for heat flow. This is not as apparent as in the axial orientation (figure 5.8), where the Cu shows a significantly higher heat flux than the other phases and has a continuous pathway through the sample. However, investigation of the Cu-filled pores clearly demonstrate a higher heat flux in the Cu than in the surrounding SiC matrix. Between the pores in the direction of heat flow, the heat flux is very high, indicating that even narrow segments of Cu are forced pathways across the sample. Examples of these are indicated by blue arrows in each of the x- and y-direction heat flux images. In addition, regions between Cu-filled pores in the direction perpendicular to heat flow, exhibit very low heat flux, indicated by darker colors, and circled in blue in each image. Evidence of these very high and low heat flux regions indicate that the heat prefers to traverse the sample through Cu-rich regions implying that the Cu does enhance the thermal conductivity in the transverse direction.

In addition to modeling the behavior of the axially-oriented discs in both the axial and transverse orientations, cross-sections of the transversely-oriented discs were also used to generate OOF meshes, indicated by configuration III. In some cases, these images contained a much higher amount of porosity than the axial cross-sections, due to the greater degree of difficulty encountered when plating samples in the transverse direction. An example of an axial cross-section from a tranverse sapele-based Cu-bioSiC sample is shown in figure 5.14. An example of the OOF modeling of this sample is shown in figure 5.15. These images show that the Cu-filled pores are still the preferred heat transfer path, but as there is much more residual porosity in this image, there are many more areas of lower heat transfer across the sample overall.

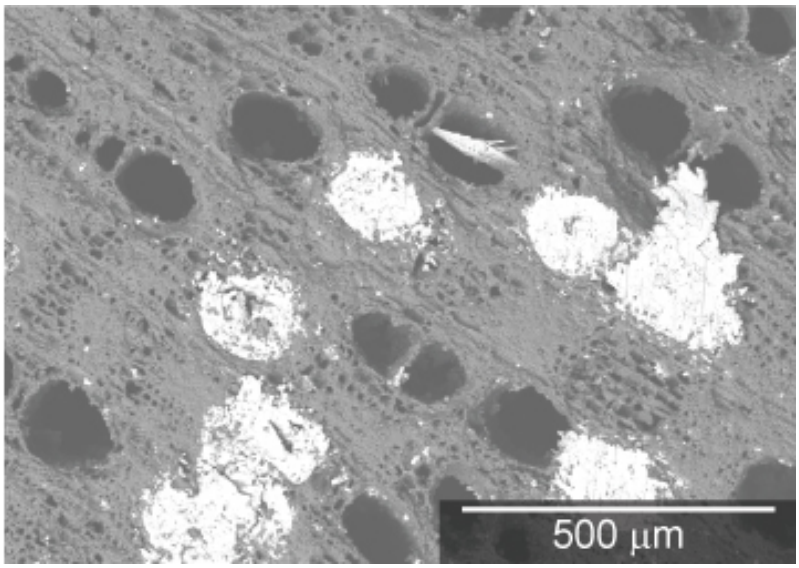

Figure 5.14. Scanning electron micrograph using the backscattered electron detector of an axial cross-section of a transverse sapele-based CubioSiC disc used for object-oriented finite-element analysis modeling using configuration III.

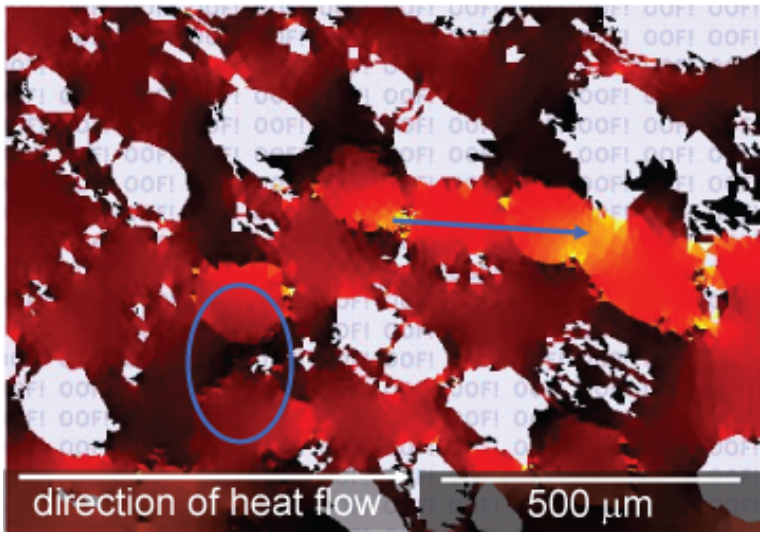

(a)

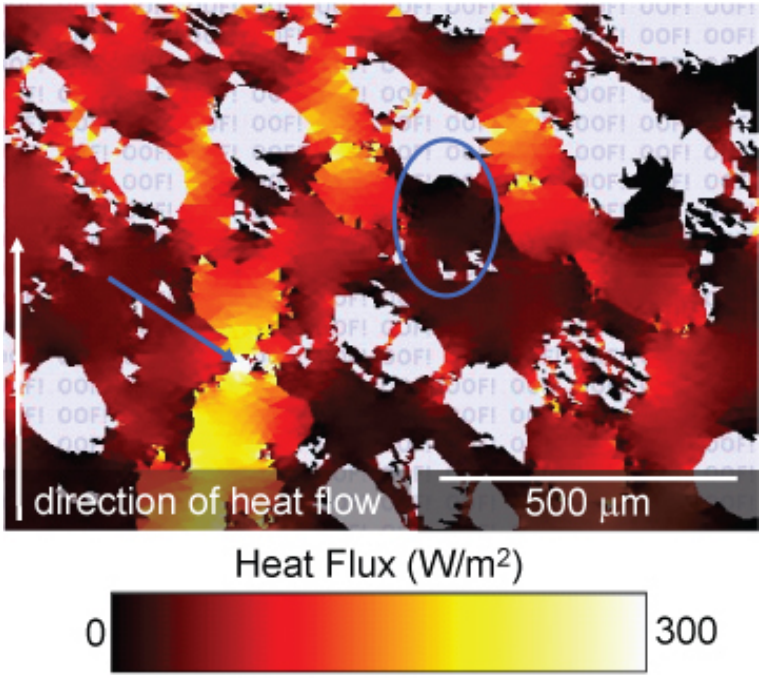

(b)

Figure 5.15. Heat flux distribution of an axial cross-section of a transverse sapele-based Cu-bioSiC measured in the (a) x-direction and (b) y-direction using configuration III.

In most cases for anisotropic bioSiC-derived materials, particularly when using the axial cross-sections (configurations II and III), the two-dimensional images are good representations of the actual samples. However, when using the transverse images (configuration I), the two-dimensional nature of the cross-section becomes limiting, by eliminating the possibility of heat flow in the third dimension. Thus, in the resulting OOF modeling, the heat flux is limited by the lower conductivity of silicon carbide. However, it is clear from using the axial cross-sections (configurations II and III), which give more insight on how the heat is actually traveling through the three dimensions and interacting with each individual phase, that Cu is in fact the preferred pathway. Configurations II and III are both useful for studying their respective material processing conditions. The cross-sections used in configuration II are accurate representations of the heat flux in the transverse direction of samples that were plated in the axial orientation, and have the majority of their pores well filled. Configuration III is a good way to learn about the heat flux distribution in the samples that were plated in the transverse orientation, and have a majority of pores still empty. Thus, configuration III is the most useful to model the Cu-bioSiC samples that were tested in this study.

The difference between the heat flux distributions resulting from configurations II and III are even more apparent when considering the quantitative data, the effective thermal conductivity, calculated from each of these cases. These k_{eff} values are calculated in the same manner as reported in section 4.1.3 for each of the three cases, configurations I-III, as shown in figures 5.11, 5.13, and 5.15. The first two configurations are expected to be similar in value, as the images both exhibit pores that have been well filled with copper. The axial cross-section of the transversely-oriented test sample, configuration

III, shows much more porosity, and thus, should exhibit a lower thermal conductivity value. A bar chart comparing the experimentally determined and OOF-calculated values for sapele-based Cu-bioSiC in the transverse orientation is shown in figure 5.16. It is clear from this chart that the two effective conductivities from configurations I and II show much higher values than that from configuration III or the transverse experimental values. These k_{eff} values from configurations I and II should be better estimates for the thermal conductivity of the well-plated axial samples tested in the transverse orientation. The lower, configuration III value, is comparable to the actual experimental results.

Poplar-based Cu-bioSiC composites were the only samples tested at high temperature in the transverse orientation. OOF was used to model the thermal conductivity up to 900°C to compare with the experimental data. The effective poplar thermal conductivity was calculated by OOF for the same three cases, configurations I, II and III. These results, plotted along with the experimental data for the particular poplar transverse sample that was cut for an axial cross-section, are shown in figure 5.17. As experimentally determined and finite-element analysis predicted, the thermal conductivity decreases with increasing temperature. The OOF calculations from configurations I and II both overestimate the experimental values. However, the values determined from configuration III match quite well with the experimental results for this poplar sample. Both the OOF values from configuration III and the theoretical calculations considering porosity take into account the poor degree of plating in the sample, and thus, better match the experimental results. This indicates that configuration III is the most appropriate method to use for the samples fabricated in the transverse orientation, and that OOF is successful at modeling the k_{eff} values from the actual sample microstructure.

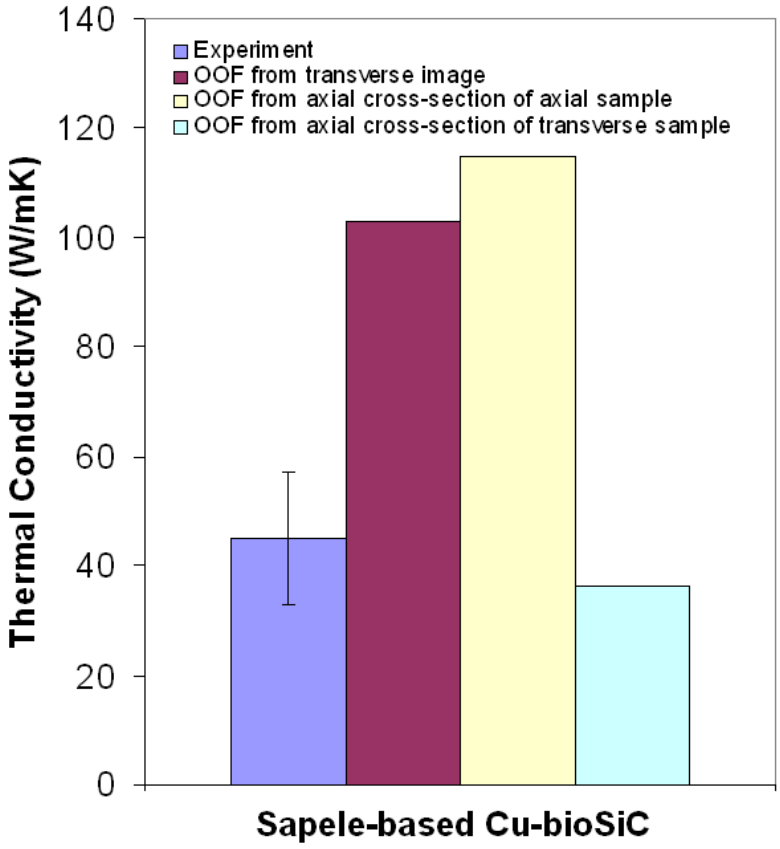

Figure 5.16. The thermal conductivity as determined experimentally and by object-oriented finite-element analysis for sapele-based Cu-bioSiC samples at 0°C in the transverse orientation.

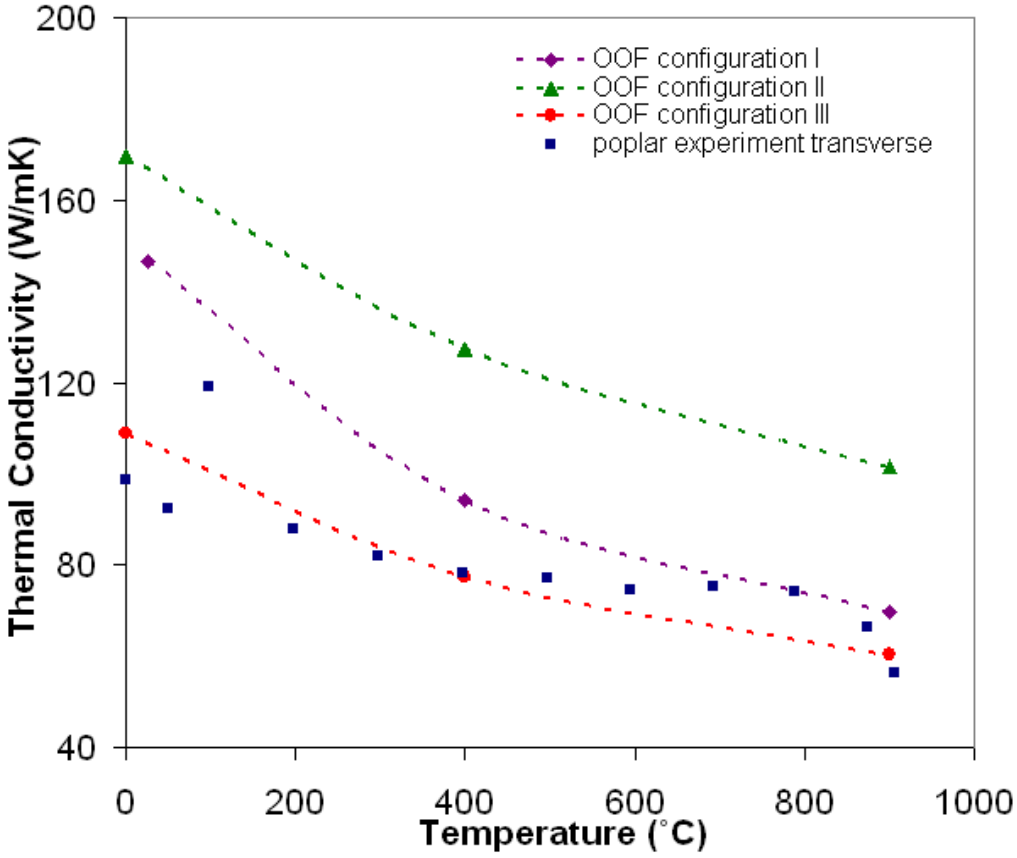

Figure 5.17. Thermal conductivity of poplar-based Cu-bioSiC composites measured in the transverse direction experimentally and modeled three ways using object-oriented finite-element analysis.

OOF modeling provides a clear understanding of how the heat is being transferred throughout the sample. These results indicate that copper is, in most cases, the preferred path for heat flux. OOF is able to model the effective thermal conductivity well in the axial orientation as a function of density, following a similar trend to the experimental data. In the transverse orientation, the effective thermal conductivity is predicted well from the OOF modeling of the cross-sections of the transverse samples. The appropriate configuration, II or III, should be used based on the orientation during sample processing for the most accurate OOF thermal conductivity and heat flux distribution predictions. Overall, OOF-based modeling is a successful method of modeling effective thermal conductivities for materials made from complex microstructures like bioSiC.

5.2. Thermal Expansion Coefficient

The coefficient of thermal expansion (CTE) of one composite sample, sapele-based Cu-bioSiC in the axial orientation, was measured. This sample had a volume fraction of copper of 31%. The testing was done by the Orton Ceramic Foundation at a heating rate of 3 degrees per minute to 1000°C in argon. The resulting CTE was determined by fitting a polynomial equation to the curve, and evaluating the derivative at specific temperatures. It was found to be 6.98 x 10^{-6} at room temperature and 7.43 x 10^{-6} at 100°C. This value is slightly less than the average between the copper and silicon carbide CTE values of 16.5 and 3.3 x 10^{-6}, respectively.[143,144] While this value is still not as low as values reported for silicon substrates (2.6 x 10^{-6} [143]) it still shows improvement and the possibility of lower thermal expansion mismatch between the two parts in microelectronics applications. This experimentally determined value is also lower than that reported in

the literature by Shu et al. They produced composites sintering copper powder with SiC particles coated by copper electroless plating, and found CTE values of 8.0-11.2 x 10^{-6} at 100°C for samples with a similar volume fraction of copper.[73]

The resulting experimentally determined value is shown in figure 5.18 with the theoretical calculations for CTE in the axial and transverse orientations based on equations 2.9 and 2.10.[42] It is clear that the experimental value does not lie on either the axial or transverse theoretical curve for its volume fraction of copper of 31%. This variation from theory can be due to the fact that the channels in bioSiC are not perfectly straight and would not be expected to fit the axial value perfectly. However, the value does lie in between the boundaries of axial and transverse samples, indicating that these theoretical values can be used as upper and lower bounds for the CTE of Cu-bioSiC composites.

5.3. Summary

The thermal conductivity of copper-biomorphic silicon carbide composites was found to increase linearly with increasing density in the axial orientation, which was in agreement with both theoretical calculations and object-oriented finite-element analysis. A maximum thermal conductivity of 207 W/mK at 0°C was achieved. The thermal conductivity was also higher in the axial orientation than in the transverse orientation. This is in part due to the inefficiency of electrodeposition in the transverse orientation. Object-oriented finite-element analysis was used to determine the heat flux distributions and calculate effective thermal conductivities in both ideal samples with the majority of pores filled, and in actual transverse microstructures that had a high level of remaining porosity. These results indicated that the conductivity would still be lower in the transverse

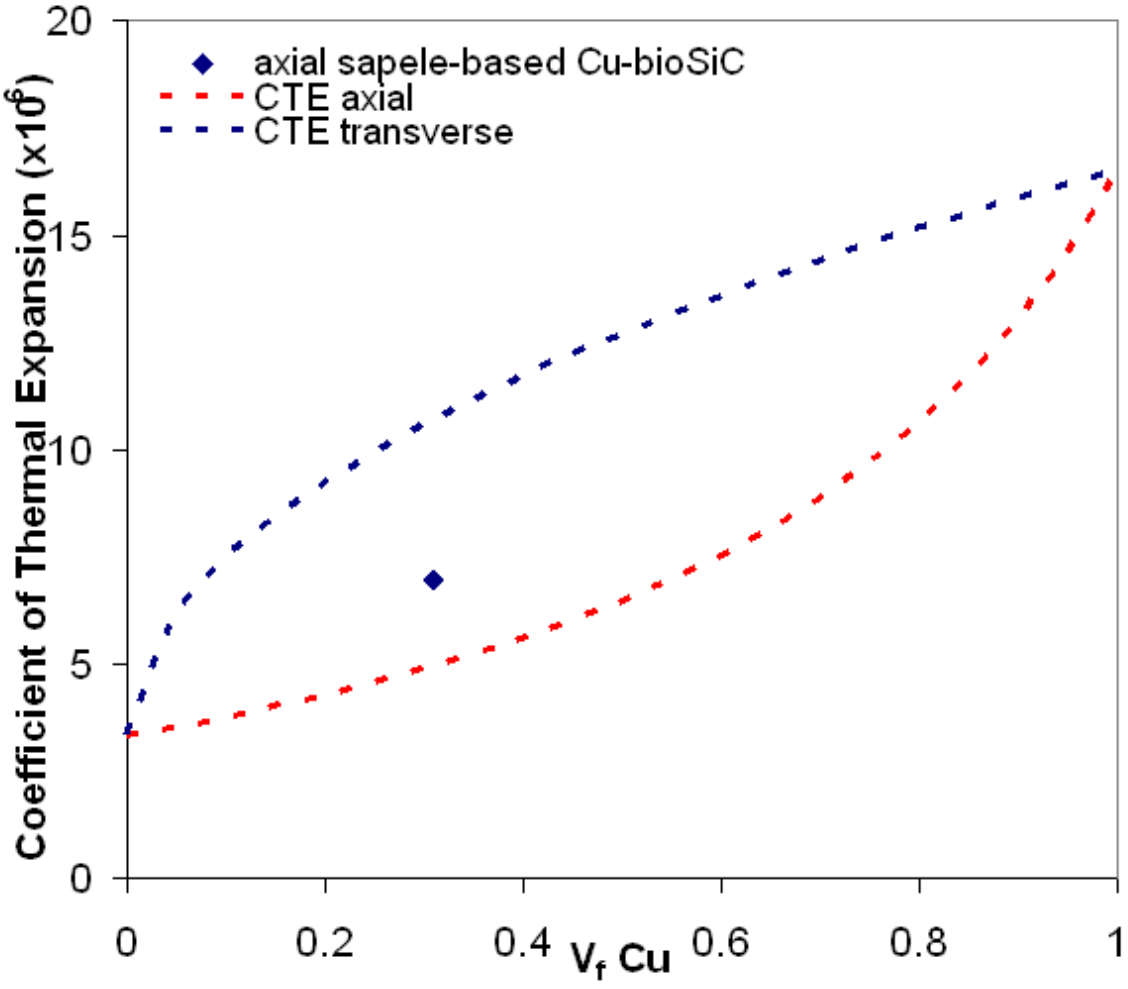

Figure 5.18. Coefficient of thermal expansion of axial sapele-based Cu-bioSiC and theoretical coefficient of thermal expansion values in both the axial and transverse orientations.[42]

orientation, even if the samples were plated fully, due to the absence of a direct copper pathway through the sample. The room temperature thermal expansion coefficient was determined to be 6.98 x $10^{-6}/^{\circ}$C, which was between the axial and transverse theoretical calculations for the CTE. The high thermal conductivity and low thermal expansion coefficient make this composite material viable for thermal management applications.

CHAPTER 6

Summary and Future Work

6.1. Summary

Porous carbon was made from five wood precursors by pyrolyzation at five different temperatures ranging from 300-1200°C. These carbon materials were studied using porosimetry, X-ray diffraction, Raman spectroscopy, thermal diffusivity, and transmission electron microscopy. It was determined that the morphology of these carbon materials did not differ with increasing pyrolyzation temperature, and the resulting electron diffraction patterns showed only evidence of an amorphous structure. However, after investigating the samples further using X-ray diffraction, Raman spectroscopy and thermal diffusivity results, there was evidence of a slight increase in long-range order with pyrolysis temperature.

Silicon carbide was successfully fabricated from these porous carbon materials. These silicon carbide materials were studied using porosimetry, transmission electron microscopy and thermal diffusivity. As in the carbon samples, the morphology of the silicon carbide materials did not vary with increasing carbon pyrolyzation temperature. In addition the thermal conductivity remained constant, unlike the thermal diffusivity of the carbon samples, which changed with increasing pyrolysis temperature. This implies that the silicon carbide is independent of the initial carbon pyrolysis temperature, because during

the infiltration step, the carbon is exposed to temperatures of 1500°C and pyrolyzed further before the SiC forming reaction occurs.

Thermal properties of porous bioSiC material made from five wood precursors were also studied. The thermal conductivity in the axial orientation was higher than that of the transverse thermal conductivity for most samples. However, ring-porous wood-based bioSiC displayed a larger degree of anisotropy than diffuse-porous wood-based bioSiC. The thermal conductivity was found to decrease with increasing temperature and porosity for both orientations. The thermal conductivity of the axially-oriented samples decreased linearly with increasing porosity, while that of the transversely-oriented samples decreased non-linearly. This was due to the higher degree of anisotropy in the ring-porous materials compared to the diffuse-porous materials. The transverse thermal conductivity was studied using object-oriented finite-element analysis (OOF). From this model, effective thermal conductivity values were found to agree well with the experimental values. The heat flux distributions throughout the samples were illustrated, indicating that the solid silicon carbide phase was the preferred path of heat flow instead of the porous regions. The properties of the bioSiC samples are tailorable depending on the initial wood precursor selected. For a more thermally insulating material, a transversely oriented, highly porous sample, such as poplar, may be the most desirable wood-based bioSiC.

Thermal shock resistance was also studied in porous silicon carbide derived from wood. The samples were quenched from a 1400°C furnace to an oil bath at room temperature. The sonic velocity of the samples was determined before and after up to five thermal shock cycles. The sonic velocity did not decrease as a result of thermal shock conditions. However, initiation of millimeter-sized cracks was evident due to microscopic investigation.

OOF modeling was used to validate the sonic velocity measurements, indicating that the newly formed cracks did not have a significant contribution to the effective modulus measurement of the sample, and thus, should not have a significant effect on the sonic velocity.

Copper-biomorphic silicon carbide composites were fabricated from four wood precursors using electrodeposition. Since electrodeposition is a room temperature process, the copper-silicon carbide reaction that occurs when copper is in the molten phase is avoided. This prohibits the undesirable copper silicide phase from forming and degrading the thermal properties of copper. The electrodeposition technique was successful in filling the majority of the larger porosity in the axial orientation of four types of bioSiC. The smaller, fiber cell-based pores remained unfilled in all wood types. The transverse orientation had less success in plating due to the long channels in the transverse direction that are not straight, leading to premature choking off of pores from the electrolyte.

The thermal properties of these Cu-bioSiC composites were also measured. The thermal conductivity of the axially-oriented Cu-bioSiC composites increased linearly with increased composite density and decreased with increased temperature. Samples in the axial orientation had significantly higher thermal conductivity values than those in the transverse orientation, but the degree of anisotropy of the samples is masked by the low plating efficiency, leading to much lower values than expected if fully plated samples were tested in the transverse direction. OOF was also used to model the thermal conductivity of these composites. In the axial orientation, the OOF models matched well with the experimental data, demonstrating linear increases in conductivity with increasing density. The copper was shown to be the preferred path of heat through the samples, leading to

the high thermal conductivity values. In the transverse orientation, the OOF effective values and heat flux distributions were calculated using three geometric configurations. Configuration III, which was using an axial cross-section of the center of these transverse samples, was the most appropriate method for the matching the experimentally determined values of the transversely-oriented plated samples. Configuration II, which used an axial cross-section of the axially-oriented plated samples, gives a good indication of the expected thermal conductivity of well-plated samples tested in the transverse direction. The heat flux distributions show that, similarly to those tested and modeled in the axial orientation, the copper is the preferred path of heat conduction due to its higher thermal conductivity, but the copper is less effective than in the axially-oriented samples because there are no continuous copper pathways in the transverse orientation. The thermal expansion coefficient of Cu-bioSiC was determined to be 6.98 x $10^{-6}/^{\circ}$C at room temperature, which lies between the theoretical values of copper and silicon carbide. For a high heat dissipation material, the most desirable wood choices would be sapele or poplar, which both exhibited the greatest degree of successful plating, as well as the greatest enhanced thermal conductivity values.

6.2. Conclusions

Porous silicon carbide derived from wood was fabricated successfully from carbon pyrolyzed at several different temperatures. The thermal conductivity was found to vary

with porosity, pore size, and, perhaps most importantly, with pore distribution. Object-oriented finite-element analysis (OOF) was successfully used to model heat flux and thermal conductivity in these complex microstructures. Thus, it is possible to select an appropriate wood precursor to create bioSiC samples with a desired thermal conductivity. The thermal shock resistance of these materials was also studied. Catastrophic failure was never seen in bioSiC samples quenched from 1400°C up to five times. The tailorable thermal conductivity and high thermal shock resistance of these bioSiC materials implies that they have the potential to perform well in environments where extreme temperature gradients can be expected.

Cu-bioSiC composite materials have been successfuly fabricated at low temperature using electrodeposition to fill pores in the porous bioSiC scaffold. Silicide formation was suppressed up to an operating temperature of 1000°C. Enhanced thermal conductivity was seen as a result of composite formation. Maximum thermal conductivities of Cu-bioSiC of up to 207 W/mK at 0°C and 178 W/mK at 900°C were achieved in the axial orientation. OOF was successfully used to analyze the heat flux distribution and calculate effective thermal conductivities. Copper has a more significant influence on the heat flux and thermal conductivity in the axial orientation than in the transverse orientation. The CTE of Cu-bioSiC composites at room temperature was found to be 6.98 x 10^{-6}/°C. Due to their improved thermal properties, Cu-bioSiC composites have potential uses in electronic packaging and other thermal management applications.

6.3. Future Work

6.3.1. Electrodeposition

It was shown that in the axially-oriented Cu-bioSiC samples, the plating was quite successful, and the majority of pores in the samples were filled with copper. However, the majority of the fiber cell-sized pores, around 2-3 μm, remained unfilled, leaving a significant amount of porosity, which limits the maximum thermal conductivity that can potentially be achieved in such samples. There is much work in the literature regarding plating efficiency of small channels, many with diameters much smaller than that of bioSiC pores. Kelly and West studied the filling ability of 200 nm trenches with several electrolyte solutions.[80] They used silicon substrates, patterned with a seed layer of copper. The filling percentage increased from 10% in a solution containing solely PEG and Cl, to 53% by adding bis(3-sulfopropyl) disulfide (SPS), to 81% by adding both SPS and Janus Green B (JGB). They found that the most improvement was made when the four additives were all used, and the majority of trenches were filled at 15 mA, as opposed to 20 mA. This implies that altering the additives in the electrolyte solution can have an impact on the plating success. In addition, a lower applied current, leading to slower plating, may allow the plating to fill more of the pores before they are choked off. A draw back may be that it would take longer to fill the larger pores if the current is decreased. Another potential variation is to remove the outer electrodeposited layer periodically throughout the process, either by sanding or polishing the surface prior to reinfiltration, or reverse plating. This will allow reopening of the choked off pores, allowing them longer exposure to the electrolyte and potentially improving plating.

The transversely-oriented samples, contrary to the axially-oriented samples, did not show as much plating success. As discussed in section 3.4.3, the majority of the deep trenches in the transverse orientation remained unplated, and the thermal conductivity of these composites did not show significant improvement. The PEG addition to the electrolyte assists in lowering the surface tension of the electrolyte, allowing it to reach further into the pores. However, the surface tension may need to be lowered further in order to reach the deeper trenches in the transverse orientation. In addition, there is a large amount of plating variation from sample to sample. Figures 6.1(a) and (b) show two poplar-based bioSiC samples plated in the transverse orientation. It is clear that figure 6.1(a) has plated with significantly more success than figure 6.1(b), even though both were exposed to the same processing conditions. Thus the issue of the natural variation from sample to sample will need to be addressed in order to create a processing protocol that is equally efficient for every sample.

Only two parameters were optimized in this electrodeposition study, which are the number of reinfiltration steps throughout the plating and the length of electroplating duration. The content of the electrolyte solution and the applied current are two variables that can use optimization to improve the plating of both the trenches with smaller diameters and the deeper trenches, as well as to work towards a more homogeneous plating in order to eliminate specimen to specimen variation.

6.3.2. Carbon Study

Transmission electron microscopy was used to study the morphology and structure of amorphous carbon samples at two pyrolysis temperatures. Further TEM studies could

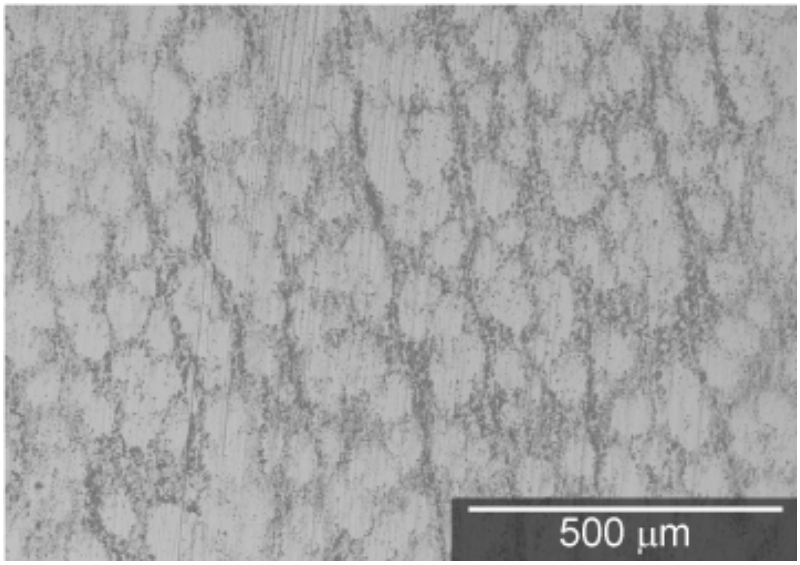

(a)

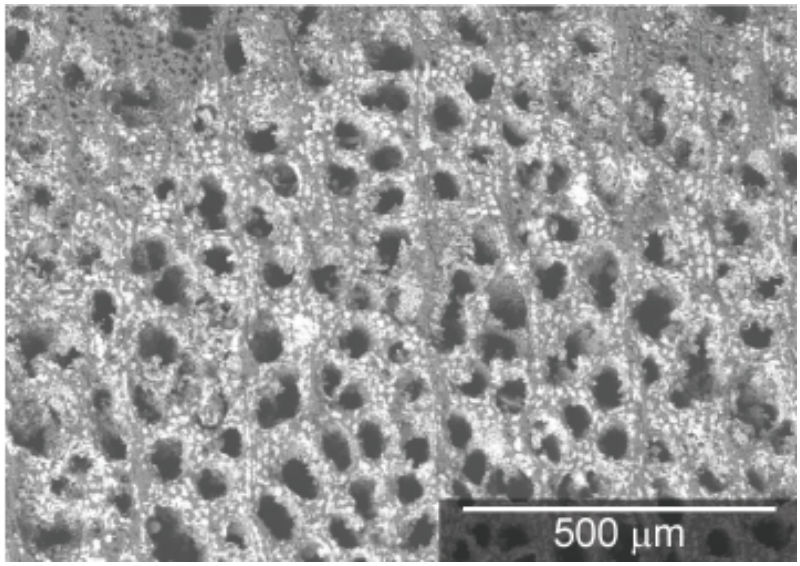

(b)

Figure 6.1. Poplar transverse Cu-bioSiC composites that plated (a) well and (b) poorly under the same processing conditions.

be carried out on the turbostratic carbon, which is formed after pyrolyzation of 2400°C. It is apparent from both the X-ray diffraction and Raman studies that the conversion to turbostratic carbon shows increased crystallinity indicated by the early stages of a sharp peak at $2\theta = 26°$, which is very close to the $2\theta = 26.5°$ of pure graphite. The electron diffraction patterns and the high resolution transmission electron microscopy images could be obtained to investigate evidence of long-range order in the material. This would manifest itself in crystallinity present in the electron diffraction pattern or any ordered appearance of the HRTEM image.

In addition, wood can also be converted into graphite using a nickel-based catalyst.[154] TEM work on this bulk material can be performed to take a closer look at the graphitic structure with electron diffraction and HRTEM to compare to the turbostratic carbon, as well as the carbons pyrolyzed at lower temperatures. These graphitic carbon specimens can then be filled with copper, either through electrodeposition or melt infiltration, and have potential for higher thermal conductivity than the Cu-bioSiC composites, due to the very high thermal conductivity value of graphite.

6.3.3. Thermal Property Characterization

Due to time constraints and equipment malfunction, only one Cu-bioSiC sample was able to be tested using a dilatometer to determine the thermal expansion coefficient. A representative sample of sapele-based Cu-bioSiC in the axial orientation, which had a high density and a high thermal conductivity, was chosen. This sample had a thermal expansion coefficient of 6.98×10^{-6}, which fell between the theoretical calculations for axial

and transverse fiber-reinforced composites. It will be useful to test other wood-based Cu-bioSiC composites in the axial orientation, in order to compare the thermal expansion coefficient as a function of volume fraction of copper. In addition, in this study, samples in the transverse orientation were not tested, because due to poor plating efficiency, they would not give a good representation of a composite value. When a successful transverse sample is fabricated, testing the transverse thermal expansion coefficient and comparing it both to the axial experimental values and the fiber-reinforced composite model values would be interesting.

6.3.4. Thermal Shock

Although the bioSiC samples withstood the thermal shock resistance experiments quite well, and did not fail catastrophically, there was evidence of crack initiation. Even though this crack initiation was not detected by the sonic velocity measurements, crack initiation implies that there was some change in the samples as a result of the introduction of these thermal stresses. Thus, a different damage characterization technique is necessary in order to successfully determine what is going on. Acoustic emission (AE) has been used to monitor crack initiation for thermal shock testing.[155] AE transducers were attached to quenching baths of either oil or water. Signals from each crack initiation were amplified and the duration, energy, and amplitude for each AE event were recorded. The number of events was determined for each ΔT value tested, and the number of AE events increased as samples began to catastrophically fail. Thus using acoustic emission to detect crack initiation events in bioSiC might prove useful in a more quantitative determination of the thermal shock resistance.

6.3.5. BioSiC Characterization

X-ray diffraction studies have confirmed the complete removal of residual silicon as a result of the etching samples in an HNO_3 and HF solution. However, it would be interesting to further confirm this removal by investigating the grain boundaries further to see if any residual silicon may remain there. This can be done by using HRTEM images to investigate the grain boundaries. EDS would not be particularly useful, in that the carbon is not easily detected by EDS, and so SiC appears as Si. However, taking electron diffraction patterns at the grain boundaries would confirm if the only phase present there is SiC, or if there are small trace quantities of residual Si.

6.3.6. Thermal Expansion Coefficient

The coefficient of thermal expansion was studied for porous bioSiC using a thermomechanical analyzer (TMA). It is also possible to use high resolution X-ray diffraction in order to determine the CTE. The sample can be heated up and the lattice parameter measured at different temperatures. From these measurements, the linear expansion as function of temperature, and thus the CTE of the material can be determined. This can provide an atomic scale determination of the expansion behavior of the material, and the expansion in different planes and orientations can also be determined, and may provide more consistent results than those from the TMA.

6.3.7. Three-Dimensional Finite-Element Analysis

In order to obtain even more information about the heat flux distributions in the bioSiC and Cu-bioSiC materials, a three-dimensional finite-element model would be useful. Using a microstructural based finite-element model is crucial for the complex microstructures of wood-based materials. X-ray computed microtomography has been performed on bioSiC samples, yielding three-dimensional reconstructions of the microstructure.[156] Using either the three-dimensional version of OOF, which is currently in progress, or another microstructural based meshing system, such as Amira, a three-dimensional mesh can be created. Then, a thermal gradient can be applied across the sample, and the resulting effective thermal conductivity values and heat flux distributions can be studied. This method has the potential to provide valuable information regarding the influence of porosity and composite phases on the heat flow throughout these bioSiC and Cu-bioSiC materials in all three dimensions.

6.3.8. Composite Residual Stresses

Due to the high thermal expansion mismatch between the copper and silicon carbide (18.2 x 10^{-6}/°C and 4.23 x 10^{-6}/°C, respectively, at 400°C, the temperature where creep and thus, stress relaxation, begins to occur in copper), it is expected that there could be damage or residual stresses remaining in the composite after heating the samples for thermal conductivity and thermal expansion testing. Back-of-the-envelope calculations of the residual stress using:

$$\sigma = \mathrm{E}\Delta\alpha\Delta\mathrm{T} \tag{6.1}$$

where σ is the residual stress, E is the modulus, $\Delta\alpha$ is the difference in thermal expansion coefficients and ΔT is the temperature difference over which the expansion is occurring, suggest the presence of high tensile stresses in the Cu which exceed 600 MPa. This is significantly higher than the ultimate tensile strength of copper (220 MPa[78]). OOF calculations also indicate high tensile stresses of about 700-800 MPa in the copper-filled pores in a microstructure composed of a regular array of circular pores. The high stresses would cause extreme deformation of the Cu phase, and perhaps cracking in the SiC phase, upon cooling. However, analysis of the samples after high temperature testing does not indicate any damage. Macroscopically, the samples appear unchanged. The samples inspected in the TEM show no evidence of dislocations, the SEM images of cross-sectioned samples exhibit no cracking, and the thermal conductivity measurements before and after high temperature testing indicate no thermal property degradation. Further investigation of these samples is necessary in order to determine the actual stress values being achieved upon heating and cooling of these samples, as well as the residual stresses that result. This testing can be done using high resolution synchrotron X-ray diffraction to determine the residual strains present in each phase, both close to and away from the interfaces.

References

[1] L. J. Gibson and M. F. Ashby. *Cellular Solids Structure and Properties- Second Edition*. Cambridge University Press, Cambridge, UK, 1997.

[2] D. J. Green and P. Colombo. Cellular Ceramics: Intriguing Structures, Novel Properties, and Innovative Applications. *MRS Bulletin*, pages 296–300, 2003.

[3] C. Zweben. Ultrahigh-Thermal-Conductivity Packaging Materials. *IEEE/CPMT Semiconductor Thermal Measurement and Management Symposium (SEMI-THERM)*, pages 168–174, 2005.

[4] C. Zweben. Advances in LED Packaging and Thermal Management Materials. *Proceedings of SPIE*, 6910, 2008.

[5] L. S. Parfen'eva, T. S. Orlova, N. F. Kartenko, N. V. Sharenkova, B. I. Smirnov, I. A. Smirnov, H. Misiorek, A. Jezowski, F. M. Varela-Feria, J. Martínez-Fernández, and A. R. de Arellano-López. Thermal Conductivity of the SiC/Si Biomorphic Composite, a New Cellular Ecoceramic. *Physics of the Solid State*, 47(7):1216–1220, 2005.

[6] A. I. Shelykh, B. I. Smirnov, I. A. Smirnov, A. R. de Arellano-López, J. Martínez-Fernández, and F. M. Varela-Feria. Linear Expansion Coefficient of the SiC/Si Biomorphic Composite. *Physics of the Solid State*, 46(2):216–217, 2006.

[7] C. Zollfrank, N. Travitzky, H. Sieber, T. Selchert, and P. Greil. Biomorphous SiSiC/Al-Si Ceramic Composites Manufactured by Squeeze Casting: Microstructure and Mechanical Properties. *Advanced Engineering Materials*, 7:743–746, 2005.

[8] T. E. Wilkes, M. L. Young, R. E. Sepúlveda, D. C. Dunand, and K. T. Faber. Composites by Aluminum Infiltration of Porous Silicon Carbide Derived from Wood Precursors. *Scripta Materialia*, 55:1083–1086, 2006.

[9] A. Herzog, U. F. Vogt, S. Siegmann, and O. Beffort. Aluminium Metal Matrix Composites Based on Biomorphic Silicon Carbide. *Advanced Engineering Materials*, 8:980–983, 2006.

[10] Y.-J. Lin and S.-Y. Lin. Fabrication of Ceramic-Metal Composites by Melt Infiltration of Moso-Bamboo-Derived Porous SiC. *Key Engineering Materials*, 351:37–42, 2007.

[11] A. R. Studart, U. T. Gonzenbach, E. Tervoort, and L. J. Gauckler. Processing Routes to Macroporous Ceramics: A Review. *Journal of the American Ceramic Society*, 89(6):1771–1789, 2006.

[12] T. Ota, M. Takahashi, T. Hibi, M. Ozawa, S. Suzuki, and Y. Hikichi. Biomimetic Process for Producing SiC "Wood". *Journal of the American Ceramic Society*, 78(12):3409–3411, 1995.

[13] P. Greil, T. Lifka, and A. Kaindl. Biomorphic Cellular Silicon Carbide Ceramics from Wood: I. Processing and Microstructure. *Journal of the European Ceramic Society*, 18:1961–1973, 1998.

[14] P. Greil, T. Lifka, and A. Kaindl. Biomorphic Cellular Silicon Carbide Ceramics from Wood: II. Mechanical Properties. *Journal of the European Ceramic Society*, 18:1975–1983, 1998.

[15] A. R. de Arellano-López, J. Martínez-Fernández, P. González, C. Domínguez, V. Fernández-Quero, and M. Singh. Biomorphic SiC: A New Engineering Ceramic Material. *International Journal of Applied Ceramic Technology*, 1(1):56–67, 2004.

[16] J. Qian, J. Wang, and Z. Jin. Preparation of Biomorphic SiC Ceramic by Carbothermal Reduction of Oak Wood Charcoal. *Materials Science and Engineering A*, 371:229–235, 2004.

[17] J. Cao, O. Rusina, and H. Sieber. Processing of Porous TiO2-Ceramics from Biological Preforms. *Ceramics International*, 30:1971–1974, 2004.

[18] J. Cao, C. R. Rambo, and H. Sieber. Preparation of Porous Al2O3-Ceramics by Biotemplating of Wood. *Journal of Porous Materials*, 11:163–172, 2004.

[19] C. R. Rambo, J. Cao, O. Rusina, and H. Sieber. Manufacturing of Biomorphic (Si, Ti, Zr)-Carbide Ceramics by Sol-Gel Processing. *Carbon*, 43:1174–1183, 2005.

[20] H. Ghanem, M. Kormann, H. Gerhard, and N. Popovska. Processing of Biomorphic Porous TiO2 Ceramics by Chemical Vapor Infiltration and Reaction (CVI-R) Technique. *Journal of the European Ceramic Society*, 27:3433–3438, 2007.

[21] M. Kormann, H. Ghanem, H. Gerhard, and N. Popovska. Processing of Carbide-Derived Carbon (CDC) Using Biomorphic Porous Titanium Carbide Ceramics.

Journal of the European Ceramic Society, 28:1297–1303, 2008.

[22] T. Fan, X. Li, Z. Liu, J. Gu, and D. Zhang. Microstructure and Infrared Absorption of Biomorphic Chromium Oxides Templated by Wood Tissue. *Journal of the American Ceramic Society*, 89(11):3511–3515, 2006.

[23] J. Dinwoodie. *Wood: Nature's Cellular, Polymeric Fibre-Composite*. The Institute of Metals, London, 1989.

[24] M. M. Tang and R. Bacon. Carbonization of Cellulose Fibers- I. Low Temperature Pyrolysis. *Carbon*, 2:211–220, 1964.

[25] M. M. Tang and R. Bacon. Carbonization of Cellulose Fibers- II. Physical Property Study. *Carbon*, 2:221–225, 1964.

[26] F. M. Varela-Feria, J. Martínez-Fernández, A. R. de Arellano-López, and M. Singh. Low Density Biomorphic Silicon Carbide: Microstructure and Mechanical Properties. *Journal of the European Ceramic Society*, 22:2719–2725, 2002.

[27] M. Singh and J. A. Salem. Mechanical properties and microstructure of biomorphic silicon carbide ceramics fabricated from wood precursors. *Journal of the European Ceramic Society*, 22(14-15):2709–2717, 2002.

[28] C. E. Byrne and D. C. Nagle. Carbonization of Wood For Advanced Materials Applications. *Carbon*, 35(2):259–266, 1997.

[29] R. E. Franklin. Crystallite Growth in Graphitizing and Non-Graphitizing Carbon. *Proceedings of the Royal Society of London. Series A, Mathematical and Physical Sciences*, 209(1097):196–218, 1951.

[30] H.-M. Cheng, H. Endo, T. Okabe, K. Saito, and G.-B. Zheng. Graphitization Behavior of Wood Ceramics and Bamboo Ceramics as Determined by X-Ray Diffraction. *Journal of Porous Materials*, 6:233–237, 1999.

[31] K. J. Masters and B. McEnaney. The Development of Structure and Microporosity in Cellulose Carbon. *Carbon*, 22(6):595–601, 1984.

[32] W. B Hillig. Making Ceramic Composites by Melt Infiltration. *American Ceramic Society Bulletin*, 73(4):56–62, 1997.

[33] E. Vogli, H. Sieber, and P. Greil. Biomorphic SiC-Ceramic Prepared by Si-Vapor Phase Infiltration of Wood. *Journal of the European Ceramic Society*, 22:2663–2668, 2002.

[34] Y Wang, S. Tan, and D. Jiang. The Effect of Porous Carbon Preform and the Infiltration Process on the Properties of Reaction-formed SiC. *Carbon*, 42:1833–1839, 2004.

[35] C. Zollfrank and H. Sieber. Microstructure Evolution and Reaction Mechanism of Biomorphous SiSiC Ceramics. *Journal of the American Ceramic Society*, 88(1):51–58, 2005.

[36] P. Greil, E. Vogli, T. Fey, A. Bezold, N. Popovska, H. Gerhard, and H. Sieber. Effect of Microstructure on the Fracture Behavior of Biomorphous Silicon Carbide Ceramics. *Journal of the European Ceramic Society*, 22:2697–2707, 2002.

[37] J.-M. Qian, J.-P. Wang, and Z.-H. Jin. Preparation and Properties of Porous Microcellular SiC Ceramics by Reactive Infiltration of Si Vapor into Carbonized Basswood. *Materials Chemistry and Physics*, 82:648–653, 2003.

[38] H. Robbins and B. Schwartz. Chemical Etching of Silicon 1. The System HF, HNO_3, and H_2O. *Journal of the Electrochemical Society*, 106(6):505–508, 1959.

[39] V.S. Kaul, K. T. Faber, R. E. Sepúlveda, A. R. de Arellano López, and J. Martínez-Fernández. Precursor Selection and its Role in the Mechanical Properties of Porous SiC Derived from Wood. *Materials Science and Engineering A*, 428:225–232, 2006.

[40] K. E. Pappacena, K. T. Faber, H. Wang, and W. D. Porter. Thermal Conductivity of Porous Silicon Carbide Derived from Wood Precursors. *Journal of the American Ceramic Society*, 90(9):2855–2862, 2007.

[41] E. Wheeler. *Wood: Macroscopic Anatomy*, volume 10 of *Encyclopedia of Materials: Science and Technology*. Elsevier, New York, 2001.

[42] K.K. Chawla. *Composite Materials Science and Engineering*. Springer, New York, second edition, 1998.

[43] C. Zweben. Metal-Matrix Composites for Electronic Packaging. *Journal of Materials*, pages 15–23, July 1992.

[44] J. Norley, J. J.-W. Tzeng, G. Getz, J. Klug, and B. Fedor. The Development of a Natural Graphite Heat-Spreader. *IEEE/CPMT Semiconductor Thermal Measurement and Management Symposium (SEMI-THERM)*, pages 107–110, 2001.

[45] G. G. Gnesin and Y. V. Naidich. Contact Reaction of Silicon Carbide with Fused Copper. *Poroshkovaya Metallurgiya*, 2(74):57–63, 1969.

[46] C. Rado, B. Drevet, and N. Eustathopoulos. The Role of Compound FOrmation in Reactive Wetting: The Cu/SiC System. *Acta Materialia*, 48:4483–4491, 2000.

[47] P. Nikolopoulos, S. Agathopoulos, G. N. Angelopoulos, A. Naoumidis, and H. Grubmeier. Wettability and Interfacial Energies in SiC-Liquid Metal Systems. *Journal of Materials Science*, 27:139–145, 1992.

[48] H. Xing, X. Cao, W. Hu, L. Zhao, and J. Zhang. Interfacial Reactions in 3D-SiC Network Reinforced Cu-Matrix Composites Prepared by Squeeze Casting. *Materials Letters*, 59:1563–1566, 2005.

[49] Z. An, M. Hirai, M. Kusaka, and M. Iwami. Surface and Interface Study of Cu (Film)/SiC (Substrate) System. *Applied Surface Science*, 216:169–173, 2003.

[50] M. Shimbo, M. Naka, and I. Okamoto. Wettability of Silicon Carbide by Aluminium, Copper and Silver. *Journal of Materials Science Letters*, 8:663–666, 1989.

[51] G. Sundberg, P. Paul, C. Sung, and T. Vasilos. Fabrication of CuSiC Metal Matrix Composites. *Journal of Materials Science*, 41:485–504, 2006.

[52] P. Majumder, R. Katamreddy, and C. Takoudis. Atomic Layer Deposited Ultrathin HfO_2 and Al_2O_3 Films as Diffusion Barriers in Copper Interconnects. *Electrochemical and Solid State Letters*, 10(10):H291–H295, 2007.

[53] Y.-L. Kuo, H.-H. Lee, C. Lee, J.-C. Lin, S.-L. Shue, M.-S. Liang, and B. J. Daniels. Diffusion of Copper in Titanium Zirconium Nitride Thin Films. *Electrochemical and Solid State Letters*, 7(3):C35–C37, 2004.

[54] C. Lee and Y.-L. Kuo. The Evolution of Diffusion Barriers in Copper Metallization. *Journal of Materials*, pages 44–49, January 2007.

[55] K. Holloway, P. M. Fryer, C. Jr. Cabral, J. M. E. Harper, P. J. Bailey, and K. H. Kelleher. Tantalum as a Diffusion Barrier Between Copper and Silicon: Failure Mechanism and Effect of Nitrogen Additions. *Journal of Applied Physics*, 71(11):5433–5444, 1992.

[56] E. Eisenbraun, A. Upham, R. Dash, W. Zeng, J. Hoefnagels, S. Lane, D. Anjum, K. Dovidenko, A. Kaloyeros, B. Arkles, and J. J. Sullivan. Low Temperature Inorganic Chemical Vapor Deposition of Ti-Si-N Diffusion Barrier Liners for Gigascale Copper Interconnect Applications. *Journal of Vacuum Science and Technology B*, 18(4):2011–2015, 2000.

[57] I. Chen and J. L. Wang. Diffusion Barrier Properties of Sputtered TiB_2 Between Cu and Si. *Journal of the Electrochemical Society*, 147(5):1940–1944, 2000.

[58] P. Alen, M Vehkamaki, M Ritala, and M Leskela. Diffusion Barrier Properties of Atomic Layer Deposited Ultrathin Ta2O5 and TiO2 Films. *Journal of the Electrochemical Society*, 153(4):G304–G308, 2006.

[59] E. R. Weber. Transition Metals in Silicon. *Applied Physics A*, 30(1):1–22, 1983.

[60] S.-Q. Wang, I. Raaijmakers, B. J. Burrow, S. Suthar, S. Redkar, and K.-B. Kim. Reactively Sputtered TiN as a Diffusion Barrier Between Cu and Si. *Journal of Applied Physics*, 68(10):5176–5187, 1990.

[61] J. O. Olowolafe, C. J. Mogab, R. B. Gregory, and M. Kottke. Interdiffusions in Cu/Reactive-Ion-Sputtered TiN, Cu/Chemical-Vapor-Deposited TiN, Cu/TaN, and TaN/Cu/TaN Thin-Film Structures: Low Temperature Diffusion Analyses. *Journal of Applied Physics*, 72(9):4099–4103, 1992.

[62] K.-C. Park and K.-B. Kim. Effect of Annealing of Titanium Nitride on the Diffusion Barrier Property in Cu Metallization. *Journal of the Electrochemical Society*, 142(9):3109–3115, 1995.

[63] K.-C. Park, K.-B. Kim, I. J. M. M. Raaijmakers, and K. Ngan. The Effect of Density and Microstructure on the Performance of TiN Barrier Films in Cu Metallization. *Journal of Applied Physics*, 80(10):5674–5681, 1996.

[64] K.-H. Min, K.-C. Chun, and K.-B. Kim. Comparative Study of Tantalum and Tantalum Nitrides (Ta_2N and TaN) as a Diffusion Barrier for Cu Metallization. *Journal of Vacuum Science and Technology B*, 14(5):3263–3269, 1996.

[65] S.-H. Kim, D.-S. Chung, K.-C. Park, K.-B. Kim, and S.-H. Min. A Comparative Study of Film Properties of Chemical Vapor Deposited TiN Films as Diffusion Barriers for Cu Metallization. *Journal of the Electrochemical Society*, 146(4):1455–1460, 1999.

[66] H. Kizil, G. Kim, C. Steinbruchel, and B. Zhao. TiN and TaN Diffusion Barriers in Copper Interconnect Technology: Towards a Consistent Testing Methodology. *Journal of Electronic Materials*, 30(4):345–348, 2001.

[67] J. Reid. Copper Electrodeposition: Principles and Recent Progress. *Japanese Journal of Applied Physics*, 40(1, 4B):2650–2657, 2001.

[68] G. Sundberg, P. Paul, C. Sung, and T. Vasilos. Identification and Characterization of Diffusion Barriers for Cu/SiC Systems. *Journal of Materials Science*, 40:3383–3393, 2005.

[69] Y. S. Touloukian, R. W. Powell, C. Y. Ho, and P. G. Klemens. *Thermophysical Properties of Matter Volume 1: Thermal Conductivity: Metallic Elements and Alloys*. IFI/Plenum, New York, 1977.

[70] M. Paunovic and M. Schlesinger. *Fundamentals of Electrodeposition*. John Wiley & Sons, Inc., New York, 1998.

[71] F. A. Lowenheim. *Electroplating*. McGraw-Hill Book Company, New York, 1978.

[72] S.-C. Chang, Y.-L. Wang, C.-C. Hung, W.-H. Lee, and G. J. Hwang. Role of Surface Tension in Copper Electroplating. *Journal of Vacuum Science and Technology*, A25(3):566–569, 2007.

[73] K.-M. Shu and G. C. Tu. The Microstructure and the Thermal Expansion Characteristics of Cu/SiC_p Composites. *Materials Science and Engineering A*, A349:236–247, 2003.

[74] P. Yih and D. D. L. Chung. Silicon Carbide Whisker Copper-Matrix Composites Fabricated by Hot Pressing Copper Coated Whiskers. *Journal of Materials Science*, 31(2):399–406, 1996.

[75] A. Brendel, C. Popescu, C. Leyens, J. Wolersdorf, E. Pippel, and Bolt H. SiC-Fibre Reinforced Copper as Heat Sink Material for Fusion Applications. *Journal of Nuclear Materials*, 329-333:804–808, 2004.

[76] A. E. Strevens, S. M. Lipson, A. Drury, M. Kr'ö'ell, H. H. H'ö'rhold, and W. J. Blau. Nanowire Array Electrode Structure for Organic Light Emitting Diodes. *Proceedings of SPIE*, 4876:168–175, 2003.

[77] E. A. Olevsky, X. Wang, A. Maximenko, and M. B. Stern. Sequential Deposition and Electroforming of Metal-Ceramic Composites for Thermal Management Applications. *Surface Engineering*, 23(1):12–17, 2007.

[78] Jr. Callister, W. D. *Materials Science and Engineering An Introduction*. John Wiley & Sons, Inc., New York, 2007.

[79] J. J. Kelly, C. Tian, and A. C. West. Leveling and Microstructural Effects of Additives for Copper Electrodeposition. *Journal of the Electrochemical Society*, 146(7):2540–2545, 1999.

[80] J.J. Kelly and A.C. West. Leveling of 200 nm Features by Organic Additives. *Electrochemical and Solid-State Letters*, 2(11):561–563, 1999.

[81] J. J. Kelly and A. C. West. Copper Deposition in the Presence of Polyethylene Glycol I. Quartz Crystal Microbalance Study. *Journal of the Electrochemical Society*, 145(10):3472–3476, 1998.

[82] J. J. Kelly and A. C. West. Copper Deposition in the Presence of Polyethylene Glycol II: Electrochemical Impedance Spectroscopy. *Journal of the Electrochemical Society*, 145(10):3477–3481, 1998.

[83] J. M. Shieh, S. C. Chang, B. T. Dai, and M. S. Feng. Investigation of Carrying Agents on Microstructure of Electroplated Cu Films. *Japanese Journal of Applied Physics*, 41(11A):6347–6350, 2002.

[84] J. P. Healy, D. Pletcher, and M. Goodenough. The Chemistry of the Additives in an Acid Copper Electroplating Bath Part I. Polyethylene Glycol and Chloride Ion. *Journal of Electroanalytical Chemistry*, 338:155–165, 1992.

[85] M. Hasegawa, Y. Negishi, T. Nakanishi, and T. Osaka. Effects of Additives on Copper Electrodeposition in Submicrometer Trenches. *Journal of the Electrochemical Society*, 152(4):C221–C228, 2005.

[86] R. W. Rice. *Porosity of Ceramics*. Marcel Dekker, Inc., New York, 2001.

[87] J. Francl and W. D. Kingery. Thermal Conductivity: IX, Experimental Investigation of Effect of Porosity on Thermal Conductivity. *Journal of the American Ceramic Society*, 37:99–110, 1954.

[88] V. R. Vedula, D. J. Green, and J. R. Hellman. Thermal Shock Resistance of Ceramic Foams. *Journal of the American Ceramic Society*, 82:649–656, 1999.

[89] R. E. Skochdopole. The Thermal Conductivity of Foamed Plastics. *Chemical Engineering Progress*, 57:55–59, 1961.

[90] L. R. Glicksman and M. R. Torpey. The Influence of Cell Size and Foam Density on the Thermal Conductivity of Foam Insulation. *Polyurethanes World Congress*, pages 80–84, 1987.

[91] D. Gaies and K. T. Faber. Thermal Properties of Pitch-Derived Graphite Foam. *Carbon*, 40:1131–1140, 2002.

[92] M. V. Swain, L. F. Johnson, R. Syed, and D. P. H. Hasselman. Thermal Diffusivity, Heat Capacity and Thermal Conductivity of Porous Partially Stabilized Zirconia. *Journal of Materials Science Letters*, 5:799–802, 1986.

[93] C. Kittel. *Introduction to Solid State Physics*. John Wiley & Sons, Inc., New York, 1996.

[94] E. Behrens. Thermal Conductivities of Composite Materials. *Journal of Composite Materials*, 2(1):2–17, 1968.

[95] C. C. Chamis. NASA Tech. Memo. presented at the 38th Annual Conference of the Society of Plastics Industry (SPI), Houston, TX. 1983.

[96] T. Behzad and M. Sain. Measurement and Prediction of Thermal Conductivity for Hemp Fiber Reinforced Composites. *Polymer Engineering and Science*, 47(7):977–983, 2007.

[97] H.-B. Shim, M.-K. Seo, and S. J. Park. Thermal Conductivity and Mechanical Properties of Various Cross-Section Types Carbon Fiber-Reinforced Composites. *Journal of Materials Science*, 37:1881–1885, 2002.

[98] W. J. Parker, R. J. Jenkins, C. P. Butler, and G. L. Abbott. Flash Method of Determining Thermal Diffusivity, Heat Capacity, and Thermal Conductivity. *Journal of Applied Physics*, 32(9):1679–1684, 1961.

[99] T. Fiedler, E. Solórzano, and A. 'Ö'chsner. Numerical and Experimental Analysis of the Thermal Conductivity of Metallic Hollow Sphere Structures. *Materials Letters*, 62:1204–1207, 2008.

[100] J. K. Farooqi and M. A. Sheikh. Finite Element Modeling of Thermal Transport in Ceramic Matrix Composites. *Computational Materials Science*, 37:361–373, 2006.

[101] S. Grandjean, J. Absi, and D. S. Smith. Numerical Calculations of the Thermal Conductivity of Porous Ceramics Based on Micrographs. *Journal of the European Ceramic Society*, 26:2669–2676, 2006.

[102] A. Hein and V. Kilikoglou. Modeling of Thermal Behavior of Ancient Metallurgical Ceramics. *Journal of the American Ceramic Society*, 90(3):878–884, 2007.

[103] S. A. Langer, E. R. Jr. Fuller, and W. C. Carter. OOF: An Image-Based Finite-Element Analysis of Material Microstructures. *Computing in Science and Engineering*, pages 15–23, 2001.

[104] S. A. Langer, W. C. Carter, E. R. Jr. Fuller, and A. Roosen. *OOF*. National Institute of Standards and Technology, Gaithersburg, MD, 1997.

[105] A. D. Jadhav, N. P. Padture, E. H. Jordan, M. Gell, P. Miranzo, and E. R. Jr. Fuller. Low-Thermal-Conductivity Plasma-Sprayed Thermal Barrier Coatings with Engineered Microstructures. *Acta Materialia*, 54:3343–3349, 2006.

[106] O. Amsellem, K. Madi, F. Borit, D. Jeulin, V. Guipont, M. Jeandin, E. Boller, and F. Pauchet. Two-Dimensional (2D) and Three-Dimensional (3D) Analyses of Plasma-Sprayed Alumina Microstructures for Finite-Element Simulation of Young's Modulus. *Journal of Materials Science*, 43:4091–4098, 2008.

[107] M. W. Barsoum. *Fundamentals of Ceramics*. Institute of Physics Publishing, Bristol, UK, 2003.

[108] W. D. Kingery, H. K. Bowen, and D. R. Uhlmann. *Introduction to Ceramics, Second Edition*. John Wiley & Sons, Inc., New York, 1976.

[109] R. A. Schapery. Thermal Expansion Coefficients of Composite Materials Based on Energy Principles. *Journal of Composite Materials*, 2(3):380, 1968.

[110] H. Wang and R. N. Singh. Thermal Shock Behavior of Ceramics and Ceramic Composites. *International Materials Reviews*, 39(6):228–244, 1994.

[111] W. D. Kingery. Factors Affecting Thermal Stress Resistance of Ceramic Materials. *Journal of the American Ceramic Society*, 38(1):3–15, 1955.

[112] D. P. H. Hasselman. Elastic Energy at Fracture and Surface Energy as Design Criteria for Thermal Shock. *Journal of the American Ceramic Society*, 46(11):535–540, 1963.

[113] D. P. H. Hasselman. Unified Theory of Thermal Shock Fracture Initiation and Crack Propagation in Brittle Ceramics. *Journal of the American Ceramic Society*, 52(1):600–604, 1969.

[114] S. Ding, Y.-P. Zeng, and D. Jiang. Thermal Shock Resistance of In Situ Reaction Bonded Porous Silicon Carbide Ceramics. *Materials Science and Engineering A*, 425:326–329, 2006.

[115] S. Ding, Y.-P. Zeng, and D. Jiang. Thermal Shock Behavior of Mullite-Bonded Porous Silicon Carbide Ceramics with Yttria Addition. *Journal of Applied Physics D: Applied Physics*, 40:2138–2142, 2007.

[116] K. Kuomoto, H. Shimizu, W. S. Seo, C. H. Pai, and H. Yanagida. Thermal Shock Resistance of Porous SiC Ceramics. *Ceramic Notes*, 90(1):32–33, 1991.

[117] J. K. Lee, J. H. Lee, and S. P. Lee. Nondestructive Evaluation of Damage Behavior of Ceramic Under Thermal Shock Cycle. *Key Engineering Materials*, 270-273:497–502, 2004.

[118] R. M. Orenstein and D. J. Green. Thermal Shock Behavior of Open-Cell Ceramic Foams. *Journal of the American Ceramic Society*, 75(7):1899–1905, 1992.

[119] J. She, T. Ohji, and Z.-Y. Deng. Thermal Shock Behavior of Porous Silicon Carbide Ceramics. *Journal of the American Ceramic Society*, 85(8):2125–2127, 2002.

[120] J. P. Singh, Y. Tree, and D. P. H. Hasselmann. Effect of Bath and Specimen Temperature on the Thermal Stress Resistance of Brittle Ceramics Subjected to Thermal Quenching. *Journal of Materials Science*, 16:2109–2118, 1981.

[121] C. Aksel, B. Rand, F. L. Riley, and P. D. Warren. Thermal Shock Behavior of Magnesia-Spinel Composites. *Journal of the European Ceramic Society*, 24:2839–2845, 2004.

[122] J. A. Coppola and R. C. Bradt. Thermal-Shock Damage in SiC. *Journal of the American Ceramic Society*, 56(4):214–218, 1973.

[123] M. Oguma, C. J. Fairbanks, and D. P. H. Hasselman. Thermal Stress Fracture of Brittle Ceramics by Conductive Heat Transfer in a Liquid Metal Quenching Medium. *Journal of the American Ceramic Society*, 69(4):C87–C88, 1986.

[124] K. T. Faber, M. D. Huang, and A. G. Evans. Quantitative Studies of Thermal Shock in Ceramics Based on a Novel Test Technique. *Journal of the American Ceramic Society*, 64(5):296–301, 1981.

[125] V. R. Vedula, D. J. Green, J. R. Hellmann, and A. E. Segall. Test Methodology for the Thermal Shock Characterization of Ceramics. *Journal of Materials Science*, 33:5427–5432, 1998.

[126] W. P. Rogers and A. F. Emery. Contact Thermal Shock Test of Ceramics. *Journal of Materials Science*, 27:146–152, 1992.

[127] E. A. Farber and R. L. Scorah. Heat Transfer to Water Boiling Under Pressure. *Trans. ASME*, 70:369–384, 1948.

[128] R. A. Bemis, K. Shiloh, and W. A. Ellingson. Nondestructive Evaluation of Thermally Shocked Silicon Carbide by Impact-Acoustic Resonance. *Journal of Engineering for Gas Turbines and Power*, 118:491–494, 1996.

[129] A. G. Evans, M. Linzer, H. Johnson, D. P. H. Hasselman, and M. E. Kipp. Thermal Fracture Studies in Ceramic Systems Using an Acoustic Emission Technique. *Journal of Materials Science*, 10:1608–1615, 1975.

[130] E. W. Washburn. The Dynamics of Capillary Flow. *Physical Review*, 17(3):273–283, 1921.

[131] A. Sadezky, H. Muckenhuber, H. Grothe, R. Niessner, and U. Poschl. Raman Microspectroscopy of Soot and Related Carbonaceous Materials: Spectral Analysis and Structural Information. *Carbon*, 43:1731–1742, 2005.

[132] K. Ishimaru, T. Hata, P. Bronsveld, D. Meier, and Y. Imamura. Spectroscopic Analysis of Carbonization Behavior of Wood, Cellulose, and Lignin. *Journal of Materials Science*, 42:122–129, 2007.

[133] L. M. III Clark and R. E. Taylor. Radiation Loss in the Flash Method for Thermal Diffusivity. *Journal of Applied Physics*, 46(2):714–719, 1975.

[134] R. B. Miller. *Forest Products Laboratory Wood Engineering Handbook*. Prentice Hall, Englewood, 1990.

[135] S. P. Gentry. Effect of Pyrolysis Temperature on Biologically-Derived Silicon Carbide, 2008.

[136] V.S. Kaul. Unpublished Work. 2005.

[137] A. Oya and H. Marsh. Review: Phenomena of Catalytic Graphitization. *Journal of Materials Science*, 17:309–322, 1982.

[138] C. E. Byrne and D. c. Nagle. Carbonized Wood Monoliths - Characterization. *Carbon*, 35(2):267–273, 1997.

[139] H. Wang and R. B. Dinwiddie. Development of a Labview^{TM} Based Portable Thermal Diffusivity System. *Destech Publishing Co., Lancaster, PA*, 2004.

[140] T. E. Wilkes, J. Y. Pastor, J. Llorca, and K. T. Faber. Mechanical Properties of Wood-Derived Silicon Carbide Aluminum-Alloy Composites as a Function of Temperature. *Journal of Materials Research*, 23(6):1732–1743, 2008.

[141] *JCPDS International Centre for Diffraction Data File 00-029-1129 (β-SiC).* JCPDS International Centre for Diffraction Data. Newtown Square, PA, 2007.

[142] H. Wang. Personal communication. 2006.

[143] Y. S. Touloukian, R. K. Kirby, R. E. Taylor, and T. Y. R. Lee. *Thermophysical Properties of Matter Volume 13: Thermal Expansion– Non-Metallic Solids.* IFI/Plenum, New York, 1977.

[144] Y. S. Touloukian, R. K. Kirby, R. E. Taylor, and P. D. Desai. *Thermophysical Properties of Matter Volume 12: Thermal Expansion– Metallic Elemcnts and Alloys.* IFI/Plenum, New York, 1977.

[145] D. Qin, C. Shen, H. Wang, L. Guan, and R. Zhang. Preparation of SiC-SiO_2-CuO Composites. *Journal of Materials Science*, 42:7457–7460, 2007.

[146] T. Ota, M. Imaeda, H. Takase, M. Kobayashi, N. Kinoshita, T. Hirashita, H. Miyazaki, and Y. Hikichi. Porous titania ceramic prepared by mimicking silicified wood. *Journal of the American Ceramic Society*, 83(6):1521–1523, 2000.

[147] *JCPDS International Centre for Diffraction Data File 00-004-0836 (copper).* JCPDS International Centre for Diffraction Data. Newtown Square, PA, 2007.

[148] ASTM Standard C373. *Standard Test Method for Water Absorption, Bulk Density, Apparent Porosity, and Apparent Specific Gravity of Fired Whiteware Products.* ASTM, West Conshohocken, PA, 1999.

[149] ASTM Standard E1269. *Standard Test Method for Determining Specific Heat Capacity by Differential Scanning Calorimetry.* ASTM, West Conshohocken, PA, 1999.

[150] H. Wang, R. B. Dinwiddie, and P. S. Gall. Multiple Station Thermal Diffusivity Instrument. *Thermal Conductivity*, 23:119–126.

[151] Y. S. Touloukian and E. H. Buyco. *Thermophysical Properties of Matter Volume 5: Specific Heat: Nonmetallic Solids.* IFI/Plenum, New York, 1977.

[152] Y. S. Touloukian, P. E. Liley, and S. C. Saxena. *Thermophysical Properties of Matter Volume 3: Thermal Conductivity; Nonmetallic Liquids and Gases.* IFI/Plenum, New York, 1977.

[153] ASTM Standard E494-05. *Standard Practice for Measuring Ultrasonic Velocity in Materials.* ASTM, West Conshohocken, PA, 1999.

[154] M. T. Johnson. Personal communication. 2008.

[155] K. J. Konsztowicz. Crack Growth and Acoustic Emission in Ceramics During Thermal Shock. *Journal of the American Ceramic Society*, 73(3):502–508, 1990.

[156] T. E. Wilkes, S. R. Stock, F. De Carlo, X. Xiao, and K. T. Faber. X-ray Computed Microtomography of Beech Wood and Biomorphic Carbon, SiC and Al/SiC Composite. *in progress*, 2008.